Engineering and the Environment

UNIVERSITY OF Southampton

Large scale, population-based finite element analysis of cementless tibial tray fixation

by Francis Galloway

Supervisors: Prof. Mark Taylor and Prof. Prasanth Nair

Thesis for the degree of Doctor of Philosophy

in the

Faculty of Engineering and the Environment
Bioengineering Science Research Group

August 2012

Univserity of Southampton

Abstract

Faculty of Engineering and the Environment
Bioengineering Science Research Group

Doctor of Philosophy

Large scale, population-based finite element analysis of cementless tibial tray fixation

by Francis Galloway

Joint replacements are a common treatment of osteoarthritis, rheumatoid arthritis, or fractures of both the hip and knee. The rising number of procedures being performed each year means that there is a need to assess the performance of an implant design in the general population. The majority of computational studies assessing implants do not take into account inter-patient variability and only use a single patient model. More often than not, it is then assumed that the results can be extrapolated to the general population.

This thesis describes a method allowing population-based assessment of joint replacements, focussing on the tibial tray component of a total knee replacement. To generate a large population of models for finite element analysis, two statistical models were used. One was of the tibia, capturing both the variability of the morphology and bone quality, and the other was of the internal knee loads during a gait cycle. Assessment of the statistical models showed that they could adequately generate representative tibiae and gait cycle loads. An automated method was then developed to size, position, and implant the tibial tray in the generated population of tibiae in preparation for finite element analysis.

The use of a population-based study, a unique approach compared to current studies, was demonstrated using three case studies assessing the performance of the tibial tray. The first case study examined the factors which might increase the risk of failure of the tibial tray and the effect of under sizing the tibial tray on primary stability. Factors such as bone quality and patient weight were seen to increase the risk of failure. It was found that under sizing the tibial tray did not significantly affect the primary stability of the tibial tray. It was also observed that the peak strain occurred during swing phase of the gait cycle, whereas peak micromotion occurred at the beginning of stance phase of the gait.

The second case study investigated the effect of tibia resection depth on primary stability of the tibial tray. A more distal resection was found to increase the peak strain and micromotion of the bone-tray interface. The worsening primary stability with a more distal resection, suggest that to obtain optimal primary stability of the tibial tray it is necessary to resect as little bone as possible.

The third case study compared three tibial tray designs. It was found that the trays with pegs or flanges surrounding the stem tended to perform better, reducing the strain and the micromotion at the bone-tray interface. It was noted that the performance of the trays predicted by the analysis was similar to that observed clinically. This shows the potential use of population-based studies to help predict the clinical outcome of joint replacements.

Acknowledgements

Completing this thesis has been one of the toughest challenges I have ever undertaken. Along the way, I've met new people, had many conversations about joint replacements and been lucky enough to travel to some exotic places to present my research. It has been a rewarding experience and there are a few people who I need to thank.

My first thanks have to go to my supervisors, Professor Mark Taylor and Professor Prasanth Nair. It was Mark who first got me interested in orthopaedic biomechanics and his enthusiasm for the topic kept me interested. Throughout my PhD, I have been expertly pointed in the right direction by both of them. In all the steps along the way, they have listened, advised and have always encouraged me to achieve my best. To Mark and Prasanth, thanks for all your patience and guidance over the last few years.

I had the opportunity to spend a few months abroad during this PhD, working with Heiko Ramm and Max Kahnt in the Medical Planning Group at the Zuse Institute in Berlin (ZIB). Without their expertise and knowledge of all things computational, much of the work in this thesis would not have been possible. I am hugely grateful for their contribution to this thesis and it was a privilege working with them. To Max and Heiko, and everyone else in the group at ZIB, Vielen Dank and a thousand apologies for my appalling German. I thoroughly enjoyed my time in Berlin.

Time spent working in the office would have been much less fun without all my friends and colleagues in the Bio group. To you all, thanks for all the coffee, tea and cake.

My family have also provided much support over the last three and a bit years. To Mum, Dad, Claire and Lydia, thanks for being there. The love and support from my wonderful girlfriend Louise has kept me going to the end. For this, thank you.

Funding for this PhD was gratefully received from the Engineering and Physical Sciences Research Council (EPSRC) and DePuy (a Johnson & Johnson Company).

To the next adventure.

Contents

List of Figures

List of Tables

Acronyms

A-P anterior-posterior.

AAM Active Appearance Model.

ACL anterior cruciate ligament.

ADL activity of daily living.

ASM Active Shape Model.

AX axial.

BMI body mass index.

CPM composite peak micromotion.

CPS composite peak strain.

CT computed tomography.

DOF degrees of freedom.

F-E flexion-extension.

FE finite element.

FFD fast form deformations.

HA hydroxyapatite.

I-E internal-external.

ICP iterative closest point.

LCL lateral collateral ligament.

M-L medial-lateral.

MBD multi-body dynamics.

MCL medial collateral ligament.

MDL minimum description length.

MRI magnetic resonance imaging.

MS musculoskeletal.

OA osteoarthritis.

PC principal component.

PCA principal component analysis.

PCL posterior cruciate ligament.

PFJ patellofemoral joint.

PMMA polymethylmethacrylate.

RA rheumatoid arthritis.

RLL radiolucent line.

RMS root-mean-squared.

RSA radiostereometric analysis.

SM statistical model.

SSIM statistical shape and intensity model.

SSM statistical shape model.

SVD singular value decomposition.

TFJ tibiofemoral joint.

THR total hip replacement.

TKR total knee replacement.

UHMWPE ultra high molecular weight polyethelene.

V-V varus-valgus.

Chapter 1

Introduction

1.1 Background

Joint replacements are a common treatment of osteoarthritis, rheumatoid arthritis, and fractures of both the hip and knee. In the UK, the number of primary total knee replacements (TKRs) has risen from 28,000 in 2004 to over 77,000 in 2010 (National Joint Registry for England and Wales, 2010). This dramatic increase in procedures means the assessment of TKRs in the general population is becoming important. Many computational studies evaluating the performance of the tibial tray often only perform testing using a model of a single patient (Barker et al., 2005; Chong et al., 2010; Hashemi et al., 2000; Keja et al., 1994; Perillo-Marcone et al., 2007; Taylor et al., 1998; Tissakht et al., 1995). A problem with such an approach is that population variability is not taken into account and the results cannot be applied to the general population.

There are a limited number of studies which use models of multiple patients in the testing of the tibial tray. One of the largest studies of the tibial tray to date (Rawlinson et al., 2005) used 9 paired tibiae in experimental tests and finite element (FE) models to study the effect of an augmented stem on a tibial tray. It was found that due to the biological variability between specimens, the displacement between the bone and implant was highly variable, and the effect of the stem inconclusive. Smaller studies only using 4 patient specific models have also been performed to investigate the link between risk of bone failure and the migration of the tibial tray (Perillo-Marcone et al., 2004), and the effect of mal-alignment on the risk of failure of the tibial tray (Wong et al., 2010).

In almost all the studies testing the tibial tray, a fixed magnitude static load is applied. Loads can be scaled by body weight, but this does not represent the significant variation in the ratio of the load components (for example anterior-posterior to axial force) known to occur between subjects (Kutzner et al., 2010).

Performing a large multiple patient studies is challenging; there is limited availability of patient geometry, kinematic, and kinetic data. Collecting clinical data is time consuming and can be expensive. The ethics of exposing patients to radiation during CT scans must

also be considered. Even with a large set of clinical data, current methods for creating bone geometry, positioning and implanting a prosthesis, and generating a FE ready model require significant manual effort. These issues and the need to understand how the differences in patients influence the success of an implant are the motivations for this thesis.

Population-based studies, which incorporate the variability of the bone and joint loading in the models, offer the potential to be able to better predict the performance of a joint replacement. One approach to generating a large population of models is to use a statistical model (SM). There are a large number of techniques for creating SMs of biological data, but most only capture the variability of shape. SMs have been expanded to include the variability of both shape and texture or intensity information as applied to the face (Edwards et al., 1998) and the femur (Bryan et al., 2010). Recently, a statistical shape and intensity model (SSIM) of the femur (Bryan et al., 2010) was used for a population-based study assessing a hip resurfacing (Bryan, 2010). A large population of femurs was sampled from the SSIM, automatically implanted with a hip resurfacing and analysed using FE to assess the risk of failure.

In the literature, there is much debate about the choice of tibial tray fixation. Cementless fixation of the tibial tray is an alternative to the more common cemented fixation (National Joint Registry for England and Wales, 2010). It is thought to be advantageous for younger more active patients, providing long-term fixation without the problems associated with cement degradation (Lombardi et al., 2007). However, there are mixed reports about the success of cementless tibial trays. Studies have reported evidence of extensive radiolucent lines indicating poor fixation (Fuiko et al., 2003), rapid early migration (Albrektsson et al., 1992), aseptic loosening, and poor survivorship in comparison to cemented implants (Berger et al., 2001; Duffy et al., 1998). Studies have also reported good long-term survivorship of cementless TKRs (around 95% after 10 years) (Baker et al., 2007; Bassett, 1998; Hofmann et al., 2001; Holloway et al., 2010; Martin et al., 1997). By using population-based studies, the factors which affect the performance of a cementless tibial tray can be investigated.

1.2 Objectives

The broad aim of this thesis is to combine two SMs, one of the geometry and modulus distribution of the tibia, and another of knee gait cycle kinetics, for use in a population-based FE study of a cementless tibial tray. The SM of the tibia was created following a similar method to Bryan et al. (2010) and Bryan (2010), using an elastic matching surface registration and volume morphing scheme. The SM of the gait cycle kinetics was based on musculoskeletal (MS) modelling data (Worsley et al., 2011). This included all six load components: the anterior-posterior, medial-lateral, and axial forces; and the flexion-extension, varus-valgus, and internal-external moments.

The large scale of population-based studies introduces the problem of how to automate the system. Registration, creation of statistical models, and generation of data are more easily

automated. More challenging is the pipeline to automatically position and implant the tibial tray. This was developed in collaboration with Zuse Institute Berlin (ZIB) and based on mesh intersection and union operations. Accurately sizing and placing the tibial tray is important because incorrect sizing or mal-positioning can cause clinical problems.

Three case studies will be used to demonstrate the use of a population-based study to assess a tibial tray, investigating the variation of strain and micromotion at the bone-tray interface. The first case study will investigate the effect of under sizing the tibial tray, the second examines what effect changing the resection level of the tibia has on the primary stability of the tibial tray, and the third will compare three tibial trays designs. In all these case studies, the intention is to show that a population-based study can help to better understand the factors which influence the tibial tray performance.

1.3 Structure of thesis

This thesis is divided into a further 9 chapters. The literature review is split into three chapters: chapter 2 is an overview of the anatomy and biomechanics of the human knee, and TKRs; chapter 3 describes the current computational assessment of the tibial tray; and chapter 4 discusses how SMs are created and used. A summary of the literature review is found in chapter 5.

The methods used in this thesis for population analysis of the tibial tray are described in chapter 6. This includes the method used to create both the tibia and gait cycle SM, and how the population of models are created, processed and analysed. The three case studies are presented after this, in chapters 7 to 9. Finally, a broad discussion of this work, assessing the limitations and potential future work is given in chapter 10.

Chapter 2

Review of human knee

There is a growing interest in understanding the knee joint as an ageing population means that joint problems are becoming more common. Treatment for diseases, such as osteoarthritis, is often a joint replacement, where an implant is used to replace the articulating surface of the joint with the aim of relieving pain and restoring function. The number of TKRs has increased dramatically in recent years, as previously mentioned in chapter 1. To be able to study the knee and TKRs it is necessary first to review the structure and function of the knee joint. This chapter covers the anatomy of the knee, kinematics and kinetics, the structure and strength of bones, and the history of total knee replacements, considering the reasons for replacement and how they fail.

2.1 Anatomy and function

The human lower limb is adapted for weight bearing, locomotion, and supporting the body in the upright, bipedal posture (Palastanga et al., 2002). It is designed for strength and stability, and many of the bones have adapted to support high mechanical stresses. The limb can be classified into four main regions, gluteal, thigh, leg, and foot (figure 2.1). The regions are split by three main joints, the hip, the knee, and the ankle, and the main supporting bones are considered to be the pelvis, femur and tibia. The motion of the lower limb is controlled by a complex system of muscles and ligaments. Many of the muscles cross over several joints and exert a force on each one. There is a significant coordination of muscle groups to control motions such as standing or walking.

There are three bones in the knee, the femur, the tibia and the patella (figure 2.2). These form two separate articulations, the tibiofemoral joint (TFJ) and the patellofemoral joint (PFJ). The TFJ can be thought of as the primary articulation, allowing a flexion-extension motion, and is the main load bearing joint. The PFJ is a secondary articulation.

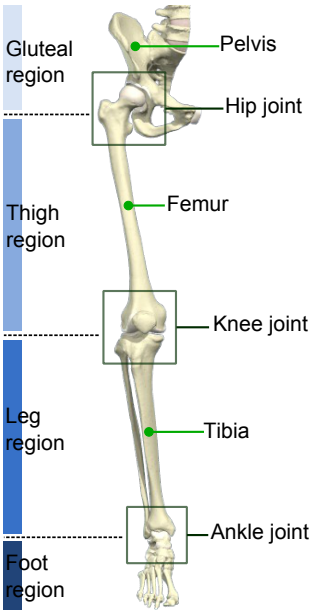

Figure 2.1: Main regions, bones and joints of the lower limb (3D anatomy image copyright of Primal Pictures Ltd, `http://www.primalpictures.com`).

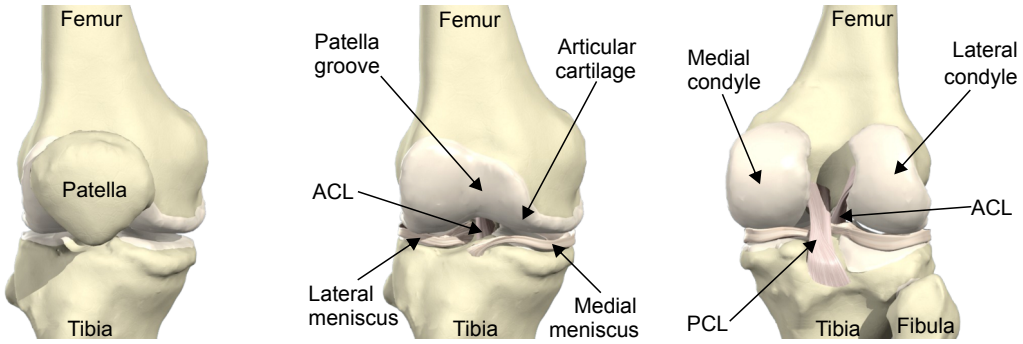

(a) Anterior with patella (b) Anterior view (c) Posterior view

Figure 2.2: The right knee joint with major structures identified (3D anatomy images copyright of Primal Pictures Ltd, `http://www.primalpictures.com`).

2.1.1 Articulating surfaces

On the distal femur, the articular surfaces are the medial and lateral condyles (corresponding to those on the proximal tibia) (figure 2.2c), and the patella groove on the anterior side (figure 2.2b). The condyles have a large, non-spherical, curvature with a reducing radius from anterior to posterior. The condyles are not symmetrical, the medial condyle is longer in the anterior-posterior (A-P) direction and narrower in the medial-lateral (M-L) direction than the lateral condyle. Between the condyles is the intercondylar notch for most of the length, and on the anterior side they are joined by the patella groove. The articular surface of the proximal tibia is also formed of two condyles, the medial and lateral (figure 2.3). These are asymmetrical surfaces separated by a raised bony region, the intercondylar eminence (figure 2.3a). The medial condyle is larger than the lateral condyle and is oval and slightly concave in shape. The lateral condyle is smaller, concave from side to side, but concavoconvex from front to back.

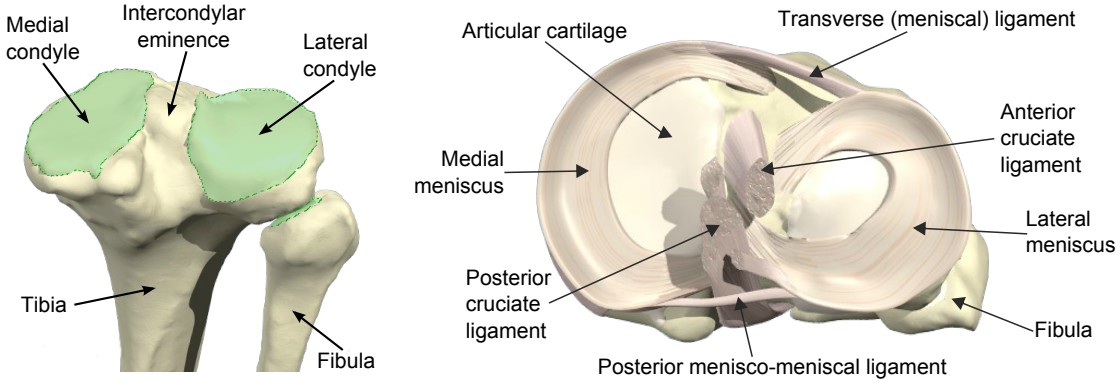

(a) Posterolateral view (b) Inferior view

Figure 2.3: The articulating surfaces of the tibia (a) highlights the condyles and (b) shows the menisci and ligaments (3D anatomy images copyright of Primal Pictures Ltd, `http://www.primalpictures.com`).

The patella is the final articulating surface, a small oval shaped bone (figure 2.2a), which can be divided into a larger lateral region and a smaller medial region by a vertical ridge. The posterior side of the patella is covered with thick cartilage to help protect it from the high stresses experienced during motion. It is attached to the tibia and femur by the patellofemoral ligaments (figure 2.5).

The articular surfaces of the bones are covered by articular cartilage, protecting the ends of the bone and aiding near friction-free motion of the joint. The cartilage varies in thickness, from 3–7 mm and has some degree of elasticity (Palastanga et al., 2002), helping to distribute the large vertical forces.

Additionally, two menisci (medial and lateral) are found in the TFJ joint attached to the tibia (figure 2.3b). These are 'half moon' shaped discs with a wedge shaped cross section of articular cartilage, which have a number of functions (Evans, 1986; Palastanga et al., 2002):

(i) Increase the congruency between the surfaces of the femur and tibia

(ii) Better distribute the weight across the joint

(iii) Reduce the friction between the articulating surfaces

(iv) Perform a role in the locking mechanism

The medial meniscus is the larger of the two, semi-circular in shape, and is broader posteriorly than anteriorly. The lateral meniscus is approximately four-fifths of a circle in shape and has uniform breadth. Both menisci are attached to the tibia by their anterior and posterior horns by ligaments.

2.1.2 Joint capsule

The knee is surrounded by a joint capsule, a composite ligament sleeve surrounding the tibia and femur formed by muscle tendons and their expansions (figure 2.4). It does not surround the joint completely. The patella and ligamentum patellae form the capsule on the

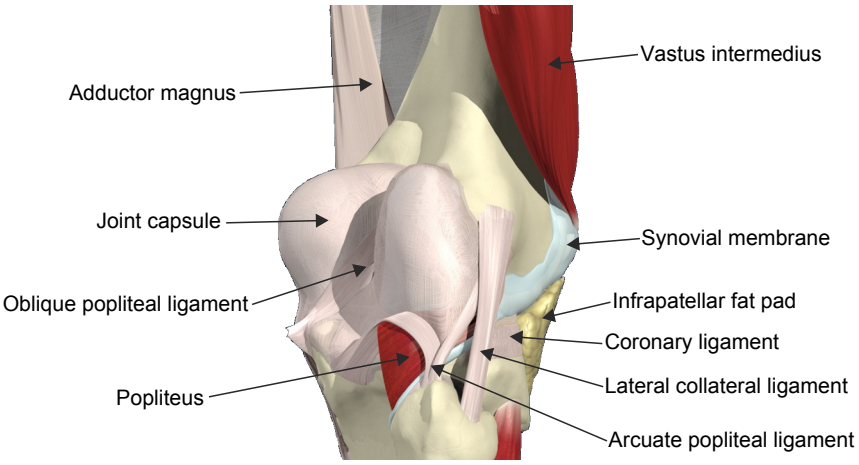

Figure 2.4: Posterolateral view of the knee showing the joint capsule and ligaments (3D anatomy image copyright of Primal Pictures Ltd, `http://www.primalpictures.com`).

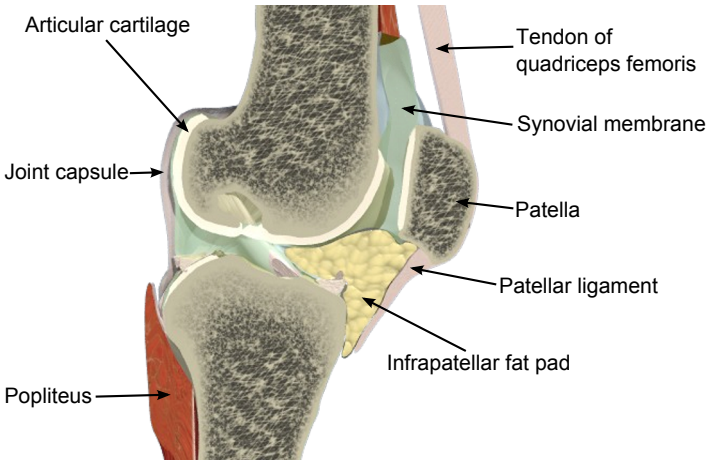

Figure 2.5: Cross section of knee showing the joint capsule (including patella ligaments), synovial membrane and articular surfaces (3D anatomy image copyright of Primal Pictures Ltd, `http://www.primalpictures.com`).

anterior of the femur and it is not attached to the tibial tuberosity (figure 2.5). The capsule is strengthened by the ligaments which hold the joint together.

Within the joint capsule is the synovial membrane which defines the joint cavity (figure 2.5). This is the largest space within the body between two articulating surfaces. The membrane covers the posterior side of the patella, covering the deep side of the infrapatella fat pad. It runs over the articular surfaces of the femur and tibia, going over the upper surface of the menisci and then underneath to the tibia. The purpose of the membrane is to lubricate the joint by secreting synovial fluid into the joint cavity.

2.1.3 Ligaments

The incongruence between the articulating surfaces means the knee joint is inherently unstable. A set of four main ligaments (figure 2.2) stabilise the joint (Palastanga et al., 2002):

- **Anterior cruciate ligament (ACL).** Attached on the anterolateral side of the tibia, it run posterior of the lateral femoral condyle and twists by approximately 110°. The ACL

tightens during extension resisting hyperextension and prevents posterior displacement of the femur (relative to the tibia).

- **Posterior cruciate ligament (PCL).** Attached on the posterior intercondylar area of the tibia, it passes the ACL on the medial side attaching to the femur on the lateral surface of the medial condyle. The PCL resists hyperflexion and anterior displacement of the femur (relative to the tibia).
- **Medial collateral ligament (MCL).** A strong flat ligament, extending from the medial epicondyle of the femur, running down and attaching to the medial tibia condyle and medial side of the tibial shaft.
- **Lateral collateral ligament (LCL).** A short rounded ligament, attached to the lateral epicondyle of the femur and running down to the head of the fibula on the lateral side.

There is also the patella ligament (ligamentum patallae) holding the patella in place (figure 2.5). This ligament is a continuation of the tendon of quadriceps femoris. It is a strong, flat band attached to the apex of the patella and extending down to the tibial tuberosity, providing support for the anterior of the knee and contributing to the strength of the joint capsule.

2.1.4 Muscles

The motions of the knee are controlled by the complex interaction of the lower limb muscles (figure 2.6) and knee ligaments. The knee is a 12 degree of freedom system, with 3 rotations and 3 translations for both the TFJ and PFJ. The primary motion of the TFJ is flexion-extension, with the hamstrings controlling flexion and the quadriceps femoris controlling extension. The muscles used in the main movements of the knee are given in table 2.1.

Table 2.1: Muscles of the knee

Motion	**Active Muscles**
Flexion	Hamstrings, Gastrocnemius, Gracilis, Sartorius
Extension	Quadriceps femoris (Rectus femoris, Vastus lateralis, Vastus medialis, Vastus intermedius), and Tensor fascia lata
Lateral rotation	Bicpes femoris
Medial rotation	Semitendinosus, Semimembranosus, Gracilis, Sartorius, Popliteus

2.1.5 Movements

Medical imaging, such as computed tomography (CT), magnetic resonance imaging (MRI), X-ray, radiostereometric analysis (RSA) and fluoroscopy, has allowed the motions of the cadaveric knee (Hill et al., 2000; Iwaki et al., 2002; Nakagawa et al., 2000) and the living knee to be studied (Johal et al., 2005). The primary motion of the TFJ is flexion-extension (F-E) with a small degree of A-P translation and internal-external (I-E) rotation. Secondary motions of M-L translation and varus-valgus (V-V) rotation also occur, however these are

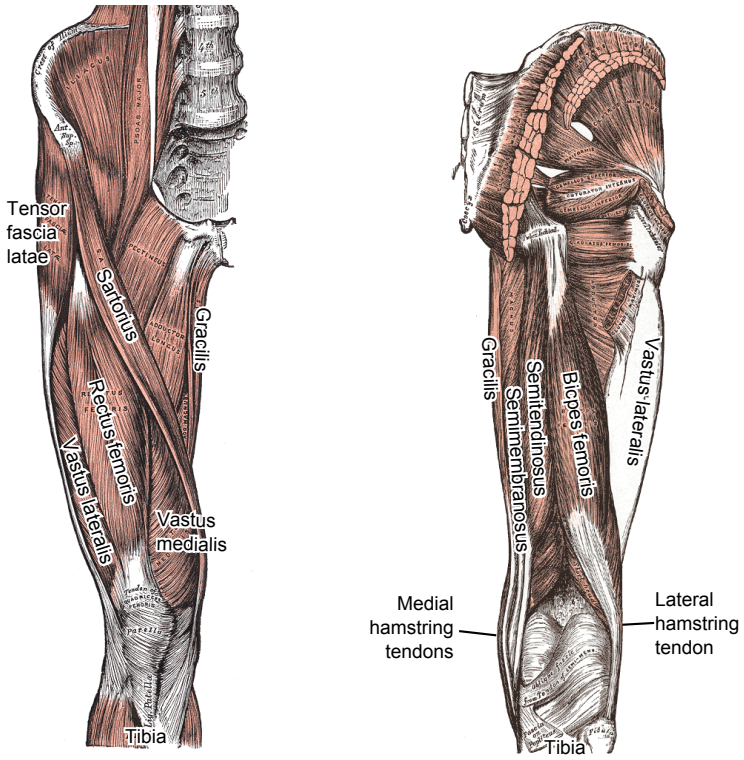

Figure 2.6: Main muscles controlling motion of the knee. Left is anterior view and right is posterior view (images from Gray, 1918).

extremely small in a healthy knee. In a review of the movement of the knee Freeman et al. (2005) divides the F-E arc into three sub arcs: (i) full extension to between 10° and 30° flexion termed 'arc of terminal extension', (ii) an arc from between 10° and 30° flexion to approximately 120° flexion called the 'active functional arc', and (iii) an arc from about 120° to full passive flexion called the 'passive flexion arc' (figure 2.7).

Arc of terminal extension. The use of this arc is limited in daily activities, except for perhaps during one-leg stance (Freeman, 2001). The arc starts from the limit of passive extension, normally between 5° flexion to 5° hyperextension and stops at a point in the arc of active function (Freeman et al., 2005). The shape of the femoral condyles results in the medial condyle 'rocking' between 30° and 10° flexion moving the point of contact with the tibia to the anterior of the condyle. As the knee extends further, the motion remains pure sliding and there is no (or very little) A-P movement of the femur (Freeman, 2001). In contrast, the lateral femoral condyle 'rolls' down over the tibial condyle, as the condyle is shorter and flatter. The combination of the two different motions of the femoral condyles relative to the tibia means that the femur internally rotates (Freeman, 2001). For the last 10° of extension, the ligaments (both cruciate and collateral) provide a progressive resistance to the movement to 'lock' the knee in full extension. Perhaps the most important ligament at this instance is the ACL which is fully elongated at approximately 10° flexion, forcing the internal rotation of the femur (Freeman, 2001) and resulting in a 'screw-home' motion.

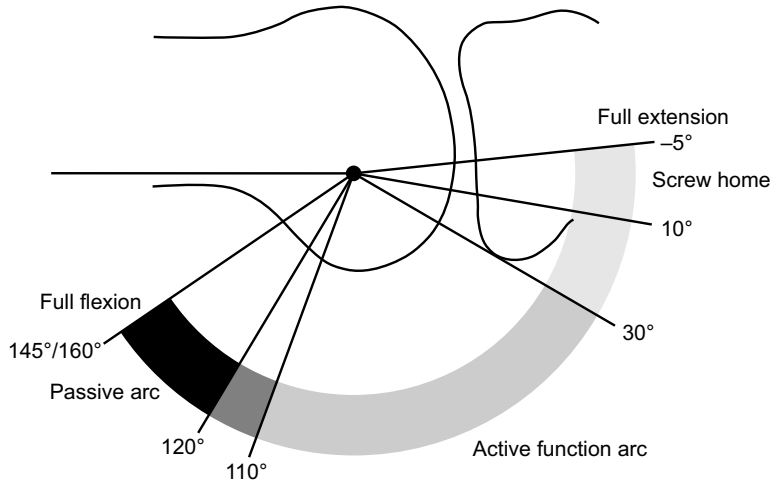

Figure 2.7: Flexion arc of the TFJ (image reprinted from Freeman, 2001, with permission from Elsevier).

Active function arc. This arc covers almost all the activities of daily living and active muscle control produces the movement, as suggested by the name (Freeman, 2001). The medial condyle is almost spherical in shape allowing F-E and I-E rotation with very little or no translation (Freeman et al., 2005). The lateral femoral condyle translates posteriorly relative to the tibia by rolling and/or sliding during flexion, and is coupled with the movement of the lateral meniscus (Freeman, 2001). The difference in relative motion of the femoral condyles relative to the tibia means that femur tends to rotate externally by about 30° between 10° and 120° flexion. The relative rotation of the femur appears not to be coupled to the flexion. That is, it is possible for the tibia to rotate by about 30° and for the femur to flex without external rotation between 20° and 90° flexion (Freeman et al., 2005). During external rotation of the tibia relative to the femur, the lateral femoral condyle moves anterior over the lateral tibial condyle, and the medial femoral condyle moves posterior over the medial tibial condyle. The opposite motion occurs in internal rotation. The medial condyle moves less in comparison to the lateral condyle because of the shape difference between them.

Arc of passive flexion. The movement in this arc is passive and in order to flex the femur/tibia beyond 120° an external force, e.g. body weight, is required. This arc is used in activities such as squatting and full kneeling and starts in the transition zone between 110° to 120° flexion and continues to the passive limit of the knee (Freeman et al., 2005). This limit differs between between populations, Caucasians can achieve around 140° flexion, whereas in Japanese, Indian and Middle Eastern populations full kneeling or squatting is common, and up to 165° flexion can be achieved (Freeman et al., 2005). To achieve this, the medial femoral condyle rolls up on to the posterior horn and the lateral femoral condyle continues to move posteriorly beyond 120° flexion until it is posterior to the tibia and rests on the posterior horn of the lateral meniscus (Freeman, 2001). As contact is lost between the tibia and femur and the movement is considered passive, the TFJ could be considered subluxed (Freeman et al., 2005).

2.1.6 Measurement of kinematics and kinetics

The knee is subjected to a wide range of loading patterns which differ between subjects and activities. To test a TKR realistically, knowledge of loading patterns from activities of daily living (ADLs) is required. Both the magnitude of the loads and the frequency with which activities occur are important. For example, although sitting (a 'passive' activity) occurs more frequently, it places a lower demand on the knee compared to stumbling (an 'active' activity), which places an extreme load on the knee, but occurs infrequently. This has been studied for total hip replacement (THR) patients (Morlock et al., 2001), and for the majority of the time the patients performed 'passive' activities. Of the 'active' activities, the most frequent was walking (10.2% of the time) followed by stair-climbing (0.4% of the time).

The kinematics of the knee can be measured or computed with a variety of methods. Often, skin or exoskeletal markers coupled with video recording is used to track motion. This is non-invasive, but the markers suffer from soft tissue artifact errors as the skin can move relative to the bone. Radiographic imaging, such as fluoroscopy, allows accurate tracking of the movement of the knee, but the subject is exposed to radiation and measurements out of plane can be inaccurate. In the past, markers rigidly fixed to the bone have been used to more accurately track movement of the knee (Lafortune et al., 1992). The disadvantage is that an invasive surgical procedure to insert intra-cortical pins is required and the subject might experience discomfort, altering the movement pattern of the activity.

Measuring the kinetics of the natural knee remains a challenge because it is simply not possible to put a device *in vivo*. MS modelling, used to predict joint kinematics and kinetics, is a major area of research in biomechanics. Inverse-dynamic models can predict the net joint loads and muscle forces, requiring motion and force data (e.g. ground reaction force data) for the body of interest. Coupled with optimisation techniques, the internal joint loads and muscle forces can be estimated. Several studies have used MS modelling to compare the kinematics and kinetics of the knee for level gait (Morrison, 1970; Taylor et al., 2004; Worsley et al., 2011), stair ascent (Costigan et al., 2002; Reid et al., 2010), sit-stand (Worsley et al., 2011), and squatting (Nagura et al., 2002). However, in the modelling process a large number of errors can be introduced, from skin artifact errors during motion capture to inaccuracies in the assumptions made during MS modelling (Riemer et al., 2008).

Telemetric prosthesis, pioneered by Bergmann et al. (1993) for the THR, have been used to measure *in vivo* joint loads. Following from this, Taylor et al. (1998) and Taylor et al. (2001) used an instrumented distal femoral replacement to measure the forces in the bone and then computed the forces at the knee. Telemeterised prosthesis for the knee have also been developed. D'Lima et al. (2006) used a tibial tray with four load cells (one in each quadrant) to measure the axial force *in vivo* for sit-stand, standing, walking, and stair ascent activities. The second generation of this device used 12 strain gauges allowing the three forces and three moments of the knee to be measured for a variety of activities: walking and jogging on a treadmill, using fitness equipment (rowing, cycling, stair-climbing, and leg-press machines), and a golf swing (D'Lima et al., 2008). However, only the peak forces in the

tibia were reported for these activities, which does not give enough information about the *in vivo* kinetics of the knee. A similar device has been implanted in five TKR patients as part of the Orthoload project (Bergmann, 2008). The load data for the three forces and three moments is published for ADLs (Heinlein et al., 2009; Kutzner et al., 2010), and is available for download. This data shows that there is large inter-patient variability in the loading for different activities.

One problem with the currently published data is that the activities are performed under laboratory conditions. The most recent development of telemeterised implants has been the miniaturisation of the sensing equipment (D'Lima et al., 2011). This has allowed the patient to perform activities outside of the laboratory in a more natural environment and internal joint loads of the knee have been measured in patients performing activities such as skiing.

The *in vivo* load data has given a wealth of information about the kinetics of the knee, particularly with the data made available from Orthoload, which provides data to validate MS models. Much of this data forms the basis of input data for pre-clinical testing, whether for experiments (e.g. simulator testing) or computational studies. Despite the range of activities for which there is data, much literature focuses on the gait loading cycle, as it is the most frequently 'active' activity. The focus of this work is also around the gait cycle and the next section looks at the loading of the knee during gait.

2.1.7 The gait cycle

The gait cycle is normally taken as the period of time from when the heel of one foot strikes the floor and continues until the heel strikes the floor again (Trew et al., 2001). There are two phases to the gait cycle, stance phase and swing phase, defined for the limb under consideration. During stance phase the limb is in contact with the floor, and during swing phase the limb is swinging forwards in preparation for the next step. In walking gait, there is a period of time when both limbs are in contact with the floor, called the double stance.

In the stance phase of gait, the lower limb must provide support for body weight, maintain balance, and allow forward propulsion (Trew et al., 2001). The stages of stance phase are (figure 2.8):

- Heel strike. In normal walking, this is the point at which the heel of leading limb first contacts the floor. The following limb is also in contact with the floor, giving double stance. The knee extends just before contact, and flexes just after.
- Foot flat. Immediately after heel strike, the foot moves to be flat on the floor and further flexion of the knee occurs.
- Mid-stance. Body is carried forward over stance limb and opposite limb is in swing phase. The knee reaches peak stance phase flexion and begins to extend again.
- Heel off. The heel lifts off the ground, preparing the limb for push off. Peak extension of the knee occurs around heel off.

- Push off. The foot pushes off against the floor providing propulsion. The knee flexes in preparation for toe off.
- Toe off. End of stance phase as the the contact between the toes and floor is lost. Knee is flexed at half the peak flexion angle in swing phase.

In the swing phase of gait, the swinging limb moves in front of the stance limb, in preparation for the stance phase (Trew et al., 2001). The limb is not lifted far from the ground to conserve energy. The stages of swing phase are (figure 2.8):

- Acceleration. Hip and knee are both flexed, and the swinging limb is accelerated forwards.
- Mid-swing. The moment the swinging limb passes the stance limb corresponding with mid-stance of the opposite limb. The knee is flexed.
- Deceleration. Muscles work to decelerate the swinging limb, ready for heel strike. The knee moves from flexion to extension.

2.1.8 Loading during gait

The patterns of kinematics and kinetics of the knee during gait depend on the population, as both are dependent on knee pathology. Generally, for a healthy population the gross flexion angle during gait has a double peak, approximately 20° in stance phase, and 60° in swing phase (figure 2.8). The resultant force is dominated by the axial force, which has a double peak during stance phase, and has a small magnitude during swing phase (figure 2.8). The resultant moment is dominated by the V-V moment (figure 2.8).

In vivo data from telemeterised implants has given an insight of the intra- and inter-patient variability of loading. From the five Orthoload TKR patients, the intra-patient peak resultant force varied by around 0.5 BW during gait, and the inter-patient variation was observed to be slightly higher, around 0.7 BW (Kutzner et al., 2010). The actual range of peak forces were 2.2 BW to 3 BW for the resultant force, −0.28 BW to 0.18 BW for the the M-L force, and −0.38 BW to 0.2 BW for the A-P force. The F-E moment ranged from 0.009 Nm/BW extension to 0.029 Nm/BW flexion, the V-V moment ranged from 0.41 Nm/BW valgus to 0.18 Nm/BW varus, and the I-E rotation moment ranged from 0.015 Nm/BW internal to 0.011 Nm/BW external. More variation was observed in the moments, particularly during stance phase of gait, and, whilst the peak to peak moments were comparable, the magnitudes of the loads between the five patients could vary considerably.

In the literature, few studies present the full set of loading data. Many just give the peak loading data, often only for axial force. With the data that is available, it can be observed that MS models often overestimate the loads in comparison to *in vivo* data (tables 2.2 and 2.3). One reason for this is simplifications made and errors introduced in the modelling process. Another reason is the different population groups studied, using MS modelling healthy and pathological (TKR or otherwise) knees can be studied, whereas using a telemeterised implant,

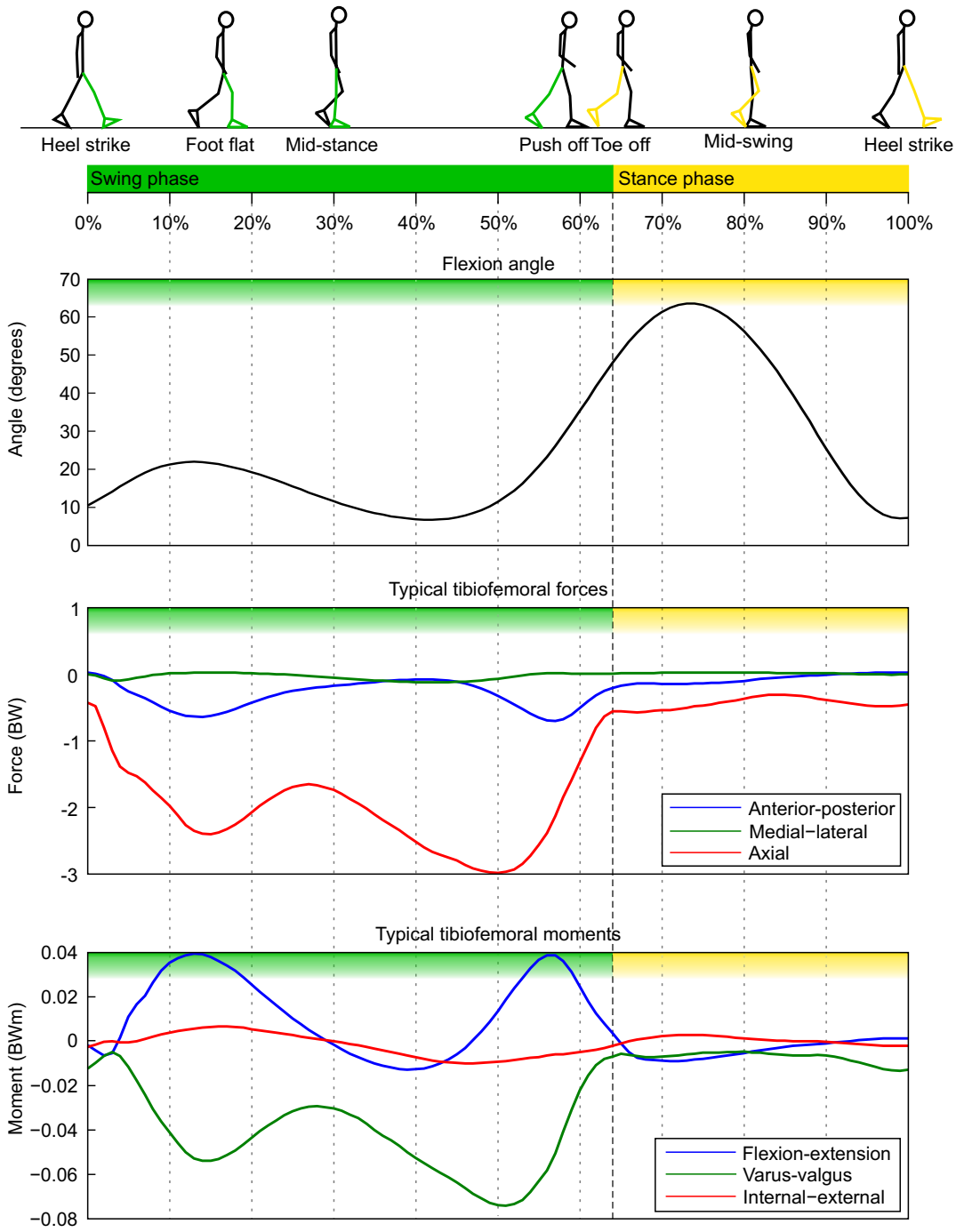

Figure 2.8: Terminology and timing of the gait cycle (based on Trew et al., 2001) with approximately corresponding flexion angle, forces, and moments. The force and moment data is averaged from MS models of 20 healthy elderly subjects (data from Worsley et al., 2011).

the patients must, obviously, have had a TKR. There are also differences in the number of subjects used in the studies. Larger groups of subjects can be used in MS studies, which are more likely to show higher inter-patient variability.

The peak loads of other ADLs are also reported in the literature. Stair ascent and descent can generate a larger peak resultant force, which averages around 3 BW compared to 2.5 BW for gait (D'Lima et al., 2007; Kutzner et al., 2010). Activities such as jogging, tennis, and

Table 2.2: Summary of peak forces during a gait cycle from both *in vivo* data and MS modelling data. The data shown is dependent on what was published (i) $F \pm \sigma$ is the mean peak force (F) and standard deviation (σ), (ii) F ($F_{\min}$–$F_{\max}$) is the mean peak force and in brackets is the range of the peaks observed, and (iii) $F_{\min}$–$F_{\max}$ is the range of the force where the sign indicates the direction.

Study	**Pathology**	**n**	**Force (BW)**		
			AX	A-P	M-L
In vivo					
D'Lima et al. (2006)	TKR	1	2.17	NA	NA
D'Lima et al. (2007)	TKR	1	0.7–2.2	0–0.3	−0.2–0.35
Heinlein et al. (2009)	TKR	2	−2.76––15	−0.29–0.28	−0.20–0.21
Kutzner et al. (2010)	TKR	5	2.3–3.0	−0.25–0.15	−0.14–0.11
MS modelling					
Morrison (1970)	Healthy	12	3.03 (2.06–4.0)	NA	0.26
Costigan et al. (2002)	Healthy	35	3.7 ± 1.1	0.51 ± 0.16	0.15 ± 0.05
Taylor et al. (2004)	THR	4	3.1 (2.9–3.2)	0.5(0.4–0.6)	NA
Shelburne et al. (2006)	Healthy	1	2.4	NA	NA
Worsley et al. (2011)	Healthy	20	3.06 ± 0.89	0.70 ± 0.31	0.14 ± 0.08

golf can generate a peak resultant force of around 4 BW (D'Lima et al., 2008) and carving the slopes whilst skiing generates a resultant force of 4.3 BW (D'Lima et al., 2011). Although these activities generate a higher peak resultant forces, it is unlikely that the 'average' TKR patient will run or ski frequently, if at all.

Comparison of the moments generated during different activities (based on the average peak for all patients) has to be drawn from Kutzner et al. (2010) as a comprehensive set of data is provided. The flexion moment during gait (0.019 Nm/BW) is within the range of other activities, 0.012 BWm during sit-stand to 0.032 BWm during stair descent. Higher valgus moments are found for activities where deep(er) flexion occurs; during knee bend the valgus moment was 0.016 BWm compared to 0.01 BWm during gait. The highest varus and F-E moments were during gait.

The peak loads during gait are similar to other activities, and, whilst higher peak loads might be seen during ADLs such as stair ascent or stair descent, more time is spent walking. Therefore, gait is a suitable loading pattern for pre-clinical testing. There is large variability observed in the knee loads which is important to account for in pre-clinical testing. In addition to understanding the loading conditions for testing, it is also necessary to examine the properties of bone as it can influence the success or failure of a TKR.

2.1.9 Structure and strength of bones

Bone is an extremely hard material formed of two components, a mineral phase, and an organic phase. The mineral phase is primarily calcium phosphate, provides resistance to tensile loads, and gives bone hardness and rigidity. The organic phase is a matrix of fibrous tissue, provides resistance to compressive loads, and gives bone its toughness and elasticity.

Table 2.3: Summary of peak moments during a gait cycle from both *in vivo* data and MS modelling data. The data shown is dependent on what was published (i) $M \pm \sigma$ is the mean peak moment (M) and standard deviation (σ), (ii) M ($M_{\min}$–$M_{\max}$) is the mean peak moment and in brackets is the range of the peaks observed, and (iii) $M_{\min}$–$M_{\max}$ is the range of the moment where the sign indicates the direction.

Study	**Pathology**	**n**	**Moment (BWm)**		
			F-E	V-V	I-E
In vivo					
Heinlein et al. (2009)	TKR	2	−0.003–0.015	−0.043–0.011	−0.01–0.01
Kutzner et al. (2010)	TKR	5	−0.009–0.019	−0.03–0.01	−0.011–0.005
MS modelling					
Costigan et al. (2002)	Healthy	35	0.06 ± 0.01	0.05 ± 0.02	0.01 ± 0.004
Worsley et al. (2011)	Healthy	20	0.04 ± 0.03	0.07 ± 0.03	0.01 ± 0.01

The composition of the two phases depends upon age, sex, anatomical position both within the body and bone, and pathology.

Bones can be classified by their shape; both the femur and tibia are long bones. This type of bone typically consists of a central cylindrical shaft (diaphysis) and two expanded ends (epiphyses) (Palastanga et al., 2002). Conical regions (metaphyses) connect the diaphysis to each epiphysis. The ends of a long bone are often wider than the shaft because they are covered in articular cartilage and must carry the joint loads. The shaft region of a long bone is made up of an outer ring of cortical bone that surrounds a cavity of marrow bone. The end regions of a long bone have an outer shell of cortical bone with 'spongy' cancellous bone inside. At the macroscale, the properties and structure of the two types of bone, cortical and cancellous, are different, but are important when examining how bone responds to an implant. Conversely, at the microscale, the properties and structure of cortical and cancellous bone can be considered similar. Bone can be classified as cortical or cancellous based on the density relative to fully dense cortical bone (normally assumed to be approximately 1.8 g/cm^3) (Huiskes et al., 2005). The relative density of cancellous bone is about 0.05 ($\sim$90% porosity) to 0.7 ($\sim$30% porosity). Cortical bone has a higher relative density, from about 0.7 to 0.95 (Huiskes et al., 2005).

Cortical bone is a solid compact tissue, and at the microstructure level is composed of three layers: a thin outer layer of laminar bone, a middle layer of interstitial bone, and an inner layer of laminar bone. The laminar bone is formed of layers concentrically arranged lamellae. Osteons, aligned along lines of high stress, make up the interstitial bone and contain the nerves and blood vessels for the surrounding tissue. Cortical bone is transversely isotropic, stronger longitudinally than transversely, with reported elastic moduli of 17.4 GPa and 9.6 GPa respectively (Guo, 2001).

Cancellous bone is composed of an interconnected series of rods and plates called trabecula (figure 2.9a), forming a porous structure. The morphology and density of cancellous bone depends on the atomic site and loading conditions. The formation and development of the trabeculae is a response to environmental mechanical factors, controlled by a biological

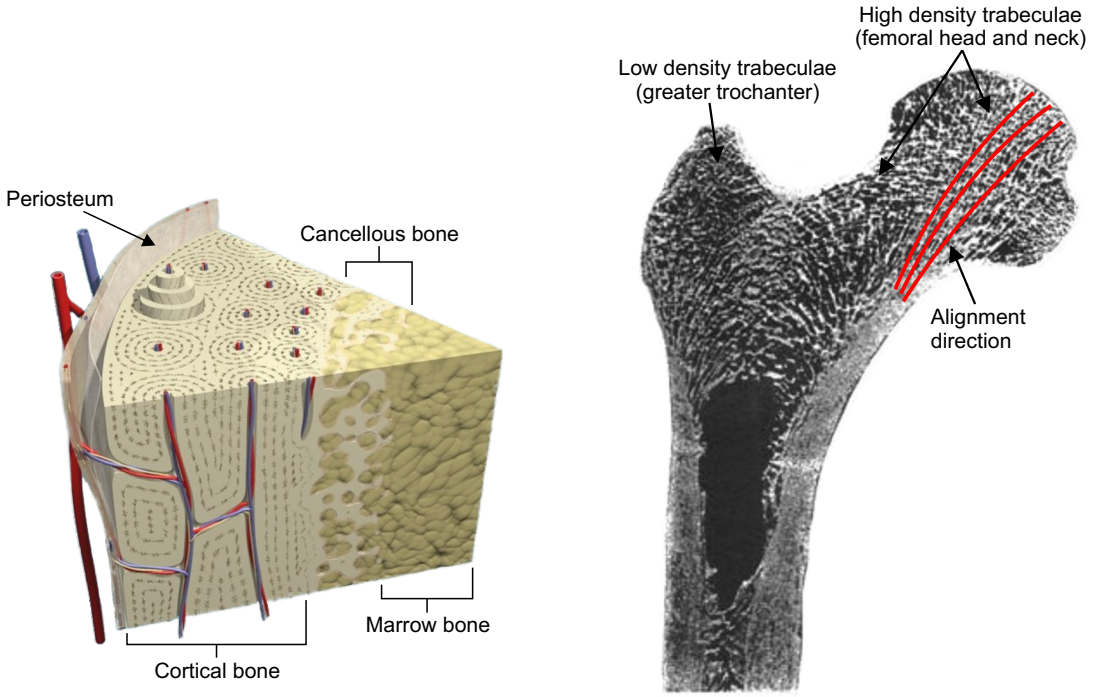

(a) Macroscale structure

(b) Trabeculae of the proximal femur

Figure 2.9: The structure of bone: (a) the macroscale structure of bone (image copyright of Primal Pictures Ltd, `http://www.primalpictures.com`) and (b) the trabecular structure of the femur (image from Huiskes, 2000, with permission from Wiley).The most dense region of trabeculae is in the femoral neck.

regulatory process, first proposed by Wilhelm Roux (Huiskes, 2000). This means that over time, bone adapts to the loads it experiences. In regions of high loads, the density of trabeculae increases and they tend to align in the load direction for maximum strength (e.g. figure 2.9b in the femoral head and neck). In regions of low loads, there is a lower density of trabeculae and the alignment is almost random (e.g. figure 2.9b in the greater trochanter of the femur).

The adaptive response of cancellous bone to loading, whereby bone is placed where it is needed, means that it is heterogeneous and anisotropic. Regional differences in volume fraction, the arrangement of trabeculae, and tissue properties results in a wide variation of mechanical properties (Keaveny et al., 2001). Heterogeneity is apparent in the proximal tibia, where the elastic modulus varies by an order of magnitude within a transverse section (Goldstein et al., 1983). Experimental tests have shown that cancellous bone is anisotropic in both modulus and strength.

The mechanical properties of bone are dependent on many factors: age, anatomic site, pathology, load direction, and load type (tension versus compression versus shear) (Keaveny et al., 2001). The most important factors affecting the elastic modulus and strength are anatomic site (Morgan et al., 2003), density (which varies with anatomic site), and load direction. Many modulus-density relationships have been reported (Helgason et al., 2008) and they generally take the form of a power law

$$E = A\rho^b, \tag{2.1}$$

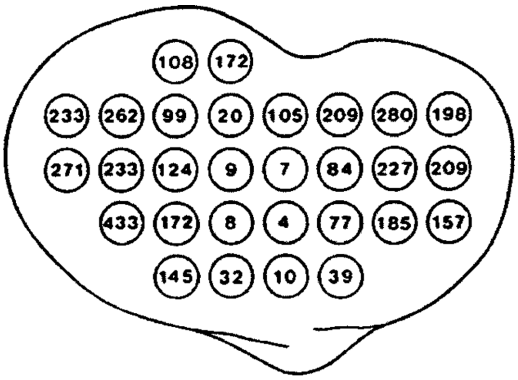

Figure 2.10: Elastic moduli of a transverse section of the proximal tibia. In the centre, the elastic modulus is below 10 MPa and around the periphery it is over 100 MPa (image reprinted from Goldstein et al., 1983, with permission from Elsevier).

where E is elastic modulus, ρ is density, and A and b are constants. Studies which have reported the dependence of elastic modulus on density also generally show the dependence of ultimate stress on density by a linear or power law relationship (Keaveny et al., 2001).

When considering the failure of bone, the anatomic site must be known, as strength, like modulus, can vary by an order of magnitude between sites. Strength behaviour of cancellous bone is complex, as it has a lower strength in shear than tension than compression. However, it is perhaps simpler to characterise failure by strain instead of stress. The linear relationship between failure stress and corresponding elastic modulus implies that the failure strain is relatively constant for cancellous bone, because the ratio between stress and strain is modulus (Keaveny et al., 2001). In bovine bone, tests have shown that yield strains are higher in compression (0.97%) than tension (0.80%) and are isotropic (Chang et al., 1999). Experimental measurements of strain have shown failure strain does not depend on density (Keaveny et al., 1994; Røhl et al., 1991), with one study suggesting a very weak dependence (Kopperdahl et al., 1998). Furthermore, yield strain of bone is dependent on the anatomic site (Morgan et al., 2003; Morgan et al., 2001).

The yield and ultimate strain of cancellous bone in the proximal tibia has been measured (table 2.4). It is likely that differences in measured values are because of experimental errors, such as end-artifacts. The strains measured by Lindahl (1976) are significantly larger than reported by other studies. Ultimate strain in compression is in the range of 1–2%, fitting in the range reported for bone at other anatomical sites, such as vertebra (1.45%) (Kopperdahl et al., 1998). The compressive strain is similar to that of other anatomic sites, 0.77% for vertebra (Morgan et al., 2001), 0.81% for vertebra (Kopperdahl et al., 1998), 0.7% for the femoral greater trochanter (Morgan et al., 2001), and 1.04% for the femoral neck (Bayraktar et al., 2004).

Understanding the properties of bone is important when using FE models. Models can now be generated by segmenting a CT scan and generating a mesh from the segmentation labels (Young et al., 2008). The advantage of this is that the material properties of the bone can be computed from the CT scan (Taddei et al., 2004). It is known that there is a linear relationship between the intensity of a CT scan and apparent density. By doing this

Table 2.4: Measured values of yield and ultimate strain of trabecular bone in the human proximal tibia.

Study	Load type	Measure	Strain (%)
Lindahl (1976)	Compression	Yield	6.9 ± 4.5
		Ultimate	11.6 ± 6.2
Røhl et al. (1991)	Compression	Ultimate	1.11 ± 0.63
	Tension	Ultimate	1.55 ± 0.49
Linde et al. (1992)	Compression	Ultimate	2.04 (0.07)
Morgan et al. (2001)	Compression	Yield	0.73 ± 0.06
	Tension	Yield	0.65 ± 0.05

conversion, an appropriate modulus-density relationship can be applied to compute the elastic modulus of each element in the mesh. The observation that the yield and ultimate strain of bone is isotropic, means that it is not an unreasonable assumption to model bone as an an elastic isotropic material. Bone heterogeneity can be modelled by assigning different moduli to elements.

It has been suggested that the risk of failure of cancellous bone, and therefore migration of an implant, is proportional to the stresses in the bone (Taylor et al., 1997; Taylor et al., 1998). This means that the failure criteria of bone is important. If the stress in bone surrounding an implant yields, or reaches ultimate strength, then it is likely that the implant will fail. However, as discussed, bone exhibits a simpler strain behaviour, which makes it a better failure criteria to use. In a FE model, the elements which exceed yield or ultimate strain can be identified and the risk of failure can be assessed.

2.2 Total knee replacement

The term total knee replacement (TKR) broadly refers to the replacement of the femoral, tibial, and patellofemoral articulating surfaces (Walker, 2005). This encompasses condylar prostheses, where only the condyles of the tibia and femur are replaced, to hinged prosthesis, where both the joint and ligaments are replaced. There are also design variations depending if the patient is undergoing a primary (replacement of the natural knee) or revision (replacement of one or more parts of the current prosthesis) procedure. Although a TKR procedure is a relatively successful treatment, replacing the natural knee with an engineered one can cause problems, leading to failure of the TKR. In this section, the common pathologies for a TKR, current designs of TKRs, and the reasons for failure are discussed. The focus is on primary condylar replacements, and, unless otherwise specified, they are simply referred to as TKRs.

2.2.1 Pathology and failure of the knee

TKRs are used to treat several pathologies of the knee, the most common being arthritis. There are two types of arthritis, osteoarthritis (OA) and rheumatoid arthritis (RA). OA is the most common form of arthritis and is a localised degenerative condition associated with

Table 2.5: Incidence of reasons for a TKR from joint register data.

Joint register	First	Second	Other
National Joint Registry for England and Wales (2011)	OA (97%)	RA (2%)	1%
Canadian Institute for Health Information (2008)	OA (93%)	RA (4%)	3%
Swedish Knee Arthroplasty Register (2010)	OA (96%)	RA (2%)	2%
Finnish National Agency for Medicines (2008)	OA (92%)	RA (4%)	4%
Australian Orthopaedic Association (2011)	OA (97%)	RA (2%)	1%
New Zealand Orthopaedic Association (2010)	OA (93%)	RA (3%)	4%

old age and natural wear of a joint. The cartilage covering the articulating surfaces of the knee softens and wears away leaving bone-on-bone contact, causing pain and stiffness.

RA is a chronic, progressive auto-immune disease in which the synovial membrane becomes thickened and inflamed. The inflammation damages the soft tissues and cartilage of the joint, again causing pain and stiffness. The onset of RA tends to occur at an earlier age than OA, and is more likely to affect women than men.

The other likely reason for a TKR is post-traumatic arthritis as a result of a serious knee injury. Perhaps a knee fracture, ligament or cartilage tear can wear the articular cartilage over time, leading to the need for a replacement.

Joint registers are maintained by several countries, recording total joint replacement patients and reasons for surgery, replacement type, and other statistics. The most recent joint registers indicate that OA is the top reason for a primary TKR and RA most often second (table 2.5). Given that arthritis is the reason for a TKR in about 97% of cases, it is not surprising that the age of the average patient is around 69 years (Australian Orthopaedic Association, 2011; National Joint Registry for England and Wales, 2011; New Zealand Orthopaedic Association, 2010; Swedish Knee Arthroplasty Register, 2010).

2.2.2 Total knee replacement designs

The current design of TKRs became popular in the 1970s with the progress of new materials in hip implants (Robinson, 2005; Walker, 2005). A TKR consists of a femoral component, which covers both the medial and lateral condyles, and a corresponding tibial component, which resurfaces proximal tibia (figure 2.11). The posterior of the patella can also be resurfaced with a small 'button-like' component. In an article about the history of TKR designs, Robinson (2005) describes two design approaches: the anatomical approach, which aims to mimic the natural knee geometry and preserve soft tissue constraints; and the functional approach, which aims to use mechanical principles to restore the movement of the natural knee, resecting the cruciate ligaments and using movable joint surfaces. Irrespective of approach, the overall goals of a TKR remain the same, to relieve pain, restore function, be durable (able withstand contact stresses and wear), and be reliable (insensitive to misalignment, size mismatch, and support variable loading conditions) (Walker, 2005). To achieve these goals, there are design factors which must be considered.

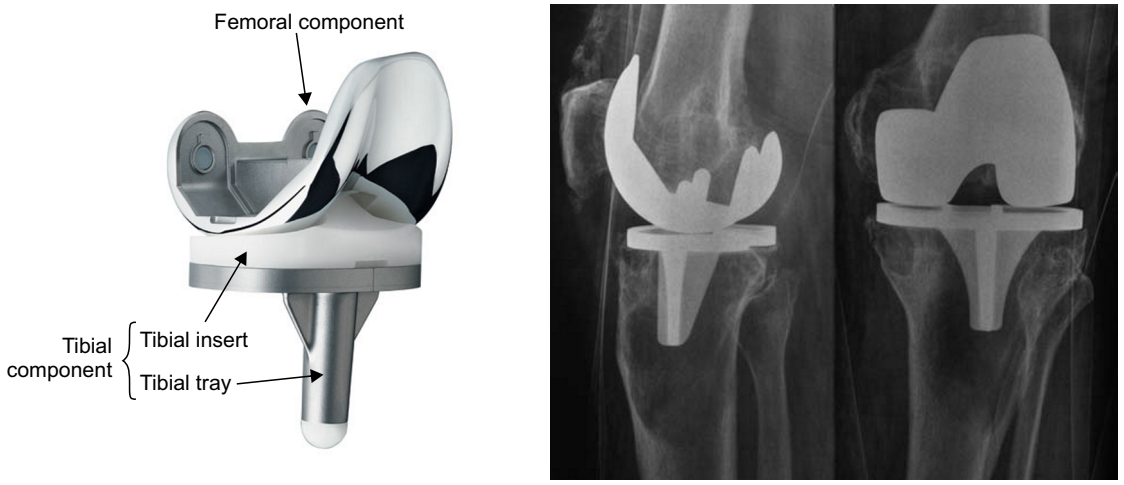

(a) Components (b) Implanted

Figure 2.11: Example of a TKR: (a) is a Depuy PFC Sigma Fixed Bearing, and (b) is a patient X-ray before a revision operation (image reproduced with permission and copyright of the British Editorial Society of Bone and Joint Surgery, Baker et al., 2007).

Materials. For any joint replacement, all the materials used must be biocompatible, non-toxic, corrosion resistant, and able to withstand the joint loads. Articulations must also be low friction to minimise factors such as wear. Metal-on-polyethylene is the 'gold' standard for TKR articulation. The femoral component is a single piece manufactured from cobalt-chromium, titanium, or ceramic. The tibial component can be either a ultra high molecular weight polyethelene (UHMWPE) monoblock, a porous tantalum monoblock (the base and stem is porous tantalum, the bearing surface is UHMWPE), or modular with two parts, a metal (often titanium or cobalt-chromium) tibial tray and a UHMWPE tibial insert which clip together. The metal backed tibial component is now most common, giving a stiffer backing and better osseointegration, but can cause stress shielding (Huiskes, 1993; Levitz et al., 1995). The patella component is usually UHMWPE.

Cruciate retaining or resecting. Almost all designs require resection of the ACL to allow space for full resurfacing of the tibia. The choice of retaining or resecting the PCL influences the selection of TKR. There is no clear evidence that either choice offers an advantage, and it really depends on the condition of the patients ligament and the surgeon's personal preference.

The anatomical approach tends to retain the PCL. The geometry of the tibial tray tends to be less conforming and have a lower profile, using the PCL to restrict A-P motion, thought to give a higher range of flexion (Walker et al., 2000). However, the PCL must be in good condition and correctly tensioned. Tibial contact pressures can increase with low profile surfaces.

Resecting the PCL requires a more functional approach to TKR design. The constraint of the PCL must be provided by the implant, and designs have used features such as more conformal geometry with a higher anterior lip or an intercondylar cam to limit the A-P motion. Without the PCL, the tibial component must withstand the larger restraint forces. Cam features can induce a high shear stress, but a more conforming geometry will reduce surface contact

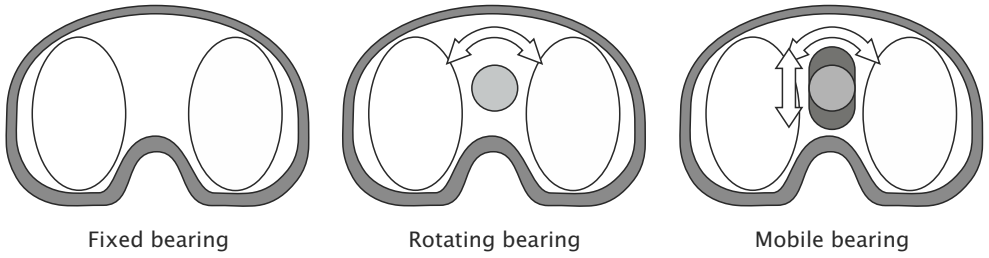

Figure 2.12: The three bearing types of the tibial component

pressure. Modern TKR designs are modular and the choice to resect or retain can be made in surgery, after the surgeon has assessed the condition of the PCL.

Tibial tray bearing. Modular TKRs mean that it is possible to allow motion of the tibial insert relative to the tibial tray. The idea is the extra bearing allows a more conforming motion of the tibia against the femur, increasing surface contact (Walker, 2005). There are three types of bearing: (i) fixed bearing allows no motion of the tibial insert, (ii) rotating bearing allows I-E rotation, and (iii) mobile bearing allows both I-E rotation and A-P translation (figure 2.12).

Fixation method. The stability of the implant fixation, whether cemented or cementless, is critical for long term success. Cemented fixation uses bone cement, polymethylmethacrylate (PMMA), to fill the gap between the implant and bone. This has the advantage that it is more forgiving as voids created from cutting inaccuracies are readily filled (Lombardi et al., 2007), and can provide more stable fixation (Carlsson et al., 2005; Ryd et al., 1990). There is evidence that the strength of the bone-cement interface is dependent on the compliance of the interface, amount of interdigitation, and the contact area between the bone and cement (Mann et al., 1997; Mann et al., 2008; Waanders et al., 2010). Poor bone-cement interface strength, perhaps from minimal penetration of the bone cement into the bone, can lead to cracks developing in the cement and loosening of the implant.

Cementless fixation relies on bone ingrowth onto the surface of the implant, which is often porous or coated with hydroxyapatite (HA), to provide fixation. It is thought to provide long-term fixation, advantageous for younger more active patients, without the problems associated with cement degradation (Khaw et al., 2002; Lombardi et al., 2007). However, there are problems with cementless implants, including evidence of extensive radiolucent lines indicating poor fixation (Fuiko et al., 2003), rapid early migration (Albrektsson et al., 1992; Ryd et al., 1990), and osteolysis (although this is mostly when screws are used to fix the implant), all of which can result in loosening.

2.2.3 Mechanisms of total knee replacement failure

There is always a risk that a TKR could fail post-operatively, requiring a revision surgery. Failure mechanisms should be thought of as a process which occurs over a period of time, to quote Huiskes (1993) “failure is virtually always a process, hardly ever an event. Such a

process develops as a mechanism and produces radiological and clinical signs along its way." Failure mechanisms of the TKR leading to revision have been discussed by Austin et al. (2004); Vince (2003). The following mechanisms are defined:

- **Aseptic loosening.** The implant becomes loose, either from accumulated damage, particle reaction, failed bonding, or perhaps malalignment of the components. Micromotion and migration can also occur.

- **Wear.** Wear of the tibial insert (polyethylene) is often a problem in TKRs. There are many factors which influence the rate of wear: the shape of the bearing surface; modular design, allowing relative motion between the tibial insert and tibial tray; additional bearing surfaces in mobile bearing and rotating platform designs; the thickness, quality, and method of sterilisation of the polyethylene; the patient weight and activity; and alignment of the TKR. Wear can either lead to particulate reactions or be destructive.

- **Debonding.** The debonding of the bone-cement, cement-implant, or bone-implant interfaces can occur due to accumulated damage, particulate reactions, or failed bonding scenarios. The formation of fibrous tissue around at the interfaces indicates debonding and can be seen on radiographs.

- **Instability.** The knee depends upon the surrounding soft tissue and ligaments to provide stability. Improper ligament balancing, particularly of the collateral ligaments, or damage to the soft tissue, can lead to the instability of the tibiofemoral joint. This is most common with valgus deformities and impairs patient mobility.

- **Patella complications.** Mal-alignment of the tibial and femoral components are linked to patella mal-tracking (Barrack et al., 2001), often indicated by anterior knee pain. Other patella complications are wear, fracture, and loosening. If the patella was not originally resurfaced, it can be, otherwise a TKR revision could be required.

- **Dislocation.** This can occur for both the tibiofemoral joint and patellofemoral joint. The likely cause is incorrect ligament balancing or severe component mal-alignment. The risk of the tibia dislocating posteriorly is increased by a patellectomy or under sizing of the femoral component.

- **Disease progression.** In the case of a patient with RA, it is likely that the joint will continue to degenerate after surgery, leading to problems with the implant.

- **Mechanical failure.** There is always a risk of complete mechanical failure of an implant. The destructive wear scenario leads to mechanical failure, particularly of the polyethylene tibial insert. Improved testing techniques and strict safety specifications mean that this is now a very rare failure mechanism.

- **Limited function.** Poor component position or improper ligament balancing can reduce the range of motion of the joint. This can stop the patient performing certain activities and impair mobility. In many cases, a revision is not performed.

- **Infection.** The risk of infection is reduced from good hygiene practice, use of antibiotics, and component and instrumentation sterilisation. Infection occurs in a few percent of all joint replacement operations, and can normally be treated with antibiotics. Only deep infections might require removal or revision of the implant.
- **Pain.** This is a very subjective measure to which there is not necessarily an underlying cause (Ritter, 1997). Classified as the 'mystery knee' (Vince, 2003), pain without cause can be a reason for a revision.

TKR failure can present in many different ways and the mechanisms are not independent of each other. For example, accumulated damage, particulate reaction, and debonding can all lead to loosening of the TKR. Survivorship studies have found the most common failure to be infection, polyethylene wear, instability, and aseptic loosening (Fehring et al., 2001; Sharkey et al., 2002). This is in agreement with the top five indications for revision from the National Joint Registry for England and Wales (2011): aseptic loosening (33%), infection (23%), pain (17%), instability (14%), and wear of polyethylene component (11%), which includes all types of TKR.

2.2.4 Survivorship of the cementless tibial tray

Currently, the majority of TKR procedures use cemented fixation for one or more components. In England and Wales, approximately 5% of the all TKR procedures are cementless (National Joint Registry for England and Wales, 2011), a decrease of 2% compared to previous years. In Australia around 27% of primary TKRs are cementless, 23% are hybrid[1], and 55% are cemented (Australian Orthopaedic Association, 2011). The proportion of cementless TKR procedures in Canada and New Zealand is around around 6%, similar to England and Wales. Only 1% of TKR procedures in Sweden are cementless (Swedish Knee Arthroplasty Register, 2008). The low proportion of cementless fixation is because of the proven clinical history of cemented fixation, considered the 'gold' standard for TKRs and is the recommended technique (Austin et al., 2004; Gandhi et al., 2009).

If this is the case, why use cementless tibial trays? The success of the cementless THR is part of the reason. Long term survival rates are high, so there is naturally an interest in using cementless TKRs. If improved long-term fixation can be achieved, then TKRs would be expected to last longer, benefiting younger more active patients. Further to this, problems associated with cement (e.g. cement debris) are avoided, bone stock is preserved and revisions are easier.

However, there are mixed reports about the success of cementless tibial trays. Clinical studies comparing cemented and cementless TKRs have reported poor survivorship. Duffy et al. (1998) reports 94% and 72% survivorship for cemented and cementless fixation respectively. These figures are for survival to revision for aseptic failure or radiographic loosening, excluding problems relating to the patella. However, the study was not randomised, nor were the patient

[1]It is assumed that this means only one or part of one component is cemented. The definition is not given in the report.

groups matched. Younger, more active patients were selected for a cementless TKR, and the higher level of activity could increase the risk of failure. Berger et al. (2001) found that whilst femoral fixation was good after 11 years (the only revisions were secondary to patella complications), 8% of the tibial components had to be revised due to aseptic loosening and 12% showed small osteolytic lesions around the screw holes.

More recent studies have shown survivorship of cementless TKRs to be comparable to cemented TKRs (Baker et al., 2007; Bassett, 1998; Hofmann et al., 2001; Holloway et al., 2010; Martin et al., 1997). A long term study of a series of 501 TKRs (277 cemented, 224 cementless) reported no significant difference in survival rates between the two types of fixation (Baker et al., 2007). For cemented fixation, 15 year survival rate was 80.7%, with a 10 year survival rate of 91.7%. For cementless fixation, the 15 year survival rate was 75.3%, with a 10 year survival rate of 93.3%. Similar survival rates are reported by other studies and are in line with recent joint register data, 96.19% survival rate for cemented TKRs and 95.25% survival rate for cementless TKRs at 7 years (National Joint Registry for England and Wales, 2011).

Apparent from survivorship studies is that loosening of the tibial tray is the most likely reason for revision. A few studies have reported a higher incidence of loosening for cementless tibial trays (Austin et al., 2004; Duffy et al., 1998). Radiolucencies can often be seen around the tibial tray indicating poor fixation. Studies report both a high (Duffy et al., 1998; Fuiko et al., 2003) and low (Bassett, 1998; Cossetto et al., 2010; Holloway et al., 2010; Martin et al., 1997) incidence of radiolucencies. However, there is often no progression of the radiolucencies, and there is no apparent link between radiolucencies and revision.

The early appearance of radiolucencies around the tibial tray (Fuiko et al., 2003), suggests that poor initial fixation could be a problem. Greater initial migration of cementless tibial trays has been measured using RSA (Albrektsson et al., 1992; Carlsson et al., 2005; Nilsson et al., 1999), and can be an indication of late aseptic loosening (Grewal et al., 1992; Ryd et al., 1995). Use of HA coatings can reduce the migration of cementless tibial trays, providing a stronger fixation than cemented implants after the initial preoperative period (Carlsson et al., 2005; Nilsson et al., 1999). From experimental studies using porous implants in dogs, it was observed that the amount of micromotion affected bone ingrowth. Micromotions less than 50 µm resulted in bone ingrowth, and greater than 150 µm resulted in fibrous tissue formation (Jasty et al., 1997; Pilliar et al., 1986).

The success of long term fixation of a cementless implant is dependent on the primary stability of the fixation. It has been suggested that the risk of cancellous bone failure, and therefore migration, is related to the initial stresses in the bone (Taylor et al., 1997). That is, if the stress or strain levels in the bone exceed the elastic limit, the implant is likely to migrate, increasing the risk of aseptic loosening. Computational testing can predict the stress, strain, and micromotion at the bone-implant interface using FE analysis. This technique of modelling can give an insight into how a bone and implant respond to loading, indicating a relative risk of failure between models. In the next section, current FE studies that model the tibia implanted with a tibial tray are reviewed, looking at how this type of analysis can be used to assess the performance of a tibial tray.

Chapter 3

Computational assessment of total knee replacements

3.1 Finite element models of the knee

Finite element (FE) analysis is common in bioengineering, particularly for pre-clinical analysis of orthopaedic implants. A review of FE models in bioengineering reports that they were first used in the field in 1972 (Prendergast, 1997). Since then, advances in computational technology have allowed FE analysis to be applied to a wide range of problems of varying complexity. Generally, FE studies are used to determine the stresses and strains in biological structures (e.g. bones and ligaments) for given load cases. They have been applied to individual bones to the musculoskeletal system, with explicit and adaptive techniques also used to model time dependent processes, such as fatigue, wear, and tissue adaptation (Prendergast, 1997).

Pre-clinical testing of joint replacements is one of the main uses of FE analysis in orthopaedics. Failure of a joint replacement *in vivo* means that revision surgery would likely be required. This requires the patient to have another major operation and is expensive for the health authority. Engineers can use FE analysis as a tool to assess implant designs, looking at factors such as joint function, implant fixation, and wear characteristics, with the aim of reducing the chances of implant failure.

FE analysis of the knee has been used to look at the strain in the bone-implant interface (Perillo-Marcone et al., 2007; Wong et al., 2010), stresses in the cancellous bone (Taylor et al., 1998), micromotion of the tibial tray (Chong et al., 2010; Keja et al., 1994; Rakotomanana et al., 1992; Taylor et al., 2012; Tissakht et al., 1995), or contact stresses between the TKR components (Halloran et al., 2005). Wear of implants can be predicted using an FE model (Knight et al., 2007; Laz et al., 2006) or a multi-body dynamics (MBD) models (Strickland et al., 2009).

3.2 Finite element models of the tibial tray

The focus of this thesis is on the proximal tibia implanted with a tibial tray. Other components of the TKR are not considered. When assessing the performance of a tibial tray, of interest is the mechanical response (stress and strain) of the bone and implant, and micromotion at the contact interface[1]. Many studies use FE analysis as a comparative tool, examining the relative changes of stress, strain, or micromotion between implant designs, fixation methods, and/or load cases. A summary of recent FE studies which examine tibial tray fixation is given in table 3.1, giving details of the study aims, applied model loads, mechanical response (if reported), micromotion (if reported), and the main findings. Where studies have compared multiple tibial tray designs or fixation methods, results are reported for what was judged to be the more common design or uncemented fixation.

Generally, most models are 3D geometry of at least the proximal tibia and tibial tray, often with the tibial insert, and a cement layer when appropriate. Hashemi et al. (2000) and Rawlinson et al. (2005) modelled a small patch of the femoral component. Perillo-Marcone et al. (2007) modelled the full femoral component and ligaments to be able to predict kinematics.

Not detailed in table 3.1 are the material properties applied to the models. The more recent studies (Chong et al., 2010; Perillo-Marcone et al., 2007; Taylor et al., 2012; Wong et al., 2010) sample intensity values for each mesh element from CT scans and convert this to an elastic modulus (see section 2.1.9) to represent the heterogeneity of bone. The number of materials in the model is reduced by grouping the elastic modulus. In earlier studies, the bone was often split into multiple regions and a different material assigned to each, assuming each region was homogeneous. If too few regions are used, intra-region variation of the bone properties is ignored.

Linear elastic isotropic material behaviour was assumed for bone in most studies, with only one study using transverse isotropic behaviour (Rakotomanana et al., 1992), and another (Rawlinson et al., 2005) using anisotropic behaviour. The problem is that anisotropic behaviour of bone is dependent on type of bone and anatomic site. Cortical and cancellous bone both have different degrees of anisotropy and it can be difficult to separate the two types of bone, particularly if the geometry is created based on a segmented CT scan.

One source of loading is from the ISO standard (ISO 14243-1, 2009). This defines a load cycle to be used for wear testing of a TKR, and can be applied to FE models (Perillo-Marcone et al., 2007; Wong et al., 2010). However, the ISO standard underestimates the peak-to-peak I-E moment compared to TKR telemetry data (Heinlein et al., 2009; Kutzner et al., 2010). The magnitude of change could have an impact on the bone-implant interface stresses and polyethylene wear, important considerations when testing a TKR.

[1] In this context, the contact interface refers to either the bone-implant interface or bone-cement interface, as these are most likely to become loose. It is often assumed that the implant is fully bonded to the cement.

Table 3.1: Summary of tibial tray fixation FE studies.

Reference	Aims	Loading	Mechanical response	Micromotion	Findings
Rakotomanana et al. (1992)	Compare fixation of two different designs of tibial tray, cemented metal tray total condylar, and porous coated anatomic (cemented and uncemented). 2D model.	Two static load cases of total magnitude 2000 N, (i) equal distribution between the medial and lateral sides, and (ii) one-third lateral and two-thirds medial distribution between condyles (varus malalignment).	Peak stresses in uncemented porous coated anatomic. Load case (i) 8.1 MPa (cancellous bone) and 18.1 MPa (cortical bone); (ii) cortical lateral 15.1 MPa and cortical medial 21.2 MPa.	Uncemented porous coated anatomic at bone-implant interface. Load case (i) vertical displacement 0.17 mm at medial and lateral edges, relative vertical displacement in centre 0.39 mm. Shear micromotion 0.05 mm max at edges. Load case (ii) tilting of implant, vertical displacements 0.0 mm lateral, 0.55 mm centre, and 0.34 mm medial. Shear micromotions 0.05 mm max.	Concentration of stresses appear at extreme edges of implant. The peak stresses of the porous coated implant lower. Different stress distributions along the pegs.
Keja et al. (1994)	Comparison of micromotion a prototype implant with perimeter fixation, and the PCA with two pegs. A combination of different materials and fixation points were tested.	Axial load of 2500 N (assumed 3 BW) equally distributed between medial and lateral side. Implant-bone interface assumed frictionless. The points of fixation (perimeter or pegs) were constrained to move with the bone, allowing no micromotion.	Not reported.	Prototype (perimeter fixation) micromotions were 17 µm av. and 37 µm max. PCA (peg fixation) micromotions were 44 µm av. and 101 µm max. The fixation constraint meant that micromotions decreased to 0 µm at fixation points.	The perimeter fixation showed lowest micromotion. Results affected by unrealistic fixation constraint, perimeter or pegs are not necessarily bonded to bone.
Tissakht et al. (1995)	Compare three fixation type of a tibial tray, close-fit, press-fit, and screw fixation, measuring the micromotion of each. The model was validated with experimental results.	Axial load of 1000 N (approx. 1.5 BW) applied to single node in center of tibial tray. Friction contact model used for bone-implant interface.	Not reported.	Micromotion was dominant in shear direction. Pattern was similar for all types of fixation. Peak to peak micromotion: Close-fit: 1.3–4.9 µm M-L, 2.5–6.8 µm A-P; Press-fit: 1.1–3.8 µm M-L, 4.2–11 µm A-P; Screw fixation: 0.0–2.5 µm M-L, 0.0–3.0 µm A-P.	Coefficient of friction value affects the micromotion. Magnitude of press-fit and close-fit micromotions are similar, screw fixation offers best initial fixation.

Table 3.1: Summary of tibial tray fixation FE studies (cont'd).

Reference	Aims	Loading	Mechanical response	Micromotion	Findings
Taylor et al. (1998)	The bone-implant interface stress measured for three tibial trays of different materials and fixations. The mean stress is compared with published migration and survivorship data.	*Uni-condylar*: 2.2 kN axial force applied to medial condyle. *Bi-condylar*: 2.2 kN axial force applied with a 60–40% ratio between medial and lateral condyles respectively.	Mean (peak) min principal cancellous bone stress for cementless implant bi-condylar load case: Medial: 1.55 (2.48) MPa Inter-condylar: 0.31 (1.02) MPa Lateral: 1.00 (1.72) MPa	Not reported.	Rank order of implants based on stress and migration data the same. Data suggests a correlation between the cancellous bone stress and implant migration.
Hashemi et al. (2000)	Compare fixation designs of a tibial tray and two friction models. Model of proximal tibia, tibial tray, tibial insert, and medial patch of femoral component.	Varus alignment with 2 kN medial axial load. Femoral component constrained to move vertically only.	Not reported.	Micromotion highest posteriorly and anteriorly. Peak to peak micromotions: *Post fixation*: 0.1–12.7 µm M-L, 1.0–22.0 µm A-P. *Screw fixation*: 0.8–12.2 µm M-L, 1.0–16.0 µm A-P.	Screw fixation reduced micromotion and lift-off.
Miyoshi et al. (2002)	Assess performance of a posterior notched and un-notched tibial tray.	2 kN axial load equally distributed between the condyles in different positions: (i) stable, load central on each condyle; (ii) unstable, load medio-posterior edge of one condyle and anterior-lateral to the middle portion of the other condyle.	Max von Misses stresses at bone-implant interface (stable/unstable): *Notched*: 11.0/13.5 MPa *Un-notched*: 11.6/12.3 MPa.	Max displacement of mid-sagittal section (stable/unstable): *Notched* 0.068/0.089 mm *Un-notched*: 0.076/0.104 mm Max displacement of resected surface (stable/unstable): *Notched*: 0.07/0.113 mm *Un-notched*: 0.073/0.114 mm	No significant difference was found between the micromotion and stress distribution of the two implant designs.
Perillo-Marcone et al. (2004)	Patient specific study correlated bone stresses with RSA results. This study used a model of a proximal tibia, tibial tray, and insert.	3 BW axial load. Medial to lateral ratio dependent on patient post-operative varus-valgus rotation.	Risk ratio (von Mises stress/ultimate compressive strength) and percent volume failed bone (PVFB) reported. Risk ratio 47.0–61.4% and PVFB 0.4–26.2% with similar rank order for patients.	Not reported.	Findings support that initial implant migration is related to initial mechanical environment. Link established between FE and clinical data.

Table 3.1: Summary of tibial tray fixation FE studies (cont'd).

Reference	Aims	Loading	Mechanical response	Micromotion	Findings
Au et al. (2005)	Investigate different shape of four tibial tray stems on bone and interface stresses.	Non-uniformly distributed axial force of 2 kN. Loading nodes were determined from experimentally determined contact patterns.	Peak stresses: *Post*: 7.5 MPa (proximal) *Cement*: 1.1 MPa (distal) *Cancellous bone*: 0.4 MPa (distal) *Cortical bone*: 4 MPa (distal)	Not reported.	Shape of the post influences the stress distribution in different regions of the tibia. Pegs reduced the cancellous bone stress for all four designs.
Barker et al. (2005)	Parametric study of 16 different circumferential flange shapes using a 2D axi-symmetrical model. Aim to minimise shear micromotion.	Axial load of 586 N assuming av. cancellous bone stress of 1.34 MPa under tibial tray. Applied 10 mm inside lateral edge with a triangular distribution. No lateral loads. Coulomb friction model for contact between tibial tray and bone. Coefficient of friction assumed 0.5 for post-bone interface, and 0.1 for tray-bone interface.	Peak stress under the load point: 'flat' post 1.33 MPa, 'optimal' post 1.24 MPa, 'capped' post 1.31 MPa. Peak stress at the periphery: 'flat' post 1.59 MPa, 'optimal' post 4.16 MPa, 'capped' post 2.28 MPa.	Peak bone-implant interface micromotion for 'flat' post 23 µm (bone relative to implant), and for tightly 'capped' post 37 µm (implant relative to bone).	Suggests circumferential flange reduces micromotion. 'Optimum' design minimised micromotion, but had the highest peak compressive bone stresses.

Table 3.1: Summary of tibial tray fixation FE studies (cont'd).

Reference	Aims	Loading	Mechanical response	Micromotion	Findings
Rawlinson et al. (2005)	Test the hypothesis that a stemmed tibial tray improves implant stability. Compared stemmed and unstemmed hybrid cemented tibial trays using 9 paired-tibiae cadavers with both experiments and cadaver specific computational models. For each pair, a stemmed tibial tray was implanted in a randomly selected side.	Two load cases for FE models: (i) 3 kN axial load with transverse displacement and rotation constrains; (ii) axial, A-P, and M-L forces from load cell in experiment with rotations constrained. 10 Nm V-V moment also applied in both cases. Distal end of tibia fully constrained.	For uncemented implant with stem, mean min principal strain at resected surface for load case (i) −0.32% and (ii) −0.46% Mean min principal stress at resected surface for load case (i) −2.7 MPa and (ii) −3.35 MPa.	Relative displacements reported in terms of percentage change between stemmed and unstemmed tibial trays. Experimental micromotion of tibial trays with stem is approx. −0.05–0.03 mm. Micromotion for FE models with stem is approx. −0.08–0.12 mm.	Experiments suggest that stem does not reduce global micromotions due to large inter- and intra-specimen variations. The FE models showed that the stem consistently reduced the compressive strains and stress in the proximal cancellous bone, with no significant different between interface and loading conditions. Cement provided stability if the stem was undersized compared to the medullary canal.
Perillo-Marcone et al. (2007)	Investigates V-V malalignment of a cemented tibial tray. FE model with full TKR, proximal tibia and ligaments.	Stanmore knee simulator data (Walker et al., 1997). AX force and F-E angle applied to femoral component. A-P and I-E torque applied to distal end of the tibia. V-V malalignment simulated by offsetting the position of the axial load medially and laterally.	Peak min. and max. principal strains of resected surface over the gait cycle. Magnitude of min. strains higher. At yield strain of 0.73%, percentage volume of bone failing is 59% (min. prin. strain) and 25% (max. prin. strain).	Not reported.	The kinematics and strain changes depending on the V-V alignment. The change in load from varus to valgus shifted the peak strains laterally.

Table 3.1: Summary of tibial tray fixation FE studies (cont'd).

Reference	Aims	Loading	Mechanical response	Micromotion	Findings
Chong et al. (2010)	Compute micromotion of a cementless metal tibial tray under different loading conditions.	(i) generic static load (AX, A-P, and M-L forces); (ii) static load at 15% of gait (AX and A-P forces); (iii) static load at 25% of the stair climbing cycle (AX and A-P forces); (iv) load representing four points in the gait cycle (AX and A-P forces). AX force distributed unequally between condyles.	Not reported.	Peak micromotion/surface area with micromotion <50 µm for each load case: (i) 150 µm/33% (ii) 107 µm/81% (iii) 218 µm/30% (iv) 133 µm/44%.	Micromotion is dependent on the activity, with stair climbing producing the highest peak micromotion. With all results combined, only approx. 20% of surface with micromotion <50 µm, limited to a posterior region of the tray underside and stem.
Wong et al. (2010)	To determine the biomechanical factors affecting the risk of tibial tray subsidence with varus malalignment. Gait cycle loading of four human knees, 2 neutral and 2 varus alignment, to measure micromotion of tibial tray. Subject specific FE models were also used to predict the volume of bone at risk of failure in the proximal tibia.	Experiments used ISO standard loading up to 100,000 cycles of gait. AX medial to lateral force ratio: (i) neutral alignment 55:45 (ii) varus alignment 75:25. Subject specific FE models used same loading simulating a single gait cycle. Additional 'paired' analysis, where both neutral and varus alignment was simulated for each model.	Volume of cortical bone at risk of failure: 50 mm^3 (neutral) and 150 mm^3 (varus). Volume of cancellous bone at risk of failure: 3800 mm^3 (neutral) and 4400 mm^3 (varus). All av. of 'paired' analysis.	Higher micromotion for varus alignment. Experimental measurements match subject specific computed micromotion. The AX micromotion for the four subjects (experiment/computed): 8/10 µm, 20/22 µm, 37/35 µm, and 38/36 µm.	Varus alignment of tibial increases the risk of cancellous bone failure, which is likely to be a cause of subsidence. Inter-patient variability of bone quality also affects the risk.

Table 3.1: Summary of tibial tray fixation FE studies (cont'd).

Reference	Aims	Loading	Mechanical response	Micromotion	Findings
Taylor et al. (2012)	Compare the micromotion of three tibial trays for five different activity cycles: level gait, stair ascent, stair descent, stand to sit, and deep knee bend. Quantify both the magnitude of peak micromotion and when in the activity cycle it occurs. Only the proximal tibia and tibial tray were modelled.	Post-operative telemeterised TKR data (Orthoload) of five complete activity cycles. All 3 forces and all 3 moments applied directly to the tibial tray. Distal end of tibia constrained.	Not reported.	Composite peak micromotion (CPM, peak micromotion of the bone-implant contact surface during the activity) for comparison. Level gait, stair ascent, and stair descent generated highest micromotions. For level gait: CPM mean 61–86 µm, CPM max. 180–225 µm, area < 50 µm 39–46%, area > 150 µm 2–16%.	Predicted micromotions for the three tibial trays appear to be agreement with the reported incidence of radiolucencies (higher micromotion, higher incidence of radiolucencies). Found that the highest micromotions occur when low AX force and moderate V-V moment. Load state occurs frequently in ADLs affecting the primary stability of the tibial tray.

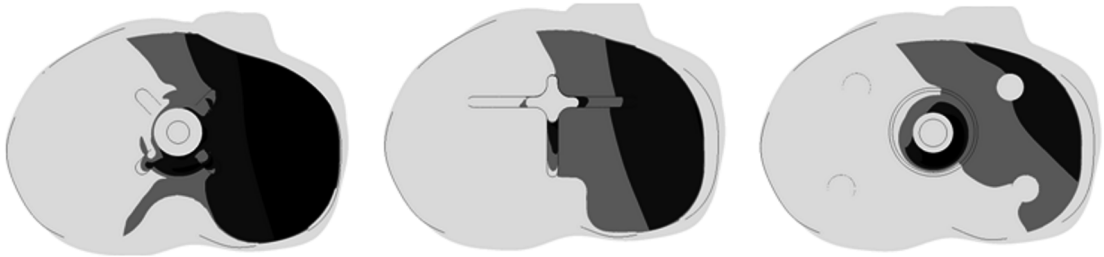

(a) LCS Complete (b) PFC Sigma (c) LCS Complete Duofix

Figure 3.1: Composite peak micromotion (CPM) plots of the bone-implant interface of three different implant designs with level gait loading. These CPM plots report the peak micromotion at each individual node of the surface that occurred during the simulated activity. Light grey corresponds to micromotions $< 50\,\mu m$ and black corresponds to micromotions $> 150\,\mu m$ (image reproduced from Taylor et al., 2012, with permission from Wiley).

Despite the availability of ISO standard data and Orthoload data, the loading applied to the models in the majority of studies is a static axial (AX) force. The force is often split between the condyles and perhaps can be considered to represent the peak load at an instance of an activity cycle. The magnitude of the AX force varies, from 586 N up to approximately 4050 N, representing a patient specific load of 3 BW (Perillo-Marcone et al., 2004).

The assumption in many studies is that the peak stress, strain, and micromotion occurs with peak axial load. During gait, this assumption is not necessarily the case. Chong et al. (2010) simulated five points during the stance phase of gait (see section 2.1.7), applying only the AX and A-P forces. The computed micromotions peaked at toe-off, not at mid-stance or contralateral heel strike where the AX force peaks. The percentage area of the tibial tray with micromotions $< 50\,\mu m$ was also lowest at toe-off. However, a full activity cycle was not simulated and nor were the internal moments of the knee applied (although the medial to lateral ratio of the AX force was unequal and could be considered to represent either a V-V moment or varus malalignment).

Full activity cycles of level gait, stair ascent, stair descent, stand to sit, and deep knee bend were simulated in a study comparing the micromotions of three cementless tibial trays (Taylor et al., 2012). Loading for each activity was taken from a patient in the Orthoload data set. All three forces and all three moments were applied directly to the tibial tray, discretised at approximately 2% intervals of the activity cycle. During gait, the peak micromotions occurred during swing phase, where the forces are negligible and there are moderate moments. The pattern of peak micromotion during gait was also found to be similar for all tibial trays (figure 3.1). It is important to note that the primary stability was considered in isolation from bearing design and the loading applied to all models was taken from a telemeterised tibial tray of a different design to any used in the study. The kinetics of the knee are dependent on kinematics, which would be a function of implant design. Hence, the forces in the knee are likely to be different between implant designs. Despite this limitation, it is clear that a TKR should be tested for a full activity cycle.

From the reviewed studies, it is apparent that the micromotion at the contact interface is highly dependent on choice of loading and contact properties. Despite this, the peak predicted

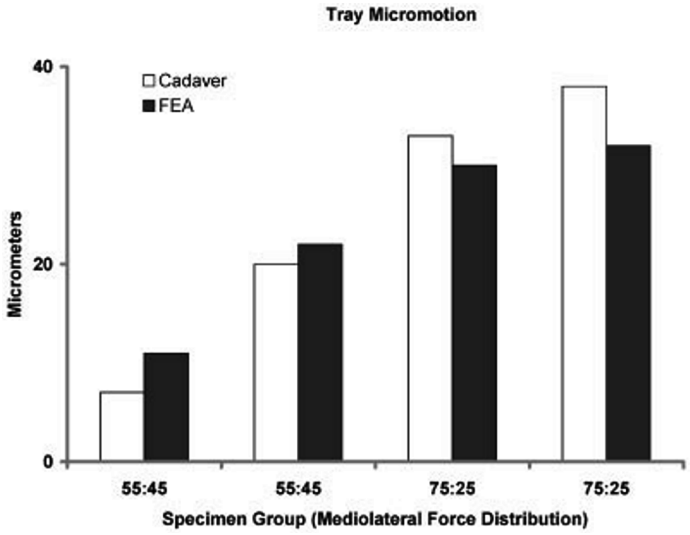

Figure 3.2: The computed superoinferior micromotion of the tibial tray relative to bone on the medial side compared to that measured experimentally in four specimens (image reproduced from Wong et al., 2010, with permission from Wiley).

micromotions are often not much greater than 150 µm, the threshold above which fibrous tissue forms. For example, during level gait, peak micromotions of 133 µm and 225 µm were reported by Chong et al. (2010) and Taylor et al. (2012) respectively. Several studies have also validated the predicted micromotions with experiments and found the magnitudes to be similar (figure 3.2), showing that FE models can predict realistic micromotion of the tibial tray. However, there were differences in the pattern of micromotion (Chong et al., 2010; Rawlinson et al., 2005; Wong et al., 2010).

There is inconsistent reporting of the mechanical response of bone. Studies use different stress and strain invariants in different regions of the model, making comparison difficult. However, stresses in the tibia were generally below the ultimate stress of cancellous bone, around 5.3 MPa for the proximal tibia (Keaveny et al., 2001). Many studies assume isotropic behaviour of bone, instead of transverse isotropic as found experimentally (Keaveny et al., 2001), which can overestimate axial stresses by up to 40% (Rakotomanana et al., 1992).

Strain in the tibia is not widely reported. The peak minimum principal strain and peak maximum principal strain at the bone-implant interface has been reported as −15% and 3.3% respectively (taken from contour plots of strain in Perillo-Marcone et al., 2007). These are high values of strain, in excess of compressive and tensile yield strain for cancellous bone. Much lower peak minimum principal strains have been reported in the medial region below the tibial tray, ranging from −1.35 % to −0.30 % depending on material properties, fixation, and applied loads (Rawlinson et al., 2005). Part of the reason for the differences in peak magnitude of strain is that different regions of the tibia are being considered, but the complexity of the models also differs. Rawlinson et al. (2005) modelled a tibia and tibial tray applying static AX, A-P, and M-L forces, with a total AX force of 3000 N. This is relatively simple compared to Perillo-Marcone et al. (2007), where a complete TKR (excluding patella component), proximal tibia, and ligaments were modelled. A full gait cycle was simulated and the patient weight was 116 kg, causing larger loads to be generated across the TFJ, leading to a higher strain.

3.2.1 Assessing the risk of failure

It is clear from the literature that an important goal of FE models in pre-clinical testing of the tibial tray is to predict the potential risk of failure. One measure often used to assess the potential risk of failure is interface micromotion, an indicator of the tibial tray primary stability. If primary stability is poor, micromotion at the bone-implant interface occurs, preventing bone ingrowth and inducing fibrous tissue formation, leading to migration. As previously discussed, early migration is a potential clinical indicator of late aseptic loosening (see section 2.2.4).

Mechanical response of the bone is another measure used to predict the potential risk of failure. A tibial tray is most likely to migrate if the surrounding bone fails, and bone is more likely to fail if the strain exceeds yield or ultimate strain. If the bone does fail, the chance of continuous migration is higher, affecting the long term success of the tibial tray. Instead of directly comparing the stress and strain, several studies compute the volume or percentage of bone at risk of failure in a given region, defining metrics such as the risk ratio, the ratio mean/median of stress in a region of interest to ultimate compressive strength (Perillo-Marcone et al., 2004; Taylor et al., 1998), and percentage of resected surface with strain (either compressive or tensile) above yield or ultimate strain (Perillo-Marcone et al., 2007).

These metrics give an immediate idea about the amount of bone at risk of failure. At the bone-tray interface, Perillo-Marcone et al. (2007) found that 59–70% of the surface had a minimum principal strain as a metric above compressive yield strain of 0.73%. If maximum principal strain was used instead, 25–52% of the surface was above a tensile yield strain of 0.65%. The high proportion of the interface surface at risk of failure could be because the yield strain threshold is too conservative.

The volume of cortical and cancellous bone was computed for four subject specific models of cadaveric knees, two in neutral alignment (AX force medial:lateral ratio of 0.55:0.45) and two in varus alignment (AX force medial:lateral ratio of 0.75:0.25). The volume of cancellous bone above fatigue strain (0.3% compressive) was significantly greater for the two models in varus malalignment. This was not the case for the volume of cortical bone above fatigue strain (0.4% compressive). For one neutral and one varus model the volume was $< 60\,\mathrm{mm}^3$, and for the other neutral and varus models the volume was $> 150\,\mathrm{mm}^3$. It would be better to express this relative to the volume of interest given the the inter-subject variation of shape, size, and therefore volume, of the tibia.

Validation of FE models is not possible in many cases, and the magnitude of stress, strain, and micromotion may not be accurately predicted. However, a relative comparison between FE models and/or clinical factors can be made. One example of this is the link between migration (a clinical factor) and initial stresses in the bone (a FE factor). Taylor et al. (1998) modelled three tibial trays (a press-fit polyethylene tray, an uncemented metal backed tray with polyethylene insert, and a cemented metal backed tray with polyethylene insert) and computed the local and global risk ratio of cancellous bone beneath the tray. The rank order of the risk ratio matched that of clinical migration data measured using RSA. Perillo-Marcone

Table 3.2: Summary of risk ratio, percent volume failed bone (PVFB) and maximum total point motion (MTPM) (Perillo-Marcone et al., 2004)

Rank	Patient	Fixation	Risk ratio	PVFB	MTPM
1	4	Cemented	38.4	0.4	0.6
2	1	Cemented	47.0	8.5	1.1
3	3	Cementless	53.8	19.3	4.9
4	2	Cementless	61.4	26.2	4.3

et al. (2004) did the same thing, except instead of using different designs of tibial tray, four patients with corresponding migration data were compared. When ranked by risk ratio and percent volume failed bone (PVFB), the order of the patients was the same as when the patients were ranked by measured migration (table 3.2). Patients with a higher risk ratio or PVFB experienced higher migration. However, assumptions were made about the loading of each model, and for one of the models the tibial tray was assumed to be fully osseointegrated as the measured migrations were small, which would affect the computed risk ratio and PVFB.

It has also been observed that regions where high tibial tray micromotion occur are similar to regions where a high incidence radiolucencies occur (Taylor et al., 2012). The limitation of this observation is that only a single FE model was used and it was not of a TKR patient with follow up data.

3.2.2 Population variation

It would be unrealistic to say that the performance of a TKR is thoroughly assessed using a single patient model. Only three studies used models of multiple patients or subjects. The largest study used 9 paired tibiae to determine the effect of a tibial tray stem augment on the micromotion and strain in the cancellous bone with both *in vitro* experiments and subject specific FE models (Rawlinson et al., 2005). The stem augment was found not to reduce micromotion but did consistently reduce the strain in the cancellous bone. Perhaps the most important observation was that the stem was beneficial in subjects with poor bone quality. Even using a small population of subjects, the effect of inter-patient variability could be seen.

Two other studies used a smaller population of four patients (Perillo-Marcone et al., 2004; Wong et al., 2010). Both observed inter-patient variability of bone quality was likely to affect the predicted volume of bone at risk of failure. These studies are about the only examples where models of multiple patients are used for analysis of the tibial tray and all are limited by the small population of patients used. Creating the models was a manual process, requiring segmenting and meshing of each patient model from the CT scans. Although multiple patient geometries are used, the loading of each model is not patient specific. Patient differences in loading are also likely to affect the primary stability of the tibial tray.

As previously discussed, the majority of studies apply a simple static load to the tibial tray. This oversimplifies the 6 degree-of-freedom time varying loads of the knee. One study used a load cycle representing five points of the gait cycle (Chong et al., 2010). The most

comprehensive loading simulated the full cycle of five ADLs, applying all forces and moments directly to the tibial tray (Taylor et al., 2012). If a study used models of multiple patients, loads were only scaled by body weight, keeping the ratios between load components fixed. This does not adequately represent inter-patient variability, where significant variation in the ratio of the force components (e.g. A-P force to AX force) is known to occur between patients (Kutzner et al., 2010).

The focus on patient specific models, particularly with only static loading, is a limitation of the current tibial tray FE studies. Recently, a population of 17 patients was used to study a hip resurfacing (Radcliffe et al., 2007a; Radcliffe et al., 2007b). Methods for determining the minimum sample size are considered, either based on precision or statistical significance between two groups of models. The approach to creating the models was 'brute force', each model was created manually by segmenting the CT scan, creating a set of contours, and then lofting the contours to generate the model. This process does not scale well with an increase in the population size. A better approach would be to generate the mesh directly from the segmented CT data, avoiding the intermediate step of converting the model to parametric geometry. There are techniques which can be used to speed up the generation of patient specific models such as automatic segmentation (Fripp et al., 2006), allowing faster segmentation of the CT scan, or mesh morphing (Couteau et al., 2000; Moshfeghi et al., 1994), where a reference mesh is created and morphed to fit the patient geometry mesh.

An alternative approach is to use a SM. A large scale FE study assessing the risk of hip fracture used a SM of the femur, incorporating both geometry and elastic modulus variation, to generate a population 1,000 femurs (Bryan et al., 2009). A similar approach was used to assess the influence of head diameter of a hip resurfacing (Bryan et al., 2012). By using a SM, a large population of models could be generated quickly and cheaply, with the advantage that only a relatively small set of training data is required. To create the femur SM, Bryan et al. (2009) used a set of 21 CT scans (although this was later increased to 46 (Bryan et al., 2010)). For a large scale study, a SM negates the need to collect a CT scan of a patient to create each model, a process which would be time consuming and expensive.

In pre-clinical testing of joint replacement, the shift from a patient specific study to a population-based study is significant. The assumption often made is that the results from a single model can be extrapolated to the general population. However, the survival rate of TKRs is 90–95% after 10 years, and with over 80,000 TKR procedures being performed each year, a significant number of implants are revised. Current pre-clinical testing does not give an insight into patient differences, which might affect the long-term success of a TKR. Population-based studies offer the opportunity to identify patient factors, such as weight, loading, bone quality, or bone size, as well as, the influence of implant design and surgical parameters on the performance of a TKR.

The main motivation for this thesis is to extend the computational testing of a TKR, specifically the tibial tray, from patient specific to population-based. A methodology for large scale, population-based testing of the tibial tray will be developed, the use of which will be demonstrated in a series of case studies. The literature reviewed until this point only concerns

the anatomy and function of the knee, and current FE models of the tibial tray. An important aspect of a population-based study is the use of a statistical model. The next chapter reviews statistical models, focusing on how they can be generated and current examples of models.

Chapter 4

Statistical models

4.1 What is a statistical model?

The idea of a statistical model (SM) is to capture the variation of an object. The magnitude of the variation can be controlled to generate new instances of the object. With the growth of medical imaging and the use of multi-modalities it is becoming important to be able to recognise, capture, and analyse images more efficiently. SMs can be used for this task allowing semi-automatic and automatic processes to segment images (Fripp et al., 2006; Heimann et al., 2006), build geometric and FE models (Baldwin et al., 2010; Bryan et al., 2010; Querol et al., 2006), identify diseases (Subsol et al., 1998), or track organ motion (Rueckert et al., 2003).

In this thesis, it is intended that SMs are used to to generate a large population of FE models of the tibiae. These would then be used in a population-based FE study to assess the performance of the tibial tray. This use of SMs has been applied to the femur to assess hip fracture risk (Bryan et al., 2009) and a hip resurfacing (Bryan et al., 2012). This type of SM is focussed on capturing the variation of the shape of an object and is referred to as a statistical shape model (SSM). A review of SSMs are given in this chapter (section 4.3). However, to be able to create a SSM, each of the objects must be described by the same set of parameters (e.g. a mesh) and aligned in the same space. To do this, a process called registration is required and this is described in the following section.

4.2 Registration schemes

In medicine, imaging is used for non-invasive assessments of patients, making it possible for doctors to obtain potentially life-saving information without putting the patient through a painful procedure. The wider use of imaging means that there has been an increase in medical data and a need to make suitable comparisons between the different data. For example, a doctor might want to compare two MRI scans of a tumour in a patient taken at two separate intervals allowing them to determine if the tumour has grown or shrunk and help guide the treatment of the patient. Modern computing provides methods for visualisation of medical

data, but the challenge is to efficiently extract useful information from the data (McInerney et al., 1996).

Registration is the alignment of two similar sets of data such that the similar patterns in each set are in the same position. These data can be images, a set of points, parametric surfaces, or a triangle mesh. Image registration is used in medicine to align or combine images of a patient taken using multiple modalities (e.g. CT and MRI), align images taken over a period of time for comparison, or in computer aided surgery where a patient specific model can be created. Registration can also be used to align data from multiple subjects. This is useful in a research setting for characterising a cohort or generating a statistical model and is the context of registration in this thesis.

There are numerous reviews of registration schemes (Crum et al., 2004; Duncan et al., 2000; Hill et al., 2001; Maintz et al., 1998; McInerney et al., 1996) each classifying algorithms in different ways. A classification is offered by Maintz et al. (1998) who categorise registration schemes into 9 categories. Whilst comprehensive, this categorisation misses some of the newer developments in non-rigid registration. Instead, registration schemes will be described in terms of three main parts; similarity measures, transformation models, and optimisation strategies similar to Crum et al. (2004). An overview of each part of registration is given in the following sections.

4.2.1 Similarity measures

Similarity measures are used to determine how well two objects match. They can be split into two broad categories, geometric approaches and intensity approaches (Crum et al., 2004). Geometric approaches match two shapes or images[1] based on explicit correspondence between identified elements or landmarks in each shape or image. The landmarks might represent important anatomical structures such as anatomical points or functional anatomical surfaces. The differences in correspondence define the transformation to align or deform one shape or image to the other.

To be able to use anatomical landmarks for registration, they have to be reliably identifiable on each image or shape. Landmarks can be identified anatomically (e.g. selecting prominent points on an image or shape) or geometrically (e.g. by change in voxel intensity in an image or surface gradients), manually or automatically. Manual placement of landmarks means that the accuracy of the locations needs to be checked. Automatic identification of landmarks requires some parameterisation of the image or shape. For example, in a study on the brain, crest lines were extracted of the gyri and sulci and registered to a reference to generate a brain atlas (Subsol et al., 1998).

It is also possible to register surfaces[2] by identifying the matching points on each surface. Point correspondence can be defined explicitly (Cootes et al., 1995) but this is not always

[1] An image in this context is either a single 2D image or a stack of 2D images (e.g. CT or MRI set). Often a region of interest (ROI) has been defined which is the area being matched.

[2] This can be defined by a point cloud, splines, parametric surfaces, or a triangle mesh.

suitable for a large number of points. Euclidean distance between points on the surfaces can be used as a measure to identify the closest points (Besl et al., 1992; Moshfeghi et al., 1994) and additional factors such as surface normals can be included (Stammberger et al., 2000).

The intensity of an image can be used as a similarity measure. This approach matches image intensity patterns using a mathematical or statistical criteria (Crum et al., 2004). This assumes that the patterns in the source and target images will be most similar at the correct registration. The choice of similarity measure depends on the modality of the images being registered. For mono-modal registration (the two images have the same modality), the squared difference or correlation coefficient between intensities can be used. For multi-modal registration (the two images have different modalities), similarity measures such as mutual information or normalised mutual information can be used. These measures use image entropy as a measure of the amount of information in the image and aim to minimise the amount of information in the combined image.

Hybrid registration algorithms use both geometric features and intensity information. In theory they are more robust because more information is used in the registration of two images. In practice, each part of similarity measure is weighted; the PASHA (Pair-And-Smooth, Hybrid energy based Algorithm) algorithm (Cachier et al., 2003) is a weighted sum of an intensity similarity, the difference between landmark correspondences and volumetric deformation, and a smoothing term.

4.2.2 Transformation models

The deformation required to warp a starting image to a target image is defined by the transformation model. Rigid transformation models can be described using 6 degrees of freedom (DOF) (3 rotations and 3 translations) to 12 DOF (3 rotations, 3 translations, 3 scalings, and 3 skews), the latter termed an affine transformation. Rigid transformation models can be applied to either type of similarity measure.

The Procrustes method can be used to find a transformation, rigid or affine, to align two shapes (Hill et al., 2001). It requires that corresponding points in both shapes or images have been identified. Cootes et al. (1995) use a modified Procrustes method to align a set of training shapes with explicit point correspondence to generate a SSM (see section 4.3), optimising the transformation by a weighted sum of squares distance between the equivalent points on different shapes.

There are several algorithms which match surface features to compute a rigid transformation, the head and hat algorithm, distance transformations, and iterative closest point (ICP) (Hill et al., 2001). Of these the ICP is the most commonly used. Proposed by Besl et al. (1992) it is an algorithm designed to register 3D shapes described in a variety of forms, as a cloud of points, line sets, triangular set, curves, or surfaces. The aim of the ICP algorithm is to transform a 'data' shape P to be in alignment with a 'target' shape X. For each point in P the closest point in X is identified, giving a new set Y. A least squares quaternion operation is

applied to the points of P and the set of closest points Y to find a rigid body transformation to minimise the distance between the points.

There are two main problems with ICP. First, there is a bottle neck in the algorithm when finding the closest points. Several techniques have been developed, k-D trees, bucketing or closest point caching to speed this up. Second, the algorithm does not necessarily converge to the global minimum. Large changes in scale, rotation, or position can not always be corrected. This can be overcome by pre-translating the models to move the centres of mass to coincide or applying a set of initial rotations about the centre of mass of the model (Besl et al., 1992).

Studies use ICP to align images or shapes before applying a non-rigid registration (Declerck et al., 1997; Yang et al., 2006) or to check the alignment of a shape (Barratt et al., 2008). ICP has also been extended to include point weight based matching (Maurer et al., 1998), and intensity based matching (Feldmar et al., 1997).

Non-rigid registration uses global rigid transformations to align images and local deformations to obtain an image match. The concepts of non-rigid registration are reviewed in the literature (Crum et al., 2004; Hill et al., 2001; McInerney et al., 1996), and a detailed mathematical review of non-rigid transformations is given in Holden (2008).

Elastic models have been used to compute the deformation of an image (Bajcsy et al., 1989). This type of transformation treats the source image as a linear elastic solid and applies a deformation 'force' derived from a similarity measure (Crum et al., 2004). The model aims to find the equilibrium between the force of the source image to the force of the target image (figure 4.1). Moshfeghi et al. (1994) applied elastic matching to 3D surfaces. A surface is warped with a decreasing volume stiffness resulting in initial transformations which are essentially rigid and as equilibrium is approached local deformations are allowed to occur. This scheme has been used to register 3D cartilage surfaces from MRI scans (Stammberger et al., 2000). Another approach to elastic matching is to use octree-splines (a hierarchical and adaptive 3D displacement grid) to represent the 3D transformation between the surfaces, minimising a least squares criterion (Couteau et al., 2000). This method was used to morph a baseline tetrahedral of a femur to 10 other patient models for FE analysis (figure 4.1).

One problem with elastic matching is that the assumption of linear elasticity means that it is only valid for small deformations. If there is a large difference between images the deformations might not be recoverable. Fluid flow models allow large deformations, but misregistration can occur because of this (Crum et al., 2004). Another option if large deformations are present is an optical model, but a constant intensity is assumed between images.

Another transformation model for non-rigid registration is spline-based. A spline is a curve described by a piecewise polynomial function and control points are used to modify the curve. With spline based registration schemes a regular mesh of control points is placed on the source and target image or shape. Spline functions are used to describe the deformation of the mesh (Crum et al., 2004).

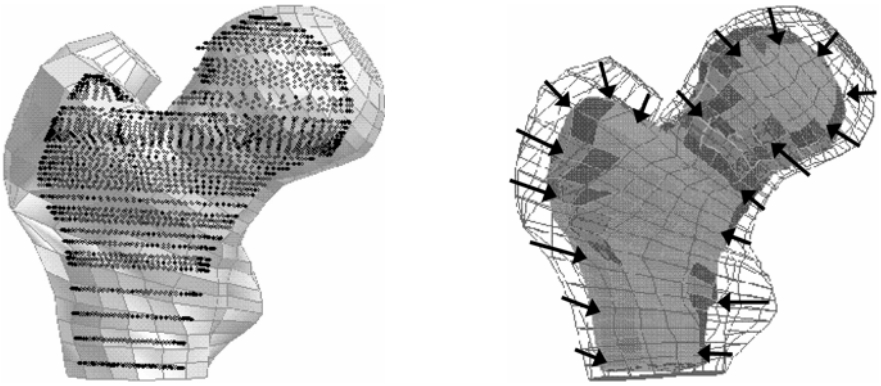

(a) Baseline mesh (grey) and surface target points (black)

(b) Baseline mesh morphed (wire-frame) to target shape (shaded grey)

Figure 4.1: An example of elastic matching. The baseline FE mesh is warped to fit the points on the surface of the target using and elastic matching scheme (images reprinted from Couteau et al., 2000, with permission from Elsevier).

Thin plate splines (Bookstein, 1989) have successfully been used in image registration. However, one problem of thin plate splines is that each control point influences the global transformation. If one point on the spline is moved, then all the other points along the spline are likely to move, limiting the ability to model local deformations. Also, as the control point density increases, the computational cost increases dramatically because more control points haves to be moved each time the spline is deformed (Crum et al., 2004; Rueckert et al., 1999).

Fast form deformations (FFD) use B-splines to overcome the control point problem. Moving a control point along the spline only transforms the curve in the local region of the point (Crum et al., 2004). Perhaps the most popular B-spline based scheme is that proposed by Rueckert et al. (1999) (for the breast), and turned into a generic registration framework by Schnabel et al. (2001). A variety of shapes have been registered using this scheme, including the brain (Rueckert et al., 2003), heart (Frangi et al., 2002), femur of apes (Yang et al., 2006), shoulder (Yang et al., 2008), and the lung (Murphy et al., 2008).

The spline based approach has been extended and optimised to improve the efficiency of the algorithms. Rueckert et al. (1999) assumes that all tissue in the image is non-rigid. In reality this is not the case, the stiffness of tissues varies from bone being (almost) completely rigid to soft tissues which are actually deformable. A tissue-dependent filter has been added to the registration scheme (Staring et al., 2007). This estimates the tissue stiffness at the control points and allows larger deformations for regions with lower stiffness.

There can be a secondary problem with the transformation model in that it might not produce a physically meaningful model. If a deformation field were to be applied to a real object, then no folding or tearing of the object is expected. To achieve this diffeomorphic transformations can be used. This type of transformation is smooth and invertible (Cootes et al., 2008). A diffeomorphic transformation can be found by placing constraints on the deformation field (Rueckert et al., 2003), creating a series of small diffeomorphic transformations (Cootes et al., 2004), or considering the deformations of an image in a reference plane (Cootes et al., 2008).

Matching of the images or shapes is specified using a similarity measure. The transformation model defines the deformation field for the registration. To obtain the best registration, the aim is to find the transformation where the maximum amount of information matches between the images. To do this, an optimisation strategy is applied.

4.2.3 Optimisation strategies

The way in which the transformation scheme is adjusted to improve the similarity measure is the 'optimisation' part of a registration scheme (Crum et al., 2004). A detailed discussion on optimisation strategies is beyond the scope of this thesis. Klein et al. (2007) is a technical comparison of optimisation methods for non-rigid registration using mutual information and B-splines. In a clinical setting real-time fast registration is becoming necessary for some applications (Klein et al., 2007). Large high resolution image sets mean that computational time to register images is a bottleneck and an optimisation strategy can help decrease the registration time.

For a rigid transformation, the ICP algorithm is often used to identify the correspondence between points in two models allowing a more automated image registration algorithm. This technique was used to build a statistical model of the wrist (Vos et al., 2004). In non-rigid registration the choice of optimiser depends on the registration problem. The more complex the transformation model, the more parameters required to describe it, and the longer it takes to find a set reasonable set of parameters. There is also the consideration that the transformation should be diffeomorphic. Standard optimisation strategies (e.g. Downhill Simplex Method, Powells Method, Conjugate Gradient Method etc.) have been applied to registration algorithms and can be gradient-free or gradient-based. A different solution to the optimisation strategy is to reformulate the problem using a Markov random field objective function (Glocker et al., 2008). In doing this two limitations of registration are overcome: the dependency on the similarity measure and on the selection of the initial conditions for optimisation.

4.3 Statistical shape models

Statistical shape modelling was first developed using 2D images. Active Contour Models (or snakes), popularised by Kass et al. (1988), used deformable contours to approximate the locations and shapes of object boundaries (McInerney et al., 1996) on the assumption that the boundary is continuous. This type of model used energy minimisation to warp the shape of the contour (similar to the idea of elastic matching). It can also be applied to a dynamic model to track the motion of an object over time (figure 4.2). Snakes can be applied to the segmentation of 2D images, making use of *a priori* knowledge to constrain the segmentation model.

Cootes et al. (1995) developed the Active Shape Model (ASM), similar to snake models, but with different global constraints. A set of manually placed points is used to represent each

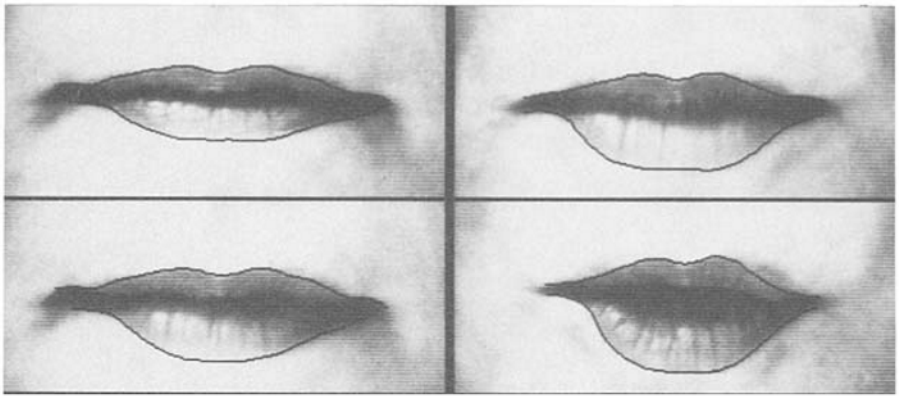

Figure 4.2: 4 frames from a short video showing snakes being used for motion tracking (images reproduced from Kass et al., 1988, with kind permission from Springer Science and Business Media). The snake is initialised to the shape of the mouth in the first frame.

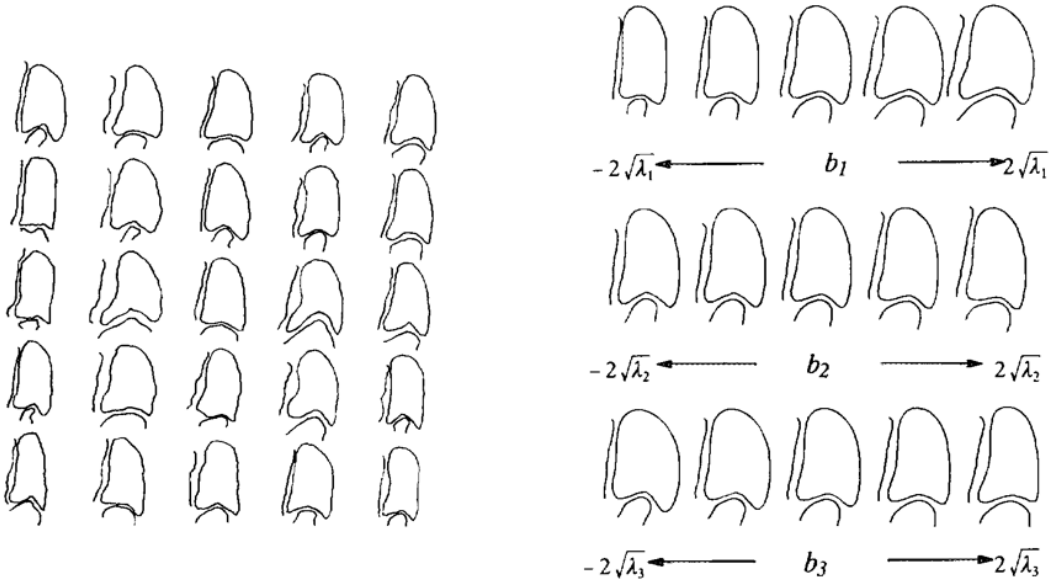

(a) Training set shapes

(b) First 3 modes of change

Figure 4.3: An ASM of a heart ventricle. (a) shows examples of the training set models. Each is made up of 96 points. (b) shows the effect of varying the first 3 shape parameters individually (images reprinted from Cootes et al., 1995, with permission from Elsevier).

training shape in an ASM, and the points must correspond from shape to shape. All the shapes are registered using a minimisation of the weighted sum of squares between points using a rigid body and scaling transformation based on the Procrustes method. Principal component analysis (PCA) is used to extract the dimensions (modes) of change in the model (figure 4.3). PCA gives a shape parameter matrix which allows the model to be used in two different ways. First, new random instances of the shape can be generated because the variation of the model is known. Second, it can be used as a classifier, estimating how well a given example shape fits the ASM.

ASMs have been expanded to Active Appearance Models (AAMs) (Edwards et al., 1998), which also include image texture (pattern intensities or colours over an image patch) or mesh

field information (data associated with an element in the mesh). The example ASM is of the face and image based. AAMs effectively combine two SMs, an ASM is used to capture the shape variation of the face using landmarks to identify facial features. Each training image is then deformed to fit the mean shape and the texture is normalised. PCA is then used to compute the combined variation of the shape and texture. AAMs have been shown to rapidly converge to find a new instance of a face.

Both ASMs and AAMs are examples of deformable models using a nearly non-rigid registration scheme using a set of landmark points. Similar to this idea, Ballester et al. (2004) uses the 4D-ICP registration scheme (Feldmar et al., 1997) to create a generalised image model (GIM). ICP is used with normal matching to register the landmarks of the training set. Each landmark is clustered and the mean position and covariance matrix is calculated. Using this information it is then possible to use the model to match a new shape using Mahalanobis distance measures. Unlike an ASM or AAM, there is no need to define an explicit relationship between the landmark points on the model and image. However, the GIM cannot be used to generate a new random instance of the model, it is better suited for inter-patient registration or identifying abnormal anatomy (Ballester et al., 2004).

All of the models described so far require a set of landmark points to be manually defined which are then used to create the SM. This process can be time consuming and introduce error in the model if the landmarks are not anatomically equivalent. Further to this, complex shapes are often represented as a 3D mesh with hundreds of points and elements, and it would not be practical to manually identify corresponding landmarks on such a shape. However, the points of the mesh can be thought to define landmarks of the shape. Kaus et al. (2003) proposed a statistical model which made use of the mesh vertices. Using an elastic matching registration scheme, each vertex in a template (or baseline) mesh was warped to a point of a segmented image that best matched the boundary criteria. This resulted in a set of training meshes which had corresponding points and could therefore be used as input to PCA. The mesh deformation was constrained by an internal energy, limiting the movement of each vertex, which helped to ensure mesh integrity and maintain the distribution of vertices of the mesh, improving the compactness of the SSM.

Using a mesh to create a SM allows further numerical analysis of the object (e.g. FE analysis). It also allows for an easier automatic method for creating a SM which avoids the ambiguity in placing landmarks. In a model of the wrist (Vos et al., 2004), each bone is represented as triangulated mesh and the mesh of the bone with the most vertices is chosen as the baseline (pivot) mesh. Point correspondence is found between this mesh and all the other meshes in the training set using the ICP algorithm. All the training set meshes are resampled to have the same density as the pivot mesh. The SM is created as per an ASM, possible because each wrist is represented by the same mesh with point correspondence between them. The size of the mesh used in this study is small (given the small size of the bones). If a more complex shape were to be used, it could become more difficult to identify point correspondence between meshes using ICP. This then becomes a problem in the SM because the shape is not compactly represented, and each point might have a large variance making the modes of change noisy.

Using a minimum description length (MDL) algorithm, it is possible to automatically find the optimal correspondence between landmarks (or points) on a set of shapes (Davies et al., 2002). By finding the optimal parameterisation of a set of shapes the computational complexity of the SM is reduced; the SM is more compact, has better specificity, and has better generalisation ability (Davies et al., 2002). This means that the noise in the modes is reduced and the variance of the first few modes of the SM is maximised. The MDL approach has been extended to 3-D (Davies et al., 2010). A disadvantage of the MDL approach is that the shape must be parameterised using a homeomorphic shape function (e.g. sphere), which is challenging in 3-D.

An alternative to using MDL is to use a FFD based registration scheme (e.g. Rueckert et al., 1999) to register the shapes. This finds the optimal deformation of a shape by manipulating a set of arbitrary control points, providing a naturally compact representation of the deformation field described at different resolutions. The deformation field of a set of shapes can then be used to create a SM. The advantage of this approach is that there is automatic correspondence between the arbitrary control points and because of the compact representation of the deformation fields, the SM is compact.

There is one feature of the models so far which has not been mentioned, and that is the creation of multi-body models. It has been shown that registering one shape of a single object class and creating a statistical model of this is possible. It has not been shown how to register and analyse two separate shapes in a single object class, e.g. the femur and tibia of the knee. Automatic correspondence methods could get confused with point correspondence between the two shapes, perhaps matching a point on the femur to a point on the tibia, thus creating an invalid object. Explicit definition of the point correspondence manually overcomes this problem. A very simple multi-body is shown in Cootes et al. (1995) with a heart ventricle (figure 4.3).

Several studies have created multi-body models of the wrist (Vos et al., 2004), the heart (Frangi et al., 2002) (figure 4.4), and the shoulder (Yang et al., 2008). The method, common to all these studies, is to register each shape separately and recombine them for PCA. This way, point correspondences are known for each individual shape and the global change in the shape is captured by PCA. To do this however, a global coordinate system is required to reduce the bias towards one particular shape.

All the models mentioned so far are surface only models. Whilst these models capture the geometric change of a shape, useful in a segmentation setting, none capture a variation of an associated field (except for Edwards et al. (1998) who presents an AAM of the face). A combined model of shape and field data has a particular application in population-based FE studies, where it would be of benefit to be able to generate meshes with associated material properties (e.g. Young's modulus) defined for each element. One example of this is Bryan et al. (2010), where an FE ready SM of the femur is generated incorporating both geometric and material properties variation. To do this, a set of femurs were segmented from CT scans and a surface was generated for each one. These were registered to a selected baseline mesh using an elastic registration scheme and the baseline volume mesh was morphed to fit each surface mesh. The material properties were sampled from the CT scan at the nodes of the

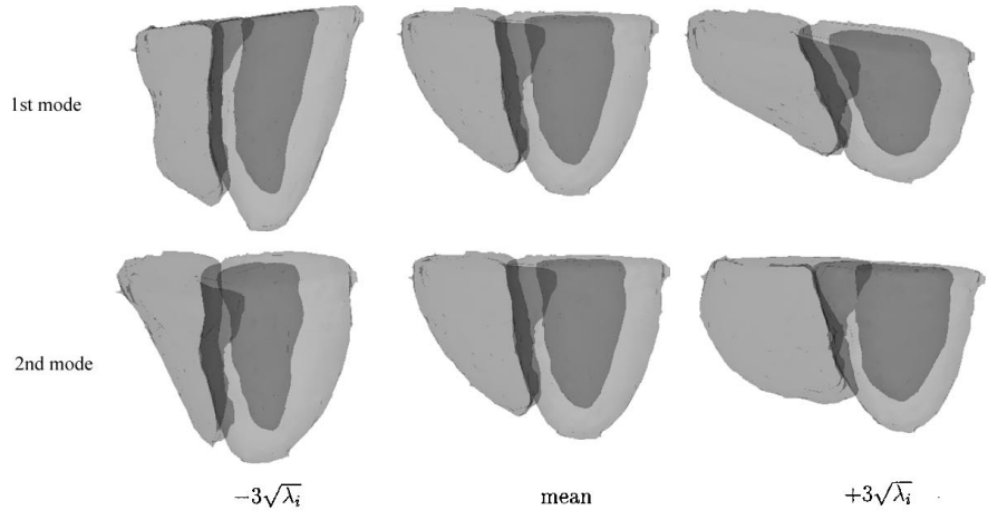

Figure 4.4: An example of a multibody statistical shape model. The first two modes of a 3-D two-chamber heart model are shown (image reproduced from Frangi et al., 2002, © 2002 IEEE).

mesh and converted to a modulus value. The material property information is added to the PCA vector. This method has been used to generate models for a FE study assessing femoral neck fracture risk (Bryan et al., 2009) and the influence of size on a hip resurfacing (Bryan et al., 2012).

Querol et al. (2006) take a slightly different approach, registering a training set of proximal femur CT scans using a non-rigid scheme and using both deformation and intensity information using PCA. There is no need to morph the shape of the intensity field as this is performed during the registration process. Calibrated CT scans were used for the training set; therefore a random instance of the model in the population will maintain the relationship between the intensity level and modulus. A FE mesh is generated for each model, the intensities are sampled from the generated volume image, and converted to Young's modulus. A simple load is applied to the model to assess the stress field (figure 4.5).

Both Bryan et al. (2010) and Querol et al. (2006) create what can be termed a SSIM. However, there are significant differences between the two approaches:

(i) Region of interest. Bryan et al. (2010) uses the full femur and Querol et al. (2006) only uses the proximal femur.

(ii) Training set size. To create the full femur SM, 46 training femurs were used. These were taken from clinical CT scans of an unknown population demographic. The SM of the proximal femur was created from a set of 11 proximal femurs. Using a larger training set size, the accuracy and generality of the SM is likely to be better.

(iii) Registration approach. Bryan et al. (2010) uses mesh based approach, whereas Querol et al. (2006) uses an image based approach. The disadvantage of image based registration is that to incorporate the image intensity each image volume must have the same resolution. For the proximal femur, the region of interest had dimensions of $175 \times 150 \times 200$ and a resolution of $1 \times 1 \times 1.65$ mm^3, a coarse resolution.

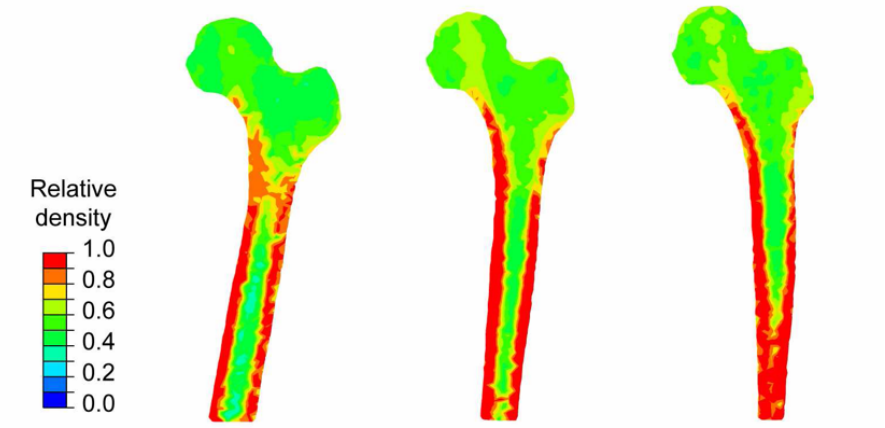

(a) Femur relative density

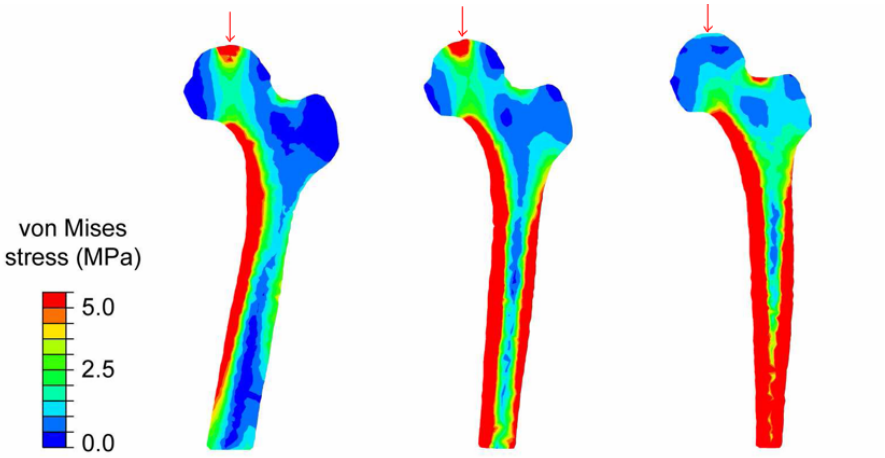

(b) Femur stress with 1600N load

Figure 4.5: Example of a statistical shape intensity model (image reproduced from Querol et al., 2006, With kind permission of Springer Science and Business Media). Shapes from left to right are: -2σ, mean, and $+2\sigma$.

(iv) Mesh density. The full femur has a much higher mesh density; proximal element size is 1 mm, and the distal element size is 3 mm, resulting in over 615,000 elements. This is compared to 3,500 elements of the proximal femur. This means that detail in the shape and material properties might be be lost.

(v) Mesh consistency. Upon generating a new instance of a proximal femur, Querol et al. (2006) had to mesh the segmented image. This means that each proximal femur is represented by a different mesh. By using a mesh based registration scheme, each generated full femur has the same mesh, and can be considered 'FE ready'. This offers an advantage in a population-based FE study, making comparison between models much easier.

These differences highlight that it is important to consider the use of the SM. If performing a FE study, it is an advantage that the SM is mesh based so that a new instance of the object is instantly ready for analysis. Image based SMs perhaps have the advantage when used for automatic segmentation, as the transformation of the shape is often applied directly to a segmented region of the image.

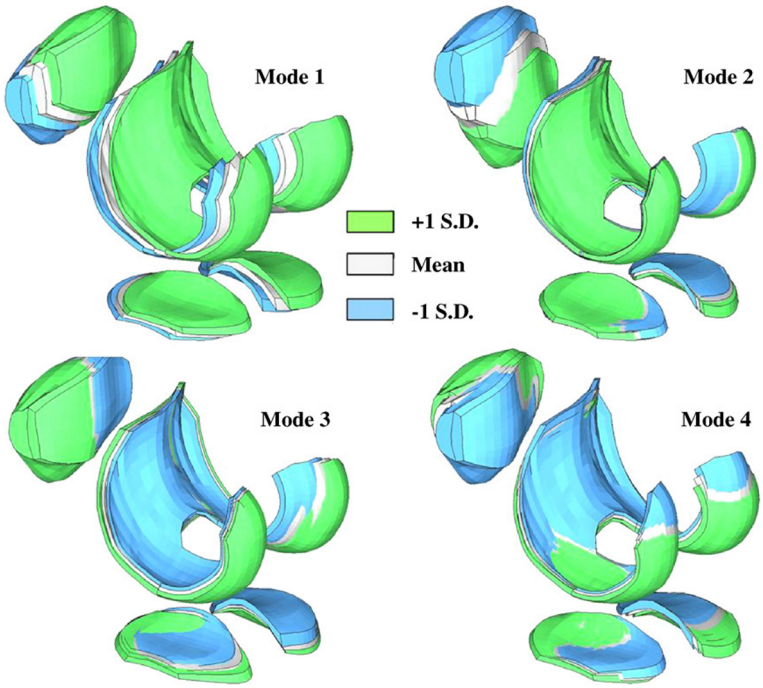

Figure 4.6: SM of knee cartilage and patella showing 4 modes of variation sampled at the mean and ±1 standard deviation (image reprinted from Baldwin et al., 2010, with permission from Elsevier).

There is also an example of a FE ready model of the articulating structures of the knee (femoral cartilage, medial tibial cartilage, lateral tibial cartilage, patella cartilage, and the patella bone as shown in figure 4.6) that uses a mesh based registration scheme (Baldwin et al., 2010). Template meshes of the geometry were segmented from a single subject and control points were defined at a suitable resolution on the template meshes. On a set of 10 MRI scans, control points were placed in positions corresponding to the template mesh control points around the perimeter of the cartilage and patella, defining a target geometry. By computing the difference in position of the two sets of control points, the template mesh was morphed to fit the generic mesh. The advantage of this method is that the mesh connectivity is maintained for each model. It also guarantees good correspondence between meshes because the control points are placed manually. However, this requires significant effort, as on average each structure requires around 160 control points to be defined, and the structures are relatively small. To morph the mesh of, say a tibia, many more control points would be needed.

4.4 Principal component analysis and statistical models

Discussion around SMs has focused on the use and properties of them. It has been mentioned that PCA can be used to create a SM, capturing the variation of the training data, and allowing the generation of new instances of shape. This is the approach taken in this thesis, and perhaps the best definition of PCA is from Jolliffe (2002):

> *"The central idea of principal component analysis (PCA) is to reduce the dimensionality of a data set consisting of a large number of interrelated variables, while retaining as much as possible of the variation present in the data set. This is achieved by transforming to a new set of variables, the principal components (PCs), which are uncorrelated, and which are ordered so that the first few retain most of the variation present in all of the original variables."*

Given this definition, PCA can be thought of as a method of extracting information from a large confusing data set. It transforms a high dimensional data set to a lower dimension representing its significant variance. In the case of linear PCA, a set of uncorrelated linear transformations can be found that retain most of the information given by the variances, correlations, or covariances of a data set. Suppose that $\mathbf{X}$ is a matrix of n observations for m experiments (i.e. each column of $\mathbf{X}$ represents a set of n measured values from an experiment), PCA theory shows that the principal components (PCs) are defined by an orthonormal transformation of $\mathbf{X}$,

$$\mathbf{Y} = \mathbf{U}^{\mathrm{T}}\mathbf{X}, \tag{4.1}$$

where $\mathbf{Y}$ are the PCs and $\mathbf{U}$ is an orthogonal matrix of eigenvectors. It is important to note that the PCs are ordered by variance, such that the 'kth PC' is the PC with the kth largest variance, corresponding to the 'kth eigenvalue' and 'kth eigenvector'. Therefore, it would be hoped that most of the variance in $\mathbf{X}$ is included in the first t PCs, where $t \ll m$.

The PCs can be derived from the eigenvectors and eigenvalues of either the covariance matrix or correlation matrix. There are two advantages of using the correlation matrix (Jolliffe, 2002):

(i) The PCs are less sensitive to the units of measurement of each element in $\mathbf{X}$, and also to wide differences in variances. This is because $\mathbf{X}$ is normalised and mean centred making the data dimensionless.

(ii) Due to the normalisation, it is easier to informally compare results from different analyses.

As will later be seen when generating the SMs of the tibia and gait cycle, reason (i) is why the PCs of the correlation matrix are computed. To compute the PCs, let the column vector $\mathbf{x}_i$ represent a registered set of data points l expressed in vector form,

$$\mathbf{x}_i = [l_1, l_2, \cdots, l_{j-1}, l_j]^{\mathrm{T}} \quad 1 \leq j \leq n. \tag{4.2}$$

The m shapes in the training set are then combined to create the training matrix

$$\mathbf{X} = [\mathbf{x}_1, \mathbf{x}_2, \cdots, \mathbf{x}_{i-1}, \mathbf{x}_i] \quad 1 \leq i \leq m. \tag{4.3}$$

In order to form the correlation matrix, the training data must be normalised

$$\tilde{\mathbf{X}} = \mathbf{D}^{-1}\mathbf{X}, \tag{4.4}$$

where $\mathbf{D}$ is a diagonal matrix composed of the row-wise standard deviation of $\mathbf{X}$. The normalised data is then mean centred

$$\hat{\mathbf{x}}_i = \tilde{\mathbf{x}}_i - \bar{\mathbf{x}}, \tag{4.5}$$

where $\bar{\mathbf{x}}$ is the row mean of $\tilde{\mathbf{X}}$. The correlation matrix can then be formed,

$$\mathbf{C} = \frac{1}{n-1}\hat{\mathbf{X}}\hat{\mathbf{X}}^{\mathrm{T}}. \tag{4.6}$$

However, rather than deriving the PCs directly from the correlation matrix, they can be found much more efficiently using singular value decomposition (SVD) (Jolliffe, 2002). This is because instead of explicitly calculating the eigenvectors and eigenvalues of the correlation matrix, they are implicitly computed. SVD can be expressed as

$$\hat{\mathbf{X}} = \mathbf{U}\mathbf{\Sigma}\mathbf{V}^{\mathrm{T}}, \tag{4.7}$$

where the columns of $\mathbf{U}$ correspond to the eigenvectors (representing the coefficients of each PC) and the diagonal of $\mathbf{\Sigma}$ are the eigenvalues (the square of which represent the variance of each PC). It is then convenient to define the weights of each PC as

$$\mathbf{b} = \mathbf{\Sigma}\mathbf{V}^{\mathrm{T}}. \tag{4.8}$$

From this, 'un-normalised' training data can be reconstructed using only t PCs,

$$\mathbf{x}_i \approx \mathbf{D}\left(\bar{\mathbf{x}} + \mathbf{U}_t\mathbf{b}_{ti}\right), \tag{4.9}$$

where the columns of the matrix $\mathbf{U}_t$ contain the first t PC coefficients, and $\mathbf{b}_{ti}$ is the vector containing the first t PC weights for data set i. Two observations can be made about equation 4.9. First, the transformation of dimensionality of the training data can be seen. Given that there can be up to m PCs, only the first t PCs need to be included to approximate the original shape. Second, by changing the PC weights, a new instance of a shape can be generated. By appropriate sampling of PC weights it is possible to generate a large population of shapes.

Chapter 5

Summary of literature

The previous chapters reviewed the literature about the knee, TKR, and computational testing of the tibial tray. A TKR is commonly used to replace the tibial and femoral articulating surfaces in patients suffering from arthritis, but the survival rate is still only 90–95% after 10 years (National Joint Registry for England and Wales, 2011). The main failure mechanism of a TKR is aseptic loosening, particularly of the tibial tray. Studies have suggested that early migration of the tibial tray is an indicator of late aseptic loosing (Grewal et al., 1992; Ryd et al., 1995). One reason for migration might be poor osseointegration, particularly in the initial post-operative period. Osseointegration is affected by the micromotion of the bone-implant interface, where large micromotions ($> 150\,\mu m$) prevent osseointegration (Pilliar et al., 1986).

Computational models using FE analysis can compute the micromotion at the bone-implant interface. It is also possible to compute the initial mechanical response of the bone. If the strain in the bone exceeds yield or ultimate limits, the bond between the implant and bone could break, resulting in loosening. Further to this, studies have also shown that there is a link between the initial mechanical response of the bone and implant migration (Perillo-Marcone et al., 2004; Taylor et al., 1998).

Current FE studies that assess the 'performance' of a tibial tray tend to look at micromotion and/or strain in the bone. Many of the studies compare the relative change of these measures to determine if a change of a model factor (e.g. design of the tibial tray) improves the outcome. A major limitation of many current studies is that they use either a model of a single patient, or models of a small number of patients. Given the inter-patient variability of the shape, size, and bone quality of the tibia, using only a single model does not represent the general population. For a TKR it is important to understand not only the implant design factors which might affect the long-term success, but also patient and surgical factors.

A second limitation of the tibial tray FE studies is often only a static axial load is applied, representing the peak during an activity cycle. The assumption is that the peak strain and peak micromotion will occur at this point. However, two studies have shown this not to be the case; the peak micromotion occurred when there was a low axial load and moderate V-V

moment (Taylor et al., 2012; Wong et al., 2010). This highlights that current FE models of the tibial tray do not apply appropriate loading conditions to assess primary stability. Low axial loading and moderate moments are likely post-operatively when only partial weight bearing is possible. It is therefore important that the primary stability is assessed under these loading conditions. None of the studies consider inter-patient variability of loads which has been observed *in vivo* (Kutzner et al., 2010). Whilst a standard load cycle can be scaled by body weight, this does not change the ratio of the load components (e.g. A-P to AX force).

These limitations in computational assessment of tibial trays could be addressed by using a population-based study to incorporate inter-patient variability. To generate a population of models, a PCA based SM can be used. The concept of SMs and the relation to registration and PCA was discussed in chapter 4. Perhaps the biggest challenge, particularly if the shape is complex, is ensuring that there is correspondence between all the training data. The data must be registered to find the correspondence between each shape. It is then possible to apply linear PCA to capture the variation of the training shapes, resulting in a SM.

Most of the SMs only include geometric variation of the shape. Few also include extra information about the shape (e.g. material properties). The most successful example of a SM that does this is of the femur (Bryan et al., 2010), where the elastic modulus data is included. A mesh based registration scheme was developed to find correspondence between each vertex of the mesh. This means that elastic modulus data can be defined at each node. A SM can be created using the node vertex positions and associated elastic modulus. This is more difficult using images, particularly 3D volumes. Registration schemes can find transformation of the region of interest (defining the shape) in an image, so that each shape can be represented in terms of the transformations of a set of control points. Including intensity information requires that the images are all of the same resolution, which can be difficult to achieve the training images are of mixed resolution. Furthermore, it is also necessary to generate a mesh for each new instance of a shape.

Given the successful use of a mesh based SM of the femur in population-based FE studies (Bryan et al., 2009; Bryan et al., 2012), it seems logical to follow a similar method for population-based FE studies assessing the tibial tray. However, only a static load was applied to the femur, as the kinetics of the hip are relatively simple in comparison to the knee. To include the inter-patient variability of loads and the intra-variability of the loads, it is proposed that a SM of knee kinetics during gait is used.

In chapter 6, the methods to generate a population of models are described. This will involve creating two SMs, one of the tibia, and another of the internal tibiofemoral joint loads for level gait. By sampling the SMs a population of tibiae with associated loads can be generated. It is then necessary to automate the implantation of the tibial tray in each tibia, as it is not feasible to do this manually. In collaboration with Zuse Institute Berlin (ZIB), tools were developed to do this. The implanted model and load cycle can then be processed for FE analysis, and a description of this process is also given.

Chapter 6

Generating a population of models for a large scale finite element study

6.1 Introduction

To be able to perform a population-based FE study assessing the tibial tray, it is necessary to generate a population of models. The limited availability of high quality clinical data has meant that it is often only possible to study a small population of patient specific models. It would be expensive and time consuming to obtain CT scans and joint load data to generate hundreds of patient specific models. The ethics of exposing so many patients to, perhaps unnecessary, radiation during a CT scan must also be considered.

Instead, a SM can be used, relying on only a small set of training data to generate a large population. To assess the tibial tray using a population-based study, it has been proposed that two SMs should be used, one of the tibia, and one of knee kinetics. The methods used to create these SMs are presented in this chapter. Further to this, the process of implanting each tibia with a tibial tray and preparing the models for FE analysis is also presented. Because a population of hundreds of models is being used, the challenge is to automate this process.

6.2 Statistical model of the tibia

The method used to generate a SSIM of the tibia follows that of Bryan et al. (2010). It is a mesh based SSIM and requires that all the training models are registered such that they all have the same mesh before PCA. The training data for the SSIM were taken from an available set of 32 full lower limb clinical CT scans of varying resolutions (slice resolution was 0.3 mm to 1.0 mm by 0.3 mm to 1.0 mm, with slice distances ranging from 0.3 mm to 2.0 mm). Unfortunately, the population demographics are unknown because patient information is incomplete.

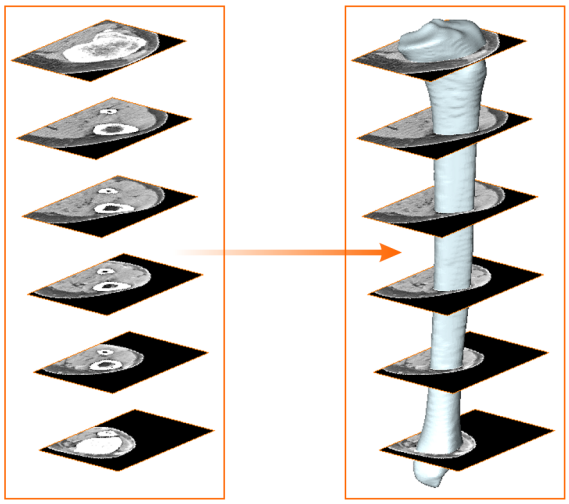

Figure 6.1: Segmentation of a tibia from a CT scan. The region of interest in the stack of CT slices (left) is labelled and then the stack of labels is used to create a surface (right).

6.2.1 Preparation of the training tibiae

The full tibia from each CT scan was segmented manually and a triangulated surface mesh of each was generated (figure 6.1) using Avizo (Visualization Sciences Group, Bordeaux, France). The tibia with length closest to the mean length of the training set was chosen as the baseline shape. The surface was split into two regions, the proximal third, and the distal two thirds. A tetrahedral FE mesh was generated using Ansys ICEM CFD (Ansys Inc., PA, USA). Different mesh sizes were set for the proximal and distal regions, the maximum element size was 1.5 mm and 5 mm respectively. The mesh size was chosen to allow accurate enough surface matching and capture enough detail of material properties in the proximal region, the region of interest. The volume mesh has 65,655 nodes forming 337,205 tetrahedra. The extracted surface of this mesh has 16,261 nodes forming 32,518 triangles.

The other surface meshes were required to have a similar number of nodes as the baseline surface for the elastic matching, and were simplified in Avizo to approximately 27,000 triangles. The reason for this is that it is necessary for the baseline surface to have a sufficient number of vertices and triangle patches to allow it to deform to the target surface (Moshfeghi et al., 1994). For example, if trying to morph a single triangle to the shape of a sphere, the triangle will become distorted. However, if the triangle is split into more triangles than those representing the sphere, it becomes possible to deform the triangle to the approximate shape of the sphere.

Before registration, all of the training surfaces were rigidly aligned to the same orientation as the baseline surface using the Iterative Closest Point (ICP) algorithm (Besl et al., 1992).

6.2.2 Surface elastic matching

The first step of registration is elastic matching of the surface meshes. The elastic matching takes two triangle surface meshes, a baseline (or reference) and a target (or goal), and deforms the baseline to match the target (figure 6.2). The algorithm described in this report is based

(a) 1 iteration (b) 50 iterations (c) 100 iterations

Figure 6.2: Elastic matching of the baseline (light) to target (dark) and different iterations.

on that used by Bryan et al. (2010) and is a combination of parts of several algorithms. ICP (Besl et al., 1992) is used to identify the closest triangle on the target for each point on the baseline. A Gaussian smoothing function is then applied to calculate the displacement vector (Moshfeghi et al., 1994). These two parts formed the original algorithm, and an additional step of Laplace smoothing (Vollmer et al., 1999) is used to smooth the mesh after the displacement vector is applied. This helps to maintain the quality of the baseline surface as it is iteratively morphed to the target surface.

The elastic matching is described using the terminology as per Moshfeghi et al. (1994). The baseline surface $\vec{S1}$ is represented by an ordered vertex list and triangle list

$$\vec{S1}(i,c) = \{(x1_i, y1_i, z1_i), \Delta_c\}\,,\ 1 \leq i \leq N1,\ 1 \leq c \leq T1, \tag{6.1}$$

where $(x1_i, y1_i, z1_i)$ is vertex i with corresponding vector notation $\vec{P1}(i)$, Δ_c is triangle patch c, $N1$ is the number of vertices, and $T1$ is the number of triangles. The same representation is used for the target surface $\vec{S2}$, such that

$$\vec{S2}(j,d) = \{(x2_j, y2_j, z2_j), \Delta_d\}\,,\ 1 \leq j \leq N2,\ 1 \leq d \leq T2. \tag{6.2}$$

Similarly, $\vec{P2}(j)$ represents vertex j, $N2$ is the number of vertices, and $T2$ is the number of triangles.

The steps of the registration algorithm to elastically deform the baseline surface $\vec{S1}$ to the target surface $\vec{S2}$ are described below and a flow chart of the algorithm is shown in figure 6.5.

Step 1: Scaling. $\vec{S1}$ is scaled to match the size of the $\vec{S2}$. The bounding box of each surface is used to compute the scaling factors. This scaling is necessary because of the large difference in ratio of length to width of the tibia.

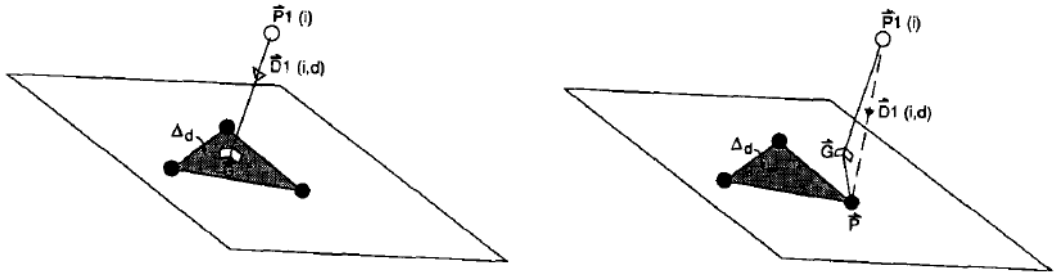

(a) Inside triangle (b) Outside triangle

Figure 6.3: How a point is determined to be in or outside the triangle patch (image reproduced from Moshfeghi et al., 1994, © 1994 IEEE).

Step 2: Initialise iterations. To deform $\vec{S1}$ to $\vec{S2}$, iterative deformation is required. The iteration counter, k, is set to 1, and the starting baseline surface $\vec{S1}^k$ is equivalent to $\vec{S1}$.

Step 3: Surface similarity measure. The similarity of the two surfaces is determined by best matching the points of one surface to those on the other surface. To best match the points of $\vec{S1}^k$ to $\vec{S2}$, a kd-tree is constructed of the triangle centroids of $\vec{S2}$. The n nearest triangles of $\vec{S2}$ to vertex $\vec{P1}(i)$ are found using an n-nearest neighbour search. A similarity measure (section 4.2.1) δ is computed,

$$\delta(i,d) = \rho(i,d) + \kappa\omega(i,d), \tag{6.3}$$

to determine which of the n triangles is the best match to $\vec{P1}(i)$. The positional difference, ρ, is dependent on if the perpendicular point of intersection $\vec{G}$ between $\vec{P1}(i)$ to the current nearest triangle Δ_d, lies inside or outside Δ_d (figure 6.3). If inside

$$\rho(i,d) = |\vec{G} - \vec{P1}(i)|, \tag{6.4}$$

otherwise, the nearest triangle vertex $\vec{P}$ to $\vec{G}$ must be found, and

$$\rho(i,d) = |\vec{G} - \vec{P1}(i)| + |\vec{P} - \vec{G}|. \tag{6.5}$$

The directional incompatibility, ω, is computed as the average of the sines of the angles between the plane of Δ_d and the planes of the triangles that share $\vec{P1}(i)$. Hence, if the planes are parallel, $\omega = 0$. The weighting of the directional measure is set by κ.

For all the points of $\vec{S1}^k$, the n nearest triangles of $\vec{S2}$ are determined, and the best match is taken as the one for which δ is minimum. This step is then repeated, reversing the roles of $\vec{S1}^k$ and $\vec{S2}$, to best match the points of $\vec{S2}$ to those of $\vec{S1}^k$.

Step 4: Calculate displacement vectors. After determining the best matching points, displacement vectors mapping one surface to the other are computed. To compute the displacement vector $\vec{D1}$, which maps $\vec{S1}^k$ to $\vec{S2}$, the actual displacement of point $\vec{P1}(i)$ in $\vec{S1}^k$ to the best matching triangle Δ_d in $\vec{S2}$ is dependent on whether $\vec{G}$ lies inside or outside

Δ_d (figure 6.3). If it is inside

$$\vec{D1}(i,d) = \vec{G} - \vec{P1}(i), \tag{6.6}$$

and if it is outside

$$\vec{D1}(i,d) = \vec{P} - \vec{P1}(i). \tag{6.7}$$

The displacement vector $\vec{D2}$, which maps $\vec{S2}$ to $\vec{S1}^{\,k}$, is similarly computed.

Step 5: Smoothen displacement. A smoothed displacement vector $\vec{DS}$ is computed by weighting the displacement of each point as the average displacement of neighbouring points

$$\vec{DS}(x,y,z) = \frac{1}{\gamma}\left[\frac{\sum_{i=1}^{N1} G1_i(x,y,z)\vec{D1}(i,d_i)}{\sum_{i=1}^{N1} G1_i} - \frac{\sum_{j=1}^{N2} G2_j(x,y,z)\vec{D2}(j,c_j)}{\sum_{j=1}^{N2} G2_j}\right], \tag{6.8}$$

where $G1$ and $G2$ are weighting functions. As suggested by Moshfeghi et al. (1994), these are defined as Gaussian functions

$$G1 = \exp\left(-\frac{1}{\sigma_k^2}\left[(x-x1_i)^2 + (y-y1_i)^2 + (z-z1_i)^2\right]\right) \tag{6.9}$$

$$\begin{aligned} G2 = \exp\Big(&-\frac{1}{\sigma_k^2}[(x - x2_j - \vec{D2}_x(j,c_j))^2 + (y - y2_j - \vec{D2}_y(j,c_j))^2 \\ &+ (z - z2_j - \vec{D2}_z(j,c_j))^2]\Big). \end{aligned} \tag{6.10}$$

The amount of smoothing is controlled by two factors: (i) a damping factor γ, and (ii) a smoothing parameter σ. The smoothing parameter is calculated each kth iteration by

$$\sigma_k = \sigma_0 f^{-k}, \tag{6.11}$$

where σ_0 is the initial value, and f is a constant $1 \leq f \leq 2$. This gradually decreases each iteration, allowing more local deformation.

Step 6: Apply deformation. The current baseline surface $\vec{S1}^{\,k}$ is then deformed by the smoothed displacement vector $\vec{DS}$, such that

$$\vec{S1}^{\,k+1} = \vec{S1}^{\,k} + \vec{DS}. \tag{6.12}$$

Step 7: Mesh smoothing. Although the displacement field of the baseline surface is smoothed and increased gradually, there is no guarantee that mesh integrity will be maintained. Points can be moved into a position that breaks the original mesh connectivity or creates distorted triangles, resulting in mesh folding (figure 6.4a). It is hard to identify exactly what causes this, but it is thought that too many points on $\vec{S1}$ are being matched to the same patch, or near the same patch in $\vec{S2}$, resulting in bunching of the points. Thus, smoothing the displacement field results in the points being folded over each other.

To help maintain the mesh integrity, the deformed mesh $\vec{S1}^{\,k+1}$ is smoothed. An improved Laplacian smoothing algorithm is used (Vollmer et al., 1999) because it avoids volume shrinkage

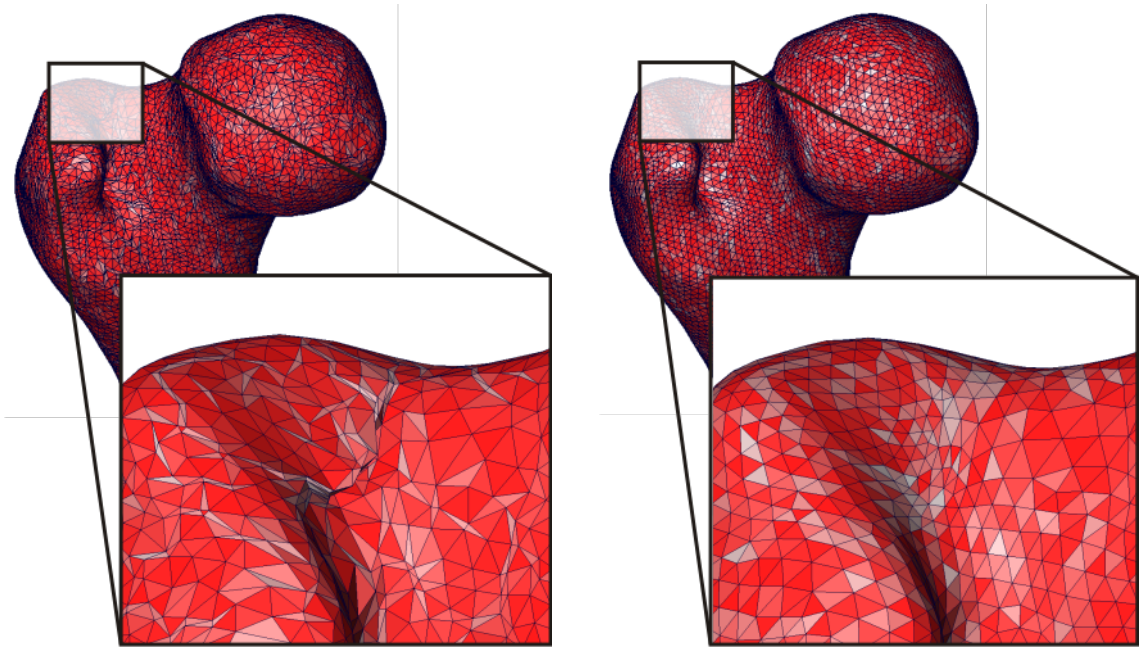

(a) Mesh folding (b) Smooth mesh

Figure 6.4: (a) shows evidence of mesh folding when no Laplace smoothing is applied during elastic matching. (b) is the same model but with 5 iterations of Laplace smoothing applied after each iteration of deformation. The colours represent triangle quality: light for low quality, red for high quality.

of the shape. Small features can be lost if too much smoothing is applied, and there is a trade-off between mesh quality and shape accuracy.

Step 8: Iterate. The algorithm iterates, repeating steps 3 to 7, to slowly deform $\vec{S1}$ towards $\vec{S2}$. Criteria can be applied to stop the iterations of elastic matching. For example, this could be either after a prescribed number of iterations $k_{\max}$, or if the magnitude of the deformation is less than a given tolerance ϵ, for example

$$\frac{1}{N_1}\sum_{i=1}^{N_1}\left|\vec{DS}(x1_i, y1_i, z1_i)\right| < \epsilon. \tag{6.13}$$

6.2.3 Parameters of elastic matching

The elastic matching algorithm is controlled by a set of input parameters. A balance is required between the parameters to achieve the necessary accuracy and mesh quality. Parameter testing was performed on a single model to heuristically establish a set of working parameters (table 6.1). Registration was run for all models using these parameters and no models required adjustment of the parameters.

The accuracy of registration is affected by the similarity measure, the sum of the positional difference distance and directional compatibility measures. The positional difference, effectively the Euclidean distance between two points, is the dominant measure. The directional compatibility measure is the likelihood that two vertices correspond, and is used to help

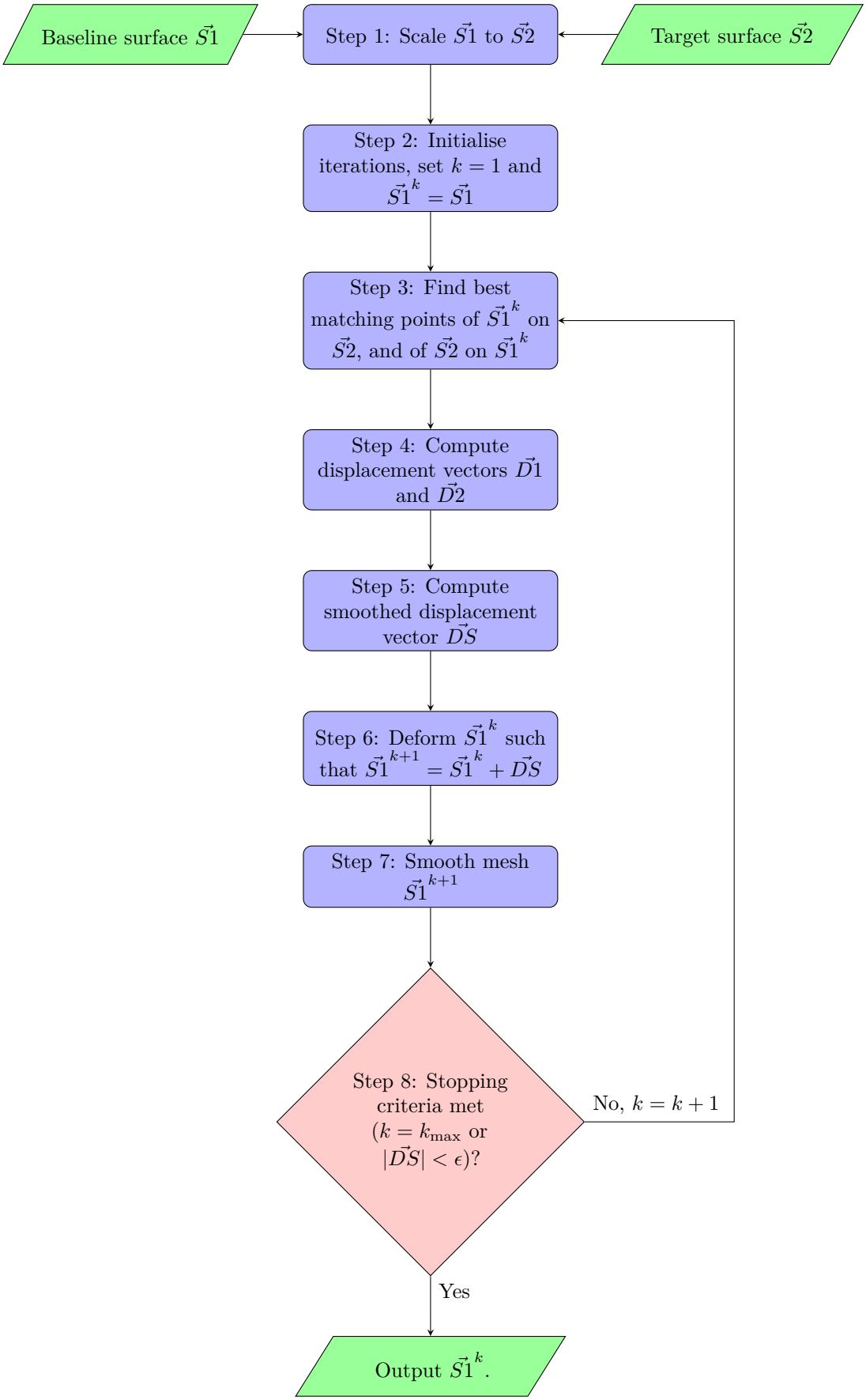

Figure 6.5: Flow chart of the steps of the elastic matching algorithm.

Table 6.1: Parameters for the elastic matching code.

Parameter	Value	Description
γ	2.0	Damping factor of displacement field. Values < 1 result in overshoot, and values > 1 result in undershoot.
σ_0	10.0	Initial value of smoothing parameter. If σ_0 is large, deformations will start rigid and slowly become non-rigid.
f	1.0715	Must be $1 \leq f \leq 2$. Controls the rate at which the smoothing parameter σ changes, influencing the rate of deformation (equation 6.11).
$k_{\max}$	100	Maximum number of iterations for the surface matching algorithm.
κ	0	Weighting of directional incompatibility measure. If $\kappa > 0$ then the orientation of the triangles is used to determine the nearest triangle.
k_{l}	5	Number of Laplace smoothing iterations.
α	0.8	Laplace smoothing 'pull' factor. Weights the inclusion of the original point and/or previous smoothed point in computing the point displacement.
β	0.2	Laplace smoothing 'push' factor. Weights the computed point displacement and/or the average displacement of the neighbouring points, in computing the point displacement correction.

decide the best matching triangle to the vertex in consideration. Heuristic testing showed that using the directional compatibility measure reduced the quality of the registered mesh and resulted in mesh folding. For this reason, directional compatibility was ignored ($\kappa = 0$), and the nearest triangle patch was determined by Euclidean distance only.

The parameters σ_0, f, $k_{\max}$, and γ influence the deformation. By increasing σ_0 or f, greater deformation can be achieved but mesh quality is reduced. It was found that a relatively high value of σ_0 and a low value of f, over a large number of iterations $k_{\max}$, was a good trade off between achieved deformation and mesh quality. The damping factor γ was set to give undershoot.

Both registration accuracy and mesh quality are affected by the Laplacian smoothing parameters α, β, and k_{l}. Small features can be lost if too much smoothing is applied, and this must be balanced with mesh quality. The number of iterations of smoothing is kept low to avoid loss of shape features, the pull factor α is high, weighting the position of the original point, and the push factor β is low, weighting the average displacement of surrounding points to obtain better smoothing quality.

6.2.4 Volume morphing

The second step of registration is volume morphing of the tetrahedral mesh. The baseline surface has been registered to each of the target surfaces, giving known displacements of the baseline tetrahedral mesh surface. This can be used to compute the internal vertex displacements. Previously, decoupled Laplace equations were used to calculate the internal vertex displacements (Bryan et al., 2010). This is a simple and efficient solution for volume morphing, but can produce very distorted elements.

Figure 6.6: Volume morphing of the baseline tetrahedra mesh to fit a target surface mesh

An alternative is to solve the equations of linear elasticity, applying the displacement of the surface vertices as Dirichlet boundary conditions. For each element

$$E = k\left(\frac{1}{V}\right)^{\gamma}, \tag{6.14}$$

where E is the stiffness, V is the volume of the element, γ is a stiffening parameter, and k is a scaling constant. Solving the internal vertex displacements using the linear elasticity equations reduces the number of distorted tetrahedra[1]. For volume morphing of the tibia, γ was set to 0 so that each element was fully elastic. A custom parallel Fortran code was used to solve the elasticity equations, decreasing the computational time from 45 minutes to 30 seconds.

To complete the registration, the baseline tetrahedral mesh was morphed to fit each of the registered training surfaces. All tibiae in the training set are then described by a tetrahedral mesh with point and element correspondence.

6.2.5 Material properties sampling

A feature of the tibia SSIM model is that the elastic modulus distribution (or field) of the tibia is included. The elastic modulus of each element in the tibia can be computed from the CT intensity. It is known that the density of bone ρ is related to the CT intensity g by

$$\rho = mg + c. \tag{6.15}$$

Normally, the calibration constants m and c are determined using a phantom which contains two materials of known densities and, ideally, would be included in the CT scan. The calibration constants can be computed by solving equation 6.15 simultaneously. Unfortunately,

[1] F. Galloway, R. Bryan, et al. (2010). "An improved registration scheme with application to statistical shape modelling of the human femur". In: *Computer Methods in Biomechanics and Biomedical Engineering*. Valencia.

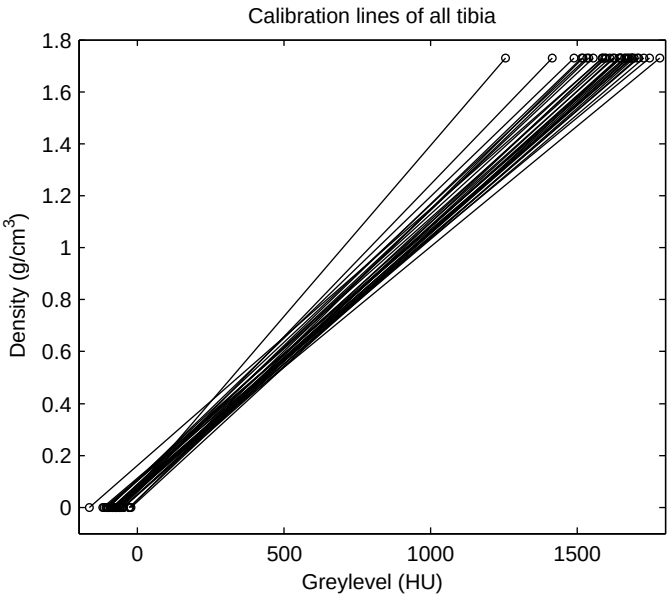

Figure 6.7: Relationships of CT intensity to bone density for all tibiae.

phantom blocks are not routinely used in clinical CT scans and are not present in any of the data sets available for this study. Instead, the CT scans are calibrated sampling the intensity of two distinct regions of bone:

(i) Bone marrow. Found in the medullary canal, it has the lowest modulus in bone. This is assumed to be water and have a relative density of $0\,\mathrm{g/cm^3}$.

(ii) Cortical bone. This region of bone is the strongest and has the highest modulus. This is assumed to have a density of $1.73\,\mathrm{g/cm^3}$.

An average of ten samples each covering a small area were taken in a region of bone marrow and cortical bone, where the lowest and highest intensity values were found respectively. For marrow bone, the intensity values ranged from $-164\,\mathrm{HU}$ to $-22\,\mathrm{HU}$ (mean $-76\,\mathrm{HU}$), and for cortical bone, the intensity values ranged from $1255\,\mathrm{HU}$ to $1781\,\mathrm{HU}$ (mean $1616\,\mathrm{HU}$), and the calibration lines for all the tibiae are shown in figure 6.7. All the calibration lines have a similar gradient, which indicates that the intensity of each CT scan represents a similar density. There is one outlier in the data, where the high density cortical bone has was found to have a lower intensity value of $1255\,\mathrm{HU}$ in comparison to the other data. In the case, it might be that the tibia actually has a lower bone density, and an intensity of $1255\,\mathrm{HU}$ does not represent a density of $1.73\,\mathrm{g/cm^3}$.

As the tibia will be modelled as a linear elastic material (see section 2.1.9), density of the tibia needs to be converted to elastic modulus. From experimental testing, density-modulus relationships have been found for many different anatomic sites (Helgason et al., 2008). The dependence of the relationship on anatomic site means it is necessary to use a density-modulus relationship for bone in the proximal tibia, because the region of interest in the FE studies is the proximal tibia. Therefore, the relationship from Linde et al. (1992) was used

$$E = 4778\rho^{1.99}, \tag{6.16}$$

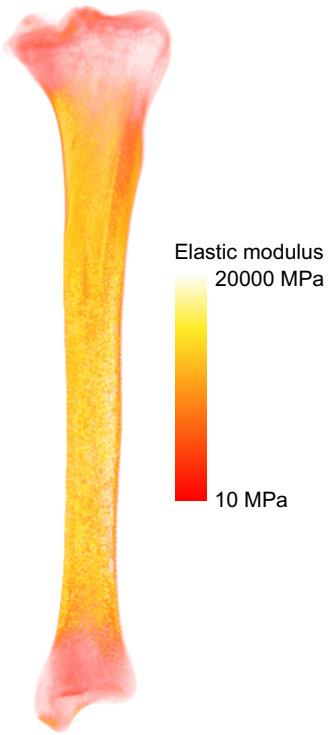

Figure 6.8: Volume rendered false colour image of a model in the training set. Lighter yellow regions are representative of cortical bone and darker red regions are representative of bone marrow.

where the elastic modulus E is in MPa, and the density ρ is in g/cm^3. For each registered tibia volume mesh, the CT intensity value was sampled at each element using Avizo. The intensity values were converted to density using the computed calibration relationship (figure 6.7), and then to elastic modulus. An example tibia, volumed rendered using elastic modulus as the colour field, is shown in figure 6.8.

To avoid FE solver problems, which can occur if elements have a modulus of around 0 MPa (e.g. the elements representing marrow bone), elements with a modulus < 10 MPa were assumed to have a modulus of 10 MPa. This threshold was chosen so that the elements did not significantly affect the strength of the tibia or load transfer through the tibia. For example, low modulus marrow bone is found in the medullary canal in the shaft of the tibia. If this were modelled with too high a modulus (e.g. 250 MPa), the strength of the shaft of the tibia would be artificially increased, changing the load distribution through the tibia. Cancellous bone has a relative density of 0.05 to 0.7 of cortical bone, corresponding to a density of 0.09 g/cm^3 to 1.21 g/cm^3, assuming the density of cortical bone is 1.73 g/cm^3. A modulus value of 10 MPa corresponds to a density value of 0.045 g/cm^3, representative of extremely weak bone.

6.2.6 Principal component analysis

The SSIM of the tibia is created using PCA following the method described in section 4.4. The vertex positions and element elastic modulus data for each tibia must be expressed as a vector

$$\mathbf{x}_i = [x_1, \cdots, x_p, y_1, \cdots, y_p, z_1, \cdots, z_p, E_1, \cdots, E_q i]^{\mathrm{T}} \quad 1 \leq i \leq m, \tag{6.17}$$

where p is the number of vertices in the mesh, and q is the number of elements in the mesh (the elastic modulus is defined on each element). These are combined in a training matrix

$$\mathbf{X} = [\mathbf{x}_1, \mathbf{x}_2, \cdots, \mathbf{x}_i]\,. \tag{6.18}$$

Because the training data has mixed units (there is both positional and modulus data) it is preferable to compute the PCs from the correlation matrix (see section 4.4). The size of the training matrix is also large (the length of a model vector is $3p + q$), and it is inefficient to explicitly compute the eigenvectors and eigenvalues of the correlation matrix. By using SVD, they can be efficiently computed.

The training matrix was normalised by row-wise standard deviation (equation 4.4) and mean centred (equation 4.5) to give $\hat{\mathbf{X}}$. PCA was carried out using SVD such that $\hat{\mathbf{X}} = \mathbf{U}\mathbf{\Sigma}\mathbf{V}^{\mathrm{T}}$ (equation 4.7). The columns $\mathbf{U}$ correspond to the eigenvectors (representing the PC coefficients), the diagonal of $\mathbf{\Sigma}$ are the eigenvalues (the square of which represent the variance of each PC), and the PC weights were computed by $\mathbf{b} = \mathbf{\Sigma}\mathbf{V}^{\mathrm{T}}$.

6.2.7 Assessment of registration

Surface elastic matching assessment

The surface registration was assessed by the accuracy of the elastic matching and the quality of the mesh. Checks for holes and intersecting triangles were also done, and none of the registered surfaces were found to have holes or intersecting triangles.

The accuracy of the elastic matching algorithm was characterised by the 'magnitude of deformation', computed from the smoothed displacement vector ($\vec{DS}$) of the final iteration. The displacement of each point was normalised and then the mean was taken. This gives an idea of the surface to surface distance. As the algorithm iterates, the deformations become smaller and more localised, hence the magnitude the deformation is an indication of how well matched the shapes are. As an independent measure, the mean 'surface to surface distance' between the registered surface and the target surface was also computed using Avizo. Both measures were computed for all tibia and were of a similar order of magnitude. The mean 'magnitude of deformation' was 0.06 mm, and the mean 'surface to surface distance' was 0.03 mm.

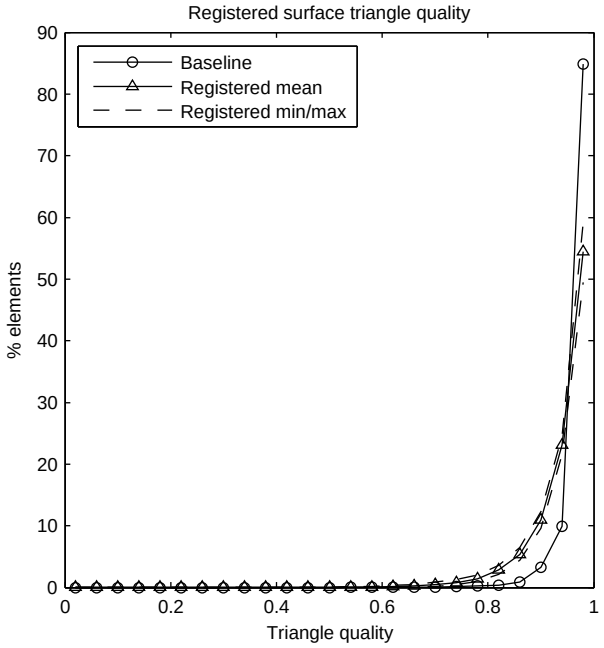

Figure 6.9: Triangle quality distribution of the registered surfaces compared to the baseline surface.

The registered surface mesh quality was checked by computing the triangle quality

$$q_{\text{tri}} = 2\frac{r}{R}, \tag{6.19}$$

where r is the inscribed radius and R is the circumscribed radius. This measures triangle quality in terms of the diameter ratio; 0 is the worst and 1 is the best. The triangle quality of each registered surface was binned into 25 bins. The distribution of the triangle quality of registered surfaces and baseline surface is shown in figure 6.9. A surface score was computed by summing the upper limits of the bins multiplied by the percentage of elements in the bin, hence, a surface with perfect equilateral triangles will have a score of 100.

The registered surface score is comparable to the baseline score, 96.2 compared to 99.0 respectively. The distribution of triangle quality shows that the for the registered surfaces, the average percentage of triangles with the best quality is 54% compared to 85% for the baseline surface. Despite this, the quality of the majority of triangles was between 0.7 and 1.0 for the registered surfaces.

Volume morphing assessment

The volume mesh quality was checked by computing the tetrahedron quality

$$q_{\text{tet}} = 3\frac{r}{R}, \tag{6.20}$$

where r is the inscribed radius of the sphere and R is the circumscribed radius of the sphere. This is the diameter ratio of a tetrahedron; 0 is the worst possible tetrahedron quality, and 1 is the best. As per the triangle quality, for each registered mesh, the tetrahedron quality

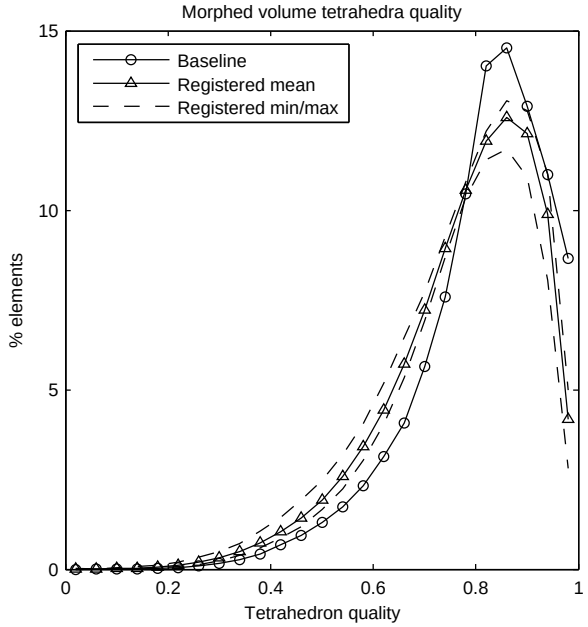

Figure 6.10: Tetrahedron quality distribution of the registered meshes compared to the baseline mesh.

was binned into 25 bins. The distribution of the tetrahedron quality of registered meshes and baseline mesh is shown in figure 6.10. A mesh score was computed by summing the upper limits of the bins multiplied by the percentage of elements in the bin, hence, a mesh with perfect equilateral tetrahedra will have a score of 100.

The distribution of the registered meshes tetrahedra quality, shows an increase in the percentage of elements with a lower quality compared to the baseline mesh. This is expected, because the shape and size of the target surface can be very different from the baseline shape, resulting in large boundary vertex displacements. This can result in the tetrahedra becoming more distorted. However, the majority of elements have a quality above 0.5, well above the limit of 0.1 which many FE codes require. The mesh scores are also comparable, an average of 79.4 for the registered meshes, and 82.8 for the baseline mesh.

6.2.8 Assessment of statistical model

Variance of principal components

A feature of PCA is that the PCs are ordered by the variance of the training data. It would be hoped that the majority of the variance is retained in the first few PCs. When sampling a SSIM, it is important to include enough PCs so that the training data is adequately represented. This could be done using a cumulative percentage variance threshold.

The choice of variance threshold to select the PCs is somewhat arbitrary, Jolliffe (2002) suggests from 70% to 90%, and others have used 95% (Bryan et al., 2010; Bryan et al., 2009; Cootes et al., 1995; Edwards et al., 1998; Yang et al., 2006). For the tibia SSIM, 24 out of 32 PCs are required to represent 95% variance (figure 6.11).

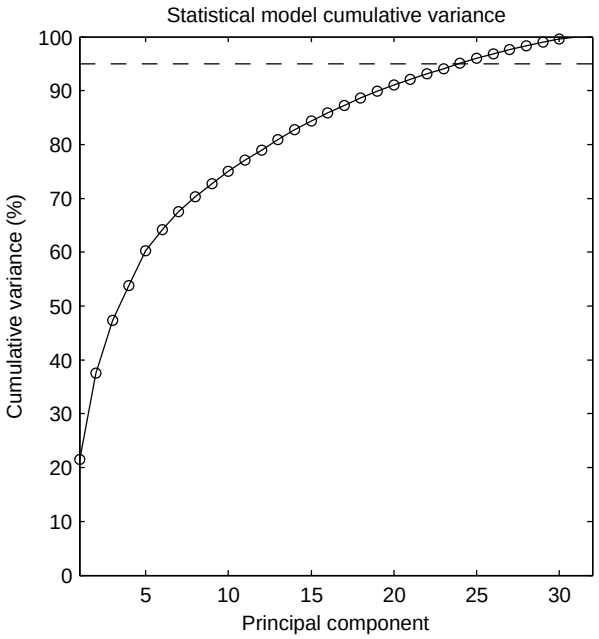

Figure 6.11: Cumulative variance of the PCs for the tibia SSIM. The dashed line marks 95% variance.

However, just selecting the number of PCs to include when sampling should not be based on percentage variance alone. It is also important to consider how accurately the SSIM can reconstruct the training data, and the predictive capability of the SSIM.

Reconstruction test

The accuracy of the SSIM was assessed using a reconstruction test. Each tibia in the training set was reconstructed using an increasing number of PCs (equation 4.9). As the SSIM includes both mesh vertex positions and element modulus, it is necessary to separate this data when computing the error between the 'original' and 'reconstructed' data. The vertex position error was computed as the mean Euclidean distance error between the corresponding vertex positions, and the modulus error was computed as the mean absolute error between the corresponding element moduli.

The median and inter-quartile range of the vertex position error decreased as the the number of included PCs used to reconstruct the data increased (figure 6.12a). At PC 1, the median vertex position error was 3.5 mm with an inter-quartile range of 2.7–4.2 mm. Including 24 PCs (which represents 95% variance), the median vertex position error is 0.4 mm with an inter-quartile range of 0.2–0.7 mm.

The SSIM is worse at reconstructing the element moduli accurately. The median modulus error decreases linearly with the increasing number of included PCs. The inter-quartile range decreases in the first few PCs, but then increases again in the later PCs. This indicates that there is a poor correlation between the element moduli in the SSIM. Including 24 PCs, the median modulus error is 227 MPa with an inter-quartile range of 144–501 MPa.

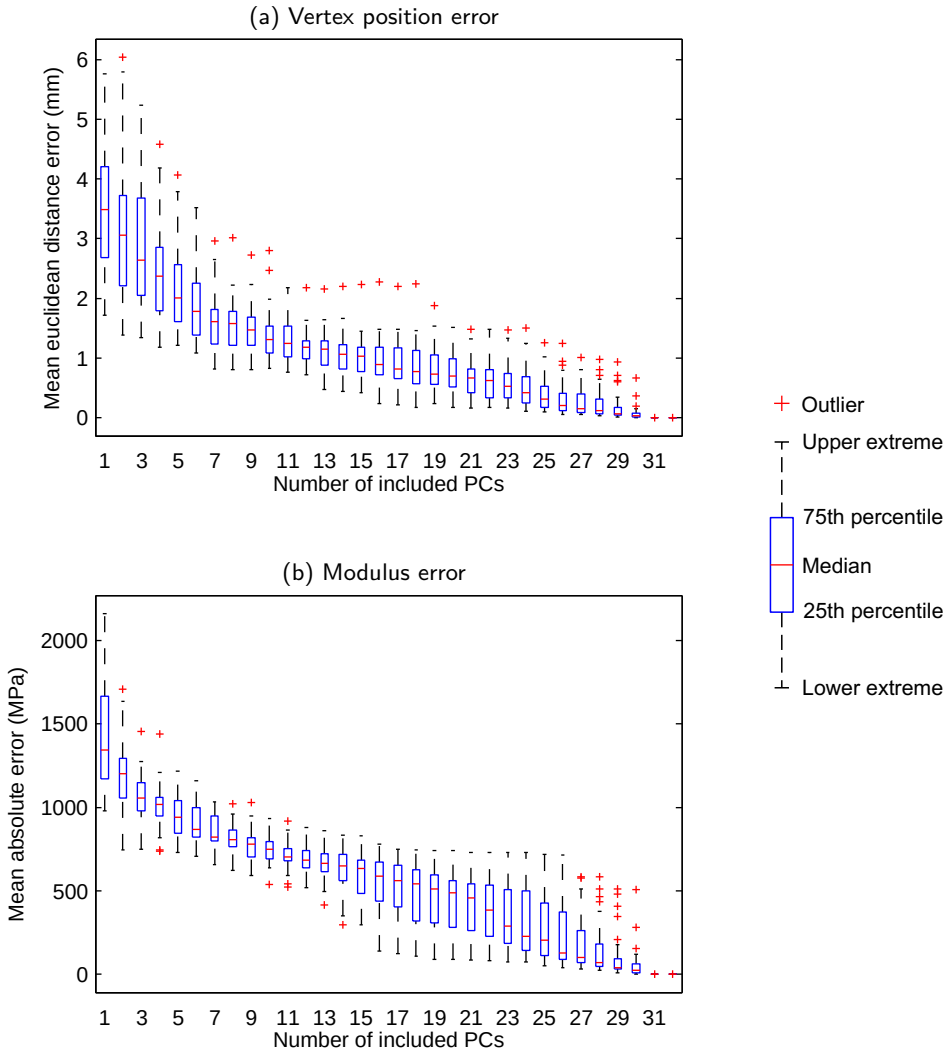

Figure 6.12: Reconstruction test error: (a) is the Euclidean distance error between vertex positions; (b) is the absolute modulus error between elements.

Leave-one-out test

A leave-one-out test was performed to assess the predictive capability of the SSIM. Each tibia model $\mathbf{x}_i$ was left out in turn, and a SSIM was created using the remaining training tibiae $\mathbf{Y}$. The PC weights $\boldsymbol{\alpha}_i$ of $\mathbf{x}_i$ are then computed,

$$\boldsymbol{\alpha}_i = \mathbf{U}^{\mathrm{T}}(\mathbf{D}^{-1}\mathbf{x}_i - \bar{\mathbf{y}}). \tag{6.21}$$

The 'left-out' tibia $\mathbf{x}_i$ can then be estimated using t PCs,

$$\mathbf{x}_i \approx \mathbf{D}(\bar{\mathbf{y}} + \mathbf{U}_t\boldsymbol{\alpha}_{ti}). \tag{6.22}$$

This is how data is normally reconstructed (equation 4.9), except that $\bar{\mathbf{y}}$ is the mean of normalised $\mathbf{Y}$, and the PCA weights $\mathbf{b}_{ti}$ are replaced by the 'left-out' PCA weights $\boldsymbol{\alpha}_{ti}$.

The 'left-out' tibia was then estimated using an increasing number of PCs. As per the reconstruction test, the vertex position error and modulus error was then computed between the 'left-out' tibia and 'estimated' tibia.

Both the vertex position error and modulus error were larger in the leave-one-out test than the reconstructed test. This is expected as the 'left-out' tibia is only being estimated by the SSIM. However, in the higher PCs, the median and inter-quartile range of the errors remain relatively large (figure 6.13).

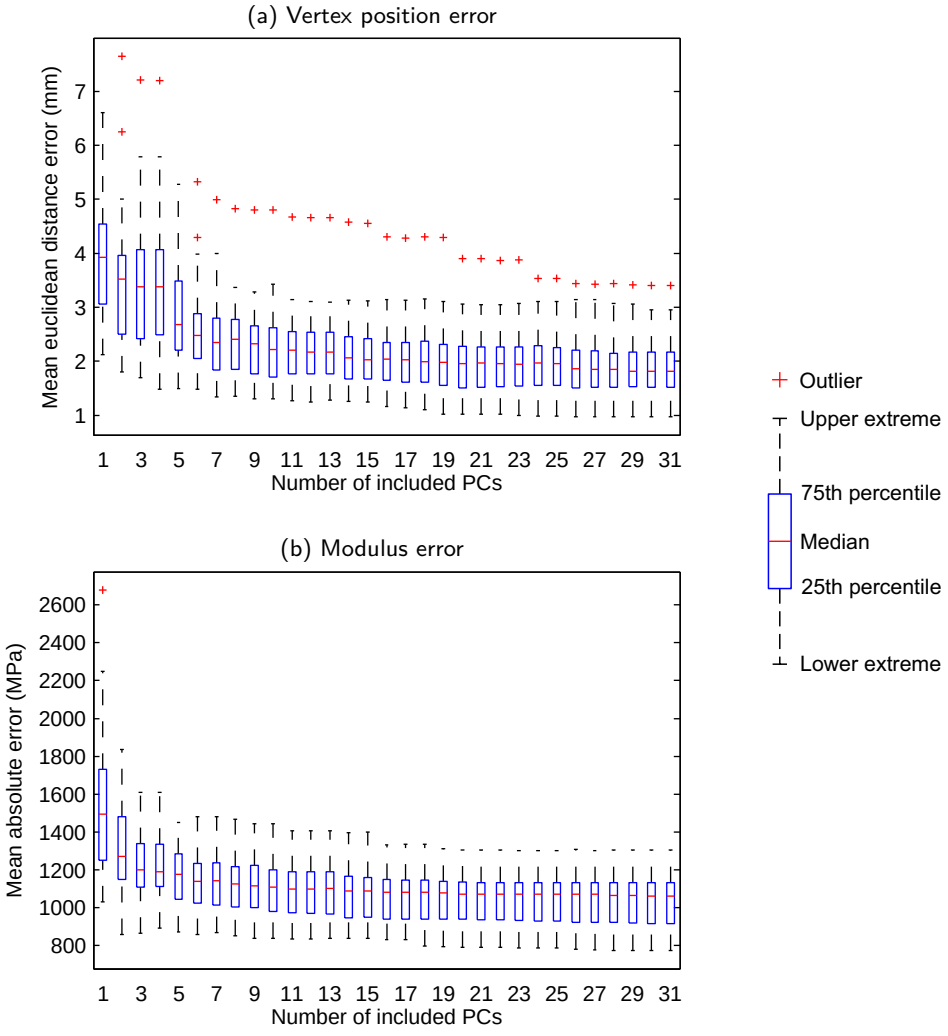

Figure 6.13: Leave-one-out test error: (a) is the Euclidean distance error between vertex positions; (b) is the absolute modulus error between elements.

The vertex position error has a median of 3.9 mm with an inter-quartile range of 3.1–4.5 mm at PC 1. Including 24 PCs, the median is 2 mm with an inter-quartile range of 1.6–2.3 mm. Including 11 or more PCs, the median and inter-quartile range of the error remains relatively constant (figure 6.13a).

The modulus error has a median of 1493 MPa with an inter-quartile range of 1249–1730 MPa at PC 1. Including 24 PCs, the median is 1069 MPa with an inter-quartile range of 928–1130 MPa. Again, when the 'left-out' data is estimated using 11 or more PCs, the median and inter-quartile range of the error remain relatively constant (figure 6.13b).

6.2.9 Interpretation of the principal components

The PCs of the SMs represent physical changes of the tibia. The changes of each PC can be seen by varying the value of the associated PC weight between an upper and lower limit. For the tibia SSIM it was seen that the distribution of the weight for the first 24 PCs (representing 95% variance) was approximately Gaussian (figure 6.14). It was assumed that for the kth PC, the weights had a Gaussian distribution with a mean μ_k and a standard deviation σ_k. In this case, $\mu_k = 0$ because the training data is normalised and mean-centred.

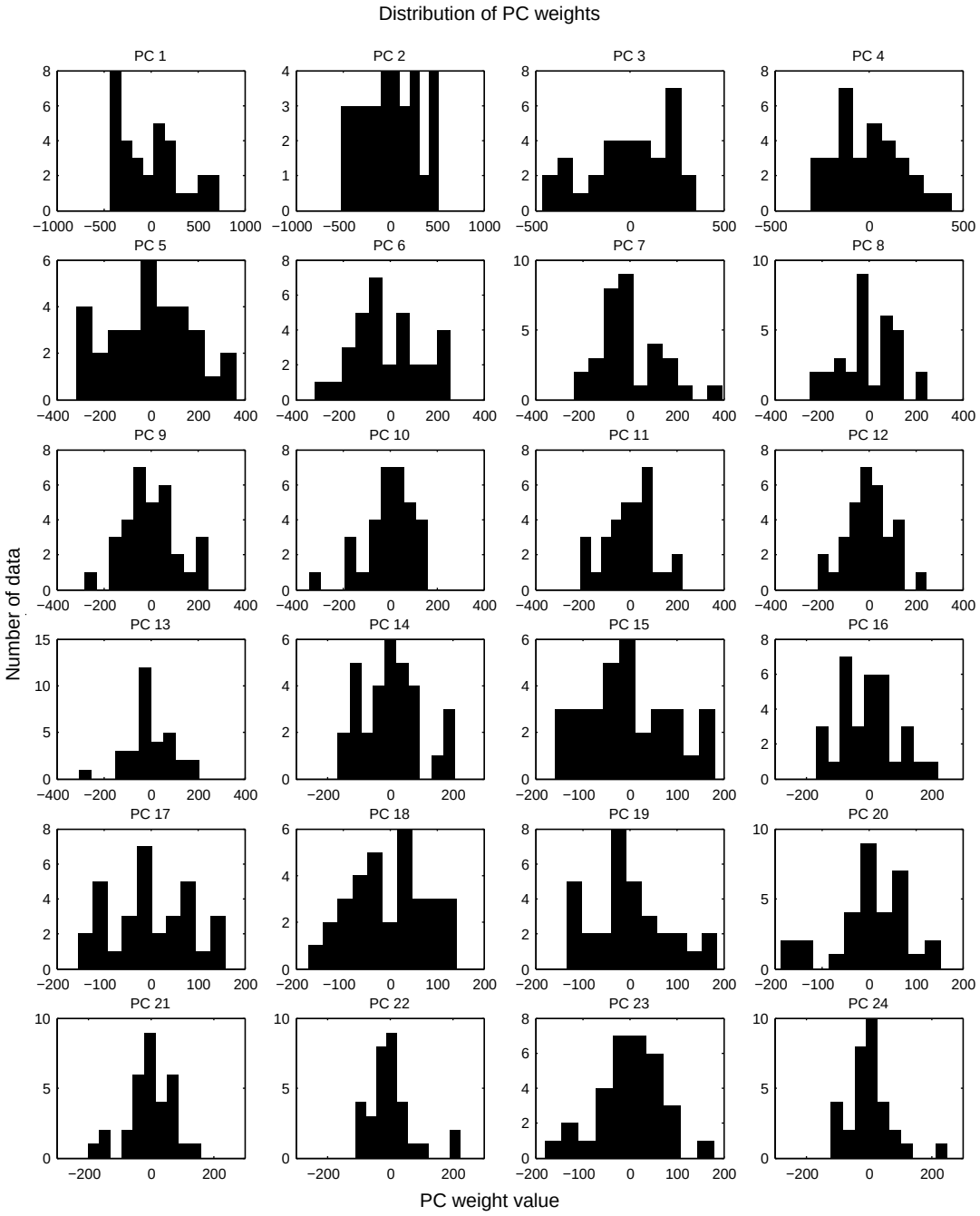

Figure 6.14: The distribution of the PC weights for the tibia model. Generally, the weights have a Gaussian distribution. Only the first 24 PCs are plotted because they represent 95% variance.

To visualise the first three PCs in isolation, a new tibia was generated with the PC weights set at $-3\sigma_k$, $0\sigma_k$, and $+3\sigma_k$. The generated tibiae are shown in figure 6.15. Each main column of the figure shows the changes of the tibia for a particular PC as the weights change from $-3\sigma_k$ to $+3\sigma_k$. Three views of the tibia are shown, the top row looks down on the condyles, the second row looks at anterior of the tibia, and the third row looks at the medial side of the tibia. The anterior and medial views are volume rendered to show the elastic modulus; lighter yellow regions represent cortical bone, and darker red regions represent marrow bone.

The first PC (left column of figure 6.15) shows changes in the scaling of the tibia. This is expected as the largest visible variation of the tibia is length. The tibia increases in size as the PC weight is changed from $-3\sigma_k$ to $+3\sigma_k$. There is also a change in the size ratio of the medial to lateral condyles (top row of left column in figure 6.15). At $-3\sigma_k$, the lateral

Figure 6.15: Changes of the tibia shape and elastic modulus distribution of the first 3 PCs in isolation. The main columns left to right show PC1 to PC3, and within these columns, left to right, show the PC weighted at -3σ, 0σ, and $+3\sigma$. The rows show different views of the tibia for each PC, top is the condyles, middle is the anterior of the tibia, and bottom is the medial side of the tibia.

condyle is smaller than the medial condyle, particularly in the A-P dimension, and at $+3\sigma_k$ the two condyles are more equal in size. In the second PC (middle column of figure 6.15), significant increase in the strength of the tibia can be seen; the mean elastic modulus of the tibia increases from a mean of 1350 MPa at $-3\sigma_k$ to a mean of 6000 MPa at $+3\sigma_k$. As the elastic modulus changes, the cortical bone of the shaft also thickens, and there is a small increase in length of the tibia. The third PC (right column of figure 6.15) shows changes in the size of the condyles and shaft diameter of the tibia. As the PC weight increases from $-3\sigma_k$ to $+3\sigma_k$, the condyles decrease in overall size, also becoming more equal in size (top row of right column in figure 6.15). This is coupled with an increase in the posterior slope of the condyles (bottom row of right column in figure 6.15). There is also a decrease in the diameter of the shaft, coupled with an increase in the strength of the cortical bone. It is also noticeable that the tibia tubercle becomes less prominent.

It is important to note that the changes do not occur in isolation, a random instance of the tibia will actually be the combined effect of several PCs, with features of a particular PC cancelled out or exaggerated further. Looking at an individual PC gives an insight as to how the size, shape, and elastic modulus distribution of the tibia varies.

6.2.10 Sampling the model

The target use of the tibia SSIM in this thesis is to be able generate a population of tibia, and it is possible to do this by sampling a selected number of PC weights. In the previous section, it was seen that the distribution of the weights for the first 24 PCs was approximately Gaussian (figure 6.14). Hence, the PC weights were randomly sampled assuming that each had a Gaussian distribution with a mean μ_k and standard deviation σ_k.

A population of 500 tibiae was generated, the first 20 of which are shown in figure 6.16. The length of the generated tibiae ranged from 28 cm to 47 cm. This was within ± 5 cm of the training tibiae lengths, which ranged from 32 cm to 44 cm. The elastic modulus of the generated tibiae was also similar to the training tibiae, with ranges of 10 MPa to 33.1 GPa and 10 MPa to 26.7 GPa respectively. It should be noted that for the generated tibiae, it was necessary to assign elements with an elastic modulus less than 10 MPa to have a modulus of 10 MPa to avoid solver problems during FE analysis, as was done for the training tibiae (see section 6.2.5). In terms of shape, each generated tibia shown in figure 6.16 has a cylindrical shaft and two expanded ends. At the proximal end, there are two distinct condylar regions separated by the intercondylar notch. The modulus distribution of each is as might be expected, the shaft consists of stronger cortical bone with a central medullary canal. The ends of each bone are weaker where only a thin cortical shell exists surrounding 'spongy' cancellous bone, made up of a network of trabeculae. Regions of high and low density cancellous bone are also visible.

Figure 6.16: Volume rendered images of the first 20 tibiae sampled from the SSIM.

6.2.11 Discussion

The registration scheme captures the shape of the training set accurately. There is only a small error in the surface to surface distance between the registered and target surfaces. The surface mesh quality is acceptable for volume morphing, with Laplace smoothing helping to maintain mesh integrity. The average tetrahedral mesh quality reduced after volume morphing, but was still found to be acceptable for FE analysis.

A limitation of the registration scheme is that point to point correspondence is not guaranteed. Ideally, by registering all the meshes, each will have the same number of vertices and elements in the same relative position. With a suitable mesh density, it is likely that points will end up approximately in the same anatomical position and landmarks can be identified by taking the average position of sets of points.

Point correspondence could be improved by landmarking each tibia. However, this relies on the landmarks being accurately defined. The automatic point correspondence uses Euclidean distance as a similarity metric and could potentially be improved by using surface curvature or triangle normals. This was tested in the current algorithm, but it was seen to reduce the mesh quality.

The SSIM is capable of reconstructing a tibia with reasonable accuracy. From the reconstruction test, the median vertex position error was 0.4 mm and the median modulus error was 227 MPa using 24 PCs. The SSIM is not as accurate at predicting new data, when 24 PCs were included, the leave-one-out test errors were was higher than those of the reconstruction test. The median position vertex error was 2 mm and the median modulus error was 1069 MPa, over four times larger than that of the reconstruction test.

Both the reconstruction test and leave-one-out test show that there is a weak correlation of elastic modulus between models. The median modulus error is of the order of hundreds of MPa and there is a wide inter-quartile range in the higher PCs. There could be several reasons for this:

(i) Correspondence between elements is not guaranteed. The position of an element in one mesh might be within cortical bone and in another within cancellous bone.

(ii) The size of the training set is small, with only 32 tibiae in the training set, and over 500,000 variables in the PCA matrix, limiting the accuracy of the SSIM.

(iii) Bone strength is related to many factors such as age, sex, disease, and activity levels. The natural variability of bone strength will be high, even within the small training set.

(iv) To compute the density of the CT scan, it is assumed that the region of highest intensity in the cortical bone has a density of 1.73 g/cm^3 and the lowest intensity in the marrow region has a density of 0 g/cm^3. These two regions of bone are manually identified and the sampled intensity is not necessarily correct for the assumed density.

The size of the training set and registration correspondence will also affect the vertex position error. The cumulative variance (figure 6.11) also indicates that the training set is small. The

first five PCs only capture 60% of the training data variance and to represent 95% variance of the training tibiae, 24 PCs are required. More training tibiae would be required to better capture population variation.

Despite only adequate reconstruction and predictive capability of the SSIM, it is intended that the SSIM is sampled to generate a large population of tibiae. In this case, it is not necessary for each tibia to be accurate or represent an real patient. The requirement is that the generated population of tibiae are representative of the training population. Although only the first three modes of change are visualised, realistic physical changes can be seen (figure 6.15), and by sampling the SSIM, a large variable population of tibiae can be generated (figure 6.16).

6.3 Statistical model of tibiofemoral joint gait cycle loads

Pre-clinical testing of TKRs currently relies on limited kinematic and kinetic data to establish boundaries of design and durability (see section 3.2). The problem is that many computational studies only apply simplified loads at an instance in an activity cycle (table 3.1). Those studies which simulate a complete activity cycle tend to apply loading based on a published testing standard (ISO 14243-1, 2009). The few studies which use models of multiple patients only scaled the loading by body weight between patients. By doing this, the ratios between the load components remain fixed; the variation in the ratio of force components (e.g. A-P to AX force) is not captured.

The knee is exposed to 6 degree-of-freedom time varying loads and large inter-patient variability has been observed from *in vivo* measurements (see section 2.1.8). Therefore, a population-based study of the tibial tray not only needs to incorporate variation of the tibia, but also of the kinetics to fully represent inter-patient variability. Using a SM, a large population of kinetic data could be generated without the time and expense of collecting motion capture data of hundreds of patients[2].

6.3.1 Training data collection and preparation

The internal tibiofemoral joint loads (anterior-posterior (F_{AP}), medial-lateral (F_{ML}), and axial (F_{AX}) forces; flexion-extension (M_{FE}), varus-valgus (M_{VV}), and internal-external (M_{IE}) moments) of a single gait cycle (heel strike to heel strike of the same leg) were taken from musculoskeletal models of 31 pre-operative TKR patients (table 6.2). These data were obtained from a separate project, Worsley (2011). An outline of the method used to create the musculoskeletal model follows.

Step 1: Motion capture. Motion capture data of an activity were taken using a 12 camera T-series Vicon motion analysis system (Vicon, Oxford, UK) using retroreflective markets.

[2]The method described in this section has been published as F. Galloway, P. Worsley, et al. (2012). "Development of a statistical model of knee kinetics for applications in pre-clinical testing". In: *Journal of Biomechanics* 45(1), pp. 191–195.

Table 6.2: Summary of participants used in study.

	Age (years)	**Weight** (kg)	**BMI** (kg/m^2)
Mean	64.3	84.9	30.8
Standard deviation	9.5	17.7	5.9
Max	81.0	127.0	42.2
Min	39.0	54.0	19.1

These were placed on key anatomical landmarks using a modified Helen Hayes marker set to be able to identify segment and joint centre locations during dynamic movement. Two Kistler force plates (Kistler Instrument AG, Winterthur, Switzerland) were used to measure the ground reaction forces during the activity. Anthropometric measurements (e.g height, leg length) were also taken.

Step 2: Model setup. The musculoskeletal model was then created using inverse dynamics musculoskeletal modelling software, AnyBody (AnyBody, Aalbord, Denmark). Using a static trial—where the patient was standing in a neutral position with arms folded at chest height—motion capture data, a baseline model of the patient was created. The rigid body model was then linearly scaled using the anthropometric measures, motion capture data, and digital camera feedback. After scaling, the model was then correctly positioned by adjusting the global position of the model, and position of the joints (by changing joint flexion, abduction, and rotation angles). The marker positions were then estimated by adjusting the position of local nodes on each segment to the position of the motion capture markers. The scaling parameters and marker positions were then used for all subsequent dynamic models of the patient.

Step 3: Kinematic analysis. The model was driven by the marker positions from the motion capture data to compute the kinematics. To minimise the error of the marker locations, a Global Optimisation Method (Andersen et al., 2009) was used. The kinematics include the position, velocity, and acceleration of each segment during the activity cycle.

Step 4: Kinetic analysis. From the kinetics and ground reaction forces, the net joint forces can be computed. The net joint forces consist of two components, the internal joint forces (joint loads) and the muscle forces. To determine the muscle forces, a min-max recruitment solver (Rasmussen et al., 2001) was used, optimising the recruitment of the muscles. The internal joint forces can then be computed.

To compute the internal tibiofemoral joint loads, patients performed three trials of walking and a gait cycle from each trial was identified using the associated force and kinematic data. Joint loads were computed for each trial, time normalised from 0–100% of gait sampled at 1% intervals and normalised by BW. The load data were collated and averaged for each patient (figure 6.17). There is no need for registration of the data, because all the load data are time normalised and each point of the load waveform naturally corresponds between patients.

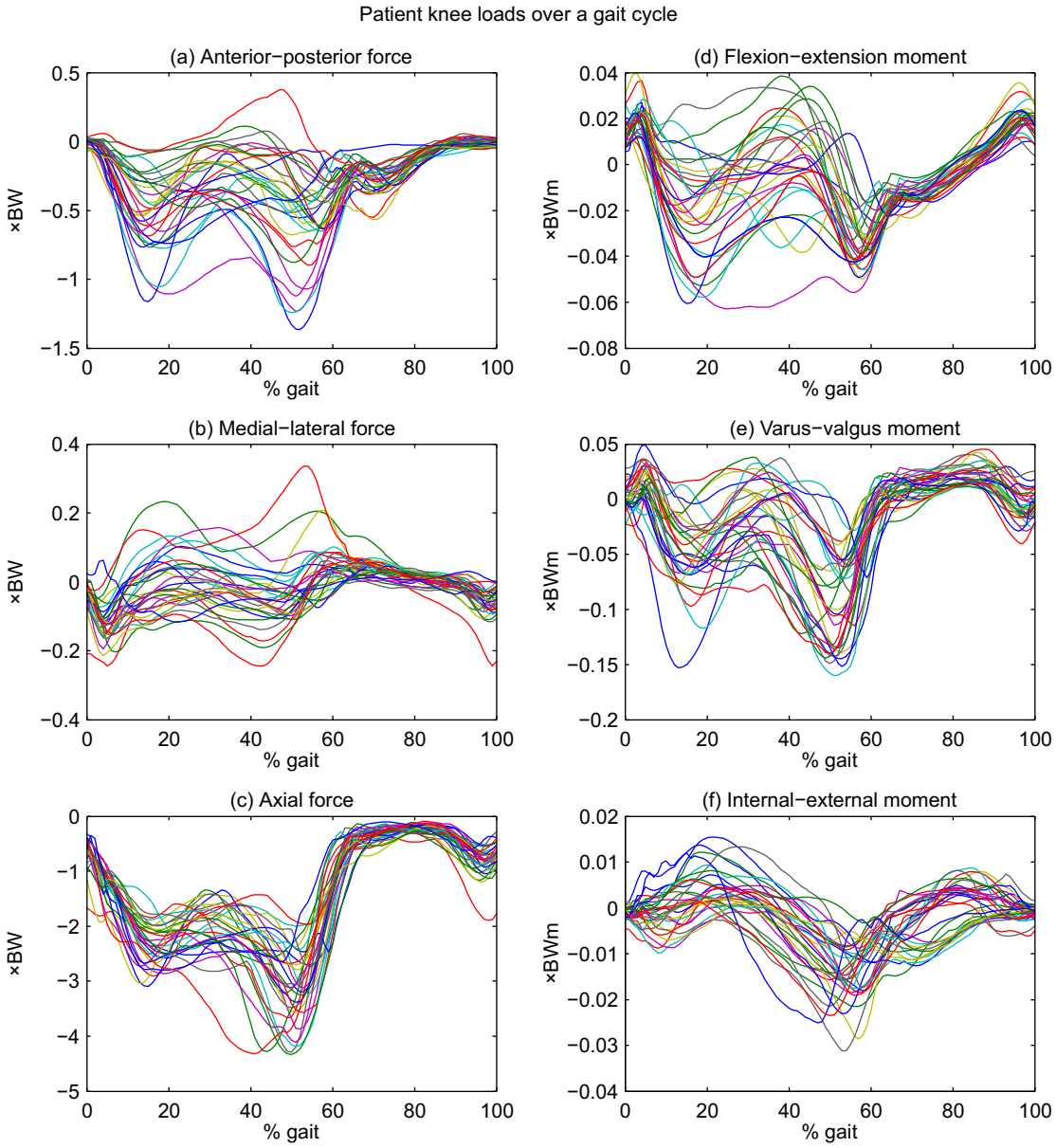

Figure 6.17: Gait cycle knee loads of all patients time normalised from 0–100% sampled at 1% intervals and normalised by body weight. The shown data are of forces in the right knee, defined in a coordinate system such that the +x is in the lateral direction, +y is in the anterior direction, and +z is in the superior direction. $+F_{\mathrm{AP}}$, $+F_{\mathrm{ML}}$, and $+F_{\mathrm{AX}}$ act in the +x, +y, and +z directions. The $+M_{\mathrm{FE}}$, $+M_{\mathrm{VV}}$, and $+M_{\mathrm{IE}}$ all act clockwise around the +x, +y, and +z axes respectively.

6.3.2 Principal component analysis

PCA has been applied to gait waveform data to differentiate between groups of patients of different pathologies (Deluzio et al., 2007; Deluzio et al., 1997) and ages (Reid et al., 2010) using the PCs. These studies apply PCA to each individual load components. In the SM of knee kinetics all the load component waveforms are included. As before, following the method described in section 4.4, PCA is used to compute a set of coefficients and weights which can be sampled to generate new instances of gait cycle loads.

Each set of patient data were arranged in a vector, $\mathbf{x}_i = [\mathbf{F}_{\mathrm{AP}}, \mathbf{F}_{\mathrm{ML}}, \mathbf{F}_{\mathrm{AX}}, \mathbf{M}_{\mathrm{FE}}, \mathbf{M}_{\mathrm{VV}}, \mathbf{M}_{\mathrm{IE}}]^{\mathrm{T}}$, and combined in a training matrix $\mathbf{X} = [\mathbf{x}_1, \mathbf{x}_2, \cdots, \mathbf{x}_i]$. As the data were of mixed units (forces are $\times$BW and moments are $\times$BWm), $\mathbf{X}$ was normalised by row-wise standard deviation (equation 4.4) and then mean centred (equation 4.5) giving $\hat{\mathbf{X}}$. PCA was carried out using SVD such that $\hat{\mathbf{X}} = \mathbf{U}\mathbf{\Sigma}\mathbf{V}^{\mathrm{T}}$. The columns of $\mathbf{U}$ correspond to the eigenvectors (representing the PCs), the diagonal of $\mathbf{\Sigma}$ are the eigenvalues (the square of which represent the variance of each PC), and the PC weights are computed by $\mathbf{b} = \mathbf{\Sigma}\mathbf{V}^{\mathrm{T}}$.

6.3.3 Assessment of statistical model

Variance of principal components

To represent 95% variance of the SM, 17 out of 31 PCs are required (figure 6.18). As per the tibia SM, it is not only important to consider the variance of the PCs, the accuracy and predictive capability of the SM must also be examined.

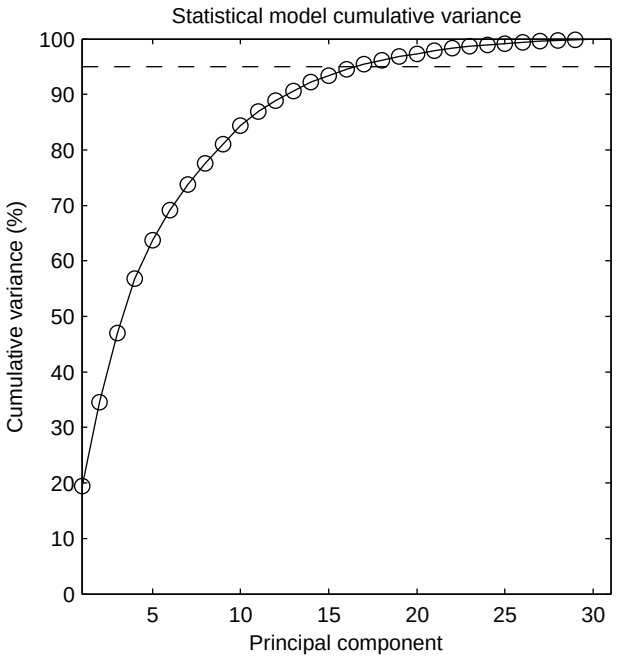

Figure 6.18: Cumulative variance of the PCs for the gait cycle SM. The dashed line marks 95% variance.

Reconstruction test

The accuracy of the model was assessed using a reconstruction test. The subject gait cycles were reconstructed (equation 4.9) using an increasing number of PCs and the root-mean-squared (RMS) error between the 'original' and 'reconstructed' data was computed for each load component.

From the reconstruction test, both the median and inter-quartile range of the RMS error between the 'original' and 'reconstructed' data decreased as the number of included PCs increased for each load component (figure 6.19). Assuming a mass of 84.9 kg (mean of the patients mass table 6.2), at 17 PCs, which represents 95% variance of the model, the median RMS error of the A-P force is 28 N, M-L force is 6.8 N, AX force is 73 N, F-E moment is 2.5 Nm, V-V moment is 4.2 Nm, and I-E rotation moment is 0.6 Nm.

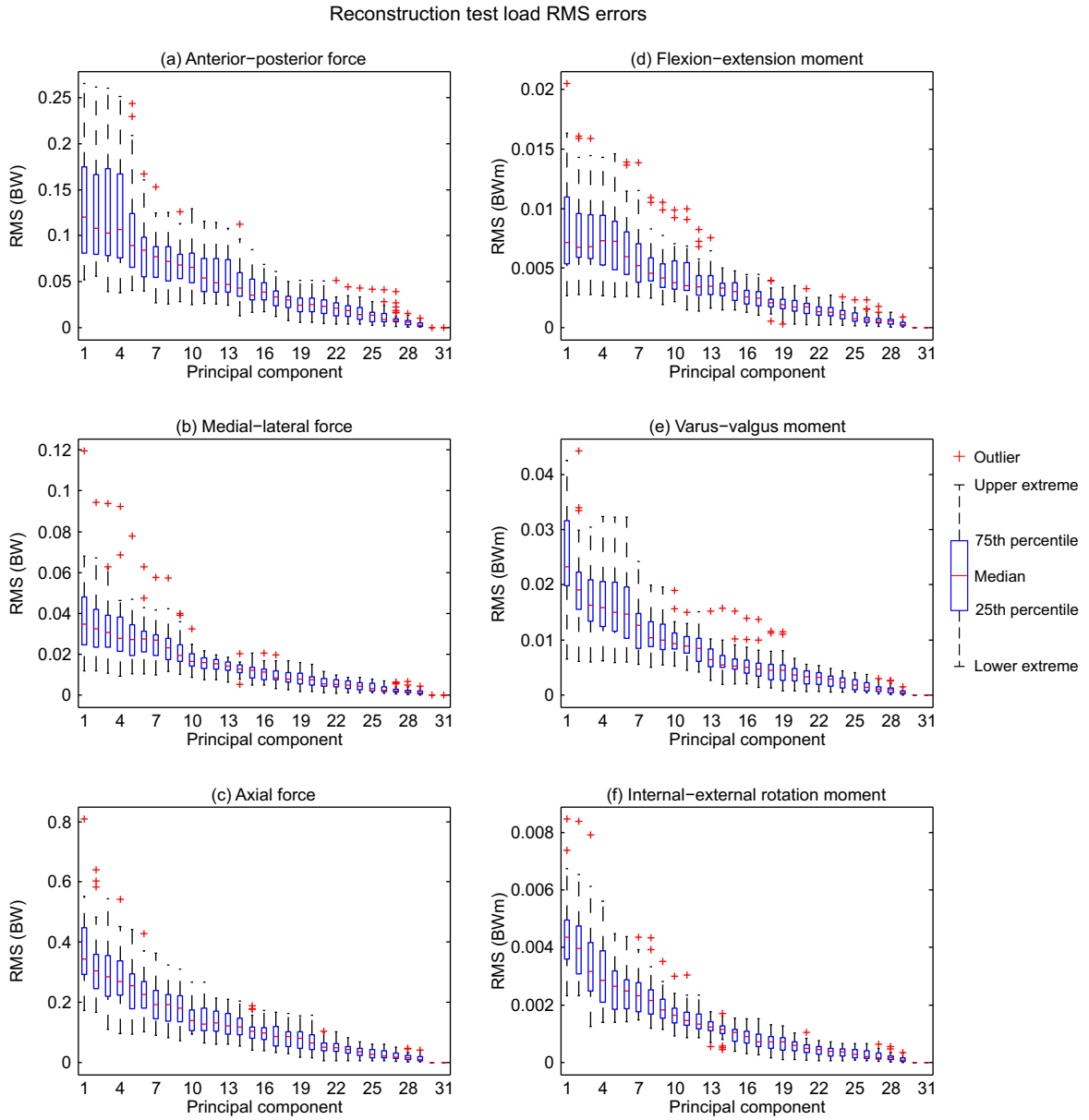

Figure 6.19: Boxplots of the knee forces and moments RMS error from the reconstruction test. The error is between the 'original' data and 'reconstructed' data.

Leave-one-out test

A leave-one-out test was performed to assess the predictive capability of the SM. Each set of patient data $\mathbf{x}_i$ was left out in turn forming a new normalised training set $\hat{\mathbf{Y}}$. PCA was applied to this training set and the PC weights $\boldsymbol{\alpha}_i$ for $\mathbf{x}_i$ (equation 6.21). The 'left-out' data was estimated using an increasing number of PCs (equation 6.22) and the RMS error between the 'left-out' and 'estimated' data was computed for each load component.

From the leave-one-out test, both the median and inter-quartile range of the RMS error between the 'left-out' and 'estimated' data decreased as the number of included PCs increased for each load component (figure 6.20). Again, assuming a mass of 84.9 kg and including 17 PCs, the median RMS error of the A-P force is 73 N, M-L force is 20.4 N, AX force is 173.2 N, F-E moment is 5.1 Nm, V-V moment is 10.2 Nm, and I-E rotation moment is 1.7 Nm. However, the inter-quartile range of the forces and moments remains relatively large as the number of included PCs increases, particularly for the A-P force and F-E moment (figure 6.20).

Sampling

Like the tibia SM, it is intended that the gait cycle SM will be used to generate a population of gait cycle loads by sampling the model. The assumption made for the tibia SM was that weights of the kth PC had a Gaussian distribution with a mean μ_k and standard deviation σ_k. This assumption should also hold for the gait cycle SM as the training data is normalised and mean centred. The distributions of the first 17 PC weights are shown in figure 6.21, and the majority are approximately Gaussian.

To show that the generated data is representative of the training data, 100 new gait cycles were generated by pseudo-randomly sampling the distribution of the first 17 PCs weights, truncated at $\pm 3\sigma_k$. As expected, the 'sampled' gait cycle loads are representative of the 'original' gait cycle loads (figure 6.22).

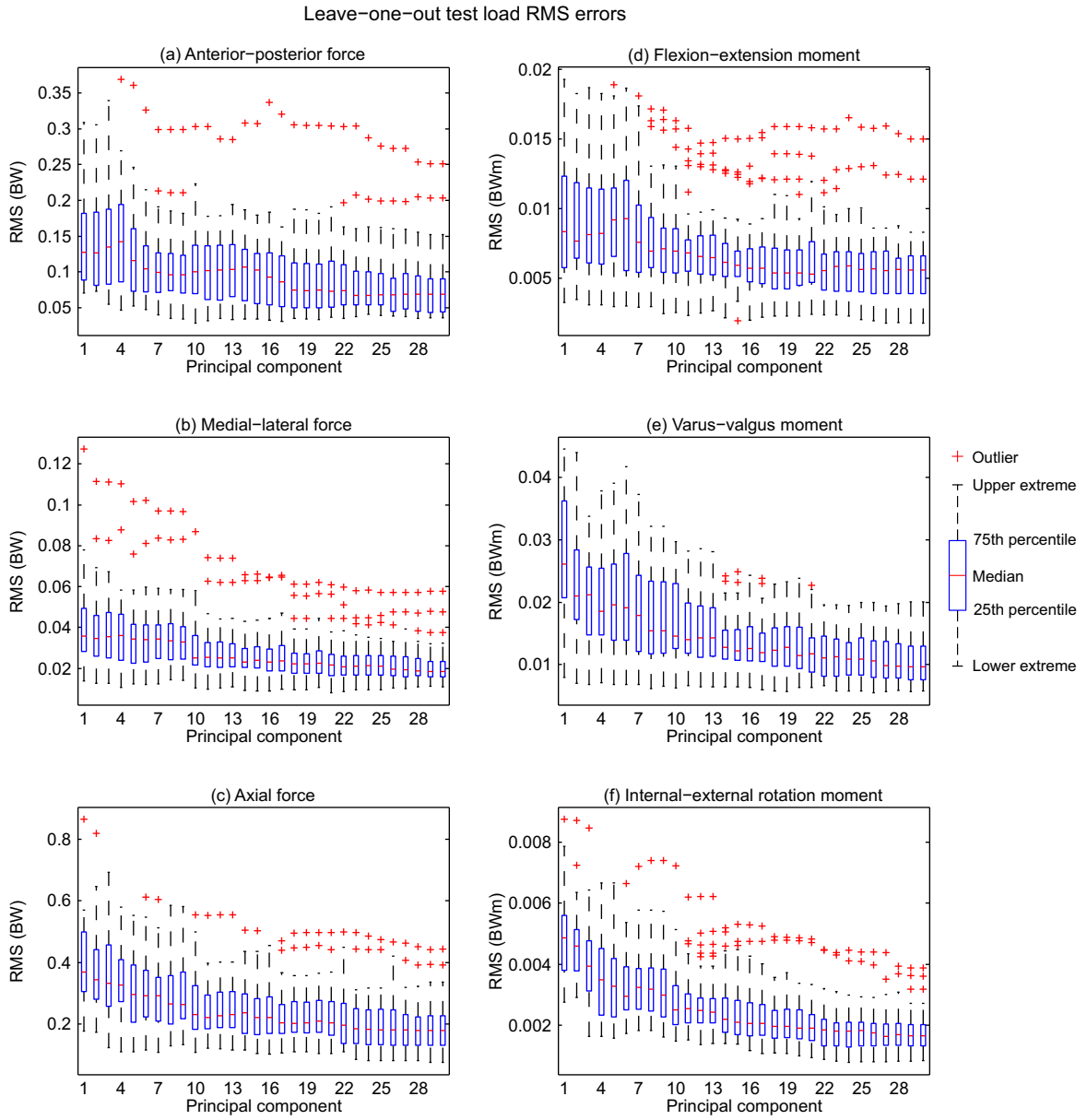

Figure 6.20: Boxplots of the knee forces and moments RMS error from the leave-one-out test. The error is between the 'left-out' data and 'estimated' data.

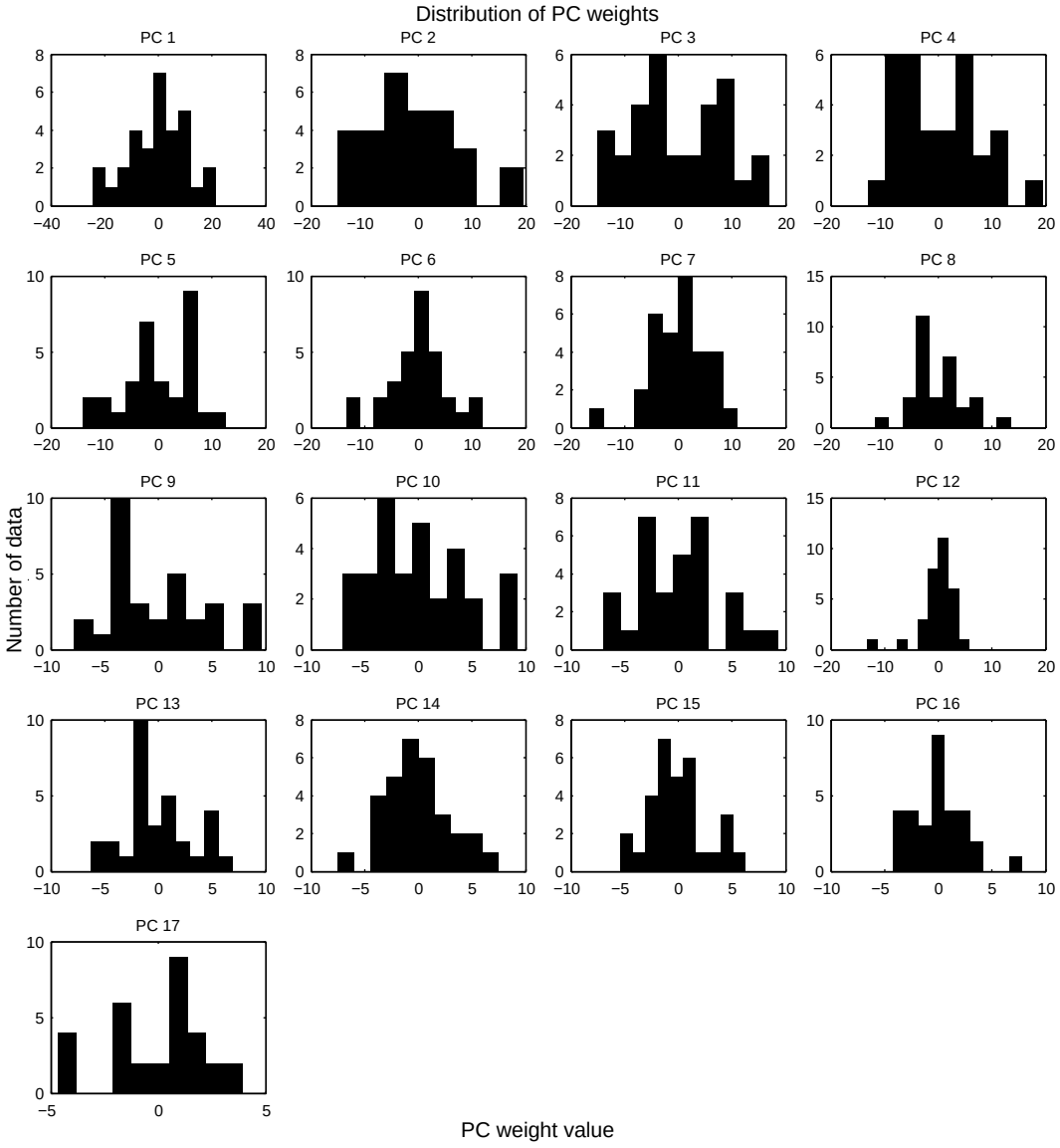

Figure 6.21: The distribution of the PC weights for the gait cycle SM. Only the first 17 PCs are plotted because they represent 95% variance. It can be seen that the weights generally have a Gaussian distribution.

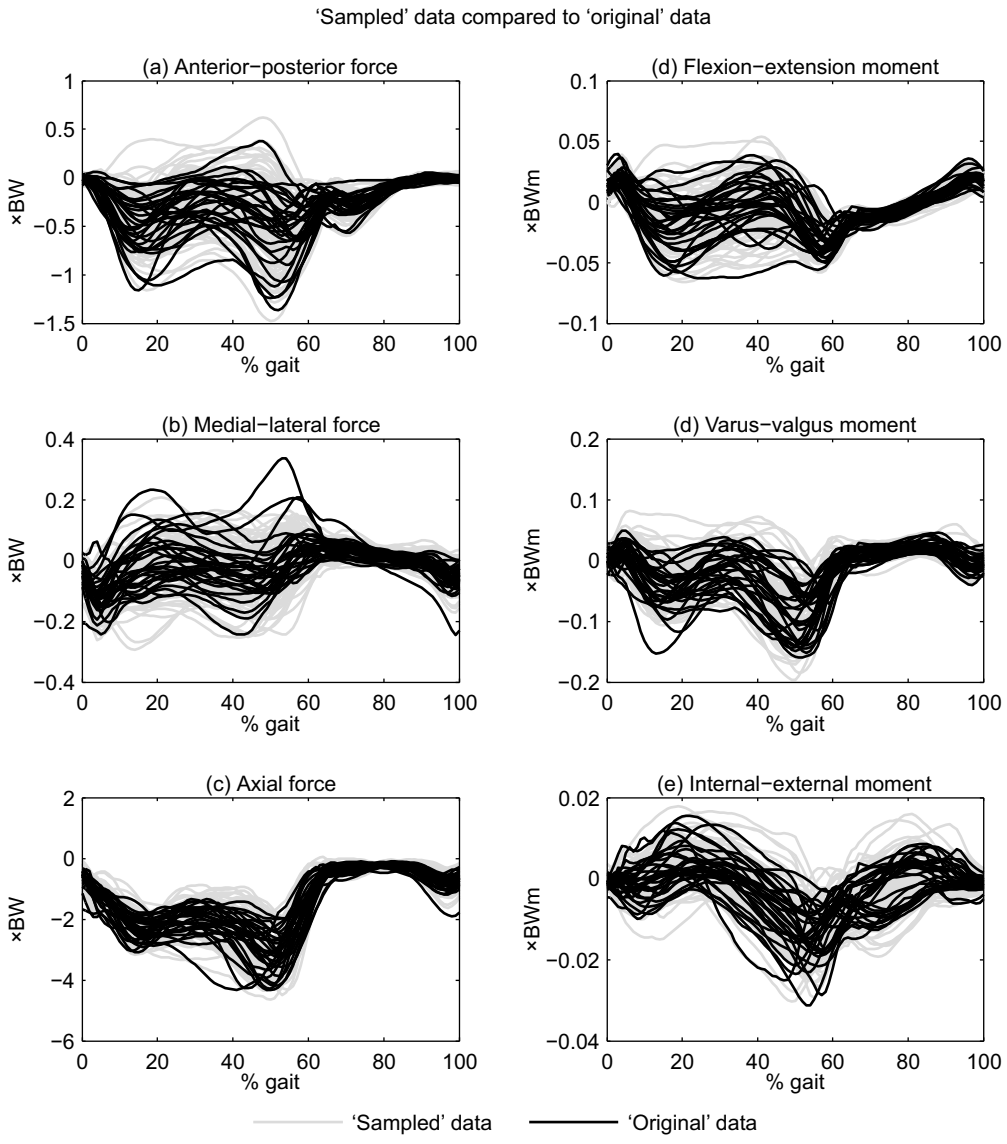

Figure 6.22: 'Sampled' gait cycle loads (light) compared to 'original' gait cycle loads (dark). As expected, the 'sampled' data are representative of the training data.

6.3.4 Discussion

The SM of the gait cycle combines all three forces and three moments of the tibiofemoral joint and applies PCA to compute a set of weights which can be sampled to generate a population of gait cycles, representative of the training data. The generated population could be used as load input in a population-based study of a TKR. This is unlike previous studies (Deluzio et al., 2007; Reid et al., 2010) where PCA was applied to each separate component and the PC scores were used to differentiate between groups.

Although the MS modelling was not performed as part of this thesis, it is important to note some of the sources of error and uncertainty of the method (Worsley et al., 2011):

- Soft tissue artefacts, caused by the movement of the skin markers relative to the bone, result in marker positional errors (Leardini et al., 2005). Optimisation techniques can be employed to reduce the uncertainty of marker positions as a result of soft tissue artefacts, but the kinematics can only be accurately predicted for gross movement patterns (Leardini et al., 2005).
- Inaccurate identification of anatomic landmarks and marker positioning can affect the predicted kinematics (Della Croce et al., 2005).
- Scaling of the MS model is generic and affects the accuracy of the estimated segment parameters (e.g. mass, centre of mass, moment of inertia), and joint parameters (e.g. joint centre). Studies have shown that the placement of the hip centre is crucial to reduce the error in hip and knee kinematics (Kadaba et al., 1990). The scaling relies on accurate identification of anatomic landmarks.
- Simplification of segments in the MS model, e.g. the foot is only modelled as a single segment.
- To reduce the complexity of the MS model and complete the inverse dynamics efficiently, constraints are applied to the joints to reduce the number of DOFs. The knee is modelled as a hinge joint, allowing only 1 DOF, but in reality the knee has 6 DOFs (section 2.1.5). This constraint is perhaps acceptable, as the errors from marker placement and soft tissue artefacts are much larger than the magnitude of secondary knee motions seen during an activity.
- The muscle forces are computed by globally optimising the muscle recruitment such that the loads on muscles are minimised. Further constraints are applied to the muscles, so that they can only work by 'pulling', and that they do not work beyond the limit of their power. The idea of doing this is to replicate the behaviour of the central nervous system.

These limitations of the MS modelling, means that the predicted kinematics can be overestimated in comparison to telemeterised implant data (section 2.1.8). A SM could have been created using the 5 sets of knee load data from Orthoload. However, significant inter-patient variability of knee loads was observed (Kutzner et al., 2010), and it was considered that the 5

sets of data were not enough to create a SM. Instead, the next best available set of data was used, taken from 31 MS models of pre-operative TKR patients.

For the gait SM, 17 out of 31 PCs were required to represent 95% variance, over half the total number, and the higher PC have only a small variance, likely to introduce noise when sampling the SM. However, the magnitude of the RMS error of each load component was considered acceptable at 17 PCs for both the reconstruction and leave-one-out tests.

The leave-one-out test indicates that the SM is less accurate at estimating data, particularly for the A-P force and F-E moment (figure 6.20). The median RMS error of the A-P force only decreases from 0.13 BW at PC 1 to 0.09 BW at PC 17 and the inter-quartile range also remains relatively large, 0.09–0.18 BW at PC 1 and 0.05–0.12 BW at PC 17 (figure 6.20).

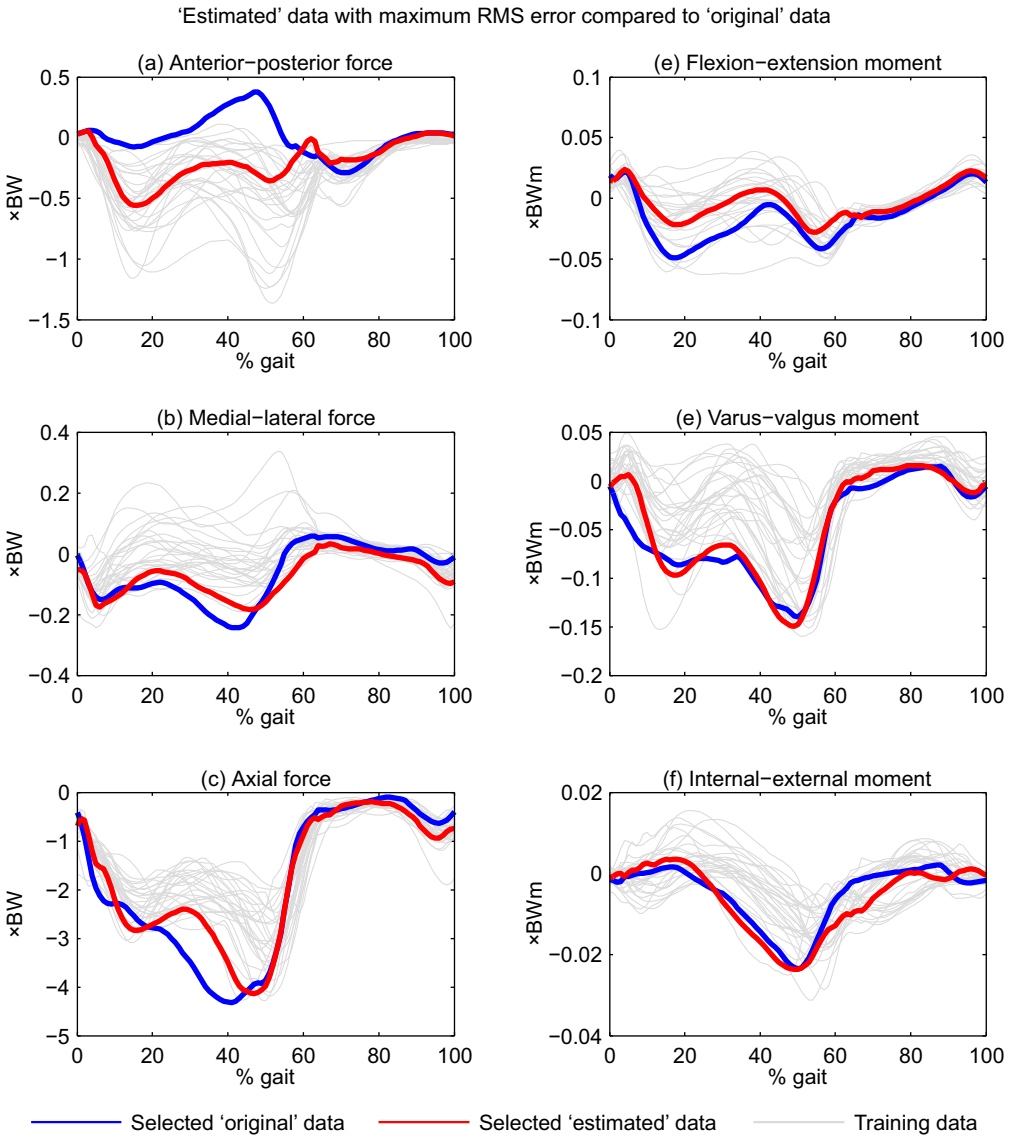

Figure 6.23: Comparison of the 'estimated' gait cycle with the maximum RMS error at 17 PCs compared to the 'original' gait cycle.

To further investigate, the 'estimated' data using 17 PCs with the maximum RMS error was examined. This shows that the 'left-out' data is perhaps an outlier of the training set; the A-P force does not fit the trend of the training data, the peaks of the FE moment are larger than average, and the peak of the AX force occurs 10% earlier in the gait cycle compared to the training data (figure 6.23). The error in the 'estimated' data is partly caused by the extreme variation in the training data and the predictive accuracy is limited by the small size of the training set.

However, the intended use of the gait cycle SM is to generate a new population of gait cycle loads. The accuracy and predictive ability is not of high importance, provided that the generated population is representative of the training data. The example sampled gait cycles (figure 6.22) show that the SM can be used to generate a new population which adequately captures the variation of the training data. There are cases where the load components of the 'sampled' gait cycles have a peak magnitude greater than the 'original' gait cycles. This is likely because a large interval is used in sampling, increasing the chance of generating an 'outlier' case. These cases are of interest, particularly in testing of a TKR, where the more extreme loads might increase the risk of failure.

6.4 Creating a population of finite element models

A large scale, population-based study requires automatic creation of the the FE models. In the context of a study assessing a tibial tray, the process to generate the models is as follows: (i) sample both the SMs (see sections 6.2 and 6.3) to generate a population of tibiae and a population of gait cycle loads; (ii) position and implant the tibial tray in the tibia; (iii) combine the implanted tibia with the gait cycle loading to create the FE model for analysis. This section describes the automated process of creating an FE model which is then used to create the population of models in the following case studies.

6.4.1 Creating the statistical models and generating the data

The tibia SM was created as described in section 6.2 using the 32 left tibiae as training data. The gait cycle SM used training data of 20 healthy elderly subjects[3] collected and processed as described in Worsley et al. (2011). It was observed that in comparison with telemetric implant data (Kutzner et al., 2010), the A-P force, F-E and V-V moments, appeared to be overestimated. Therefore, these load components were scaled by a factor of 0.5 to bring them into line with the telemetric implant data (figure 6.24). The gait cycle SM was then created as described in section 6.3.

[3]The initial paper, Galloway, Worsley, et al. (2012), submitted to Journal of Biomechanics used this set of data. In the review process the size of data set was queried, and as a result the data set used in the paper was changed to one of 31 pre-operative TKR patients, collected and processed using the same method (Worsley, 2011). However, the work for this thesis had progressed using a gait cycle SM based on 20 healthy elderly subjects and it was decided that this should not be changed.

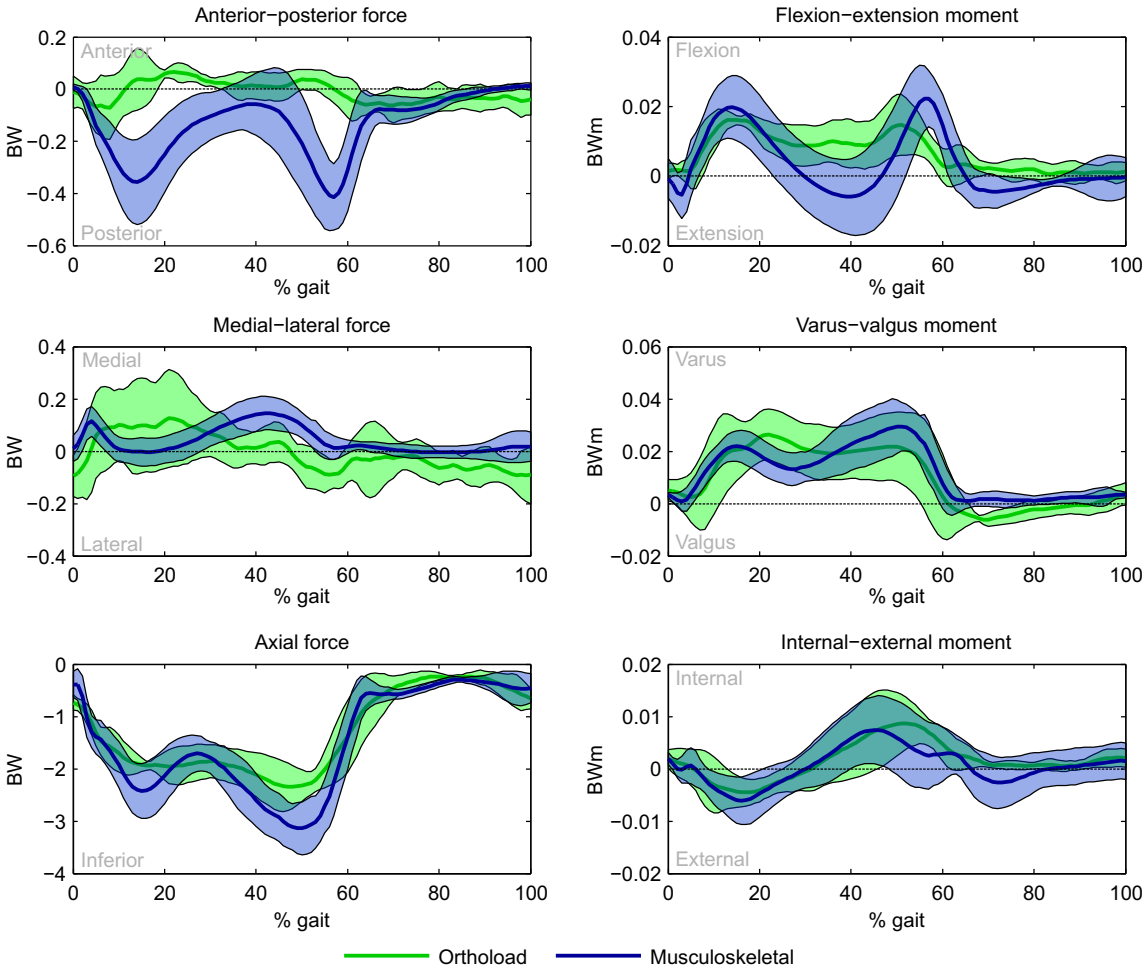

Figure 6.24: Comparison of the internal joint reaction forces from Orthoload (light) and musculoskeletal models (dark). The A-P force, F-E moment, and V-V moment of the musculoskeletal data have been scaled by 0.5. The heavy line represents the mean of each component and the shaded area is ±1 standard deviation. The forces and moments act in the directions defined in figure 6.28.

To obtain a large number of possible models, the tibia SM and gait cycle SM were sampled separately to generate an initial set of 500 tibiae and gait cycles (see sections 6.2.10 and 6.3.3). Each generated tibia was associated with a gait cycle. A threshold of 95% variance was used to select the number of PCs used to sample the SMs. The first 24 of 32 PCs were used for the tibia SM, and the first 13 of 20 PCs were used for the gait cycle SM. For both the SMs, the PC weights were assumed to have a Gaussian distribution, truncated to $\pm 3\sigma_t$. A limitation using two separate SMs is that there is a dissociation between the generated tibia and gait cycle.

The limited predictive accuracy of the tibia SSIM meant it was possible that elements of generated tibiae could have an elastic modulus near or less than 0 MPa. Elements with low modulus values could also potentially cause problems during FE analysis. Therefore, if an element had a modulus less than 10 MPa, it was assigned a value of 10 MPa. This modulus threshold was for reasons given in section 6.2.5. No adjustments were made to the generated gait cycles.

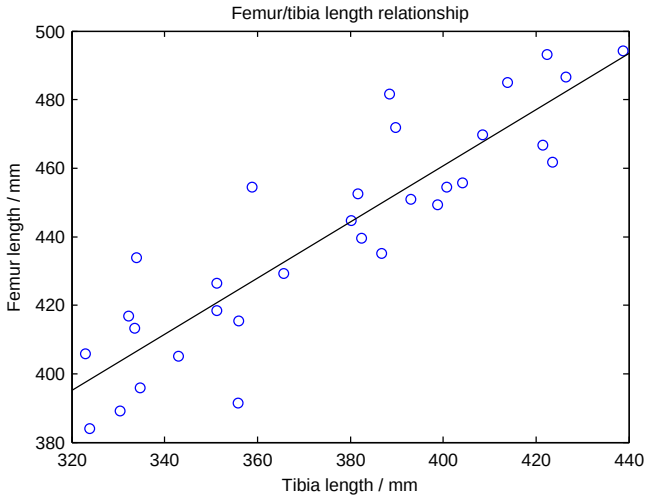

Figure 6.25: Correlation between the femur and tibia lengths with the linear regression shown.

6.4.2 Predicting model weight

The load components of the gait cycle were normalised in terms of body weight. To convert back to a force or moment, a weight of the model is required. Unfortunately, patient information corresponding to the training tibiae was not available and the weight of each sampled model had to be estimated.

Stature estimation from long bones is often used in forensic science when only partial skeletal data is available. To do this, generic limb ratios can be used (Winter, 1990). Studies have also found relationships between long bone length and stature for specific populations, e.g. Turkish (Duyar et al., 2003) or Japanese (Hasegawa et al., 2009). The limitation of these studies is that the relationships are for specific populations; the training tibiae for the SM are of an unknown demographic. Despite a published relationship between tibia length and stature (Duyar et al., 2003), this was not used as it applied to young Turkish males, who may have a very different stature compared to the average TKR patient. One study found a generic, combined race and gender, ratio between femur length and stature (Feldesman et al., 1996), and was used by Bryan et al. (2009) to estimate the height of a population of femurs.

In the current study femur length is unknown for the generated models. As the training tibiae were taken from CT scans of the full lower limb, a linear regression between the tibia and femur length was found (figure 6.25). Combined with the generic femur-stature ratio (Feldesman et al., 1996), the relationship between tibia length t and height h is

$$h = \frac{132.7716 + 0.82t}{0.2675} = 496.3426 + 3.0654t. \tag{6.23}$$

A body mass index (BMI) for each model was randomly sampled from a distribution based on the National Healthy and Nutritional Examination Survey (NHANES, 1999), carried out by the US Center for Disease Control and Prevention. The mass of each model was then calculated by

$$m = bh^2 \tag{6.24}$$

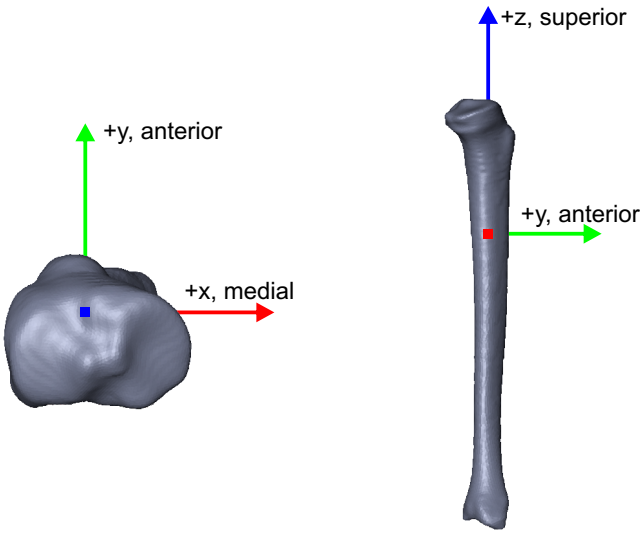

Figure 6.26: Tibia aligned to the coordinate system axes in a medial view (left) and inferior view (right).

where m is mass in kg, h is height in m, and b is BMI in kg/m^2. The sampling of the BMI distribution means that the estimated weight of the model is effectively random, and there is no link between tibia, joint loads, and patient weight.

6.4.3 Positioning and implantation of the tibial tray

To be able to position the tibial tray correctly, each tibia was aligned in a coordinate system such that +x is medial, +y is anterior, and +z is superior (figure 6.26) using the transformation described by Fitzpatrick et al. (2007). The tibial tray was then positioned as follows:

(i) From landmark sets defining the medial and lateral condyles, the lowest condylar point is identified.

(ii) The cutting plane is positioned the desired depth below the lowest condylar point (normally around 2 mm), parallel to the transverse plane. A resected surface is created.

(iii) The M-L width of the resected surface is measured, taken as the distance between the most medial and most lateral points of the resected surface.

(iv) The size of tibial tray is chosen, such that it is the largest size with an M-L width less than the resected surface M-L width.

(v) The tibial tray is positioned such that the bottom surface is on the same plane as the resected surface. In the M-L direction, it is centred on the central point of the M-L width vector. In the A-P direction is centred on the central point of the resected surface.

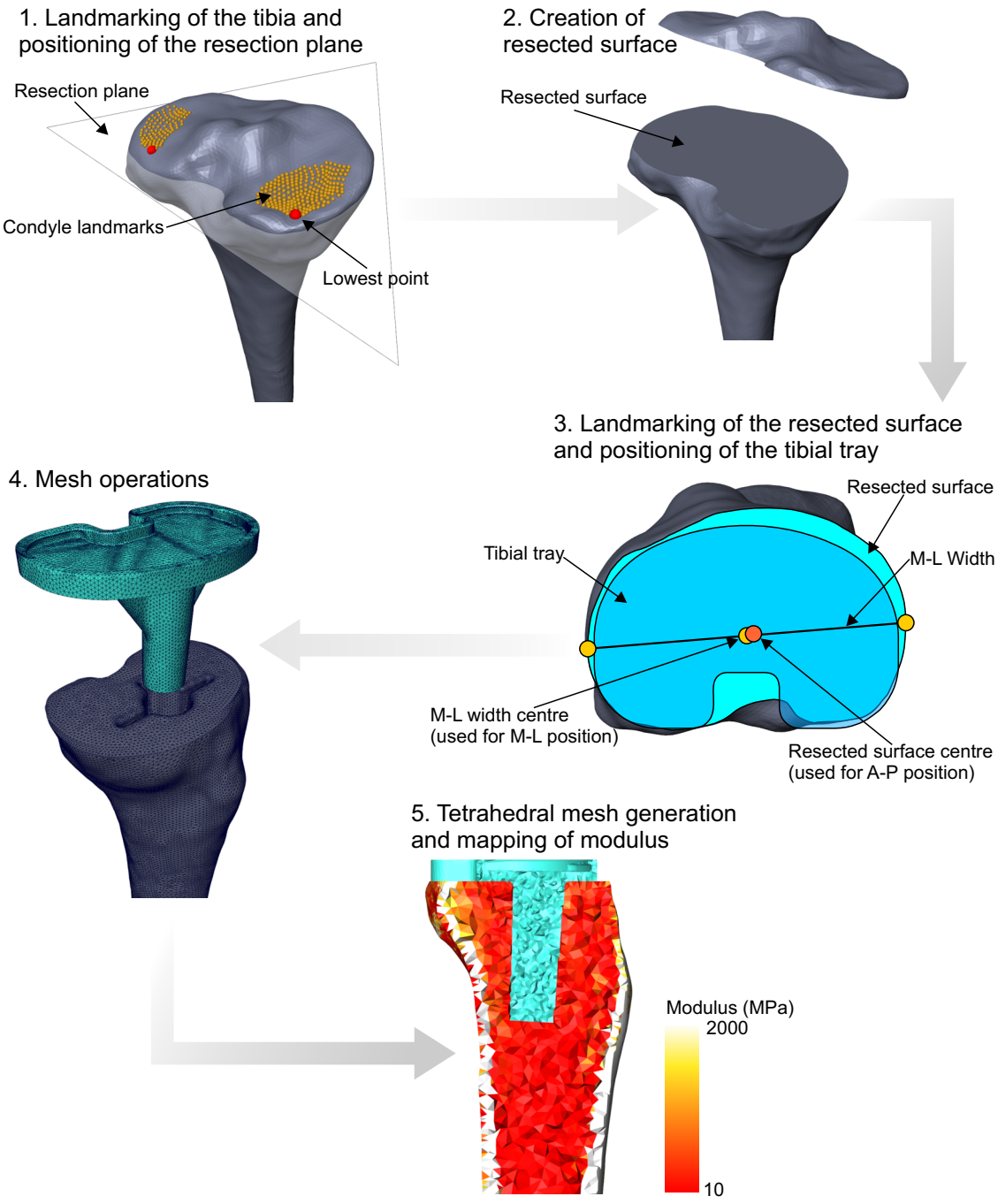

Figure 6.27: The steps to position and implant the tibial tray.

To create a new mesh of the tibia implanted with the tibial tray, mesh operations were required. A custom extension was developed for ZIBAmira in collaboration with Zuse Institute Berlin (ZIB), specifically to do the necessary mesh operations to implant the tibial tray:

(i) The tibia surface was resected using mesh cutting operations.

(ii) The implant surface was merged using a mesh union operation.

(iii) The surface was remeshed to ensure good element quality (Kahnt et al., 2011; Zilske et al., 2008).

(iv) A tetrahedral mesh is generated from the implanted tibia surface using an advancing front algorithm.

(v) The elastic modulus was mapped to the new tetrahedral mesh from the original tibia tetrahedral mesh.

An overview of the position and implantation process is show in figure 6.27. All the positioning and implantation of the tibial tray was done using ZIBAmira 2010.07-rc3 (Zuse Institute Berlin (ZIB), Berlin, Germany—`http://amira.zib.de`). The scripting capability of ZIBAmira meant that all of the processes could be automated. A ZIBAmira TCL script was used to run the positioning and implantation process. If geometric errors occurred during the mesh operations or mesh generation, the tibial tray was translated alternately forwards and backwards by increasing increments of 0.1 mm. If a geometric error still occurred after 40 position adjustments (allows the tray to be moved up to 2 mm anterior or posterior from the initial position), the implantation was considered failed, and the model was excluded.

6.4.4 Pre-processing the finite element models

The mesh of the combined tibia and tibial tray was imported into Abaqus 6.9-2 (Simulia, RI, USA). An Abaqus/CAE Python script was used to pre-process the model, applying the appropriate material properties, loads, and boundary conditions.

To model the heterogeneity of bone, the mesh was grouped into many homogeneous sections, each having a different material property. The elements were grouped by modulus in 10 MPa bands to define the material sections. This reduced the number of material sections in the model to approximately 1,500. The tibial tray was modelled as a single homogenous section and appropriate material properties were assigned (see the case studies).

The contact surfaces of the bone and tray were detected, defining the bone-tray interface. In all the case studies, it was assumed that the tray was debonded from the tibia, simulating initial post-operative conditions, modelled as hard contact with Coulomb friction. It was also assumed that the tibial tray was porous-coated and a friction coefficient of 0.6 was used (Chong et al., 2010).

The gait cycle loads from the SM were time normalised from 0% to 100% in 1% intervals. Every other time point in the gait cycle was taken as a load step (i.e. 2% intervals resulting in 51 load steps) to reduce computational time of the analysis. All loads were assumed to act at

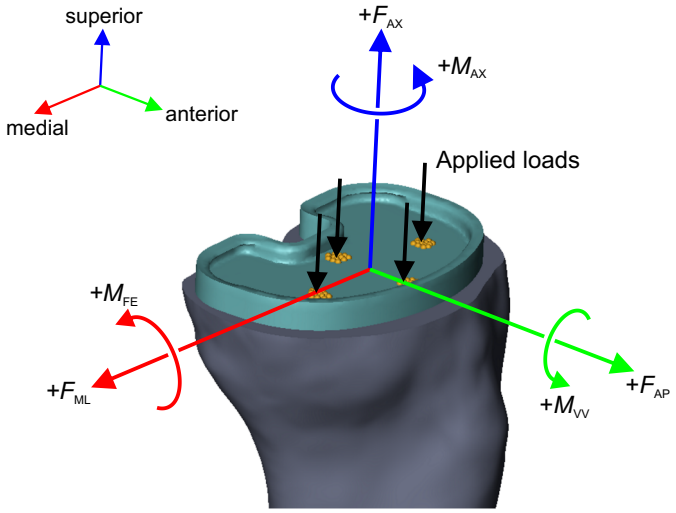

Figure 6.28: The directions in which the forces and moments act on the tibia.

Table 6.3: Loads split over the four groups of nodes on the tibial tray. The fraction and direction of a load is given for the positive direction. r_a, r_p, r_m, and r_l are the moment arms from the centre to the anterior, posterior, medial, and lateral node groups respectively.

	Node set			
Load	**Medial**	**Lateral**	**Anterior**	**Posterior**
Anterior-posterior force (F_{AP})			$+0.5y$	$+0.5y$
Medial-lateral force (F_{ML})	$+0.5x$	$+0.5x$		
Axial force (F_{AX})	$+0.5z$	$+0.5z$		
Flexion-extension moment (M_{FE})			$+0.5r_a z$	$-0.5r_p z$
Varus-valgus (M_{VV})	$-0.5r_m z$	$+0.5r_l z$		
Internal-external moment (M_{IE})	$+0.25r_m y$	$-0.25r_l y$	$-0.25r_a x$	$+0.25r_p x$

the centre of the knee relative to the tibia. The three forces, $+F_{AP}$, $+F_{ML}$, and $+F_{AX}$, act in the medial (+x), anterior (+y), and superior (+z) directions (figure 6.28). The three moments, $+M_{FE}$, $+M_{VV}$, and $+M_{IE}$, act clockwise in the medial (y-z), frontal (x-z), and horizontal (x-y) planes (figure 6.28).

The position of the four load points were initially manually landmarked medial, lateral, anterior, and posterior relative to the centre of the tibial tray. The landmarks were transformed to the tray position and surface nodes within a 2.5 mm radius are found to create four sets of nodes (figure 6.28). The forces were equally split between the appropriate node sets (table 6.3). The moments were converted to a force, taking the moment arm as the distance from the centre of the tibial tray to the centre of a set of nodes, and then split equally between the appropriate node sets (table 6.3).

6.4.5 Running the finite element analysis

An Abaqus job was created for successfully implanted tibiae. The jobs were submitted on a Linux cluster, using four processors and 4GB of RAM per node. This allowed multiple jobs to run simultaneously, with each one taking 5–7 hours to solve.

6.4.6 Post-processing the finite element models

Post-processing of the FE results was automated using Abaqus Python. Results were extracted for the region of interest, the bone-implant interface[4]. For all case studies, two metrics were computed, the strain and micromotion. The equivalent strain (ϵ, referred to as strain) was computed from the principal strains (ϵ_1, ϵ_2, and ϵ_3) of the bone-implant interface tetrahedra,

$$\epsilon = \sqrt{\frac{(\epsilon_1 - \epsilon_2)^2 + (\epsilon_2 - \epsilon_3)^2 + (\epsilon_1 - \epsilon_3)^2}{2}}. \tag{6.25}$$

The strain of the bone-implant interface surface was assumed to be the strain in the tetrahedra which contained the triangle as a face. The micromotion of the bone-implant interface was computed as the magnitude of the relative displacement between every matched pair of nodes at the bone-implant interface. This is actually the resultant micromotion, and in further analysis of the results, it was not possible to identify lift-off or shear motions. For each triangle of the bone-implant interface, the micromotion was averaged from the nodes.

In the analysis of the FE results, only the resection interface was considered. This was defined as the bone of the resected surface directly in contact with the tibial tray, excluding the stem of the tray. The performance of the tibial tray was assessed using the mechanical response of the resection interface. Strain of the bone gives an indication of the risk of migration, and micromotion affects the amount of bone ingrowth, important for long-term stability (section 3.2.1). The peak strain and micromotion over the gait cycle therefore represent the worst mechanical response during the load cycle.

For each step of the gait cycle, the strain and micromotion were computed, and from these data the 'composite peak' was computed for both metrics. The composite peak strain (CPS) is the peak strain of each element which occurs during the complete gait cycle (an example of how the CPS is computed is shown in figure 6.29). The CPS can be computed for all elements in the model. The composite peak micromotion (CPM) is the peak micromotion of each element which occurs during the complete gait cycle. This can only be computed for the nodes and/or elements of the contact interface. From computing the CPS and CPM, it is also known when in the gait cycle the peak strain and peak micromotion occurred in each element. From this information, two further metrics were output, the 'CPS percent gait', defined as the time in the gait cycle (in terms of % gait) at which the peak strain occurs, and the 'CPM percent gait', defined as the time in gait cycle (in terms of % gait) at which the peak micromotion occurs.

[4]When referring to an interface, the first named part is the side of interest. The bone-implant interface refers to the elements of the bone in contact with the implant, and the implant-bone interface would be the elements of the implant in contact with the bone.

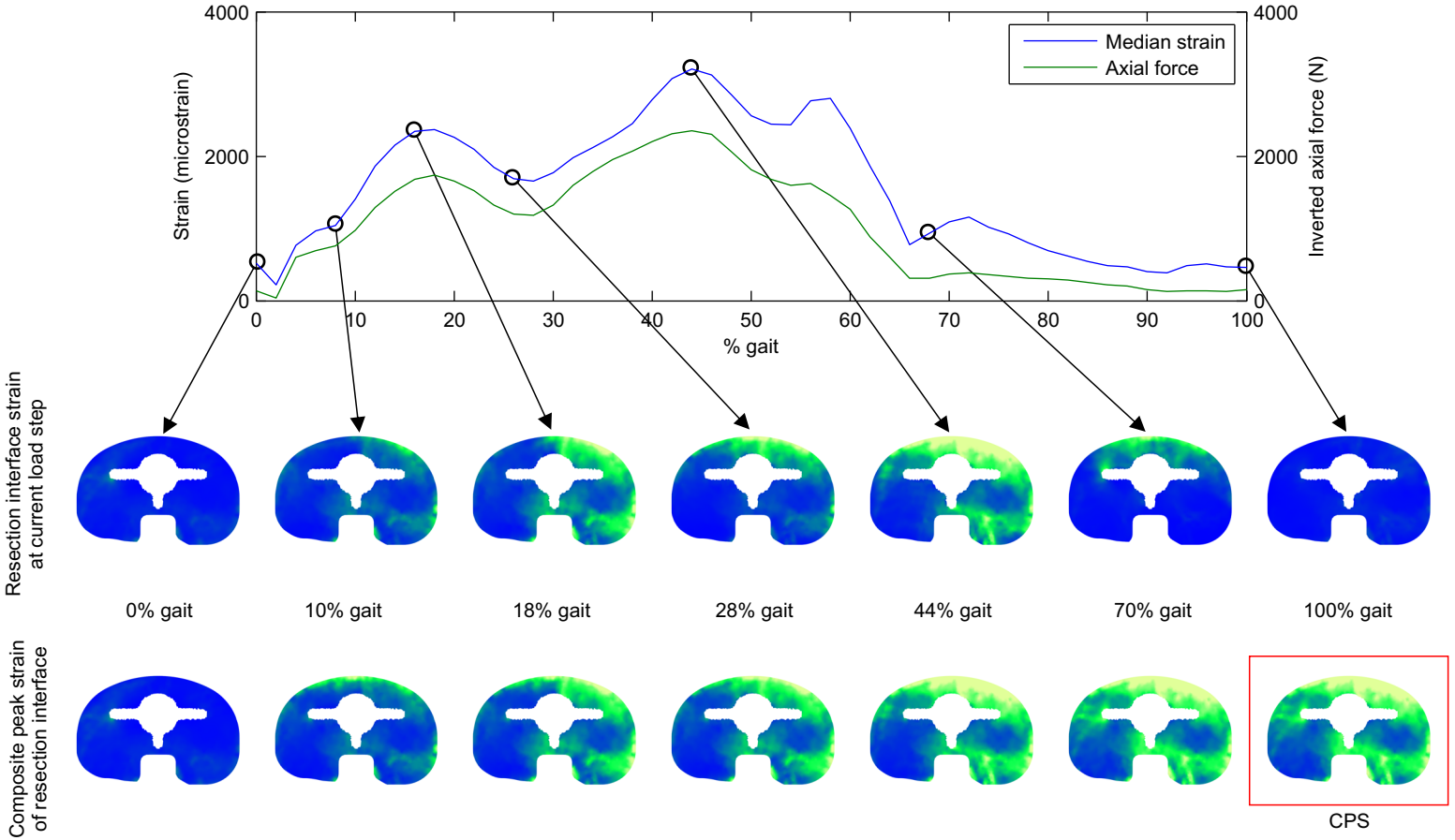

Figure 6.29: Example showing how the CPS is computed. The graph shows the mean strain of the resected surface and axial force over the gait cycle. The upper set of images show the resected surface strain at a given point in the gait cycle. The lower images shows the peak strain of the resected surface found in all steps of the gait cycle up to the given point. The highlighted image is the CPS.

6.4.7 Discussion

An overview of the method is shown in figure 6.30, highlighting the complexity of the system. Significant consideration has to be given to how to manage and store the data, run processes in parallel, and catch processing errors. Much of the data management and processing was controlled using Python. To reduce disk usage, it was also necessary to restrict the FE model output to only the strain and displacements of bone-implant interface region (although other outputs in the model could be requested), compressing the output database when necessary.

The size of the training sets for each SM were 32 tibiae and 20 healthy subjects for the tibiae SM and the gait cycle SM respectively. These sets represent only a small proportion of the general population, and sampling the PC weights to $\pm 3\sigma$ increases the chances of 'outlier'. However, these cases are of interest, because they represent the 'worst-case' scenarios. Increasing the size of the training sets would improve the representation of the sampled population.

By sampling the two SMs separately, assigning a tibia a gait loading cycle, and then predicting the weight of a model by sampling an independent BMI distribution, the link between the tibia and applied loads was broken. This neglects the two-way interaction which exists; bone strength is affected by loading, and loading is affected by bone morphology. To capture this link, and the further link to patient information (e.g. height, weight, BMI, age), a data set of CT scans, motion capture data, and patient information would be required for a SM.

The positioning of the tibial tray follows a typical surgical procedure as much as possible. The automation of the procedure will result in cases where the tibial tray is likely to be badly positioned, whereas a surgeon would make the necessary adjustments. An image of the tibial tray was taken for each model, and, by observation, it was judged that the tray was well positioned for the majority of models: central on the resected surface, minimal overhang, and no excessive I-E rotation.

To allow for cases where there was an overhang between the tibial tray and tibia, it was necessary to define the region of the base of the tibial tray which could be remeshed. Two contours defined this region, the exterior contour was around the boundary of the tibial tray, and the interior contour, offset by up to 2–5 mm from the exterior contour. This means that the implantation process is sensitive to the position of the tibial tray relative to the tibia. If the tray overhangs the bone too much, such that the boundary of the tibia is inside the interior contour, the implantation process would fail. If the initial implantation attempt failed, the tibial tray was alternately moved anterior and posterior by an increasing increment. Although this meant that some tibiae could not be implanted with a tibial tray, the requirement to define such a region means that models where the tray might excessively overhang the tibia were rejected. Clinically, excessive overhang could mean the tray impinges on ligaments causing the patient pain.

The surface mesh based approach used to create the mesh of the implanted tibia has several advantages over other approaches. One method is to convert the geometry to parametric

surfaces, commonly used in computer aided design packages. This allows for reliable and accurate Boolean operations, but converting a polygonal mesh to a parametric surface is not always reliable for complex shapes and it is not always suited to automation. Another method is to convert the geometry to an image space and perform image Boolean operations. This conversion is reasonably robust when dealing with large connected geometries, but the accuracy of the conversion is reliant on the resolution of the image. A high image resolution can unnecessarily increase the number of elements. Problems can also occur if there are small disconnected regions of geometry in the image. The advantage of using mesh based intersection and union operations is that the operations are relatively easy to handle and automate. The accuracy of the operations is also better because there is no need to convert the geometry to another form.

In vivo data from telemeterised TKRs is considered the 'gold standard' measurement of the internal forces and moments in the knee. However, given the observed inter-patient variability of the telemetric data (Kutzner et al., 2010), the five available sets of data (Bergmann, 2008) were not considered enough to create a SM. The next best available data of internal knee loads for this study were from musculoskeletal models of 20 healthy subjects. These were used to create the gait cycle SM from which the load cycles for the models were sampled. However, errors and assumptions inherent the MS modelling process (see section 6.3.4) limit the accuracy of the predicted kinematics. It is often found that the forces and moments are overestimated in comparison to *in vivo* data (tables 2.2 and 2.3). One of the largest source of errors is soft tissue artefacts (leading to movement of the markers relative to the bone), affecting the accuracy to which the movements can be captured. Further to this, assumptions made in the MS model such as modelling the knee with 1 DOF, use of a generic linear scaling law, and not taking into account the surface interaction of the femur and tibia may also contribute to the overestimation of the loads (Worsley, 2011).

When comparing the MS modelling and *in vivo* data, it was seen that the pattern of the loading knee between the data were similar (figure 6.24). Therefore, to bring the magnitude of the MS modelling loads more inline with the *in vivo* data, selected loads were scaled. Only the A-P force, F-E moment, and V-V moment were scaled by a factor 0.5 as these were seen to be the most overestimated. From initial testing of models with unscaled loads, peak micromotion greater than 500 µm was seen at the interface in the majority of models, significantly larger than the threshold at which fibrous tissue forms (150 µm). By scaling the loads, the majority of models had a peak micromotion closer to the fibrous tissue threshold. Alternative methods could have been used to scale the MS modelling loads. The ratio between the peak *in vivo* data to the peak of the MS model data could have been used to determine the scaling factor. The MS modelling loads could also be scaled such that they are within ± 1 or ± 2 standard deviations of the *in vivo* loads.

There are also other limitations in the FE model. In this study, the gait cycle loads are assumed to be evenly distributed and the tibiofemoral contact area is static. This is not the case *in vivo*, where the tibiofemoral contact area moves as the knee flexes and extends (Iwaki et al., 2002) and soft tissue constraints influence the load distribution.

In processing the results of the FE analysis, only the resected interface of the model was considered. The assumption is that for the tibial tray to migrate or subside, this interface must fail, and because the bone supporting the base of the tibial tray is likely to be stronger than that at the base of the stem, it will support higher loads. Another reason for ignoring the stem is that abnormally high strain and micromotion was often seen at the base of the stem. This is likely for two reasons (i) the bone is much weaker and has a lower modulus at the base of the stem, and (ii) the perfect fit between the tray and tibia might cause an increase in strain, particularly around sharp features. A surgeon might drill a slightly deeper hole for the post, relieving distal load transfer, reducing the strain.

The method for creating and analysing a population of models is demonstrated using three case studies. In chapter 7 the effect of under sizing the tibial tray on the primary fixation is investigated. Chapter 8 shows how a population-based study can be used to investigate a surgical factor, looking at the effect that changing the resection level of the tibia has on the predicted success of a tibial tray. The final case study, in chapter 9, investigates if the population-based model can be used to compare the 'performance' of three different designs of tibial tray.

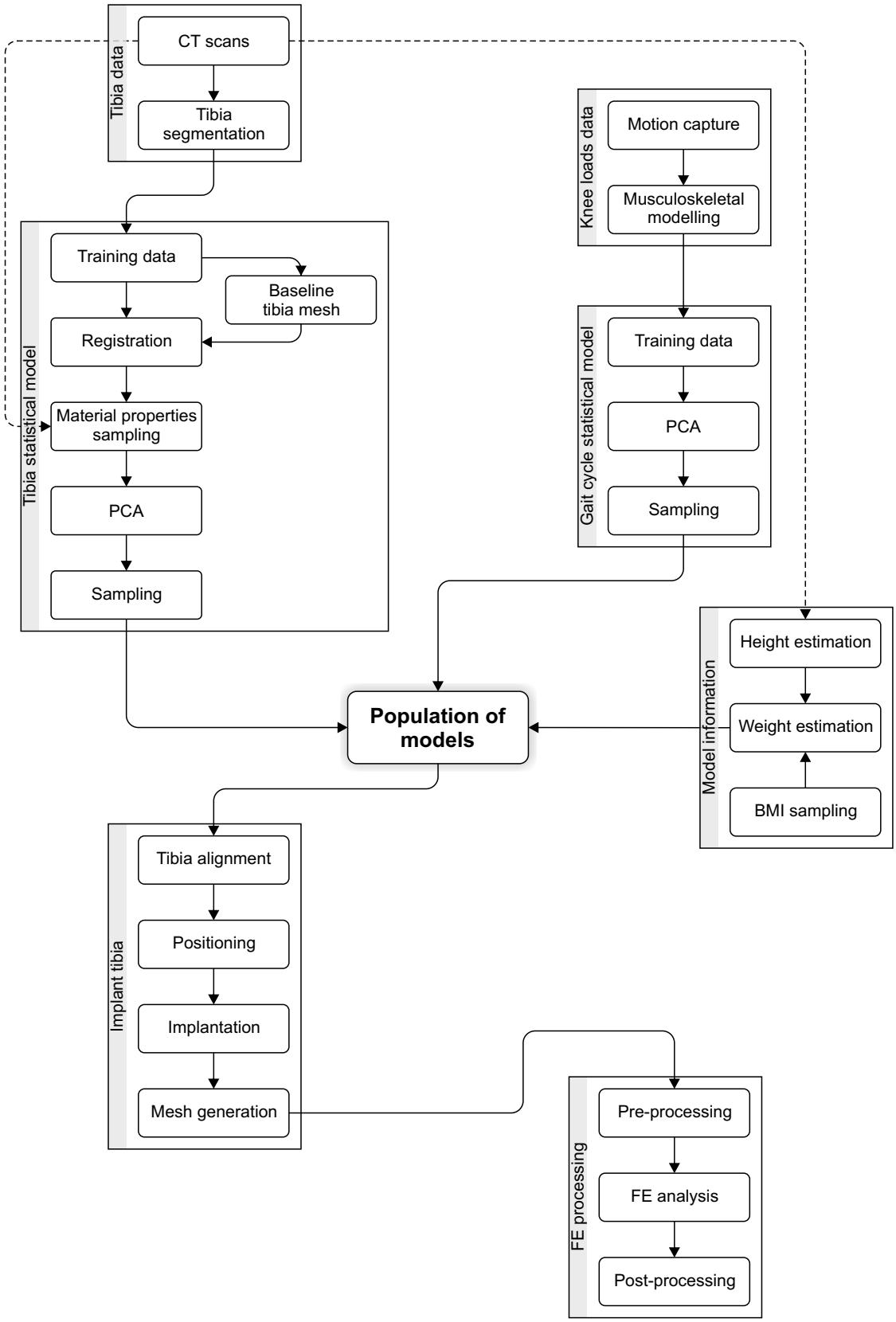

Figure 6.30: Flow chart of the method used to create a population of tibiae implanted with a tibial tray for FE analysis.

Chapter 7

The effect of under sizing a cementless tibial tray on primary stability

7.1 Introduction

TKRs are commonly used to treat a diseased knee, replacing the articulating surfaces of the femur, tibia, and patella with metal and polyethylene components (section 2.2). When performing a TKR, a surgeon must decide where to place the components and which size of components to use. The components of a TKR are available in a series of sizes, designed to account for population variability. Generally, for a primary TKR, a surgeon selects a size of tibial tray to maximise the coverage of the tibial plateau. It is possible that the surgeon might have to down size the tibial tray to match the size of the femoral component. Most manufacturers allow for at least one difference in size between the components, but, for example, if the femoral component needs to be made two sizes smaller, then under sizing the tibial tray could be beneficial to avoid post-operative problems reduced range of motion and joint instability (Gonzalez et al., 2004).

By maximising coverage of the tibial plateau, the most even load distribution is obtained and optimal fixation can be achieved (Incavo et al., 1994; Lemaire et al., 1997). In doing this, the amount of supporting cortical bone is increased. Because it is stronger than cancellous bone, it is more able to support the loads transferred from the tibial tray. This would reduce the stress and strain in the cancellous bone supporting the tibial tray. It is has been proposed that the migration of an implant is related to the strain distribution in the bone (Taylor et al., 1997), and early migration of the tibial tray has been linked to later aseptic loosening of the tibial tray (Grewal et al., 1992; Ryd et al., 1995).

Long-term reliable fixation of the tibial tray largely depends on the primary stability of the fixation. High micromotion ($> 150\,\mu m$) at the bone-tray interface have been found to promote fibrous tissue formation, whereas low micromotion ($< 50\,\mu m$) allowed bone in-growth (Jasty

Table 7.1: Load distribution in two different sections of the proximal tibia; a section at the bone-implant interface, and a section below the fixation pegs of the tray. Results for three models are shown: (3) 'large' tray and high cortical modulus; (4) 'large' tray and reduced cortical modulus; and (5) 'small' tray and reduced cortical modulus (source Cheal et al., 1985).

Model	**Tray size**	**Cortical modulus (MPa)**	**Axial load distribution in bone (%)**	
			Cortical	Cancellous
Section at bone-cement interface				
3	Large	15,000	62.2	16.5
4	Large	7,000; 450	9.3	56.4
5	Small	7,000; 450	1.9	55.4
Section distal to implant pegs				
3	Large	15,000	83.2	16.8
4	Large	7,000; 450	68.1	31.9
5	Small	7,000; 450	62.4	37.6

et al., 1997; Pilliar et al., 1986). Regions of fibrous tissue, and hence high micromotion, show as radiolucent lines (RLLs) on X-rays. The incidence of RLLs gives the surgeon an indication of the quality of fixation of the tibial tray. For some tray designs, the incidence of RLLs has been at over 90% (Aebli et al., 2004; Fuiko et al., 2003) suggesting that the mechanical conditions for fixation are not optimal.

It has been seen that the majority of tibial tray designs can offer between 80–90% coverage of the tibial plateau (Incavo et al., 1994; Westrich et al., 1997), and it is suggested that the optimum is around 85% (Incavo et al., 1994). There is very little literature investigating what effect reduced coverage has on the outcome of a TKR. Cheal et al. (1985) investigated the structural importance of the cortical bone using FE analysis observing the pattern of load transfer in the proximal tibia for a fully osseointegrated tibial tray. Compressive axial loads were directly transferred to the proximal cancellous bone, and the highest bone stresses occurred at the distal end of the fixation posts. Below this region, at the interface between the metaphysis and diaphysis, the loads were transferred to the cortical bone. Reducing the size of the tray had no significant effect on the load distribution in either the cortical or cancellous bone (table 7.1), but the peak stresses did increase in the cancellous bone.

It has been reported that the failure of a tibial tray is related to BMI and tibial tray size (Berend et al., 2008). However, the stress in the tibia was simply estimated as the ratio of patient weight to tibial tray area, hence a larger mass and smaller implant will increase stress. This fits with the findings of Cheal et al. (1985), but because it was a clinical based study, no information was obtained about the stress distribution.

As discussed in chapter 3, computational testing of TKRs often only uses a model of a single patient or a limited number of patients. In this study, a population of models is used to assess the performance of a cementless tibial tray (P.F.C.® Sigma®, DePuy® Inc, USA). To do this, the strain and micromotion of the bone-tray interface are examined as they influence the migration risk and quality of initial fixation respectively. This study will, first, demonstrate

that a population-based study can be used to identify model factors that increase the risk of failure of the tibial tray and explore whether the factors influencing strain and micromotion are similar. Second, the effect of under sizing the tibial tray on primary stability will be investigated.

7.2 Methods

A large population of tibia and associated gait cycles were generated using the method as described in section 6.4.1. The population of tibiae were implanted with a 'correct size' tibial tray using the method described in section 6.4.3. The same population of tibiae were also implanted with an 'under size' tibial tray, where the size of tibial tray was one smaller than used for the corresponding 'correct size' model. All models were processed as described in sections 6.4.4 to 6.4.6. In the the post-processing of the FE results, the strain and micromotion were computed for each point in the gait cycle. From these data, the 'composite peak' was computed. The CPS is the peak strain of each each element which occurs during the complete gait cycle, and the CPM is the peak micromotion of each element which occurs during the complete gait cycle (section 6.4.6). The point in the gait cycle at which the CPS and CPM occurred for each element was also recorded. These are termed the 'CPS percent gait' and 'CPM percent gait' respectively (section 6.4.6). Only the resection interface was considered in the analysis of the results. This was defined as the bone of the resected surface directly in contact with the tibial tray, excluding the stem of the tray.

The stability of the analysis was checked by computing the population median of the median and 95th percentile of the CPS and CPM for an increasing number of models. Before analysis of the FE results, 'extreme outliers', classified as models with a median CPS greater than ultimate strain (11 000 microstrain), and median CPM greater than 500 microns were excluded. It was considered that if the bone supporting the tibial tray had a strain exceeding ultimate strain then it would fail, causing migration of the tibial tray. If the micromotion at the bone-tray interface was over three times the fibrous tissue limit of 150 µm, then no bone ingrowth would occur to ensure good fixation of the tibial tray. It was also necessary to exclude models found to have a positive AX force during the gait cycle. Physically, a positive AX force acts upwards, and would therefore pull the tibial tray out of the bone. Physiologically, the internal forces experienced in the knee are from the femur acting on the tibia or vice versa, and therefore the tibia would not experience an upwards force.

Metrics based on the CPS and CPM were computed: area of CPS above yield strain, area of CPM < 50 µm, area of CPM ≥ 50 µm and < 150 µm, and area of CPM > 150 µm. To assess the risk of failure, only the 'correct size' models were considered[1]. The models were separated into two groups, 'higher risk' and 'lower risk'. A model was considered 'higher risk' if the

[1]This analysis is similar to that of another study carried out during this thesis investigating an osseointegrated tray, which served as a pilot study. A manuscript of the osseointegrated tibial tray study has been submitted for publication as F. Galloway, M. Kahnt, H. Ramm, et al. (2012). "A large scale finite element study of a cementless osseointegrated tibial tray". In: *Journal of Biomechanics* Submitted.

CPM area with a micromotion $> 150\,\mu m$ was above 15%, and if the CPS area with a strain >7300 microstrain was above 20%.

A Mann-Whitney U-test was used to test if model factors were significantly different between the two groups ($\alpha = 5\%$). The factors considered were the median elastic modulus of the interface, model weight, model BMI, tibia length, condylar width (as measured to size the tibial tray), and the peak forces and moments in all directions (e.g. the peak anterior force is the maximum of F_{AP} and the peak posterior force is the minimum of F_{AP}). Two further factors were also compared between the two groups, the peak of the absolute ratio of M_{VV} to F_{AX}, and the peak of the absolute ratio of M_{IE} to F_{AX}.

To investigate the effect of down sizing the tibial tray on primary stability the 'correct size' and 'under size' populations were compared. In this comparison, only models common to both populations were included in the analysis. Models for which the tibial tray could not be down sized (i.e. the 'correct size' model was implanted with the smallest possible size tray) were excluded. A U-test ($\alpha = 5\%$) was used determine if there were significant differences between CPS and CPM metrics of the two populations. Additionally, the percentage area of cortical bone supporting the tibial tray, defined as the percentage area of the resection interface with a modulus $> 2500\,MPa$, and the percentage area of the tibial plateau covered by the tibial tray (called area coverage) were also included in the metrics. The resection interface surface was visualised for selected models to see if there were visual differences in the distribution of the CPS, 'CPS percent gait', CPM, and 'CPM percent gait'.

7.3 Results

The results of this study are presented in two parts. In the first part, the risk of failure analysis is described, which only considers the 'correct size' population. The second part is a comparison between the 'correct size' population and the 'under size' population. Before presenting these results the number of models which were successfully implanted and analysed using FE are noted. From the initial population of 500 models, it was necessary to exclude models at each stage of the analysis. For the 'correct size' population, 451 (90.2%) tibiae were implanted with a tibial tray, and FE analysis was completed for 449 (89.8%) models. For the 'under size' population, 481 (96.2%) tibiae were implanted with a tibial tray, and FE analysis was completed for 478 (95.6%) models. The main reason the implantation process failed was due to geometric limitations. FE analysis failed because the analysis did not converge.

Determining the number of required models was done by computing the stability of the CPS and CPM for both the 'correct size' and 'under size' populations. For both populations it can be see that the change in the population median of the median CPS and CPM reduces as the number of models included increases (figure 7.1). At around 250 models and above, both the population median of the median CPS and CPM remain relatively constant, indicating stability. A similar trend was also seen for the population median of the 95th percentile CPS

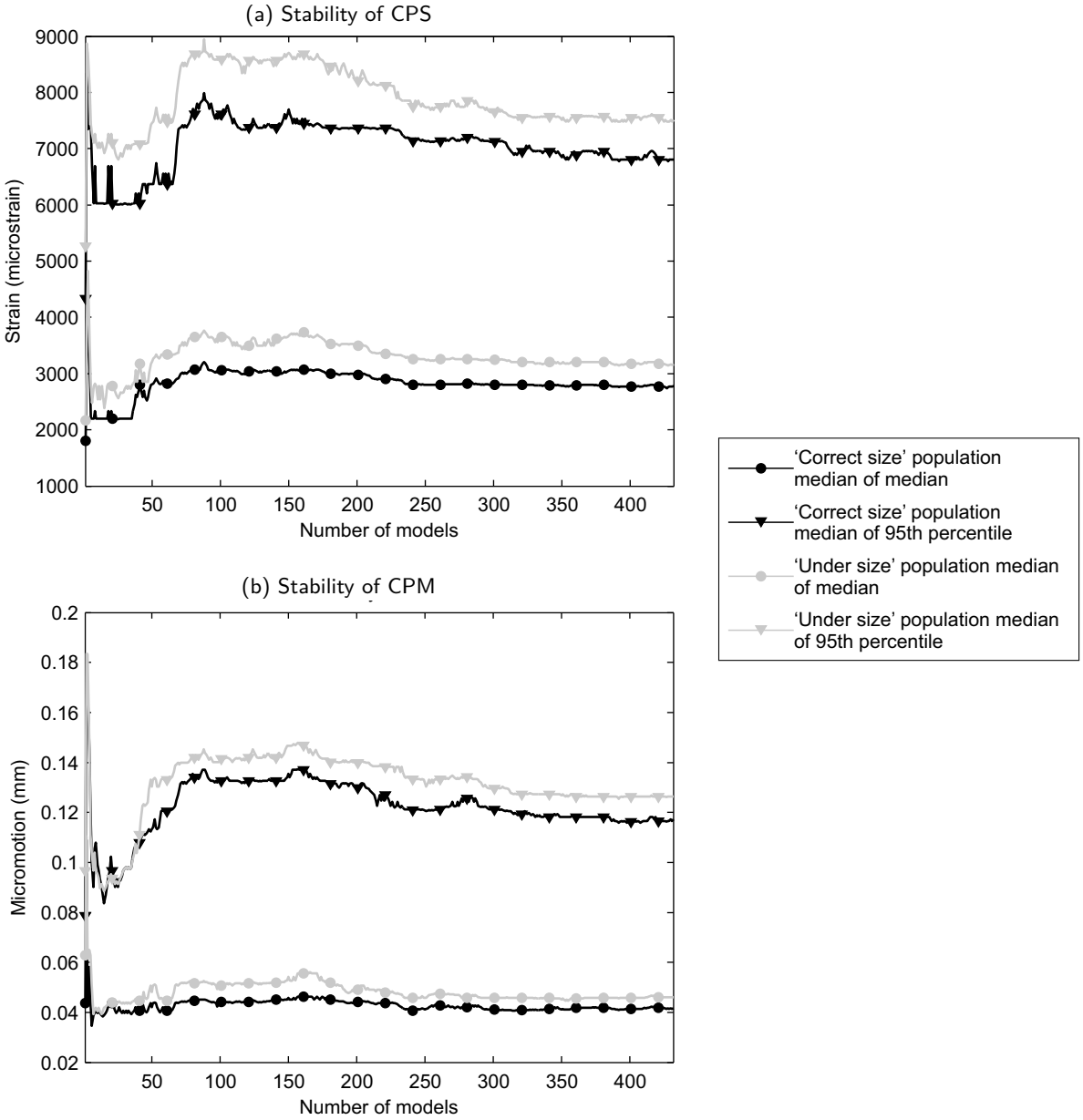

Figure 7.1: Stability of the CPS and CPM. The stability is computed as the cumulative median of the median CPS, 95th percentile CPM, median CPM, and 95th percentile CPS.

and CPM. Therefore, further analysis of the results should be done with over 250 models to reduce the likelihood of outlier data affecting the analysis.

The analysis of the models only considers the CPS of the resection interface. This only shows the strain at the surface of the tibia and may not reflect the internal strain in the tibia. To show the distribution of internal strain in the tibia, the CPS of the proximal tibia was visualised for three example models (figure 7.2). The three selected models were chosen based on the median CPS: figure 7.2(a) is the model with the population 25th percentile of median CPS ('25th percentile' model), figure 7.2(b) is the model with the population median of median CPS ('median' model), and figure 7.2(c) is the model with the 75th percentile of median CPS ('75th percentile' model).

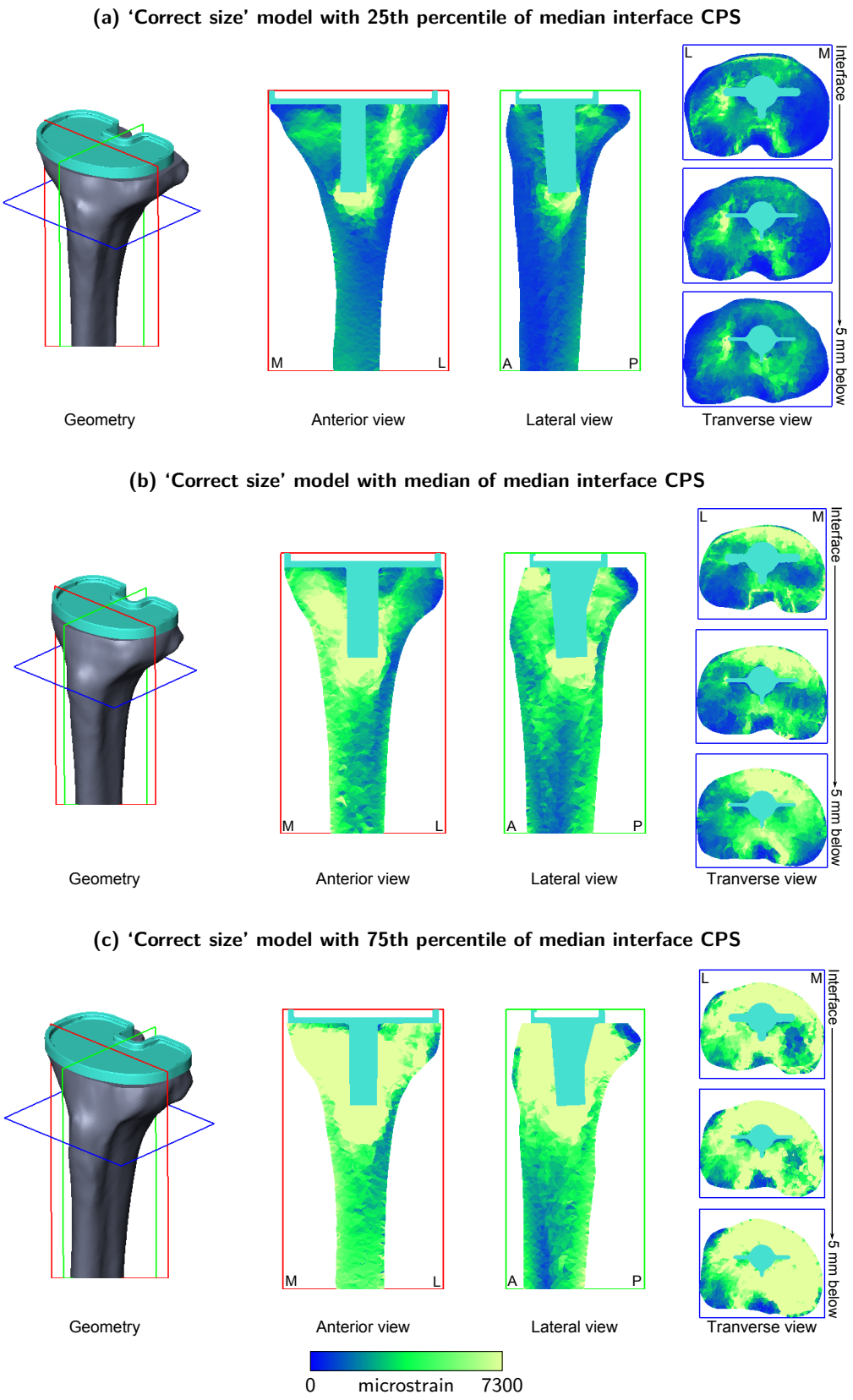

Figure 7.2: Visualisation of the CPS through sections of the proximal tibia. Three models were selected by value of the median CPS of the resection interface: (a) has a value equal to the population 25th percentile, (b) has a value equal to the population median, and (c) has a value equal to the population 75th percentile. For each model, the geometry, a frontal section (anterior view), sagittal section (lateral view), and three transverse sections (inferior view) are shown. The top transverse section is the resection interface, the middle is 2 mm below the interface, and the bottom is 5 mm below the interface.

For each model in figure 7.2, the geometry, a frontal section (anterior view), sagittal section (lateral view), and three transverse sections (inferior view) are shown. The transverse sections show that the distribution of peak strains distal to the interface (middle and bottom transverse sections) is similar to the interface (top transverse section), the regions where bone tends to yield are around the anterior edge and on the medial side. However, noticeably for the '75th percentile' model, there is a visible increase in the amount of bone which has a strain above yield (the light coloured regions) at more distal sections in the tibia. This is likely because the more distal bone is weaker in comparison to the interface bone. The frontal and sagittal sections show that the peak strains occur around the stem of the implant, particularly at the bottom of the stem and medial to the stem.

To better show where the high magnitude CPS occurs, the strain colour field was changed such that the dark regions (blue) represent strains less than yield strain (7300 microstrain), and the light regions (light green) represent strains greater than ultimate strain (11 000 microstrain). The transverse sections of '75th percentile' model are shown in figure 7.3, and this shows that the areas of very high magnitude CPS are found in similar locations and are also similar in size in all the transverse sections.

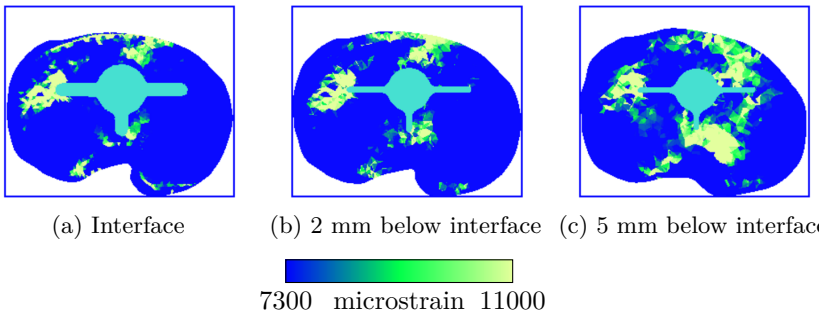

Figure 7.3: Transverse sections of the '75th percentile' model from figure 7.2c. The key of the strain field has been changed such that dark colours represent 7300 microstrain (yield strain) and below, and light colours represent 11000 microstrain (ultimate strain) and above.

.

7.3.1 Risk of failure analysis

Only the 'correct size' models were used in the risk of failure analysis and it was necessary to exclude models from this analysis. A further 65 models were excluded because they were identified as 'extreme outliers', or they had a positive axial force during gait. The remaining 384 models were then divided into two groups; 'lower risk' and 'higher risk'. Models at risk of failure were considered to be those for which the area of CPS >yield strain (7300 microstrain) was above 20% or the area of CPM >150 microns was above 15%.

Using these thresholds, there were 106 models in the 'higher risk' group. The majority of models in the 'higher risk' group had a median CPS >3000 microstrain and a median CPM >50 microns (figure 7.4). These limits are below yield strain of bone and above the level of micromotion at which fibrous tissue forms respectively. The median elastic modulus of the 'higher risk' group was 240 MPa compared to 460 MPa of the 'lower risk' group (table 7.2).

Many studies assume that there is a correlation between the peak strain and peak micromotion at the bone-tray interface. Only a weak correlation was found between the median CPS and median CPM (figure 7.4). Generally, as the median CPS increases, the CPM increases, but the spread of the data also increases. Also seen is that models with a low resection interface modulus are generally classified as 'higher risk'; the majority of models in this group had a resection interface modulus of $< 400\,\text{MPa}$ (figure 7.4). A strong correlation between the median CPS and median modulus was seen (figure 7.5a), as the strength of the interface surface increases, the median CPS decreases. Between the modulus of the interface surface and median CPM, the correlation is weaker (figure 7.5b). Models with a low interface modulus tend to have a higher median CPM.

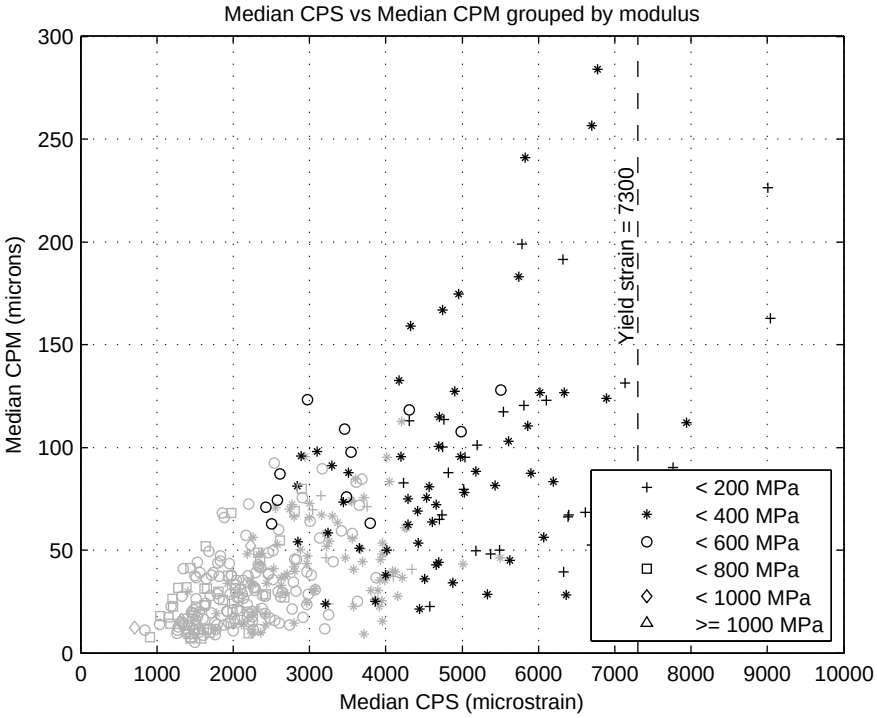

Figure 7.4: The influence of the median modulus of the interface surface on the median CPS and median CPS. The light markers are the 'lower risk' group, and the dark markers are the 'higher risk' group.

To test the significance in difference between models factors of the two groups, a U-test was used. The factors which were *not* significantly different between the two groups were the peak M_{VV} to F_{AX} ratio, model weight, peak lateral force, peak anterior force, peak valgus moment, and peak external moment (table 7.2). The factors which had the most significance were the median modulus, model BMI, and peak extension moment.

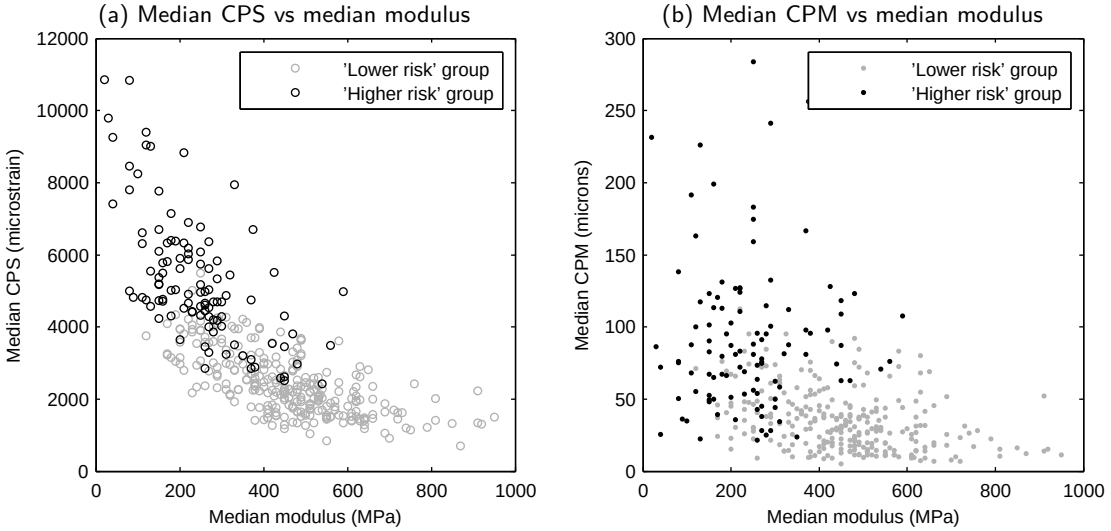

Figure 7.5: Correlation of the median CPS and median CPM with median modulus of the interface surface. Light markers are the 'lower risk' group, and dark markers are the 'higher risk' group.

Table 7.2: Comparison of factors between the 'lower risk' and 'higher risk' groups. * denotes the metric was significantly different between the two groups ($p < 0.05$).

		'Lower risk', n = 268			**'Higher risk', n = 106**		
Metric	p	**Min**	**Median**	**Max**	**Min**	**Median**	**Max**
Median modulus (MPa)*	0.0000	120.0	460.0	950.0	20.0	240.0	590.0
Model BMI (kg/m^2)*	0.0001	17.0	27.9	47.7	17.7	30.7	43.5
Peak extension moment (Nm)*	0.0027	−30.7	−6.9	−1.6	−26.5	−8.6	−2.0
Peak medial force (N)*	0.0037	33.4	120.5	269.0	49.4	138.9	282.3
Condylar width (mm)*	0.0040	60.2	79.6	94.7	65.6	76.8	93.0
Peak internal moment (Nm)*	0.0045	1.3	6.9	21.7	2.0	8.4	22.5
Tibia length (mm)*	0.0053	284.5	380.5	469.4	301.7	370.6	450.7
Peak axial force (N)*	0.0062	−4543.4	−2581.1	−1135.5	−4402.6	−2747.3	−1319.8
Peak varus moment (Nm)*	0.0078	10.8	25.6	52.9	12.1	28.1	47.4
Peak flexion moment (Nm)*	0.0111	5.9	18.1	35.7	7.2	20.8	51.4
Peak M_{IE}:F_{AX} ratio*	0.0144	0.004	0.014	3.800	0.006	0.016	1.333
Peak posterior force (N)*	0.0445	−775.0	−331.5	−108.6	−887.8	−374.3	−118.1
Peak M_{VV}:F_{AX} ratio	0.0546	0.007	0.012	10.800	0.007	0.013	1.167
Model weight (kg)	0.0581	36.4	76.1	149.2	42.8	79.2	123.4
Peak lateral force (N)	0.1480	−125.1	−18.1	23.6	−125.7	−11.2	24.1
Peak anterior force (N)	0.2349	−3.5	13.2	329.6	−11.4	16.1	297.2
Peak valgus moment (Nm)	0.3110	−9.8	−1.0	1.5	−12.3	−1.2	1.5
Peak external moment (Nm)	0.6639	−15.1	−4.7	0.4	−14.4	−4.4	−0.4

7.3.2 Population comparison analysis

In the comparison analysis, the models common to both the 'correct size' and 'under size' populations were selected leaving only 432 models. From these 67 models were excluded from the analysis analysis because they were identified as 'extreme outliers', had a positive axial force during gait, or the tray was not down sized. This left 365 models for the comparison analysis.

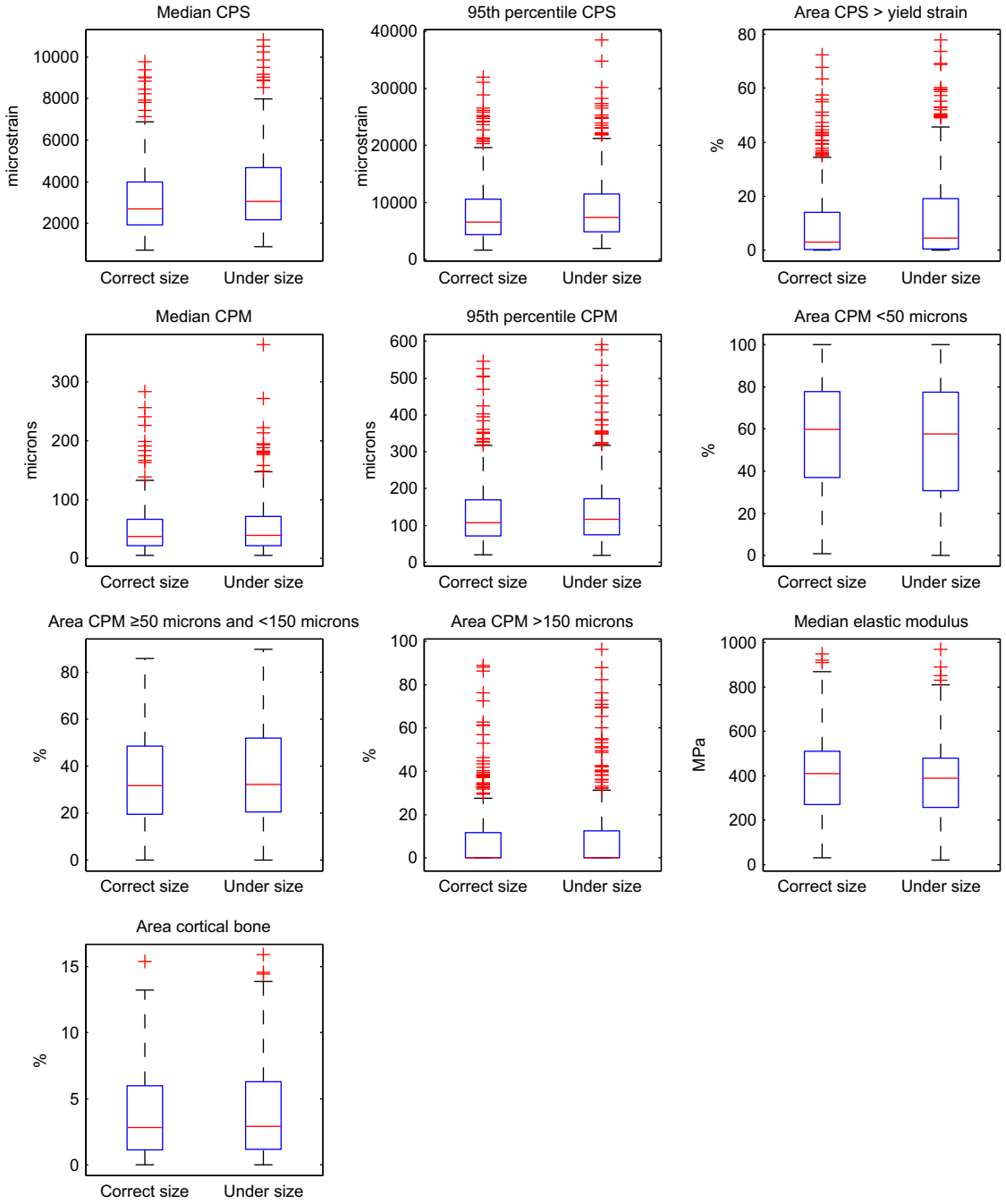

Figure 7.6: Boxplots of the metrics comparing correct size models with under size models. On each box, the red line is the median, the lower and upper edges of the box are the 25th and 75th percentiles, the whiskers mark the most extreme data not considered outliers, and the red crosses are the data considered outliers.

To compare the two populations a U-test was used to test for significant differences between the CPS and CPM metrics. The metrics compared were: median CPS, area CPS > yield strain, median CPM, area CPM <50 microns, area CPM ≥50 microns and <150 microns, area CPM >150 microns, median elastic modulus, and area cortical bone (figure 7.6). Only the median CPS was significantly different between the two populations (table 7.3).

In general the inter-quartile range of all the metrics was similar for the populations (figure 7.6). The 'under size' population experienced higher peak strains and peak micromotion; the population median of the median CPS and median CPM were higher (table 7.3), and the population maximum of the median CPS and median CPM were also higher (table 7.3). The area of the interface surface experiencing different levels of micromotion were similar for the two populations, as was the area of the interface surface greater than yield strain (figure 7.6 and table 7.3).

The area of supporting cortical bone was similar for the two populations (median (min–max) of 2.8% (0–15.4%) and 2.9% (0–15.9%) for the 'correct size' and 'under size' populations respectively), but the average coverage of the tibial plateau was 86% for the 'correct size' population and 77% for the 'under size' population. However, the area of supporting cortical bone was also found to reduce the median CPS (figure 7.7a) and median CPM (figure 7.7b).

To see if the there was a difference in the distribution of the CPS and CPM between the 'correct size' and 'under size' populations, the resection interface was visualised (figure 7.8). The rows of figure 7.8 are the models with a value of median CPS equal to the minimum extreme, 25th percentile, median, 75th percentile, maximum extreme, and outlier (as defined in figure 7.6) values of the 'correct size' population. The visualised models represent the distribution of the median CPS in the 'correct size' population. To be able to compare the changes between the populations, the same models from the 'under size' population were also selected.

In the first column of figure 7.8, the interface surface CPS of the models from the 'correct size' population are visualised. In the second column the interface surface CPS of the 'under size' models are shown. It can be seen that there is little difference in the distribution of

Table 7.3: Comparison of metrics between the 'correct size' and 'under size' populations. A Wilcoxon-Mann-Whitney test was used to test for significant differences between metrics. * denotes significant ($p < 0.05$).

		'Correct size'			**'Under size'**		
Metric	p	**Min**	**Median**	**Max**	**Min**	**Median**	**Max**
Median CPS (microstrain)*	0.0003	706.2	2682.6	9788.8	875.5	3045.4	10 826.1
Area CPS > yield strain (%)	0.0566	0.0	3.0	72.4	0.0	4.4	77.9
Median elastic modulus (MPa)	0.0681	30.0	410.0	950.0	20.0	390.0	970.0
Area CPM < 50 µm (%)	0.2111	0.7	59.9	100.0	0.0	57.6	100.0
Median CPM (µm)	0.2249	5.2	37.7	283.9	5.7	39.6	363.5
Area CPM ≥ 50 µm & < 150 µm (%)	0.3409	0.0	31.7	85.8	0.0	32.2	89.7
Area CPM > 150 µm (%)	0.4837	0.0	0.0	89.0	0.0	0.0	96.4
Area cortical bone (%)	0.6738	0.0	2.8	15.4	0.0	2.9	15.9

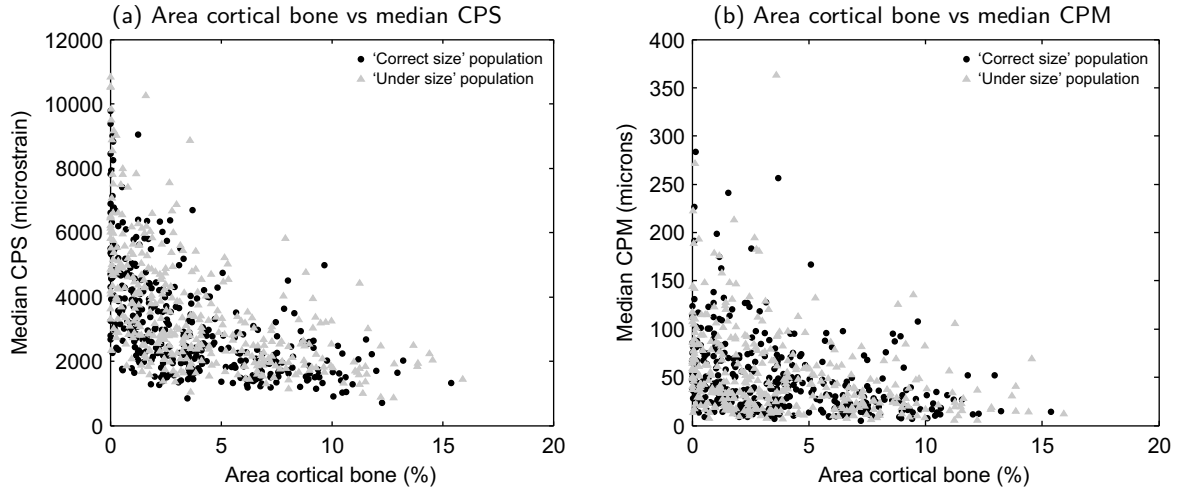

Figure 7.7: Correlation of the area of supporting cortical bone with (a) median CPS and (b) median CPM for both populations.

CPS between the two populations; regions of high and low peak strains correspond. There is also little difference between in the distribution of the CPM between the two populations (columns 5 & 6). A correlation between the distribution of CPS and modulus of the interface surface can be seen, higher strains occur in regions of lower modulus. For example, for the '75th percentile' model there is a region of high modulus on the medial side of the interface surface (column 9 & 10). This corresponds to the regions of low CPS (columns 1 & 2). It is also observed that for models with a low median CPS (e.g. 'min extreme' model), the interface surface has a larger proportion of higher modulus bone (indicated by the area of lighter colours), compared to models with a higher median CPS (e.g. '75th percentile' model).

When computing the CPS and CPM of the interface surface, it is known which load step in the FE analysis the peak strain and peak micromotion occurs. Each load step of the FE analysis corresponds to a point in time of the gait cycle. The 'CPS percent gait' was defined as the the time in the gait cycle (in terms of % gait) at which the peak strain of the interface surface occurs. The 'CPM percent gait' was defined as the time in gait cycle (in terms of % gait) at which the peak micromotion occurs.

It was found that the CPS and CPM of the interface surface occur at different times during the gait cycle. The third column of figure 7.8 shows the 'CPS percent gait' and the seventh column shows the 'CPM percent gait'. In these columns, the dark colours represent the stance phase of gait (from 0% to around 60%), and light colours represent the swing phase of gait (approximately 60% onwards). It can be seen that the CPS tends to occur earlier in the gait cycle (mainly darker colours on the interface surface) than the CPM (interface surface is mostly light colours) for all the selected models. For the 'correct size' population, the median 'CPS percent gait' was 54% gait, whereas the median 'CPM percent gait' was 62% gait.

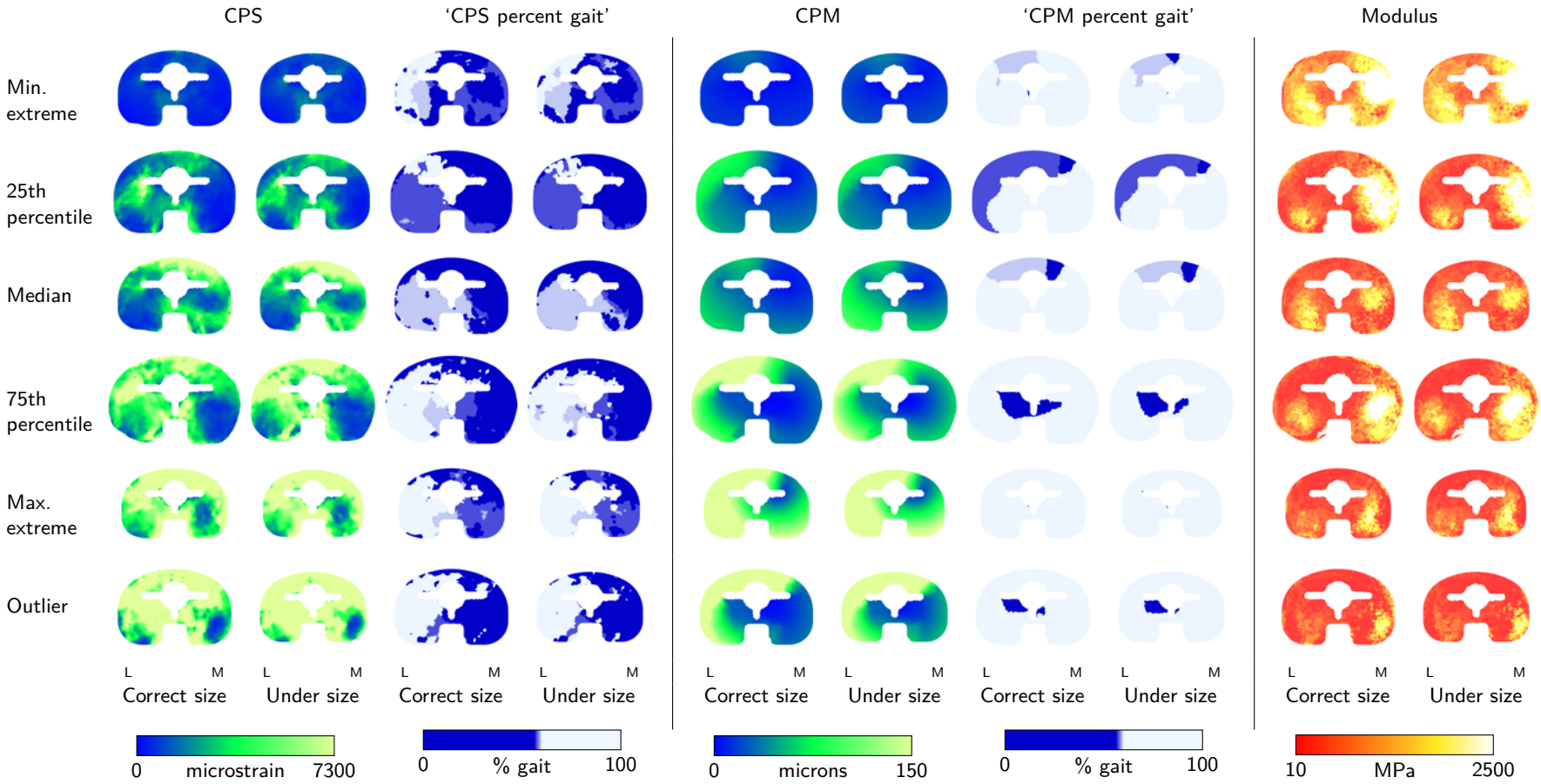

Figure 7.8: Visualisation of the CPS, 'CPS percent gait', CPM, 'CPM percent gait', and modulus of the resected interface surface. For each metric, the left column shows models from the 'correct size' population and the right column shows models from the 'under size' population. Each row is of the same model. The selected models are those with the 'correct size' population minimum extreme, 25th percentile, median, 75th percentile, maximum extreme, and outlier values of resection interface median CPS.

7.4 Discussion

Demonstrated in this case study was the use of a large population of models incorporating inter-patient variability of the tibia and loading to examine the effect of under sizing the tibial tray on primary stability. To see if enough models were included in the population, the stability of the median CPS and median CPM was used as a guide (figure 7.1). The metrics stabilised at 250 models, and in the analysis of the populations, over 350 models were used, reducing the effect noisy data might have on the analysis.

It is necessary to draw some comparison between the strain and micromotion estimated in this study to other studies considering only the 'correct size' population. Strain in the resected interface is not well reported in the literature. Perillo-Marcone et al. (2007) reported the peak maximum and minimum principal strains over the gait cycle (equivalent to CPS) for a single patient. The pattern of strain was similar to the current study, with higher strains seen around the lateral and anterior edges. Between 59–70% of the resection interface was found to exceed compressive yield strain, a much larger area than found in this study. A reason for this is that the patient modelled by Perillo-Marcone et al. (2007) weighed 116 kg which would increase the joint loads, resulting in higher strain in the tibia.

The magnitude of the micromotion is similar to that observed in other studies, the range of the median CPM was 5 µm to 284 µm for the 'correct size' population. Chong et al. (2010) reported a peak of 133 µm during gait, and Taylor et al. (2012) reported a peak of 180 µm for the P.F.C.® Sigma® tray during gait. The median area of CPM < 50 µm is also similar, Chong et al. (2010) reported an area of 44%, and Taylor et al. (2012) reported an area of 40%, compared to 58% in this study. The variability of the tibia shape, size, and modulus distribution, as well as variable loading cycles is likely to be the cause of the differences.

From the visualisation of the resection interface (figure 7.8), it is noticeable that the models with higher strain (e.g. '75th percentile' model) have poorer bone quality. This is also seen comparing the 'lower risk' and 'higher risk' groups (figure 7.5a), the median modulus of the resection interface was significantly larger in the 'lower risk' group (460 MPa) than the 'higher risk' group (240 MPa). Models in the 'higher risk' group had a larger median CPS (4970 microstrain) compared to the 'lower risk' group (2260 microstrain). Between the 'correct size' and 'under size' population the median CPS is significantly different and the median modulus of the resection interface is also lower in the 'under size' group (table 7.3). Clinical studies have found that the tibial tray is more likely to experience continuous migration, particularly in the first few months post-operatively, in patients with a lower pre-operative bone density (Li et al., 2000; Petersen et al., 1999). The migration of the tibial tray is thought be related to the initial strain in the bone (Taylor et al., 1997) and has been linked to failure of the tray in the long-term (Ryd et al., 1995). Therefore, models with a lower interface modulus would be expected to have a higher risk of failure.

In this study, only a weak correlation was found between the median CPS and median CPM (figure 7.4). A reason for the poor correlation between strain and micromotion is perhaps related to the load cycle. The assumption made by many studies is that the peak strain

and micromotion occur with the peak axial load. Visualisation of the point in the gait cycle at which the CPS and CPM occurred showed that the CPS occurs earlier in the gait cycle (figure 7.8). For the 'correct size' population, the median 'CPS percent gait' was 56% gait corresponding to the second peak of axial force. The median 'CPM percent gait' was 62% gait, which is approximately the beginning of swing phase where the axial load is low and there are moderate moments. This supports Taylor et al. (2012) who also found that the peak micromotion tended to occur in the swing phase of gait. Further, as part of an RSA study, the inducible displacements of the tibial tray were computed by taking radiographs of the knee unloaded and loaded with the patient standing putting weight on the knee (Petersen et al., 1999). No correlation between pre-operative bone density and inducible displacements of the tibial tray was found. To compare to the results of this study, the bone density can be considered as the modulus of the interface surface, and the inducible displacements can be considered as the CPM of the interface surface, and it was found that there was a weak correlation between the median CPM and modulus of the interface surface (figure 7.5b).

This evidence suggests that the peak strain of the resection interface is dependent on the bone quality and axial force during gait. This is supported by Rawlinson et al. (2005), who found that tibiae with poor bone quality benefited from an augmented stem to increase stability and reduce bone strain. The peak micromotion, however, seems to be independent of bone quality and dependent on the moments during gait as it occurs later in the gait cycle (figure 7.8).

Before the analysis of the results, models considered 'extreme outliers' were excluded. The reason for doing this was to avoid the results becoming skewed by models which experienced extremely high strains and micromotions. It was considered that if a model had a median CPS greater than ultimate strain, or if the median CPM was greater than 0.5 mm, the model could be considered a failure. Investigation of the characteristics of these models found that the majority had an interface modulus of < 100 MPa, and for some models the median interface modulus was as low as 20 MPa. The low modulus of the interface surface would mean that the tibial tray would be poorly supported, increasing the risk of failure of the tibial tray. In these cases, the surgeon might consider an alternative fixation such as cemented or using screws. The geometry of the 'extreme outlier' models was comparable to the 'correct size' population. The lengths of the 'extreme outlier' tibiae ranged from 307 mm to 419 mm and the lengths of the 'correct size' population ranged from 284 mm to 469 mm. The condylar widths (as measured to size the tibial tray) ranged from 71 mm to 82 mm for the 'extreme outlier' tibiae, and from 60 mm to 95 mm for the 'correct size' population.

One of the assumptions made in this study, is that for the tibial tray to migrate or subside, the bone directly supporting the tibial tray must fail first. Strain is used to determine the failure of bone and as a factor to determine the risk of failure of a model. However, the resection interface might not be the location the highest strain, higher strains could be generated in softer bone more distally located in the tibia. Visualisation of the CPS through transverse sections of the proximal tibia (figure 7.2) showed that the CPS of the interface was indicative of the CPS more distally in the tibia. Although a larger area of bone experienced a strain greater than yield in the more distal transverse sections, the regions of very high peak strains

(greater than ultimate strain) were found to be in similar locations in all the transverse sections (figure 7.3). Importantly, this holds true for the different models. For a comparative analysis it is reasonable to use the peak strain of resection interface.

7.4.1 Risk of failure analysis

The first analysis performed only considered the 'correct size' population and was divided into two groups representing 'lower risk' and 'higher risk' of failure. Figure 7.6 shows that if the area CPS > yield strain is over 35%, or if the area CPM > 150 microns is above 35%, the model was an outlier (figure 7.6). It is argued here that if over one third of the resection interface experiences micromotion greater than 150 µm the risk of failure is increased as fibrous tissue would form. Clinically, these regions would show as RLLs (Fuiko et al., 2003) and a surgeon is likely to be concerned if the incidence of RLLs is high and they progressed. Similarly, if over one third of the resection interface experiences strain greater than 7300 microstrain (yield strain), then the risk of migration is higher (Taylor et al., 1997), which could lead to aseptic loosening (Ryd et al., 1995). Models at 'higher risk' were identified using more conservative thresholds—if area CPS >yield strain was above 20% or the area CPM > 150 µm was above 15%.

Grouping the models using these criteria resulted in 278 models classified as 'lower risk' and 106 as 'higher risk'. In the 'higher risk' group, almost all the models have a median CPS below yield strain (figure 7.4), with a group median of 4426 microstrain. This level of strain suggests that the strain threshold is perhaps too low. The majority 'higher risk' models have a median CPM greater than the osseointegration limit of 50 µm (group median is 80 µm). With this level of micromotion, fibrous tissue is more likely to form at the interface increasing the risk of failure. The threshold used for area CPM > 150 µm seems appropriate.

In comparison to long-term survivorship rates of cementless TKRs, reported at >95% (National Joint Registry for England and Wales, 2011), the proportion of models in the 'higher risk' group is overestimated. Although a direct comparison is not possible, reported survivorship rates also include failure of the other TKR components experiencing a varied loading cycle, whereas in this study only the tibial tray was modelled with gait cycle loading. Also, the strain in the bone, used as a criteria to determine the 'higher risk' models, is influenced by the modulus of the tibia. The modulus distribution of the tibia is dependent on the chosen modulus-density relationship and further inaccuracies are introduced when sampling the SSIM. Establishing better threshold limits is a challenging problem. One way to do this could be to perform a study using multiple tray designs with known detailed clinical histories. It would then be possible to correlate the patient characteristics and clinical outcomes with model characteristics and the predicted biomechanical response.

Comparing peak loads between the two groups, the 'higher risk' group was generally subjected to larger peak loads (table 7.2), implying a greater contact force in the knee. Part of the reason for this is that the model mass and BMI are larger in the 'higher risk' group, increasing the magnitude of the loads. It was also found that the models in the 'higher risk' group were

smaller than the 'lower risk' group, the tibiae were 9.9 mm shorter, and the condyles were 2.8 mm narrower. The strength of the interface was also weaker for the 'higher risk' group. Larger loads, applied to a smaller, weaker tibia, would result in a higher strain in the bone, leading to increased risk of failure. Berend et al. (2008) reported that the risk of failure of a tibial tray was dependent on BMI and tray size, but did not consider factors such as such as bone modulus in the stress calculation and simply estimated stress as the ratio of patient weight to tray area. In this study, the size of the tibial tray did not influence the risk of failure of a model. The distribution of tray sizes between the 'lower risk' and 'higher risk' groups was similar.

There is evidence as to why a few of the factors might be significantly difference between the 'lower risk' and 'higher risk' groups. Previous studies of multiple patients have suggested that the variability of bone quality and loading affected the volume of bone at risk of damage (Wong et al., 2010). Varus alignment of the tibial tray increases the likelihood of revision (Fang et al., 2009; Ryd et al., 1995), and the peak varus moment is larger in the 'higher risk' group. FE studies have also shown that with varus alignment, a larger volume of bone is at risk of failure (Perillo-Marcone et al., 2004; Wong et al., 2010). In this study, the 'higher risk' group had a larger peak varus moment and could be considered in varus alignment.

7.4.2 Population comparison analysis

The second analysis compared the 'correct size' and 'under size' populations. It was found that only the median CPS was significantly different between the two populations (table 7.3). It is expected that the 'under size' population has a lower modulus because the tray has a smaller area and by positioning it centrally on the resected surface it is not supported by the cortical shell. This would therefore lead to an increase in the strain. However, the area of cortical bone was approximately 3% for both populations, and both populations had a similar distribution of area of cortical bone (figure 7.7a). This is further evidence that it is the overall quality of the resection interface which influences the strain.

Accurately identifying the metaphyseal shell of the proximal tibia is difficult because it is very thin, the metaphyseal cortical shell is perhaps only 1 mm thick. It would be expected that by down sizing the tray, the area of supporting cortical bone would be reduced. A tray one size smaller is 2–4 mm smaller in M-L width. It was assumed that the cortical bone had a modulus of > 2500 MPa, low in comparison to experimentally measured values (Guo, 2001). However, error is introduced by sampling the density of the elements from the CT scan (as was done for the SM training tibiae, section 6.2.5). An element might be positioned over both cancellous and cortical bone, or the boundary of cortical bone and air, and because the density is averaged at several positions in the element it is underestimated. Further error is introduced from sampling the SM. The modulus is not accurately reconstructed or estimated in comparison to the shape (section 6.3.3).

The micromotion was not significantly different between 'correct size' and 'under size' populations. To achieve a similar absolute magnitude of micromotion, the rotation of the smaller

tray must be larger, resulting in larger lift-off of the tray, likely caused by a shortened moment arm. The regions of high micromotion ($> 50\,\mu m$) are found around the anterior, lateral, and posterior regions of the interface (figure 7.8). This suggests that the periphery of the tray does not contribute to stability of the tray and that the keel is providing most of the resistance against micromotion.

Visualisation of the CPS and CPM (figure 7.8) shows that the distribution of the CPS and CPM is similar for both populations. This supports the findings of Cheal et al. (1985) that down sizing the tibial tray increased the peak stress in the proximal tibia bone, but did not affect the stress distribution. Cheal et al. (1985) found that the largest change in load distribution was in the cortical bone at the bone-cement interface, where it reduces from 9.3% to 1.9% (table 7.1), and more of the load is transferred through the fixation posts. It is likely that a similar effect occurs in this study although the post of the tray was ignored.

7.5 Conclusions

This case study has assessed the effect of under sizing the tibial tray has on the primary stability, using SMs to generate a large population of models. The key findings of this case study were:

- Peak strain was seen to be dependent on the bone quality and axial loading, occurring during stance phase of gait.
- Peak micromotion was dependent on the knee moments and independent of bone quality and occurred at the beginning of swing phase of gait.
- Models considered at higher risk of failure had a smaller tibia with lower bone quality, higher weight, and larger peak loads.
- Under sizing the tibial tray caused a 1.1 percentage increase in strain, and a 1.05 percentage increase in the micromotion of the resection interface. This suggests that under sizing the tibial tray has minimal influence on the predicted strain and micromotion in the tibia.

Chapter 8

The effect of resection level on the fixation of a cementless tibial tray

8.1 Introduction

The depth to which the tibia is resected is dependent on many factors including bone quality and knee deformities. The effect of resection depth on the initial mechanical response of the tibia is relatively unknown. Berend et al. (2010) has examined the effect of resection depth on strain in the cortical shell of the proximal tibia. Using composite models of tibiae, tibial trays were implanted at 5 mm and 15 mm below the joint line, which represent the extreme resection levels used depending on bone quality and knee deformities observed clinically. With a neutral axial load, the shear strains increased by up to 281% at the more distal resection level in the peripheral regions directly below the tibial tray. Berend et al. (2010) suggests that the reason for the increase in the peripheral strain is due to increased edge loading. By making a more distal resection, the geometry of the resected surface changes meaning that a smaller tibial tray is required. The position of the tray had to be more posterior, resulting in an increase in posterior strain.

One of the factors which might affect the fixation of the tibial tray is the strength of bone quality. In the previous case study (chapter 7), the modulus of the resection interface affected the strain. A limitation of the work by Berend et al. (2010) is that by using a composite tibia, the modulus of the cortical and cancellous bone are homogeneous throughout. Experimental studies have found that the modulus of the cancellous bone changes with resection depth. Goldstein et al. (1983) measured the strength of the subchondral bone at 4 resection levels up to a depth of 40 mm below the subchondral plate. At the most distal resection, the strongest bone was adjacent to the cortex. These concentrated regions of strength extended proximally and inward beneath the tibial condyles. At the proximal resection, the medial side was found to be stronger and stiffer than the lateral side. A central column of low modulus trabecular bone was also found, extending from the the intramedullary space to the intercondylar space. The pattern of variation in strength was similar in the sample population, although the

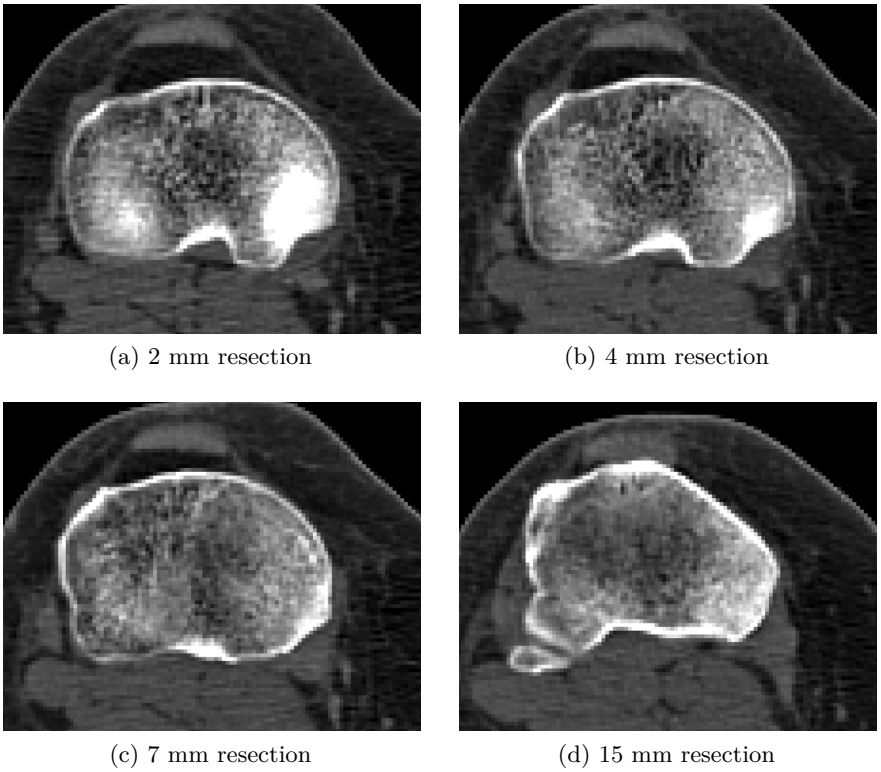

(a) 2 mm resection (b) 4 mm resection

(c) 7 mm resection (d) 15 mm resection

Figure 8.1: Slices from a CT scan of the left tibia at different resection levels. The cortical shell thickens at deeper resections. Orientation of the scans is such that left is lateral, and top is anterior.

magnitude of strength could vary by up to two orders of magnitude.

Hvid et al. (1986) measured the penetration strength of the subchondral bone in five valgus and seven varus human tibiae. Each tibia was resected as if for a TKR procedure and a 2 cm thick section of bone was further resected. The penetration strength was then measured at 2 mm intervals up to a depth of 10 mm. At the most proximal resection level, the mean sample values show that the bone is stronger on the medial side (13–35 MPa) and the central bone was weaker (3 MPa). The strength of cancellous bone on the side of the stronger condyle reduced by 40–60 % relative to the central condylar value of the most proximal resection, and was more pronounced within the first 6 mm. Below the weaker condyle the decrease in strength is less noticeable, only 0–25 %.

Although the strength of cancellous bone decreases with resection depth, the cortical shell thickens from the epiphysis (proximal resection, figure 8.1a) to the diaphysis (distal resection, figure 8.1d). Because the cortical bone is much stronger than cancellous bone, the overall modulus of the resection interface might increase, providing better support for the tibial tray. However, the change in geometry of the proximal tibia, which narrows from the metaphysis to the diaphysis means that it might be necessary to down size the tibial tray. This could mean that the tray is not supported by the peripheral cortical bone, reducing the fixation quality and primary stability.

In this study, it is hypothesised that the decrease in modulus with resection depth will increase the peak strain. However, this may be confounded by two factors, the change in amount of

supporting cortical bone and the change in size of the tray. Population-based FE analysis will be used to investigate the effect of resection depth on the fixation of a cementless tibial tray (P.F.C.® Sigma®, DePuy® Inc, USA). As per the previous case study, the investigation will focus on the strain and micromotion of the bone-tray interface.

8.2 Methods

As per the previous case study, a large population of tibia and associated gait cycles was generated (section 6.4.1). The population tibiae were implanted with a tibial tray at four different resection levels (RLs), 2 mm, 4.5 mm, 7 mm, and 15 mm below the lowest point of the condyles (section 6.4.3). Each of these population of tibiae are referred to as RL1, RL2, RL3, and RL4 respectively, and RL1 is considered standard surgical procedure. All models were pre-processed for FE as described in section 6.4.4, run as an FE job as described in section 6.4.5, and post-processed as described in section 6.4.6. For further analysis, the CPS and CPM of the resection interface were computed for each model.

The stability of the analysis was checked by computing the median and 95th percentile of the CPS and CPM and then calculating the population median of each metric as an increasing number of models were included. Before analysis, 'extreme outliers' were excluded from the population. 'Extreme outliers' were classified as models with a median CPS greater than ultimate strain, and median CPM greater than 500 µm. In chapter 7, it was found that models classed as 'extreme outliers' had lower bone quality compared to the remaining population. If the bone quality is very bad, then a surgeon might choose an alternative fixation method (e.g. cemented or screws) to achieve better fixation of the tibial tray. The shape and size of the 'extreme outlier' tibiae was similar to the rest of the population. It was also necessary to exclude models from the analysis which had a positive axial force during the gait cycle as this is non-physiological loading.

Metrics based on the CPS and CPM were computed; median CPS, area of CPS above yield strain, median CPM, area of CPM < 50 µm, area of CPM ≥ 50 µm and < 150 µm, and area of CPM > 150 µm. The amount of cortical bone supporting the tibial tray was also computed for all populations. This was taken as the percentage area of the resection interface with a modulus >2500 MPa. The area of the tibial plateau covered by the tibial tray (called area coverage) was also computed as the actual area and the percentage area. Further to this analysis, the interface surface was visualised for selected models to see if there were visual differences in the distribution of the CPS and CPM between the populations.

8.3 Results

In each population the number of models successfully implanted and then analysed were: RL1, 451 (90.2%) implanted, 449 (89.8%) analysed; RL2, 434 (86.8%) implanted, 429 (85.8%) analysed; RL3, 451 (90.2%) implanted, 448 (89.6%) analysed; RL4, 355 (71.0%) implanted,

352 (70.4%) analysed. The main reason the implantation process failed was due to geometric limitations, and FE analysis failed because the solution did not converge. The analysis of the FE results only included 228 out of the initial 500 tibiae. This was the number of models in common between all the populations, after the 58 outliers were excluded. The outliers included those models where the axial load was positive during the gait cycle.

The stability of the analysis was computed for both the CPS and CPM. Stability of the results was judged to be when the population median of the CPS and CPM were relatively constant. It was seen that the population median of the CPS stabilised at about around 150 models (figure 8.2a), and the population median of the median CPM stabilised around 200 models (figure 8.2b).

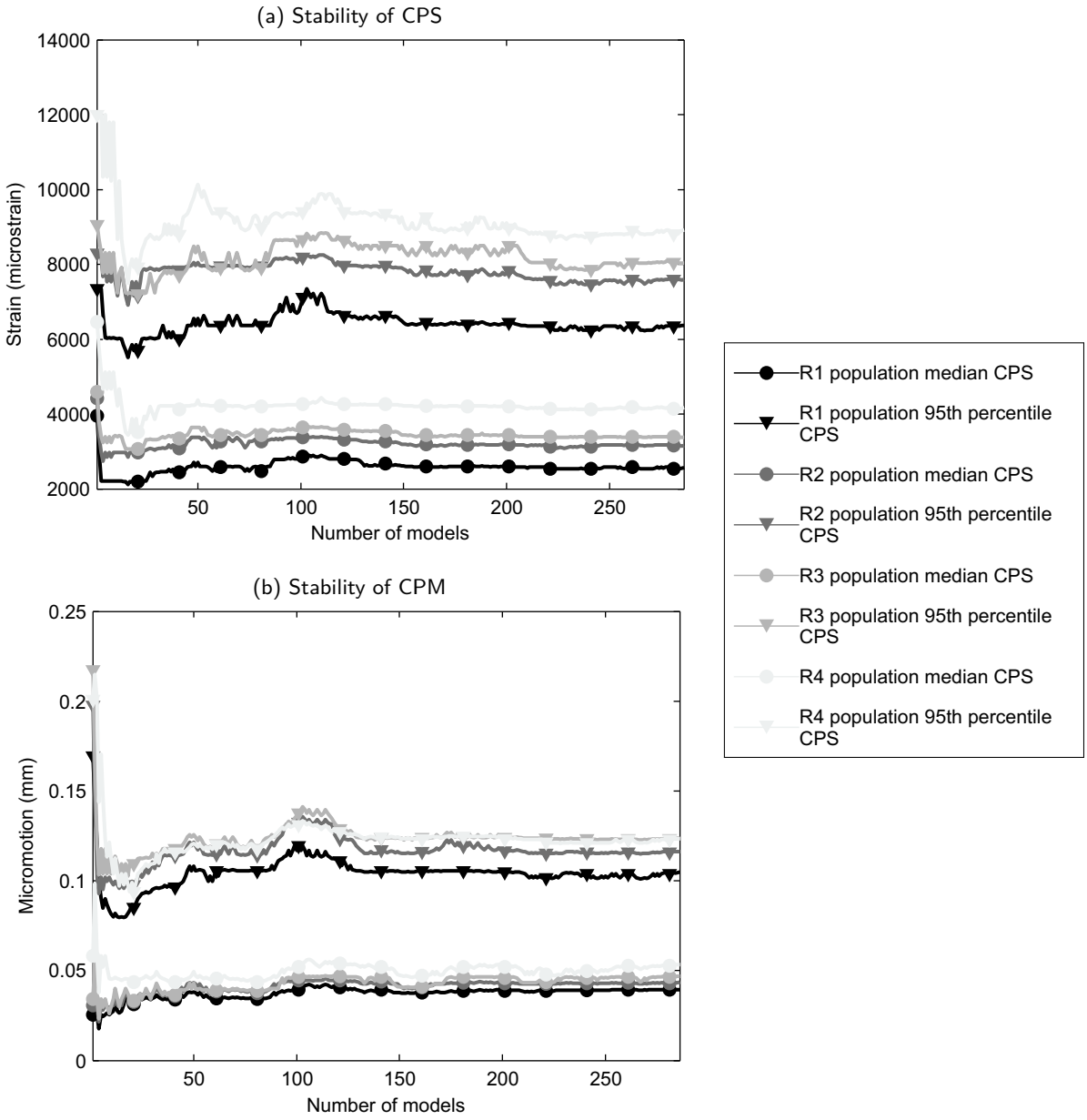

Figure 8.2: Stability of the CPS and CPM for all the populations. The stability is computed as the cumulative median of the median CPS, 95th percentile CPS, median CPM, and 95th percentile CPM.

Comparing the CPS metrics between the resection levels, the population median CPS increases from 2430 microstrain at RL1 to 3920 microstrain at RL4 (figure 8.3 and table 8.1). This is coupled with an increase in the area above yield strain from 2% at RL1 to 8% at RL4 (table 8.1). There is little difference in the micromotion between the resection levels, the median CPM was 35 µm at RL1, 37.5 µm at RL2, 38 µm at RL3, and 40.8 µm at RL4. The area of the resected surface with a CPM < 50 µm decreases by 10% from RL1 to RL4.

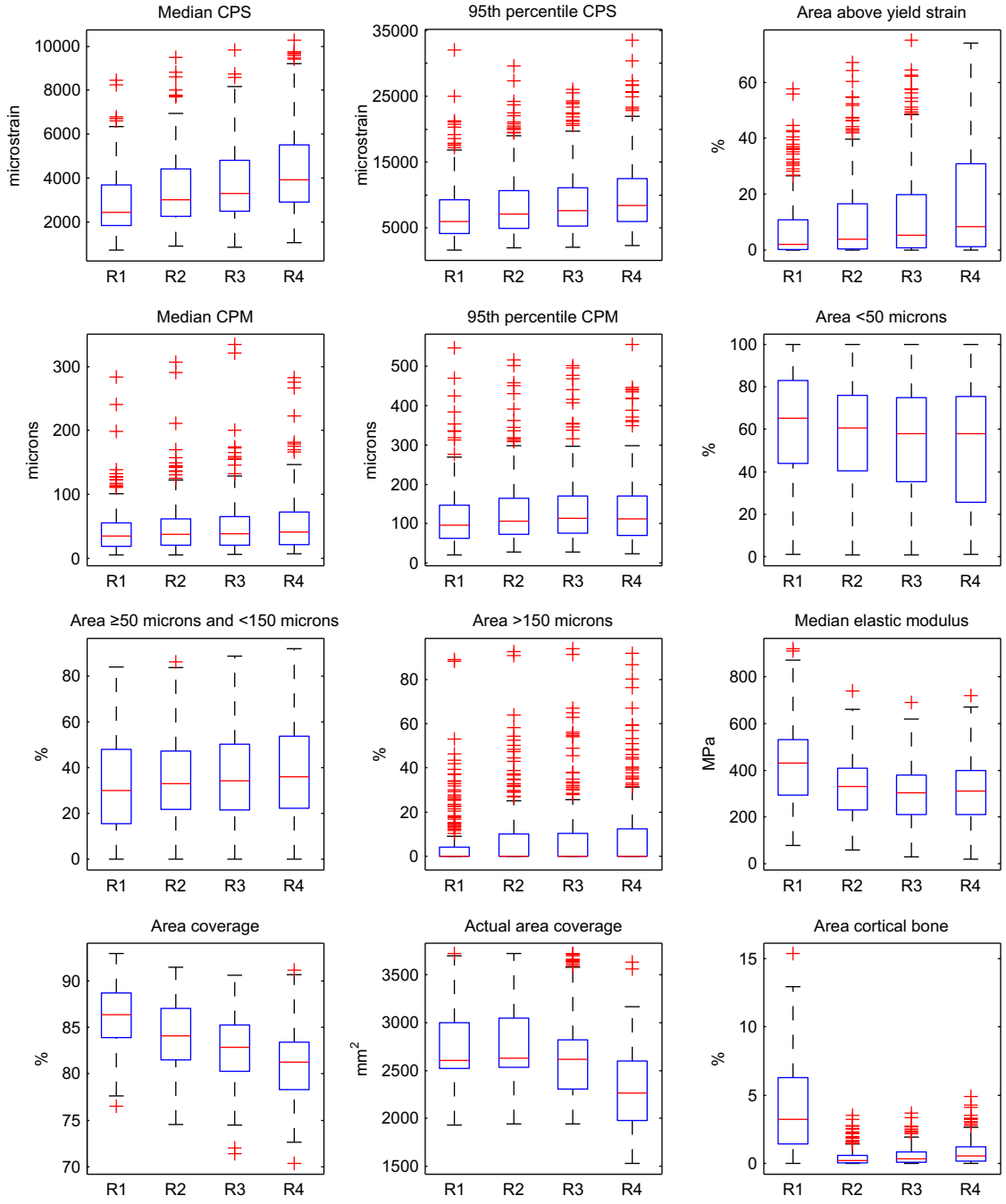

Figure 8.3: Boxplots of the metrics for all populations. On each box, the red line is the median, the lower and upper edges of the box are the 25th and 75th percentiles, the whiskers mark the most extreme data not considered outliers, and the red crosses are the data considered outliers.

Increasing the resection depth reduced the population median elastic modulus of the interface from 430 MPa at RL1 to 310 MPa at RL4, with a reduction of 100 MPa between RL1 and RL2. The change in area of cortical bone does not follow this pattern, from RL1 to RL2 there is a decrease from 3.2% to 0.2%, a small increase of 0.1% at RL3, and a further increase of 0.2% to RL4. Noticeably, the inter-quartile range of area of cortical bone is large at RL1 and significantly reduced at RL2, RL3, and RL4 (figure 8.3). The distribution plot of modulus (figure 8.6) shows that there is an increase in modulus around the periphery of the interface surface at RL4.

The number of size changes of tibial tray between resection levels is shown in figure 8.5. The majority of models do not require a change of tibial tray with the change in resection depth from RL1 to RL2 and RL2 to RL3. The tray was one size smaller for 9 models at RL2 compared to RL1, and 26 models for RL3 compared to RL2. At RL4, the majority of models required a tray one size smaller from RL3, with 37 models requiring a tray two or more sizes smaller.

Visualisation of the CPS through sections of the proximal tibia showed that the distribution of strain was similar at each resection level (figure 8.4). The same model is shown for all resections levels, and it has a median CPS equal to the RL1 population median. At all resection levels, higher strains are found on the medial side of the tibia. A region of high peak strain is found around the distal part of the stem of the implant, as seen in the sagittal and frontal sections (anterior and lateral views respectively). The distal end of the tibial tray stem would likely be located close to the intramedullary canal. This was modelled with very low modulus elements, and under small loads these would generate high strain. The sharp features at the distal end of the stem may also cause increased strain. There is also a region of high peak strain running down the posterior side of the stem of the implant (lateral view). The more distal transverse sections (middle and bottom images), show that the distribution of the strain is similar to the interface (top image), higher strains are found on the medial side, and the peak occurs around the anterior edge and posterior of the tibial tray. Importantly, at all resection levels, in all the transverse sections, the area of the section experiencing different levels of strain (e.g. greater than yield) appears to be approximately equal. This indicates that the resection interface CPS is representative of the strain more distally in the tibia.

Figure 8.6 shows how the CPS, CPM, and modulus change at different resection levels. Each row is a model with a value of the median interface CPS equal to minimum extreme, 25th percentile, median, 75th percentile, maximum extreme, and outlier CPS of the RL1 population (as defined in figure 8.3). For each selected model, the CPS, CPM, and modulus of the resection interface was visualised at each resection level. These are shown in the columns of figure 8.6.

The first four columns are plots of the resection interface CPS at the different resection levels: the first column is RL1, the second column is RL2, the third column is RL3, and the fourth column is RL4. At RL1, the distribution of the CPS is similar for all models, regions of high strain are found around the anterior periphery of the interface, and for models with a higher median CPS strain (e.g. 'maximum extreme' model) on the lateral side of the interface. As

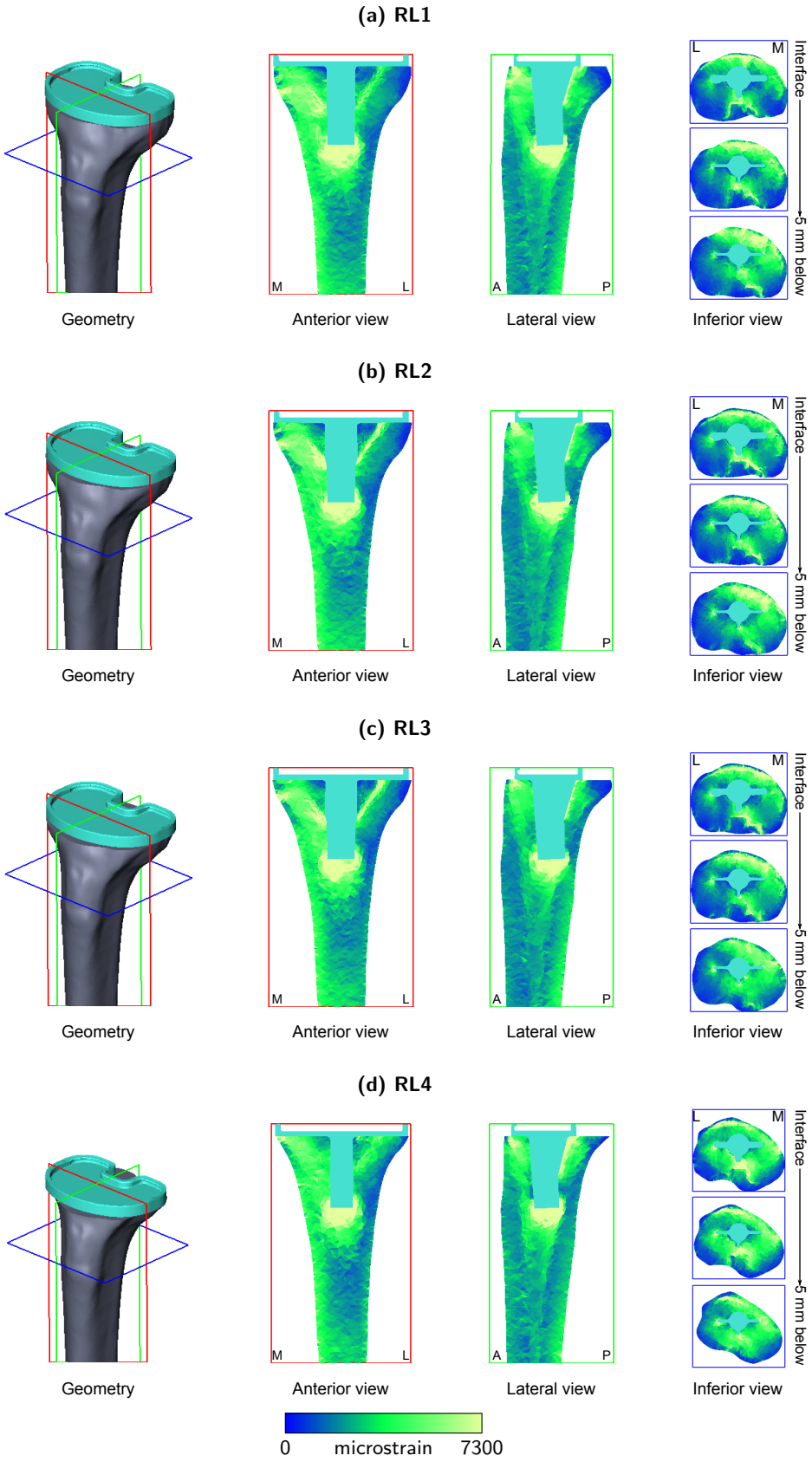

Figure 8.4: CPS visualised in sections of the proximal tibia. The model shown has the median value of resection interface median CPS in the RL1 population. The views from left to right are: the geometry with the view planes shown, frontal section (anterior view), sagittal section (lateral view), and three transverse sections (inferior view). The top transverse section is the resection interface, the middle is 2 mm below the interface, and the bottom is 5 mm below the interface.

the resection depth is increased from RL1 to RL4, the CPS of the interface increases; the area of bone with a strain greater than yield (shown by the lighter colours) becomes larger. The distribution of the CPS also changes, regions of high strain spread to the medial side of the interface.

The next four columns are the CPM of the resection interface at RL1 (fifth column) to RL4 (eighth column). The distribution of the CPM is similar at all resection levels. With the exception of the 'outlier' model (last row), peak micromotions are found towards the periphery of the resection interface. As the resection level decreases, the area of the resection interface experiencing higher micromotion (e.g. between 50 µm and 150 µm as indicated by the green/light green colour) increases. This can be seen for the 'median' model (third row), where at RL1 there are lower micromotions on the lateral side compared to RL4.

In the last group of four columns, the modulus of the resection interface is visualised. Again, the four resection levels of the selected models are shown from RL1 (ninth column) to RL4 (twelfth column). At RL1, the strongest bone of the interface surface is found on the medial side of the interface. As a deeper resection is made, the strength of the medial bone reduces. This change in modulus is seen for all models. The decrease in modulus on the medial side from RL1 to RL4 corresponds to an increase in strain. As found in chapter 7, models with a high median CPS have a low interface modulus.

It was also found that the peak strain and micromotion occurred at different times during the gait cycle. For the RL1 population, the peak CPS occurred earlier, at approximately 54% gait, and the peak CPM occurred later at 62% gait. This was inline with the findings from chapter 7.

Table 8.1: Summary of metrics for each resection level.

	RL1			RL2			RL3			RL4		
Metric	**Min**	**Median**	**Max**	**Min**	**Median**	**Max**	**Min**	**Median**	**Max**	**Min**	**Median**	**Max**
Median CPS (microstrain)	706.2	2432.8	8456.2	880.3	2991.5	9487.8	833.0	3301.3	9836.2	1056.5	3917.8	10 280.5
95th percentile CPS (microstrain)	1625.2	5975.2	32 017.1	1978.7	7075.4	29 614.7	2076.6	7593.5	26 064.1	2348.4	8388.6	33 529.7
Area above yield strain (%)	0.0	2.1	57.6	0.0	3.9	67.1	0.0	5.3	75.1	0.0	8.3	74.1
Median CPM (µm)	5.2	35.0	283.9	5.6	37.5	306.5	6.5	38.0	334.7	7.0	40.8	282.3
Area < 50 µm (%)	1.0	65.2	100.0	0.8	60.6	100.0	0.9	57.9	100.0	1.1	58.0	100.0
Area ≥ 50 µm and < 150 µm (%)	0.0	30.0	84.1	0.0	32.9	86.4	0.0	34.3	88.8	0.0	36.1	92.1
Area > 150 µm (%)	0.0	0.0	89.0	0.0	0.0	92.5	0.0	0.0	93.9	0.0	0.0	91.8
Median elastic modulus (MPa)	80.0	430.0	920.0	60.0	330.0	740.0	30.0	305.0	690.0	20.0	310.0	720.0
Area coverage (%)	76.5	86.3	93.0	74.6	84.1	91.5	71.4	82.9	90.6	70.4	81.3	91.2
Actual area coverage (mm^2)	1929.7	2606.1	3723.9	1938.8	2628.0	3724.0	1943.8	2618.9	3722.8	1527.4	2262.5	3635.9
Area cortical bone (%)	0.0	3.2	15.4	0.0	0.2	3.5	0.0	0.3	3.7	0.0	0.5	4.9

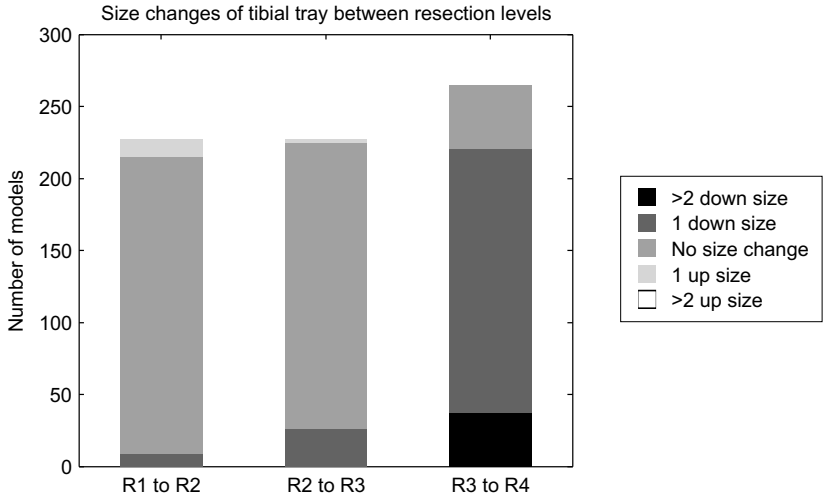

Figure 8.5: The number of tibial tray size changes each time the resection depth increased.

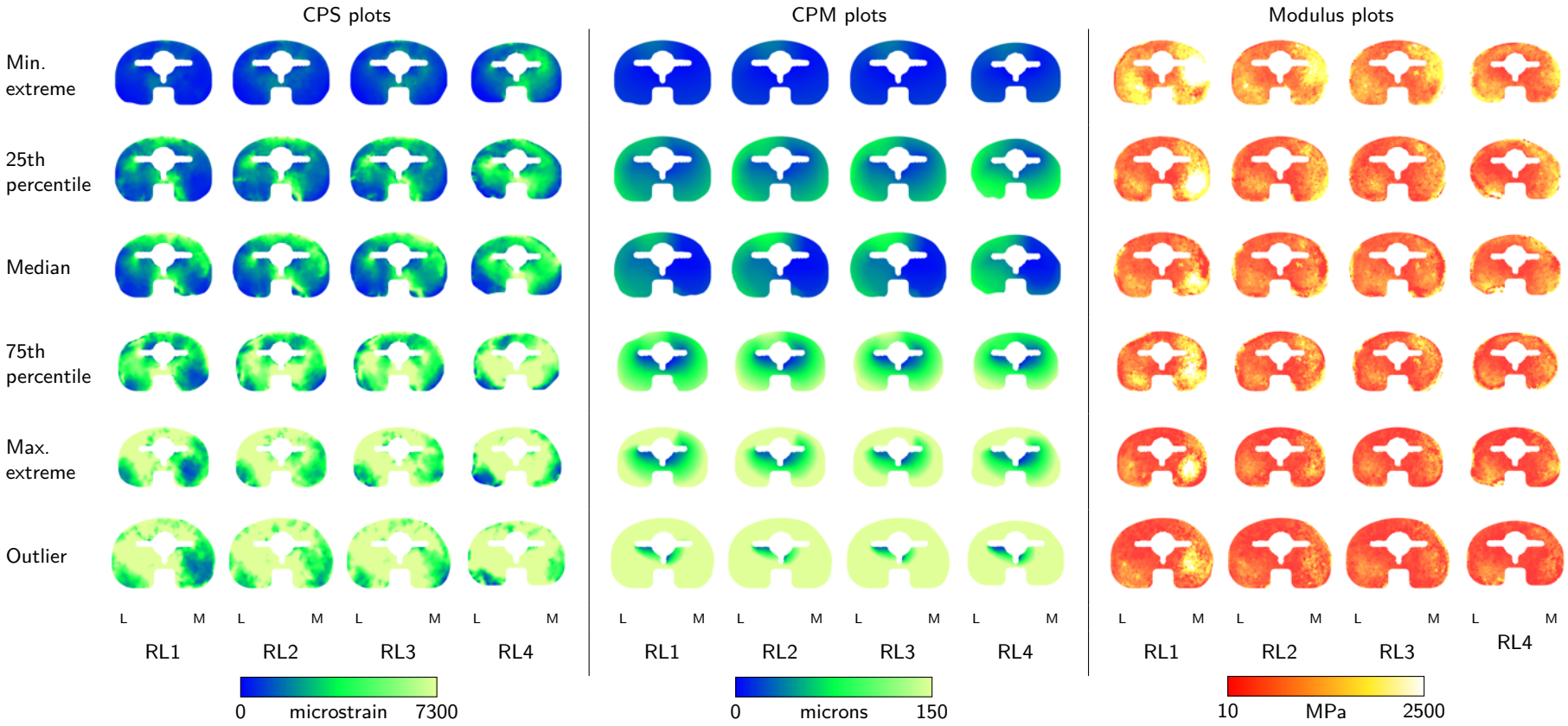

Figure 8.6: Visualisation of the resection interface CPS, CPM, and modulus of at each resection level. Each row is of the same model, chosen based on the value of the median CPS. The models shown have the minimum extreme, 25th percentile, median, 75th percentile, maximum extreme, and outlier values of the median CPS of the RL1 population. The columns show the CPS, CPM, and modulus of the resection interface at different resection levels, RL1 to RL4.

8.4 Discussion

In this study the effect of resection level on the primary stability of the tibial tray was examined using a large population of models. As per the previous case study (chapter 7), to check the stability of the system, the population median CPS and CPM were computed with an increasing number of models (figure 8.2). For all populations, both the median CPS and CPM had stabilised when approximately 150 models were included. At RL1 the population median CPS was lowest. This is expected because the resection interface modulus at RL1 is 100 MPa greater than other resection levels. This is consistent with the findings of chapter 7 where the lowest strain was found in models with the highest modulus. Between RL1 and RL2, the difference in median CPS is 500 microstrain and there is also a decrease the interface modulus. However, the difference in median CPS between RL3 and RL4 is 600 microstrain but there is no change in the median modulus (table 8.1).

From RL3 to RL4, a large proportion of models required the tray to be at least one size smaller (figure 8.5). Although this is due to the change in geometry of the resected surface, the tray coverage of the resected surface also reduced from 86% at RL1 to 81% at RL4. In terms of actual area, at RL1, RL2, and RL3, the median area of coverage was around 2600 mm^2, and at RL4 this reduces to 2260 mm^2. With an increase in the resection depth there is a decrease in the area of supporting cortical bone. From RL2 downwards, less than 1% of the supporting bone is classified as cortical. It is hypothesised that the increase in strain when the resection depth changes from RL1 to RL2 is due to the decrease in modulus of the resection interface. However, the increase in strain when the resection depth changes from RL3 to RL4 is likely because the majority of tibial trays were down sized by at least one size (figure 8.5). A smaller size of tibial tray carrying the same loads over a smaller area would lead to an increase in the strain.

The distribution of the CPS changes as the resection depth increases; there is an increase in strain in the medial and lateral regions of the interface (figure 8.6). Berend et al. (2010) also found that a more distal resection increased the strain in the proximal tibia, but direct comparison was not possible because only cortical shear strains were reported. The percentage area with a strain above yield strain also increases with resection depth.

There was an increase in the median CPM at more distal resection levels. The highest micromotion was found at RL4, with a median CPM of 40.8 µm (min. 7.0 µm and max. 282.3 µm), close to the fibrous tissue threshold. It is thought that this is also due to the reduction in tray size. As the micromotion occurs when there are moderate moments and low axial force, the shorter moment arms about the centre of the tray would likely cause a greater rotation of a smaller tibial tray. A greater rotation of the tibial tray would mean that a larger proportion of the interface would experience a larger resultant micromotion. At RL1, the median of the interface area with CPM < 50 µm was 65.2%, which decreased to 58% at RL4 (table 8.1). However, the median of the interface area with CPM > 50 µm and < 150 µm increased from 30% at RL1 to 36.1% at RL4 (table 8.1).

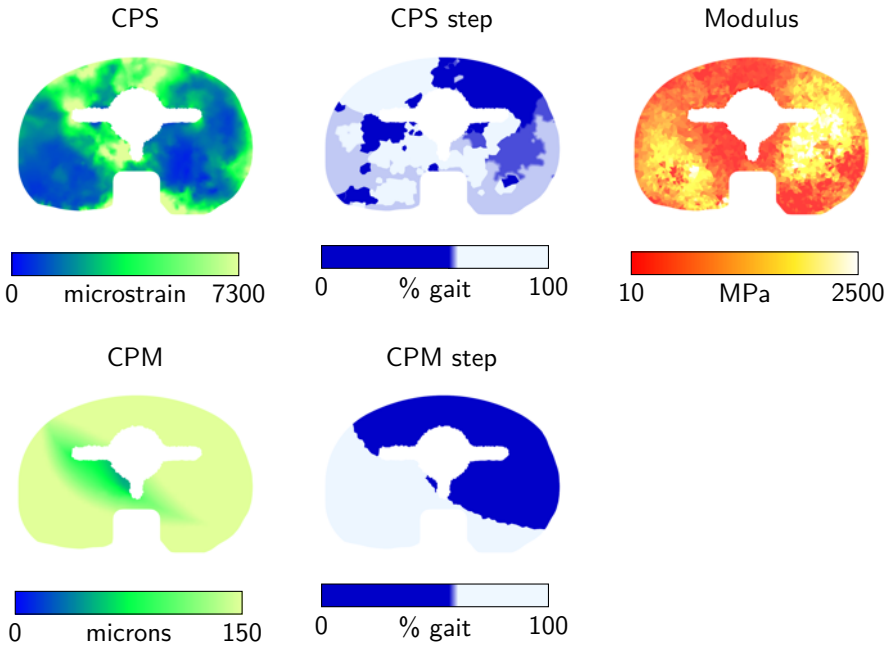

Figure 8.7: Plots of the resection interface CPS, 'CPS percent gait', CPM, 'CPM percent gait', and modulus of an excluded model which experienced a positive axial force during the gait cycle.

The pattern of change in resection interface modulus with resection depth matches the *in vivo* patterns found by Goldstein et al. (1983) and Hvid et al. (1986). The bone on the medial side was strongest, particularly in more proximal locations (e.g. at RL1 in figure 8.6). There was a greater reduction in strength on the medial side from RL1 to RL4 compared to the lateral side, as Hvid et al. (1986) observed, and stronger bone is found around the periphery at more distal resection levels. The similarity in the pattern of modulus shows that the population of models sampled from the SM are representative of real tibiae. However, the magnitude of the modulus differs. For example, at RL1, there are regions of modulus exceeding 2500 MPa. This is an order of magnitude higher than the modulus of the most proximal resection reported by Goldstein et al. (1983). In this case study, RL1 could be more proximal as it was taken just below the condyles and stronger cortical bone could be exposed. Inaccuracy of the density-modulus relationship used, and inaccuracy in the modulus estimation from the statistical model could also be a cause of the difference in modulus.

It was only briefly discussed in chapter 7 the reason why models with a positive axial force were excluded from the analysis. The reason given was because a positive AX force acts upwards to pull the tray out of the bone. Physiologically this would not occur. In models with a positive axial force, most of the resection interface experienced a peak micromotion $> 150\,\mu m$, and the load step at which this occurred correlated with the point in the gait cycle at which a positive axial force occurred. Shown in figure 8.7 is an excluded model from the RL1 population which experienced a positive axial force. The median modulus of the resection interface was 520 MPa, greater than the median of the population. The median CPS was 2450 microstrain, again around the median of the population, and the distribution of the CPS is comparable to the 'median' model shown in figure 8.6. However, 74% of the resection interface of the model experiences a peak micromotion $> 150\,\mu m$ and the CPM occurs at either 2%

or 72% gait. Examining the gait cycle loads, at 2% gait, there is a positive axial load, and hence the tibial tray is pulled upwards breaking the contact between the tray and bone. At 72% gait, the axial load is low (0.5 BW), and there is a varus moment acting. This means that there is a large axial load on the medial side and a low axial load on the lateral side. Hence, at the anteromedial of the tray experiences high micromotion early in the gait cycle and the posterolateral of the tray experiences high micromotion during swing phase. This skews the CPM of the interface (median of 174 µm) and therefore it was considered necessary to exclude these models from the analyses.

8.5 Conclusions

This case study has shown the effect of changing the resection level on the primary stability of the tibial tray. By making a more distal resection, both the peak strain and micromotion increased but the reason for these changes depend on the depth of resection. From RL1 to RL2 there was a significant decrease in modulus, coupled with a decrease in the area of supporting cortical bone, causing an increase in strain. From RL3 to RL4 there was also an increase in the strain, despite only a small change in modulus and area of supporting cortical bone. The cause of this was thought to be due to the tray after being down sized to fit the tibial plateau at RL4, meaning the loads were transferred across a smaller area. It was also hypothesised that by down sizing the tray, the moments caused an increase in the peak micromotion. In conclusion, the decrease in the bone quality of the interface, coupled with the increase in strain and micromotion at more distal resection levels, suggests that a minimal resection should be taken to obtain the good primary stability.

Chapter 9

Comparison of three tibial tray designs

9.1 Introduction

There are a large number of TKR designs on the market today for a surgeon to choose from, each advertised with features designed to improve the outcome for the patient. More often than not, a surgeon will use an implant they have clinical experience with, to provide the best possible treatment for the patient. Many of the TKR designs share common features. They invariably consist of four components, a metal tibial tray, a polyethylene tibial insert, a metal femoral component, and a patella resurfacing (see section 2.2.2). There are variations in the size and shape of the components dependent on the type of TKR, fixed bearing or mobile bearing, PCL retaining or PCL resecting.

Another aspect to consider for a TKR is the fixation technique, whether it is cemented or cementless. There are mixed reports about the survivorship of cemented and cementless TKRs. Some report less than 75% survivorship of cementless implants (e.g. Duffy et al., 1998), but more recent studies report greater than 95% survivorship (e.g. Baker et al., 2007; Cossetto et al., 2010). Discussed in section 2.2.2, was the use of cementless fixation, particularly for younger more active patients, as it is thought to provide long-term fixation without the problems associated with cement degradation. To achieve successful long-term fixation of a cementless TKR, osseointegration is necessary. Micromotion at the bone-implant interface has been seen to inhibit bone ingrowth, above 150 µm and fibrous tissue can form (Jasty et al., 1997; Pilliar et al., 1986). There is evidence of a correlation between the initial stability and migration of the tray of the tibial tray (Fukuoka et al., 2000). Measurements of the tray 'micromovement' were made during a TKR procedure using sensors attached to the tibial cortex. Patients were then followed-up for two years, and using RSA the migration of the tray was measured. Clinical studies have also found a link between early migration and late aseptic loosing (Grewal et al., 1992; Ryd et al., 1995), and therefore long-term stability of the tibial tray has been linked to initial fixation.

In post-operative radiographic assessment, the presence of radiolucent lines (RLLs) at the bone-tray interface can indicate poor fixation. A RLL represents a gap between the tray and surrounding bone, perhaps due to imperfect cuts of the tibial plateau (Aebli et al., 2004), or micromotion at the bone-tray interface (Fuiko et al., 2003). Reports of radiolucencies are more commonly associated with cementless fixation and vary widely for different TKRs. Despite reports of high incidences of RLLs for a particular tibial tray (Aebli et al., 2004; Fuiko et al., 2003), most were non-progressive and did not affect fixation. However, as Taylor et al. (2012) notes, the presence of RLLs is an indication that the conditions for fixation are not optimal.

To improve the primary stability of the tibial tray, pegs and keels can be added to provide additional stability. Few computational studies have investigated the effect that such features have on primary stability. Hashemi et al. (2000) investigated two designs of the Howmedica porous coated anatomic tibial tray fixed, one fixed using three screws, and one fixed using a single anterior screw and two posterior pegs. Micromotion and lift-off were reduced when the three screw design was used. Au et al. (2005) looked at the effect the shape of the stem and addition of pegs had on the bone stress for a cemented tibial tray. A tapered stem was found to reduce the overall stress and compressive stress at the base. Pegs also helped to reduce the stress around the central stem. Stability of the tibial tray can also be improved by extending the length of the stem (Albrektsson et al., 1990; Lee et al., 1991; Stern et al., 1997; Yoshii et al., 1992) and is often necessary in cases where bone quality is poor (Rawlinson et al., 2005).

In experimental tests, Walker et al. (1981) tested twelve designs of a generic tibial tray made of both metal and plastic implanted in foam. The relative deflections were measured under three loading conditions: (i) an axial force with anterior-posterior force, (ii) an axial force with internal-external rotation moment, and (iii) an axial force with a varus-valgus moment. Based on the combined relative displacements of all three load cases, the metal trays with either a single post or two pegs generated the least displacement.

Taylor et al. (2012) compared three commercially available tibial trays (P.F.C.® Sigma®, LCS® Complete™ MBT, and LCS® Complete™ Duofix®, all DePuy® Inc, USA) in a single patient model simulating five ADLs. The implant designs were ranked by the magnitude of micromotion and the rank order was found to be similar to the reported incidence of RLLs in survivorship studies. The Duofix tray generated the lowest micromotion and is reported to have a low incidence of RLLs (6%, Cossetto et al., 2010). The PFC Sigma had higher micromotion than the Duofix and literature reports the incidence of RLLs—for tibial trays where the RLLs were cause for concern—to be 16% (Khaw et al., 2002) and 28% (Duffy et al., 1998). The micromotion of the LCS was highest and a high incidence of RLLs is reported (>90%, Aebli et al., 2004; Fuiko et al., 2003). A similar rank order is found in joint register data, from the National Joint Registry for England and Wales (2011), the PFC Sigma has a lower revision rate than the LCS, 1.08% and 1.76% respectively. The limitation of this comparison is that the joint register data includes all cemented and cementless trays, and all variations of the implant designs.

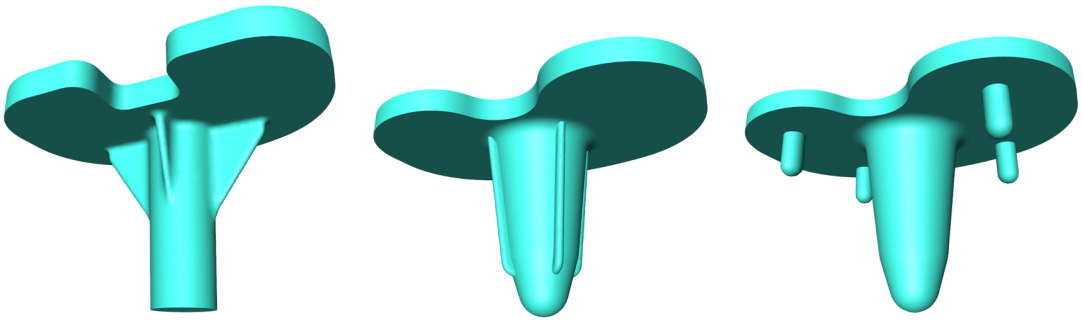

(a) PFC Sigma (b) LCS (c) Duofix

Figure 9.1: The base features of the three tibial trays.

The three trays have different stem designs which likely affect the generated micromotion. The stem of the LCS is conical, with four small flanges running down the post. The PFC Sigma has three flanges (medial, lateral, and posterior) extending from mid-way down the stem to the base of the tray. The Duofix stem has no additional keels or flanges, but has four short peripheral pegs. Because peak micromotion has been found at the beginning of swing phase (Taylor et al., 2012, chapter 7), when there is a low axial load and moderate moments, the addition of the flanges and pegs are likely to provide better resistance to the moments, enhancing the stability of the tray. Further to this, Taylor et al. (2012) suggests that as the four pegs on the Duofix tray are likely to be located in stronger cancellous bone, they provide better support and resistance to the moments.

The aim of this study is to evaluate three tibial tray designs, comparing mechanical response of each design in a population. The tibial tray designs to be compared are the P.F.C.® Sigma®, LCS® Complete™ MBT, and LCS® Complete™ Duofix® (all DePuy® Inc, USA), referred to as PFC Sigma, LCS, and Duofix respectively. In contrast to Taylor et al. (2012), the three tray designs are tested in a large population, accounting for variation of tibia shape and modulus, and loading. By using a large population, it can be seen how sensitive each implant design is to population variation.

9.2 Methods

The method for this case study follows that of chapters 7 and 8. A large population of tibiae and associated gait cycles were generated from two separate SMs (see section 6.4.1). The population of tibiae were each implanted with the three commercially available tibial trays the PFC Sigma, LCS, and Duofix. The sizing, positioning, and implantation, of the trays was done as described in section 6.4.3. For FE analysis, all the models were processed as described in sections 6.4.4 and 6.4.5. In the post-processing of the FE results, as described in section 6.4.6, the strain and micromotion were computed for each step in the load cycle and from this the CPS and CPM were computed. The point in the gait cycle at which the CPS and CPM occurred for each element was also recorded, termed the ‘CPS percent gait’ and ‘CPM percent gait’ respectively.

As in the previous case studies, the stability of the analysis was checked by computing the population median of the median and 95th percentile CPS with an increasing number of models. The same was done using the median and 95th percentile CPM. Before analysis of the FE results, the common models in each population were identified. 'Extreme outliers', classified as models with a median CPS greater than ultimate strain (11 000 microstrain), and median CPM greater than 500 microns, were then excluded from the analysis. These limits were chosen for reasons given in chapter 7, where it was found that the 'extreme outlier' generally had a very low modulus compared to the population. This could mean that the surgeon may choose an alternative fixation method (e.g. cemented) to ensure good primary fixation of the tibial tray. Further to excluding models considered 'extreme outliers', it was also necessary to exclude models found to have a positive AX force at any point in the load cycle as this is a non-physiological load.

To compare the populations, only the resection interface between the bone and tibial tray, excluding the stem of the tibial tray was considered. For this region of bone, metrics based on the CPS and CPM were computed: median CPS, area of CPS above yield strain, area of CPM $< 50\,\mu m$, area of CPM $\geq 50\,\mu m$ and $< 150\,\mu m$, and area of CPM $> 150\,\mu m$. The median elastic modulus, area of coverage, actual area coverage, and area of cortical bone of the interface surface were also computed.

The resection interface CPS, 'CPS percent gait', CPM, and 'CPM percent gait' were also visualised to see the variation in the distribution of the peak strain and micromotion. From each population, only the models the population minimum extreme, 25th percentile, median, 75th percentile, maximum extreme, and outlier value of median CPS were visualised.

9.3 Results

For each tray design the number of models successfully implanted and then analysed were: PFC Sigma, 451 (90.2%) implanted, 449 (89.8%) analysed; LCS, 421 (84.2%) implanted and analysed; Duofix 418 (83.6%) implanted, 417 (83.4%) analysed. Errors due to geometric artefacts were the main cause of models failing during the implantation process, and convergence problems were the main cause of models failing during FE analysis. Of the initial 500 tibiae only 300 models were included in the analysis, the number of models in common between all the populations, excluding 67 outliers. The outliers included 48 models for which the AX force was positive at a point the gait cycle. As found in the previous case studies, the 'extreme outliers' did not differ from the population in terms of shape or size of the tibia, but did generally have a lower bone strength.

In determining the stability of the CPS and CPM, all the models were included. For all populations, the population median CPS stabilised when approximately 250 models were included (figure 9.2). Similarly, the population median CPM stabilised at approximately 250 models (figure 9.2). Therefore, a sufficient number of models were included in the analysis.

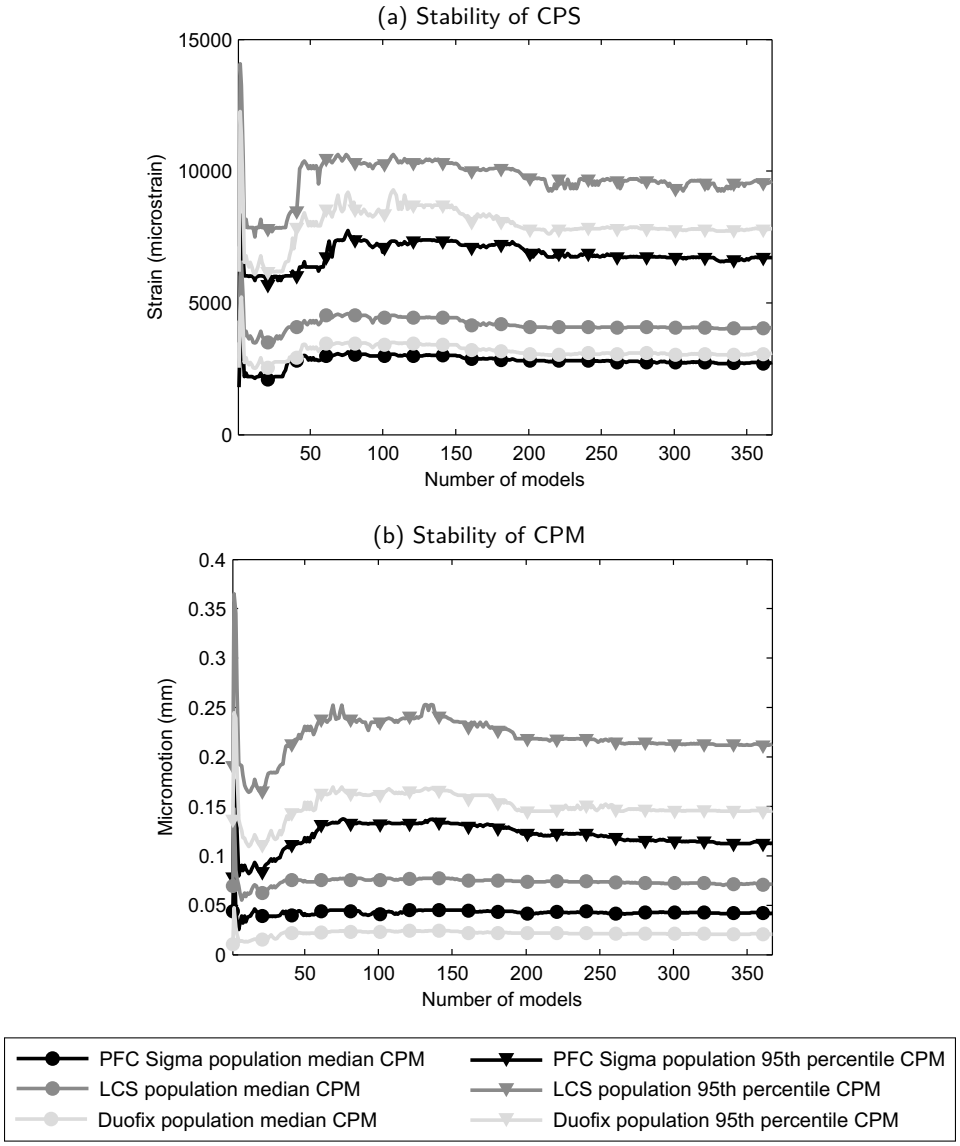

Figure 9.2: Stability of the CPS and CPM for all the populations. The stability is computed as the cumulative median of the median CPS, 95th percentile CPM, median CPM, and 95th percentile CPS.

Of the three tray designs, the PFC Sigma had the lowest peak strains (population median CPS 2560 microstrain) and the smallest area greater than yield strain (population median 2.6%). The LCS tray had the highest peak strains (population median CPS 3920 microstrain) and the largest area greater than yield strain (population median 10.7%) (table 9.1). The inter-quartile range of the area greater than yield strain was also wider for the LCS tray (figure 9.3).

The Duofix tray generated the least micromotion, having the lowest population median CPM (16.8 µm) and largest area of CPM < 50 µm (75%). Again, the LCS generated the largest micromotion, with a population median CPM of 60 µm and area of CPM < 50 µm of 46% (table 9.1). It also had the largest CPM area > 150 µm of 17%. It is notable that the inter-quartile range of the micromotion metrics for Duofix is often smaller than the PFC Sigma and LCS (figure 9.3). For all three trays, the elastic modulus, coverage, and area of cortical bone was comparable and all had a similar inter-quartile range (figure 9.3).

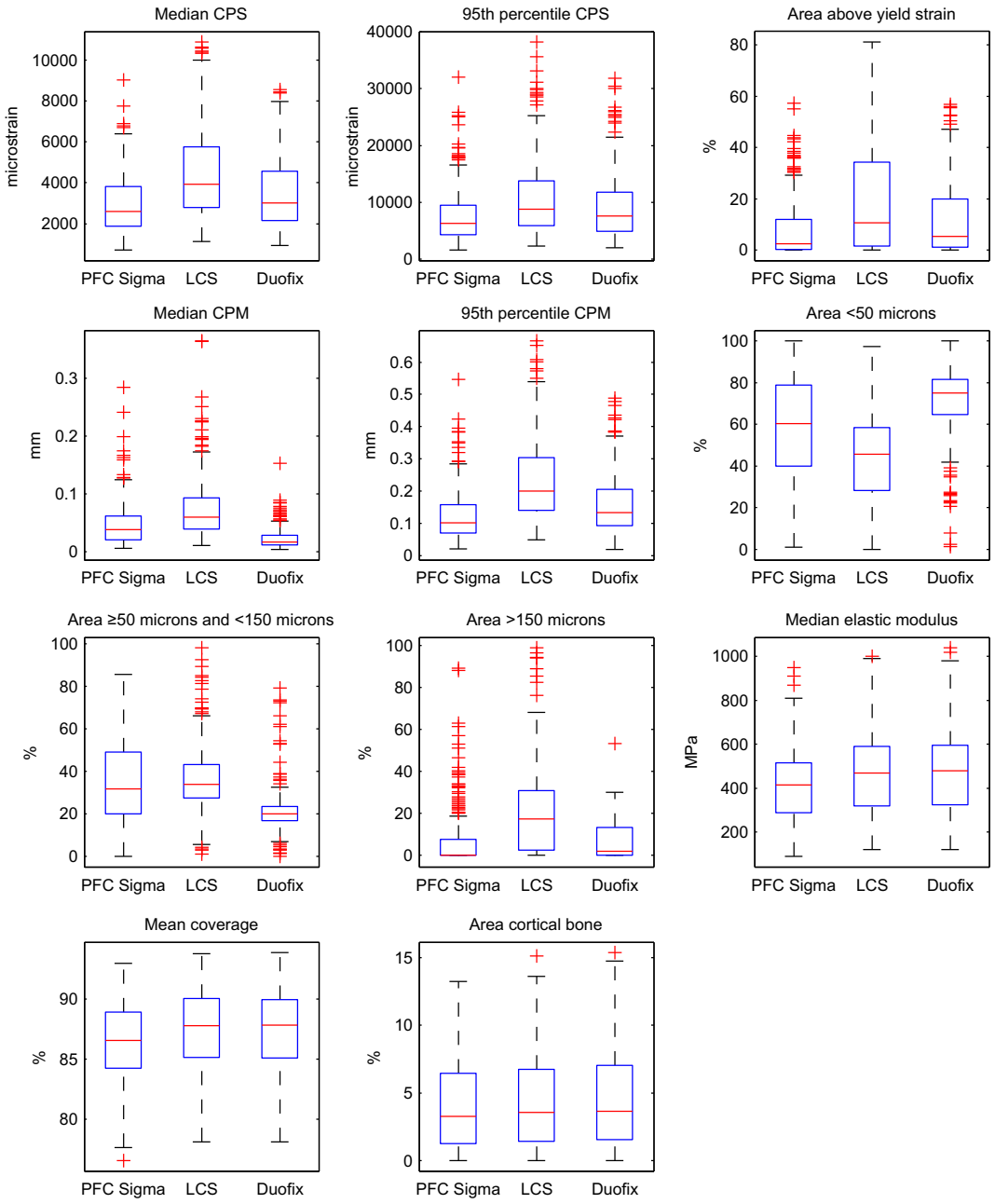

Figure 9.3: Boxplots of the metrics for all populations. On each box, the red line is the median, the lower and upper edges of the box are the 25th and 75th percentiles, the whiskers mark the most extreme data not considered outliers, and the red crosses are the data considered outliers.

The CPS in the proximal tibia for an example model from each population is shown in figure 9.4. The models have a the median CPS value for the respective populations. The top transverse section shows the CPS of the interface surface. The second section is 15 mm below the interface and higher strains around the post can be seen, likely because the bone is softer. In the shaft of the tibia, the magnitude of the strain reduces as the load is transferred through stronger cortical bone. The same pattern is seen for all the models.

Visualisation of the CPS, 'CPS percent gait', CPM, and 'CPM percent gait' of the interface surface for each of the populations is shown in figure 9.5. The top row shows the CPM plots from Taylor et al. (2012) for the three tray designs. The remaining rows of the show the

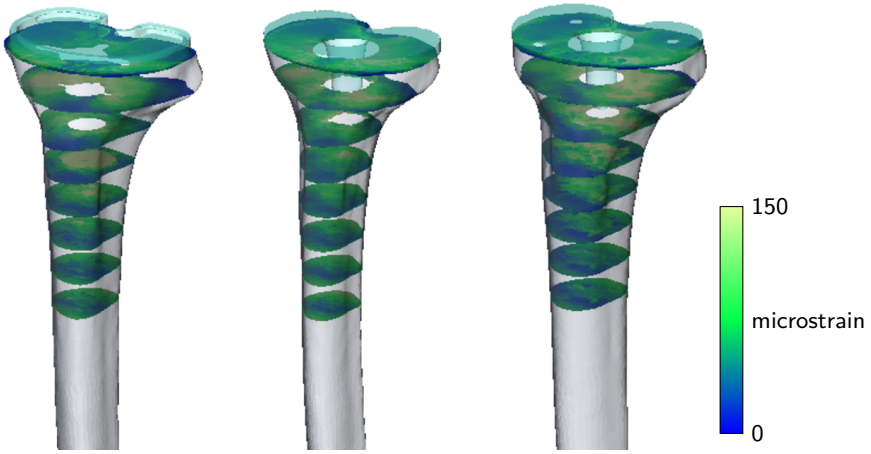

(a) PFC (b) LCS (c) Duofix

Figure 9.4: Peak strain in transverse sections of the proximal tibia for each population. The shown models have a median CPS value equal to the respective population median.

results from this study. Each column are the models from the specified population (PFC Sigma, LCS, or Duofix), and these are grouped by metric (CPS, 'CPS percent gait', CPM, and 'CPM percent gait'). From top to bottom, the rows are the model which had the population minimum extreme, 25th percentile, median, 75th percentile, and maximum extreme values of median CPS. This means that, for each of the metrics the same model is shown for each of the populations. For example, in the first, fourth, seventh, and tenth columns of the second row, the resection interface CPS, 'CPS percent gait', CPM, and 'CPM percent gait' are visualised for the same model from the PFC Sigma population. The resection interface of this model has a median CPS equal to the population 25th percentile of the PFC Sigma population.

From figure 9.5, it is seen that the CPS distribution of the interface surface (columns 1–3) is similar for all three trays. Higher strains are found on the lateral side in the region of weaker bone and around the stem of the tray. For the Duofix tray (column 3), concentrated strains occur around the pegs, particularly on the anterior side. This more apparent in the 'minimum extreme', '25th percentile', and 'median' models (rows 1–3). The CPM plots of the interface surface (columns 7–9) show that the peak micromotion generally occurs on the anterior edge of the tray, particularly in models experiencing lower strain (rows 1–3). For the PFC Sigma and LCS models experiencing higher strain (columns 7 & 8, rows 4 & 5), the micromotion increases in lateral region, whereas for Duofix (column 9, rows 4 & 5), the micromotion increases in the anterior region.

Also shown in figure 9.5 is the 'CPS percent gait' and 'CPM percent gait' of the resection interface for each population (columns 4–6 and columns 10–12 respectively). The peak strain tends to occur earlier in the gait cycle than the peak micromotion. The median load step for CPS is 52% gait, 54% gait, and 52% gait for PFC Sigma, LCS, and Duofix respectively, all towards the end of stance phase. The median load step for CPM is 60% gait, 58% gait, and 56% gait for the PFC Sigma, LCS, and Duofix respectively, all approximately the beginning of swing phase.

Table 9.1: Summary of metrics for each tray design.

	PFC Sigma			LCS			Duofix		
Metric	**Min**	**Median**	**Max**	**Min**	**Median**	**Max**	**Min**	**Median**	**Max**
Median CPS (microstrain)	706.2	2599.8	9042.6	1132.6	3918.9	10 895.9	945.2	3003.5	8555.9
95th percentile CPS (microstrain)	1625.2	6304.9	32 017.1	2318.2	8841.0	38 196.2	2059.8	7583.1	31 760.1
Area above yield strain (%)	0.0	2.6	57.3	0.0	10.7	81.2	0.0	5.4	57.0
Median CPM (microns)	5.2	37.7	283.9	10.7	59.8	364.5	3.6	16.8	152.6
Area <50 microns (%)	1.0	60.4	100.0	0.0	45.7	97.1	1.4	74.9	100.0
Area $\geq$ 50 microns and <150 microns (%)	0.0	31.8	85.8	1.1	33.9	98.3	0.0	20.1	79.3
Area >150 microns (%)	0.0	0.0	89.0	0.0	17.1	98.9	0.0	1.7	53.2
Median elastic modulus (MPa)	90.0	415.0	950.0	120.0	470.0	1000.0	120.0	480.0	1040.0
Mean coverage (%)	76.5	86.6	93.0	78.1	87.8	93.8	78.1	87.8	93.9
Area cortical bone (%)	0.0	3.3	13.2	0.0	3.6	15.1	0.0	3.7	15.4

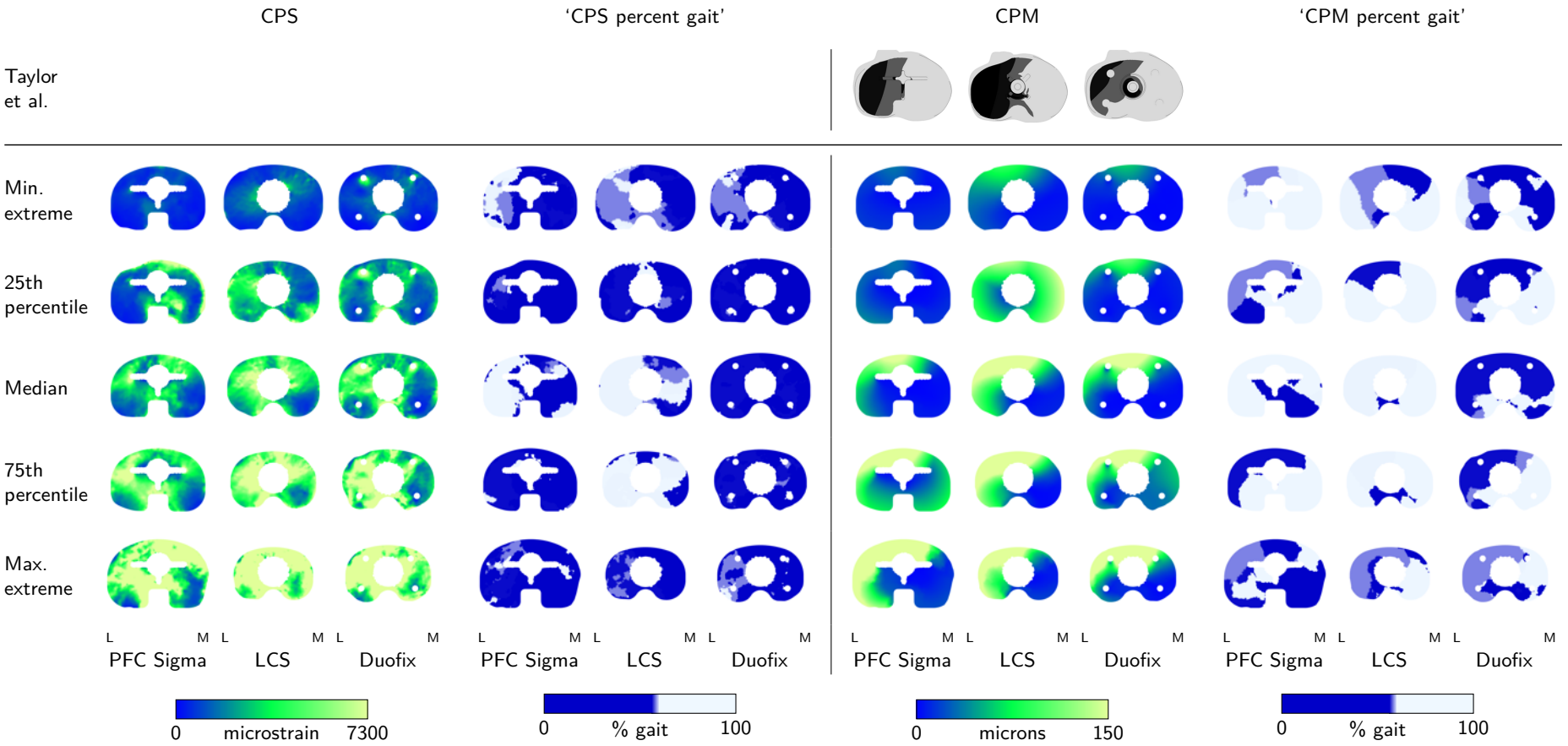

Figure 9.5: Visualisation of the resection interface CPS, 'CPS percent gait', CPM, and 'CPM percent gait' for selected models from each population. Each column are the selected model from a population, grouped by the metrics. The selected models from each population were chosen based on the value of the median CPS. The values of the median CPS used were minimum extreme, 25th percentile, median, 75th percentile, and maximum extreme (top to bottom) of the respective population. The CPM plots from Taylor et al. (2012) are shown for comparison.

9.4 Discussion

This case study demonstrates the use of a population-based analysis of three different tibial tray designs in order to compare the rank order of the designs. Again, the use of SMs allowed the generation of a population of 500 models that were automatically implanted with three different tibial tray designs. From the initial population of each tray design, models were excluded if the implantation process failed, FE analysis failed, the model was considered an 'extreme outlier', or the model experienced a positive AX force. This left only 300 models in common between the populations which were used in the analysis. The stability analysis using all possible models, showed that the population median CPS and CPM for all tray designs stabilised when 250 models were used. It was considered, that despite excluding a large number of models from the analysis, 300 models were sufficient and the remaining 'outliers' would not skew the population metrics.

Taylor et al. (2012) investigated the primary stability of the same three tray designs as used in this study, reporting the CPM and associated metrics. The rank order of the implants in terms of micromotion is the same between this study and Taylor et al. (2012), Duofix generated the least micromotion and LCS the most. Although only a model of a single patient was used by Taylor et al. (2012), the mean CPM is comparable to the population mean for all the tray designs (table 9.2). Taylor et al. (2012) reported a smaller area of the resection interface with a CPM $< 50\,\mu m$ and a smaller area of the resection interface with a CPM $> 150\,\mu m$ compared to the populations. However, the maximum peak micromotion found in the population is 2–3 times larger than Taylor et al. (2012) reports for all implant designs. Because of the variation in the population, it is likely that models with high loads or very low bone modulus generate the very large peak micromotion.

These differences could also be related to the FE models. Taylor et al. (2012) assumes the PFC Sigma is manufactured from a titanium alloy with a modulus of 110 GPa. In this study,

Table 9.2: Comparison of CPM metrics for the three implant designs between this study and Taylor et al. (2012). For the population, the mean±standard deviation of the population is given for each metric.

Implant	Metric	Population	Taylor et al.
PFC Sigma	Mean (microns)	56 ± 38	65
	Maximum (microns)	612	180
	Area <50 microns (%)	58 ± 27	40
	Area >150 microns (%)	7 ± 14	2
LCS	Mean (microns)	95 ± 57	86
	Maximum (microns)	797	225
	Area <50 microns (%)	42 ± 23	39
	Area >150 microns (%)	20 ± 20	16
Duofix	Mean (microns)	46 ± 27	61
	Maximum (microns)	639	198
	Area <50 microns (%)	72 ± 16	46
	Area >150 microns (%)	7 ± 9	5

it is assumed the PFC Sigma is cobalt-chrome with a modulus of 210 GPa. The stiffer tray is less likely to flex under load resulting in smaller micromotions as seen in the population. For the Duofix tray, Taylor et al. (2012) assumed a coefficient of friction of 0.8 for the porous coated tray and pegs, and 0.4 for the stem, whereas a coefficient of 0.6 was assumed for the entire interface in this study affecting the strength of the contact interface and resultant micromotion. The gait cycle loading used by Taylor et al. (2012) was taken from telemetric implant data (Kutzner et al., 2010). For the population study, the loading is sampled from a SM based on data from musculoskeletal models. The predicted loads from musculoskeletal models are known to be overestimated in comparison to telemetric data (Worsley et al., 2011) and in this study the A-P force and V-V moment were scaled by 0.5 to bring them inline with telemetric data (see section 6.4.7).

One advantage of a population-based study is that the distribution of the peak strain and micromotion can be seen. Considering only micromotion, an ideal implant would have a low median CPM and the spread of the median CPM would be narrow. The low median CPM is advantageous in terms of clinical performance indicating that the chance of bone in-growth is higher. A low spread of median CPM suggests that the device has a more predictable response independent of patient variability. For the three implants, the Duofix tray had the lowest population median CPM and the narrowest inter-quartile range, whereas the LCS tray had the highest population median CPM and the widest inter-quartile range (figure 9.3). This suggests that the Duofix tray is less sensitive to population variability perhaps because of features of the tray design. For strain, the PFC Sigma tray had the lowest population median CPS with the smallest inter-quartile range. Again, the LCS had the highest population median CPS with the largest inter-quartile range (figure 9.3). The LCS tray was more sensitive to the population variability.

The distribution of the CPM showed that the largest micromotion was found on the anterior and lateral side of interface for all three trays. This is different to Taylor et al. (2012), where all three trays generated higher micromotion on the lateral side (figure 9.5). This perhaps is a result of differences in the loading, where in this study the overestimation of loads by the MS modelling, high F-E moments are generating the anterior micromotion. This is particularly apparent for the Duofix tray, where the micromotion is almost completely in the anterior region between the two pegs (figure 9.5) and is likely anterior lift-off generated by the F-E moment. Chong et al. (2008) show a similar distribution of peak micromotion at toe-off for a tray with a central stem and anterior keel. The peak micromotion was found in the anterior region of the bone-tray interface. This design was compared to one similar to the PFC Sigma, and the anterior keels helps to reduce the peak micromotion, a similar effect the pegs have on the Duofix tray.

The clinical performance of all three tibial tray designs is widely reported in literature: PFC Sigma (Baker et al., 2007; Duffy et al., 1998), LCS (Aebli et al., 2004; Fuiko et al., 2003), and Duofix (Cossetto et al., 2010; Holloway et al., 2010). These studies often report the incidence of radiolucencies at the bone-tray interface, which is an indication of the micromotion and poor osseointegration. The lowest incidence of RLLs was reported for the Duofix tray, between

4 and 6% (Cossetto et al., 2010; Holloway et al., 2010). The majority of the RLLs were on the medial side and did not extend around the adjacent pegs (Cossetto et al., 2010), whereas in this study the highest micromotion was predicted in the anterior region of the interface and there is evidence of high micromotion around the anterior pegs (figure 9.5). The difference in the pattern is likely due to the loading applied to the FE models, which is based on MS model data. It has been seen that the predicted moments from MS models are overestimated in comparison to *in vivo* telemetric implant data (figure 6.24). This would affect the load distribution in the models, and the F-E moment is likely generating the anterior micromotion. For the PFC Sigma, the literature found reporting radiolucencies refer to the previous design of tibial tray, the P.F.C.® (DePuy Inc, USA). The reported incidence of RLLs were 16% (Khaw et al., 2002) and 28% (Duffy et al., 1998).

In contrast, for the LCS, two studies reported over a 90% incidence of RLL (Aebli et al., 2004; Fuiko et al., 2003). Both studies report the highest incidence of RLLs at the tibial plateau around the periphery of the implant, and Fuiko et al. (2003) also reports that they are wedge shaped, increasing in width from the centre to the periphery. The micromotion pattern generated by the LCS is similar to this. Generally the lowest micromotion is found around the stem and the highest at the periphery, particularly on the lateral side (figure 9.5).

The design features of each tray also affect the pattern of strain and micromotion. Much of the literature focuses on the parameters of the central stem, investigating the effect of stem length on stability (Albrektsson et al., 1990; Lee et al., 1991; Stern et al., 1997; Yoshii et al., 1992), or the shape of the stem (Au et al., 2005). In this study, all the tray designs have a stem of a similar length and should provide a similar amount of stability. It is suggested that the four peripheral pegs used for the Duofix help to resist the V-V moment (Taylor et al., 2012). Walker et al. (1981) also saw this effect and suggesting that the tray is stiffened by the pegs. Evidence for this can be observed from the composite peak plots (figure 9.5). As previously discussed, the largest micromotion are generated in the anterior region, not laterally as for the PFC Sigma and LCS, hence there is better resistance to the V-V moment. Increased strain is often seen around the pegs which often occurs later in the gait cycle (e.g. 25th percentile model) which would be expected if the pegs are supporting a greater load. Stability of the implant could also be increased because the because the pegs are likely to be located in better quality peripheral cancellous bone, which provides better support for load transfer. Clinical evidence also suggests the pegs help to provide better stability, the survivorship rate for the Duofix is reported at >95% (Cossetto et al., 2010; Holloway et al., 2010). This is further shown by a case series using a cemented pegged tibial tray with no central stem in which only 1% of patients required revision due to aseptic loosening (Miller et al., 2001).

The LCS tray only has flanges running down the stem to provide extra stability, and it is likely that these provide most resistance against the I-E moment and shear forces. The pattern of micromotion from the CPM plot suggests that there is anterolateral lift-off. As the LCS relies on the stem for stability, resistance to lift-off, particularly in poor quality bone under V-V load is a function of the length of the stem (Lee et al., 1991; Walker et al., 1981; Yoshii et al.,

1992). The reduction of micromotion of the PFC Sigma tray suggests that the flanges from the stem provide extra stability. A disadvantage of the CPM plots is that only the resultant micromotion is computed, and therefore the difference between lift-off and rotation can not be identified.

The contribution made by this study is that a population of models is used, introducing intra-patient variability. This is important in the evaluation of an implant design, as the mechanical response of the tibia can be assessed considering the variation of the tibia geometry, density, and knee loads. The sensitivity of the implant design to changes in the population can also be assessed, whereas this is not possible when only using a model of a single patient. However, there are still a number of limitations to be considered, similar to those of Taylor et al. (2012). The same load profile was applied to all three implants, but the kinetics of the knee are a function of the kinematics, which would be a function of the geometry of the TKR. The differences in geometry between TKR designs means that, for example, the loads in the knee with a Duofix TKR would be different to the PFC Sigma TKR. Applying the same load to all three trays allows a direct comparison of the tray design in isolation of the loading. In this study, all three trays were assumed to be manufactured from the same material and the coefficient of friction of the bone-tray interface was the same. Again, this allows a comparison of the tray designs in isolation of the variables. Actually, the PFC Sigma and LCS trays are manufactured with a porous coating, whereas the Duofix has a HA porous coating. Clinically, the Duofix HA coating would affect the long-term fixation, and, as Taylor et al. (2012) notes, could be the reason why a reduced incidence of RLLs are seen.

9.5 Conclusions

In this final case study a robust evaluation of three tibial trays was performed. The use of a population-based study meant that that sensitivity of each implant design to population variability could be seen. From the comparison analysis, the key conclusions are:

- The LCS tray was most sensitive to the population variation, for both strain and micromotion. The population median CPS and median CPM were both larger than for the PFC Sigma and Duofix trays.
- The Duofix tray generated the least micromotion, with the lowest population median CPM and smallest inter-quartile range, indicating it was least sensitive to population variation. It is thought that this is perhaps due to the four peripheral pegs supporting the tray, which help to resist micromotion.
- In terms of strain, the PFC Sigma was least sensitive to the population variation. It had the smallest population median CPS and narrowest inter-quartile range of the CPS.
- The rank order of the implants by micromotion agreed with the reported incidence of radiolucent lines.

Chapter 10

Discussion, conclusions, and future work

10.1 Significant findings

The aim of this thesis was to create, develop, and implement a framework to assess the performance of a cementless tibial tray in a large population. The use of population-based analysis was a unique approach compared to current computational studies. SMs were used to generate a population of models that incorporated variability of both the tibia and complete loading cycle. An automated workflow was used to process the population of models, involving implanting the tibial tray in the tibia and running FE analysis. Three case studies demonstrated the use of a population-based analysis to assess the fixation of the tibial tray, looking at the effect of surgical variability and implant design. The significant findings of the case studies are summarised here.

The first case study (chapter 7) examined the effect of under sizing the tibial tray. It was observed that there was a weak correlation between peak strain and micromotion. Models which experienced high strain had low bone quality, but not necessarily low micromotion. It was also found that the peak strain occurred during the stance phase of gait when axial loads were high, whereas peak micromotion occurred at the beginning of swing phase of gait when low axial loads and moderate moments acted. This is contrary to the assumption that many previous studies have made that peak strain and micromotion occur with peak axial load. Models considered to be at higher risk of failure had lower bone quality, higher weight, and larger peak loads. Further to this, the results suggested that under sizing the tibial tray did not necessarily increase the risk of failure of the tibial tray.

In the second case study (chapter 8), the effect of changing the resection level on the primary stability of the tibial tray was examined. By making a more distal resection, both the peak strain and micromotion increased, but the reason for these changes depended on the depth of resection. There was a large change in the modulus with a small change in resection depth, which resulted in an increase in strain. At the most distal resection, it was hypothesised that

the down sizing of the tibial tray caused the increase in peak strain and micromotion. The results suggest that a minimal resection should be taken to obtain optimal primary stability.

In the third case study (chapter 9), three designs of cementless tibial trays were compared. It was seen that the LCS tray had a worse micromotion response than either the PFC Sigma or Duofix trays, suggesting it is more sensitive to population variability. The peripheral pegs on the Duofix tray improved the primary stability, reducing the variability of the micromotion response. The rank order of the three tray designs in terms of peak micromotion was comparable with the incidence of RLLs seen clinically. This finding shows that there is potential for using population-based analysis to be used to predict clinical outcomes.

10.2 Discussion

Computational modelling has become a fundamental tool in orthopaedic biomechanics and is widely used in the testing of new implant designs. The advantage of computational evaluation is that it allows the same model to be tested under multiple conditions quickly and easily, not always possible with experiments. For example, in the context of implant design, it is possible to test and compare different design configurations to identify those which perform best. A significant limitation of the majority of published computational studies is that only a single patient model or small number of models are used and, in many cases, idealised conditions are assumed such as perfect implant position, non-eccentric loading, and simplified material properties. More often than not, it is assumed that the results can be extrapolated to the general population, despite the variability of the population.

To date, few studies have incorporated inter-patient variability in testing the tibial tray and those that do use a small number of models: Perillo-Marcone et al. (2004) and Wong et al. (2010) used four models, and Rawlinson et al. (2005) used 9 paired models. Significantly, the loading of each model was the same, despite known population variability (Kutzner et al., 2010). A small population of 16 patients was used in the testing of a hip resurfacing (Radcliffe et al., 2007a; Radcliffe et al., 2007b), where all the models were manually created and analysed. Although these studies only used a small population, the importance of inter-patient variability was apparent.

Recently, a SM of the femur has been used for population-based analysis of hip fracture risk (Bryan et al., 2009) and to assess the performance of a hip resurfacing (Bryan, 2010). In this thesis, SMs were used to assess the performance of a TKR in a large population, using methods similar to Bryan (2010). However, the case studies (chapters 7 to 9) include variability of *both* the tibia and complete load cycle of level gait. The relative complexity of the knee kinetics and kinematics, which are dependent on the knee geometry, in comparison to the hip meant that it was important to include loading variation in the population analysis. To do this a second SM of the gait cycle loads was developed (section 6.3). The use of a full activity load cycle is also unique compared to the majority of other computational studies, where often only the peak force(s) during an activity cycle are applied.

An important question for this thesis is why use a SM to generate a population of models rather than a large set of 'real' data? The advantage of a SM is that there is a statistical link in the data. For example, the link between the shape and modulus distribution of the tibia, or between the axial force and varus-valgus moment is maintained, whereas individual sets of data would not hold this information. Another advantage of a SM is that since the data is available in parametric form, it becomes possible to use the results of the simulations to construct surrogate models or emulators (Gorisse et al., 2010) that map the input parameters varied in the simulation to outputs of interest. These kinds of models have potential use for pre-clinical decision support and provide deeper insights into the relationship between the biomechanical response of the tibia, patient metrics, and clinical variables. A further benefit of using a SM is that only a small set of training data is required to generate a large population of models; a population of 500 tibiae were generated from a training set of only 32 CT scans. Obtaining high quality CT scans of 500 patients would be a time consuming process requiring ethical approval. SMs overcome a primary limitation in using models of multiple patients for implant testing; the availability of enough high quality CT data required to create the models.

Issues relating to the methodology used to create the SM of both the tibia and gait cycle loads are dealt with elsewhere (see sections 6.2.11, 6.3.4 and 6.4.7). There are a broader set of issues relating to the use of a SM to generate models for a population-based analysis. It is not known how well the generated data, from either the tibia SM or the gait cycle SM, really represents the general population. To obtain variation in the generated data, the PC weights were assumed to have a normal distribution and were sampled with an interval of 3 standard deviations (see sections 6.2.10 and 6.3.3). A wide sampling interval was chosen to maximise variability of the generated data. For the evaluation of an implant design, large variability in the population is desired as the implant would be assessed in more extreme cases. These cases are of interest because they are the cases in which an implant is more likely to fail. The disadvantage of using such a large sampling interval is that it more likely that invalid data is generated.

Ensuring the generated data is valid is a significant problem, particularly from the tibia SM. Bryan (2010) attempted validation of the population of femurs by comparing geometric metrics of a 'real' population to those of the 'generated' population, showing that the shape and size of the femur broadly correlates. Unfortunately, no set of 'real' population measurements of the tibia to compare to the 'generated' population could be found. Validating the bone modulus distribution is far more challenging. To do this, Bryan (2010) ran a FE analysis on a selection of femurs and examined the distribution of strain generated in the bone. Given that elastic isotropic behaviour of bone is assumed, the strain will be related to the modulus of the bone. The selection of the bone-modulus relationship could therefore affect the strain distribution. Provided the comparisons are made between models in the same study, this is not a problem, but comparison with experimental and clinical data is limited.

Using FE analysis to help validate the SM can certainly identify problems with the generated data. In all three case studies in this thesis, anomalous patterns of peak micromotion were

observed for some models. The peak micromotion was found to be occurring very early in the gait cycle where loads were very low (see chapter 8). Investigation of these cases showed that the axial force was positive, i.e. acting as a force pulling the tibial tray out of the bone. This tended to occur at two points in the gait cycle, the beginning of stance phase and the end of stance phase/beginning of swing phase, the points at which the axial force changes the most. This suggests that some of the training data is out of phase, perhaps because of the natural variability of the length of the two phases of gait or the start and end of the gait cycle has not been accurately identified. In this thesis, the models with a positive axial force were simply excluded from the analyses because it is a non-physiological load case. It would have perhaps been better to inspect the generated load profiles and resample the SM if a load profile was generated with a positive axial force, increasing the number of models analysed in the cases studies.

The idea of PCA is that the data is transformed into a set of PCs so that the first few retain most of variance in the training data. The first three PCs of the tibia SM and gait cycle SM capture 46% and 48% of the total variance respectively. For both models, over half the total number of PCs are required to represent 95% of the total variance. For both the SMs, the size of the training sets are relatively small—32 tibia for the tibia SSIM and 20 healthy subjects for the gait cycle SM—with high variability between data sets. This limits the compactness and the predictive accuracy of the SMs. For the tibia SSIM, this is confounded by the accuracy of the registration scheme and quality of data sources. For example, the lack of phantom data to calibrate the density of the training data CT scans is likely to introduce errors in the material properties. The higher PCs with a small variance are likely to represent noise of the training data, and including them when sampling the SM may introduce artefacts in the generated data. Using a larger set of training data might improve the compactness and predictive accuracy of the SM. However, unless the size of the training set is sufficiently increased, the variability of the training data might also increase with the effect of reducing the compactness of the SM. It is noted that both SMs are based on linear PCA. In reality, there may be non-linear correlations in the training data. By using non-linear transformations, the variance of the data might be better captured.

The motivation for using SMs to generate a population for a large FE study was due to the lack of clinical data. In this thesis, the best available sets of data were used to create the SMs. It was found that the SMs could sufficiently represent the training data and by sampling the SMs a population of models was generated, representing the variability of the training data. Sampling the SM might create ‘outlier’ data, but these cases are of interest when evaluating a medical device. The ideal device would be robust to the large variation of the population.

One of the main aims of this thesis was to perform population-based analysis of the tibia implanted with a tibial tray using SMs to generate the initial population of models. Three cases studies showed the use of population-based FE analysis for the assessment of the primary stability of the tibial tray. A specific discussion about each case study was previously given. Not discussed were the wider limitations of the population-based FE analysis which all the case studies have in common.

Perhaps the largest limitation of the case studies is that the population of data is generated from two separate models (mentioned very briefly in section 6.4.7). The population of tibiae were generated from a SM of the tibia and the load cycles were generated from a SM of the gait cycle. Because the two SMs were based on completely separate training data, the link between the shape, size, and density distribution of the tibia and the loading is lost. According to Wolff's law, bone adapts to the loads it carries, strengthening along paths of high loads. The random association of a tibia with a load cycle means that a tibia with an even bone density distribution of the medial and the lateral condyles could be associated with gait cycle loads representing a varus knee. In a varus knee, it is expected that the bone density of lateral condyle is lower than that of the medial condyle which experiences higher loading. The morphology of the tibia will also affect the loads in the knee; a tibia with larger flatter condyles will not experience the same loads as a tibia with smaller deeper condyles. Further to the random association of tibiae and gait cycles, the weight estimated for each model is also random. Whilst, effort was made to provide a link between tibia length and height (figure 6.25), the BMI of each model was sampled from a distribution based on published data. This could mean that a model has an inappropriate weight for the size of tibia and load cycle.

The only reason for these dissociations is the lack of a data set of a single series of patients containing CT scans, computed knee loads, and patient information (e.g. height, weight, BMI, age). It is perfectly feasible to combine all this information in a single SM so that sampling the model would generate a tibia, a load cycle, and patient information which were linked.

In all the case studies, it is assumed that the loading cycle generated from the gait cycle SM can be applied to all knee configurations, irrespective of whether it is implanted with a TKR, and of implant design. In reality, the kinetics are highly dependent on the kinematics, which in turn depend on the geometry and soft tissue of the knee. This means that healthy patients will generate different load patterns than TKR patients and load patterns will not be the same for different implant designs. However, there is little data on *in vivo* loads and that which does exist is of multiple patients with the same implant design (Heinlein et al., 2009; Kutzner et al., 2010). It is also important to note that the results of the cases studies are specific to the TKR modelled (other assumptions aside).

The analysis of the models only considered the resection interface, the bone at the resected surface directly in contact with the tray, ignoring the stem. The resection interface is not necessarily the region of bone which experiences the highest strain, more distal weaker bone could experience higher strain, but for the tibial tray to migrate, it is assumed that the bone directly in contact with the tibial tray must fail first. The strain in the proximal tibia could be analysed, but it is the mechanical conditions of the bone-tray interface which will affect the primary stability of the implant the most. If processes such as bone remodelling were being considered, then it would be necessary to consider a larger region of the proximal tibia.

In large analyses like these, it is necessary to know if enough models have been included in the population. A simplistic approach was taken in this thesis by simply computing the stability of the population median and 95th percentile CPS and CPM with an increasing number of models. In all case studies it was found that the CPS and CPM stabilised at around 150

models (figures 7.1, 8.2 and 9.2). There was no significant change in the median CPS or CPM using more than 150 models, suggesting that the analysis of the population will not be so affected by anomalies in the data. The number of models analysed in all the case studies was greater than 200 after outliers were excluded, above the point at which stabilisation occurs.

None of the case studies included all of the generated population in the analysis. The main reason for excluded models from the analysis was because a positive axial force occurred during the gait cycle. However, for all the case studies, the tibial tray was not implanted in 10 to 15% of the tibiae. For 20–30% of these failures, there was too much overhang between the tray and bone (see section 6.4.7) and the rest of the failures were due to geometric errors. The implantation process was based on surface mesh intersection and union operations. These types of operation are sensitive to the mesh geometry and can introduce intersecting triangles, triangles with small angles, or narrow inter-boundary regions (Kahnt et al., 2011). This can cause problems when remeshing the surface (which was done to improve triangle quality) or generating a tetrahedral mesh using an advancing front algorithm (as used to mesh model). The implantation method used in this thesis was developed in collaboration with ZIB, and development of the method continued separately from this thesis. A new method has since been developed, based on an 'oracle' mesh generation procedure (Kahnt et al., 2011). The advantage of this method is that no Boolean operations are necessary before generating the tetrahedral mesh and features, such as sharp edges, are preserved. If future studies were to be performed, it would be advantageous to use this method to generate the mesh.

A potential use of population-based studies is to assess how sensitive an implant design is to variation in the population. In the current work results can only be compared between populations within the same study, to say otherwise requires validation of the studies. This would not be validation in the traditional sense which checks that the FE models are predicting accurate results in comparison to experimental data, but rather comparing the trends found in the population study to trends in clinical data. For example, if clinical data might show that a particular size of the implant tends to fail, then it would be necessary to investigate if the population study were able to predict that the same size implant was at a higher risk of failure. A major hurdle in doing this is obtaining a large set of clinical data which provides this information. One source is joint registers, which now record nearly 10 years of data for some implants. With access to such data, it would become possible to show that a population study can predict trends seen clinically.

Beyond the limitations of the SMs and with the FE analysis, much time and effort was spent in developing the pipeline to automate the processing of the models and the data analysis. However, it is still a somewhat ad-hoc workflow with three distinct parts. The registration and SM workflow was based on that of Bryan (2010), using MATLAB to integrate the separate software components. The workflow to then create and analyse a model (involving implanting the tibia with a tibial tray (ZIBAmira), pre-processing the model for FE analysis (Abaqus), FE analysis (Abaqus), and post-processing of the FE analysis (Abaqus), each of which was automated) was integrated using Python scripts. Analysis of the FE results was done using MATLAB. Better integration of the workflow would help reduce the time take to run a study

and make it easier to catch and fix models with errors.

A further challenge of the data processing was in the analysis and interpretation of the results. A relatively simplistic approach was taken to analyse the results, choosing to focus on metrics relating to the peak strain and micromotion generated in each model. This (partially) ignores the time-history of how the strain and micromotion change during the gait cycle. With a large number of models methods to efficiently process and visualise this information are required. Also, in this thesis, potential links between the tibia morphology and performance of the tibial tray were not investigated. Whilst not the aim of the case studies in this thesis, the advantage of performing a population-based analysis is that these links could be investigated.

10.3 Future work

Currently, the use of population-based studies in the evaluation of joint replacements is very limited. This thesis has demonstrated the use of population-based FE analysis to evaluate the primary fixation of the tibial tray extending the work of Bryan (2010). There is certainly future potential for using this type of analysis to help inform surgical decisions and evaluate new implant designs.

There are numerous improvements which could be made to the methodology and workflow used in this thesis. Further work is required to improve the accuracy of the registration scheme used to register the tibiae, perhaps focussing on how better automatic correspondence can be found between models or how intensity information can be incorporated in the registration algorithm. Changes in registration scheme could also be coupled with the use of a minimum description length algorithm (e.g. Davies et al., 2002) to automatically select the "best" parameters to create the SM. This method aims to minimise the number parameters required to build the SM to maximise the variance of the first few PCs. This results in a model with better compactness, specificity, and generalisation ability (Davies et al., 2010). Improvements can also be made to the gait cycle SM. One improvement could be to create the gait SM using frequency response of the force and moments, instead of the time waveforms. The force and moment waveforms can be transformed to the frequency domain using a Fourier transform. This could potentially remove the phase errors found in the generated gait cycles.

The model processing workflow also needs refining to better integrate all the tools used. This would provide a much better framework within which a population analyses can be performed, with a more flexible interface for analysis of the results, perhaps incorporating data mining tools to investigate relationships in the data.

Perhaps the most important aims for the future are to provide better validation of the SM and population-based FE analysis. It would be advantageous if a larger set of training data could be collected for generating the SM, ideally including CT scans, load cycle data, associated patient information (e.g. height, weight), and follow-up clinical data. More knowledge about the population being modelled and analysed would help to show that the SM is generating realistic models and the FE analysis is predicting realistic outcomes. More sophisticated

techniques to construct a statistical model of the PC weights based on Markov chain Monte Carlo simulation (Ghanem et al., 2006) could be used to improve the sampling of the SM. This would help ensure that the SM is more fairly sampled and the generated population better represents the training data.

Population analysis offers the opportunity to investigate many more surgical conditions and tray designs than those presented in this thesis. The method presented allows for this and, for example, the effect of anterior-posterior position or varus-valgus alignment could easily be investigated. There is also the potential to increase the complexity of the SM model to include other structures of the knee such as the femur and soft tissues, thus also increasing the complexity of the FE analysis. Of course, this would raise many new challenges, but it would provide an even more realistic evaluation of a TKR.

References

Aebli, N., J. Krebs, D. Schwenke, et al. (2004). "Progression of radiolucent lines in cementless twin-bearing low-contact-stress knee prostheses". In: *The Journal of Arthroplasty* 19(6), pp. 783–789.

Albrektsson, B. E. J., L. V. Carlsson, M. A. R. Freeman, et al. (1990). "The effect of a stem on the tibial component of knee arthroplasty. A roentgen stereophotogrammetric study of uncemented tibial components in the Freeman-Samuelson knee arthroplasty". In: *Journal of Bone and Joint Surgery* 72-B(2), pp. 252–258.

Albrektsson, B. E. J., L. V. Carlsson, M. A. R. Freeman, et al. (1992). "Proximally cemented versus uncemented Freeman-Samuelson knee arthroplasty. A prospective randomised study". In: *Journal of Bone and Joint Surgery* 74-B(2), pp. 233–238.

Andersen, M. S., M. Damsgaard, and J. Rasmussen (2009). "Kinematic analysis of over-determinate biomechanical systems". In: *Computer Methods in Biomechanics and Biomedical Engineering* 12(4), pp. 371–384.

Au, A. G., A. B. Liggins, A. Amirfazli, et al. (2005). "A parametric analysis of fixation post shape in tibial knee prostheses". In: *Medical Engineering & Physics* 27(2), pp. 123–134.

Austin, M. S., P. F. Sharkey, W. J. Hozack, et al. (2004). "Knee Failure Mechanisms After Total Knee Arthroplasty". In: *Techniques in Knee Surgery* 3(1), pp. 55–59.

Australian Orthopaedic Association (2011). *Australian National Joint Replacement Registry: Annual Report 2011*. Tech. rep. Adelaide: Australisan Orthopaedic Association.

Bajcsy, R. and S. Kovacic (1989). "Multiresolution elastic matching". In: *Computer Vision, Graphics, and Image Processing* 46(1), pp. 1–21.

Baker, P. N., F. M. Khaw, L. M. G. Kirk, et al. (2007). "A randomised controlled trial of cemented versus cementless press-fit condylar total knee replacement: 15-year survival analysis". In: *The Journal of Bone and Joint Surgery* 89-B(12), pp. 1608–1614.

Baldwin, M. A., J. E. Langenderfer, P. J. Rullkoetter, et al. (2010). "Development of subject-specific and statistical shape models of the knee using an efficient segmentation and mesh-morphing approach". In: *Computer Methods and Programs in Biomedicine* 97(3), pp. 232–40.

Ballester, M. A. G., X. Pennec, M. G. Linguraru, et al. (2004). "Generalized image models and their application as statistical models of images". In: *Medical Image Analysis* 8(3), pp. 361–369.

Barker, D. S., K. E. Tanner, and L. Ryd (2005). "A Circumferentially Flanged Tibial Tray Minimizes Bone-Tray Shear Micromotion". In: *Proceedings of the Institution of Mechanical Engineers, Part H: Journal of Engineering in Medicine* 219(6), pp. 449–456.

Barrack, R. L., T. Schrader, A. J. Bertot, et al. (2001). "Component rotation and anterior knee pain after total knee arthroplasty". In: *Clinical Orthopaedics and Related Research* 392, pp. 46–55.

Barratt, D. C., C. S. K. Chan, P. J. Edwards, et al. (2008). "Instantiation and registration of statistical shape models of the femur and pelvis using 3d ultrasound imaging". In: *Medical Image Analysis* 12(3), pp. 358–374.

Bassett, R. W. (1998). "Results of 1,000 Performance Knees Cementless Versus Cemented Fixation". In: *Journal of Arthroplasty* 13(4), pp. 409–413.

Bayraktar, H. H., E. F. Morgan, G. L. Niebur, et al. (2004). "Comparison of the elastic and yield properties of human femoral trabecular and cortical bone tissue". In: *Journal of Biomechanics* 37(1), pp. 27–35.

Berend, M. E., M. A. Ritter, H. C. Hyldahl, et al. (2008). "Implant Migration and Failure in Total Knee Arthroplasty is Related to Body Mass Index and Tibial Component Size". In: *Journal of Arthroplasty* 23(6 (S1)), pp. 104–109.

Berend, M. E., S. R. Small, M. A. Ritter, et al. (2010). "The Effects of Bone Resection Depth and Malalignment on Strain in the Proximal Tibia After Total Knee Arthroplasty". In: *The Journal of Arthroplasty* 25(2), pp. 314–318.

Berger, R. A., J. H. Lyon, J. J. Jacobs, et al. (2001). "Problems With Cementless Total Knee Arthroplasty at 11 Years Followup". In: *Clinical Orthopaedics and Related Research* 392, pp. 196–207.

Bergmann, G., F. Graichen, and A. Rohlmann (1993). "Hip joint loading during walking and running, measured in two patients". In: *Journal of Biomechanics* 26(8), pp. 969–990.

Bergmann, G. (2008). *Orthoload*.

Besl, P. J. and N. D. McKay (1992). "A Method for Registration of 3-D Shapes". In: *IEEE Transactions on Pattern Analysis and Machine Intelligence* 14(2), pp. 239–256.

Bookstein, F. L. (1989). "Principal warps: thin-plate splines and the decomposition of deformations". In: *IEEE Transactions on Pattern Analysis and Machine Intelligence* 11(6), pp. 567–585.

Bryan, R. (2010). "Large Scale , Multi Femur Computational Stress Analysis Using a Statistical Shape and Intensity Model". PhD thesis. University of Southampton.

Bryan, R., P. S. Mohan, A. Hopkins, et al. (2010). "Statistical modelling of the whole human femur incorporating geometric and material properties". In: *Medical Engineering & Physics* 32(1), pp. 57–65.

Bryan, R., P. B. Nair, and M. Taylor (2009). "Use of a statistical model of the whole femur in a large scale, multi-model study of femoral neck fracture risk". In: *Journal of Biomechanics* 42(13), pp. 2171–2176.

Bryan, R., P. B. Nair, and M. Taylor (2012). "Influence of femur size and morphology on load transfer in the resurfaced femoral head: A large scale, multi-subject finite element study". In: *Journal of Biomechanics* 45(11), pp. 1952–1958.

Cachier, P., E. Bardinet, D. Dormont, et al. (2003). "Iconic feature based nonrigid registration: the PASHA algorithm". In: *Computer Vision and Image Understanding* 89(2-3), pp. 272–298.

Canadian Institute for Health Information (2008). *Canadian Joint Replacement Registry (CJRR) 2007 Annual Report - Hip and Knee Replacements in Canada.* Tech. rep. Ottawa: CIHI, pp. 1–136.

Carlsson, Å., A. Björkman, J. Besjakov, et al. (2005). "Cemented tibial component fixation performs better than cementless fixation". In: *Acta Orthopaedica* 76(3), pp. 362–369.

Chang, W. C. W., T. M. Christensen, T. P. Pinilla, et al. (1999). "Uniaxial Yield Strains for Bovine Trabecular Bone are Isotropic and Asymmetric". In: 17(4), pp. 582–585.

Cheal, E. J., W. C. Hayes, C. H. Lee, et al. (1985). "Stress analysis of a condylar knee tibial component: influence of metaphyseal shell properties and cement injection depth". In: *Journal of Orthopaedic Research* 3(4), pp. 424–434.

Chong, D. Y. R., U. N. Hansen, and A. A. Amis (2008). "A Possible Tibial Prosthesis Interface Micromotion at Gait: Mini-keel vs Standard Designs". In: *Journal of Biomechanics* 41(S1), S238.

Chong, D. Y. R., U. N. Hansen, and A. A. Amis (2010). "Analysis of bone-prosthesis interface micromotion for cementless tibial prosthesis fixation and the influence of loading conditions". In: *Journal of Biomechanics* 43(6), pp. 1074–1080.

Cootes, T. F., S. Marsland, C. J. Twining, et al. (2004). "Groupwise Diffeomorphic Non-rigid Registration for Automatic Model Building". In: *European Conference on Computer Vision*, pp. 316–327.

Cootes, T. F., C. J. Taylor, D. H. Cooper, et al. (1995). "Active Shape Models - Their Training and Application". In: *Computer Vision and Image Understanding* 61(1), pp. 38–59.

Cootes, T., C. Twining, K. Babalola, et al. (2008). "Diffeomorphic statistical shape models". In: *Image and Vision Computing* 26(3), pp. 326–332.

Cossetto, D. J. and A. D. Gouda (2010). "Uncemented Tibial Fixation Total Knee Arthroplasty". In: *The Journal of arthroplasty.*

Costigan, P. A., K. J. Deluzio, and U. P. Wyss (2002). "Knee and hip kinetics during normal stair climbing". In: *Gait & Posture* 16(1), pp. 31–37.

Couteau, B., Y. Payan, and S. Lavallee (2000). "The mesh-matching algorithm: an automatic 3D mesh generator for finite element structures". In: *Journal of Biomechanics* 33, pp. 1005–1009.

Crum, W. R., T. Hartkens, and D. L. G. Hill (2004). "Non-rigid image registration: theory and practice". In: *British Journal of Radiology* 77(Suppl_2), S140–S153.

Davies, R. H., C. J. Twining, T. F. Cootes, et al. (2002). "A Minimum Description Length Approach to Statistical Shape Modeling". In: *IEEE Transactions on Medical Imaging* 21(5), pp. 525–537.

Davies, R. H., C. J. Twining, T. F. Cootes, et al. (2010). "Building 3-D Statistical Shape Models by Direct Optimization". In: *IEEE Transactions on Medical Imaging* 29(4), pp. 961–981.

Declerck, J., J. Feldmar, M. L. Goris, et al. (1997). “Automatic registration and alignment on atemplate of cardiac stress and rest reoriented SPECT images”. In: *IEEE Transactions on Medical Imaging* 16(6), pp. 727–737.

Della Croce, U., A. Leardini, L. Chiari, et al. (2005). “Human movement analysis using stereophotogrammetry. Part 4: assessment of anatomical landmark misplacement and its effects on joint kinematics”. In: *Gait & Posture* 21(2), pp. 226–237.

Deluzio, K. J. and J. L. Astephen (2007). “Biomechanical features of gait waveform data associated with knee osteoarthritis: an application of principal component analysis”. In: *Gait & Posture* 25(1), pp. 86–93.

Deluzio, K. J., U. P. Wyss, B. Zee, et al. (1997). “Principal component models of knee kinematics and kinetics: Normal vs pathological gait patterns”. In: *Journal of Human Movement Science* 16, pp. 201–217.

D’Lima, D. D., S. Patil, N. Steklov, et al. (2011). “The 2011 ABJS Nicolas Andry Award: ’Lab’-in-a-Knee: In Vivo Knee Forces, Kinematics, and Contact Analysis”. In: *Clinical Orthopaedics and Related Research* 469(10), pp. 2953–2970.

D’Lima, D. D., S. Patil, N. Steklov, et al. (2006). “Tibial forces measured in vivo after total knee arthroplasty”. In: *The Journal of Arthroplasty* 21(2), pp. 255–262.

D’Lima, D. D., S. Patil, N. Steklov, et al. (2007). “In vivo knee moments and shear after total knee arthroplasty”. In: *Journal of Biomechanics* 40(S1), S11–S17.

D’Lima, D. D., N. Steklov, S. Patil, et al. (2008). “The Mark Coventry Award: in vivo knee forces during recreation and exercise after knee arthroplasty”. In: *Clinical Orthopaedics and Related Research* 466(11), pp. 2605–2611.

Duffy, G. P., D. J. Berry, and J. A. Rand (1998). “Cement versus cementless fixation in total knee arthroplasty”. In: *Clinical Orthopaedics and Related Research* (356), pp. 66–72.

Duncan, J. S. and N. Ayache (2000). “Medical Image Analysis: Progress over Two Decades and the Challenges Ahead”. In: *IEEE Transactions on Pattern Analysis and Machine Intelligence* 22(1), pp. 85–106.

Duyar, I. and C. Pelin (2003). “Body Height Estimation Based on Tibia Length in Different Stature Groups”. In: *American Journal of Physical Anthropology* 122(1), pp. 23–27.

Edwards, G. J., A. Lanitis, C. J. Taylor, et al. (1998). “Statistical models of face images - improving specificity”. In: *Image and Vision Computing* 16(3), pp. 203–211.

Evans, P. (1986). *The Knee Joint*. 1st. Edinburgh: Churchill Livingstone.

Fang, D. M., M. A. Ritter, and K. E. Davis (2009). “Coronal alignment in total knee arthroplasty: just how important is it?” In: *The Journal of Arthroplasty* 24(6 (Suppl 1)), pp. 39–43.

Fehring, T. K., S. Odum, W. L. Griffin, et al. (2001). “Early failures in total knee arthroplasty”. In: *Clinical Orthopaedics and Related Research* (392), pp. 315–318.

Feldesman, M. R. and R. L. Fountain (1996). “"Race" specificity and the femur/stature ratio”. In: *American Journal of Physical Anthropology* 100(2), pp. 207–224.

Feldmar, J., J. Declerck, G. Malandain, et al. (1997). “Extension of the ICP Algorithm to Nonrigid Intensity-Based Registration of 3D Volumes”. In: *Computer Vision and Image Understanding* 66(2), pp. 193–206.

Finnish National Agency for Medicines (2008). *The 2006 Implant Yearbook on Orthopaedic Endoprostheses: Finnish Arthroplasty Register*. Tech. rep. Finland: National Agency for Medicines.

Fitzpatrick, C., D. FitzPatrick, D. Auger, et al. (2007). "A tibial-based coordinate system for three-dimensional data". In: *The Knee* 14(2), pp. 133–137.

Frangi, A. F., D. Rueckert, J. A. Schnabel, et al. (2002). "Automatic construction of multiple-object three-dimensional statistical shape models: Application to cardiac modeling". In: *IEEE Transactions on Medical Imaging* 21(9), pp. 1151–1166.

Freeman, M. (2001). "How the knee moves". In: *Current Orthopaedics* 15(6), pp. 444–450.

Freeman, M. A. R. and V. Pinskerova (2005). "The movement of the normal tibio-femoral joint". In: *Journal of Biomechanics* 38(2), pp. 197–208.

Fripp, J., S. K. Warfield, S. Crozier, et al. (2006). "Automatic Segmentation of the Knee Bones using 3D Active Shape Models". In: *Pattern Recognition, 2006. ICPR 2006. 18th International Conference on*. IEEE, pp. 167–170.

Fuiko, R. and A. Zembsch (2003). "Osteointegration and Implant Position After Cementless Total Knee Replacement". In: *Clinical Orthopaedics and Related Research* 408, pp. 201–208.

Fukuoka, S., K. Yoshida, and Y. Yamano (2000). "Estimation of the migration of tibial components in total knee arthroplasty: A roentgen stereophotogrammetric analysis". In: *The Journal of Bone and Joint Surgery* 82-B(2), pp. 222–7.

Galloway, F., R. Bryan, M. Taylor, et al. (2010). "An improved registration scheme with application to statistical shape modelling of the human femur". In: *Computer Methods in Biomechanics and Biomedical Engineering*. Valencia.

Galloway, F., M. Kahnt, H. Ramm, et al. (2012). "A large scale finite element study of a cementless osseointegrated tibial tray". In: *Journal of Biomechanics* Submitted.

Galloway, F., M. Kahnt, H. Seim, et al. (2010). "A large scale finite element study of an osseointegrated cementless tibial tray". In: *Proceedings of the International Society for Technology in Arthroplasty*. Dubai.

Galloway, F., P. B. Nair, and M. Taylor (2012). "Population based finite element study of the effect of under sizing a cementless tibial tray on primary stability". In: *Transactions of Orthopaedic Research Society*. San Francisco, CA.

Galloway, F., P. Worsley, M. Stokes, et al. (2012). "Development of a statistical model of knee kinetics for applications in pre-clinical testing". In: *Journal of Biomechanics* 45(1), pp. 191–195.

Gandhi, R., D. Tsvetkov, J. R. Davey, et al. (2009). "Survival and clinical function of cemented and uncemented prostheses in total knee replacement: a meta-analysis." In: *The Journal of Bone and Joint Surgery* 91-B(7), pp. 889–895.

Ghanem, R. and A. Doostan (2006). "On the construction and analysis of stochastic models: Characterization and propagation of the errors associated with limited data". In: *Journal of Computational Physics* 217(1), pp. 63–81.

Glocker, B., N. Komodakis, G. Tziritas, et al. (2008). "Dense image registration through MRFs and efficient linear programming". In: *Medical Image Analysis* 12(6), pp. 731–741.

Goldstein, S. A., D. L. Wilson, D. A. Sonstegard, et al. (1983). "The mechanical properties of human tibial trabecular bone as a function of metaphyseal location". In: *Journal of Biomechanics* 16(12), pp. 965–969.

Gonzalez, M. H. and A. O. Mekhail (2004). "The Failed Total Knee Arthroplasty: Evaluation and Etiology". In: *The Journal of the American Academy of Orthopaedic Surgeons* 12(6), pp. 436–446.

Gorisse, D., K. Crombecq, I. Couckuyt, et al. (2010). "A Surrogate Modeling and Adaptive Sampling Toolbox for Computer Based Design". In: *Journal of Machine Learning Research* 11, pp. 2051–2055.

Gray, H. (1918). *Anatomy of the human body*. 20th ed. Philadelphia, PA, USA: Lea & Febiger.

Grewal, R., M. G. Rimmer, and M. A. R. Freeman (1992). "Early migration of prostheses related to long-term surviorship". In: *Bone and Joint Surgery* 74-B(2), pp. 239–242.

Guo, X. E. (2001). "Mechanical Properties of Cortical Bone and Cancellous Tissue". In: *Bone Mechanics Handbook*. Ed. by S. C. Cowin. 2nd. New York: Informa Healthcare. Chap. 10, pp. 1–23.

Halloran, J. P., A. J. Petrella, and P. J. Rullkoetter (2005). "Explicit finite element modeling of total knee replacement mechanics". In: *Journal of Biomechanics* 38(2), pp. 323–331.

Hasegawa, I., K. Uenishi, T. Fukunaga, et al. (2009). "Stature estimation formulae from radiographically determined limb bone length in a modern Japanese population". In: *Legal Medicine* 11(6), pp. 260–266.

Hashemi, A. and A. Shirazi-Adl (2000). "Finite Element Analysis of Tibial Implants - Effect of Fixation Design and Friction Model". In: *Computer Methods in Biomechanics and Biomedical Engineering* 3(3), pp. 183–201.

Heimann, T., I. Wolf, and H.-P. Meinzer (2006). "Active Shape Models for a Fully Automated 3D Segmentation of the Liver – An Evaluation on Clinical Data". In: *Medical Image Computing and Computer-Assisted Intervention – MICCAI 2006*. Vol. 4191. Lecture Notes in Computer Science. Springer Berlin Heidelberg. Chap. 6, pp. 41–48.

Heinlein, B., I. Kutzner, F. Graichen, et al. (2009). "ESB Clinical Biomechanics Award 2008: Complete data of total knee replacement loading for level walking and stair climbing measured in vivo with a follow-up of 6-10 months." In: *Clinical Biomechanics* 24(4), pp. 315–26.

Helgason, B., E. Perilli, E. Schileo, et al. (2008). "Mathematical relationships between bone density and mechanical properties: A literature review". In: *Clinical Biomechanics* 23(2), pp. 135–46.

Hill, D. L. G., P. G. Batchelor, M. Holden, et al. (2001). "Medical Image Registration". In: *Physics in Medicine and Biology* 46(3), R1–R45.

Hill, P. F., V. Vedi, A. Williams, et al. (2000). "Tibiofemoral movement 2: the loaded and unloaded living knee studied by MRI". In: *The Journal of Bone and Joint Surgery* 82-B(8), pp. 1196–1198.

Hofmann, A. A., J. D. Evanich, R. P. Ferguson, et al. (2001). "Ten- to 14-Year Clinical Followup of the Cementless Natural Knee System". In: *Clinical Orthopaedics and Related Research* 388, pp. 85–94.

Holden, M. (2008). “A Review of Geometric Transformations for Nonrigid Body Registration”. In: *IEEE Transactions on Medical Imaging* 27(1), pp. 111–128.

Holloway, I. P., P. J. Lusty, W. L. Walter, et al. (2010). “Tibial fixation without screws in cementless knee arthroplasty”. In: *The Journal of Arthroplasty* 25(1), pp. 46–51.

Huiskes, R. (1993). “Failed innovation in total hip replacement: Diagnosis and proposals for a cure”. In: *Acta Orthopaedica Scandinavica* 64(6), pp. 699–716.

Huiskes, R. (2000). “If bone is the answer, then what is the question?” In: *Journal of Anatomy* 197(2), pp. 145–156.

Huiskes, R. and B. van Rietbergen (2005). “Biomechanics of Bone”. In: *Basic Orthopaedic Biomechanics and Mechano-Biology*. Ed. by V. C. Mow and R. Huiskes. 3rd. Philadelphia, PA, USA: Lippincott Williams & Wilkins. Chap. 4, pp. 123–179.

Hvid, I. and S. L. Hansen (1986). “Subchondral bone strength in arthrosis: Cadaver studies of tibial condyles”. In: *Acta Orthopaedica* 57(1), pp. 47–51.

Incavo, S. J., P. J. Ronchetti, J. G. Howe, et al. (1994). “Tibial plateau coverage in total knee arthroplasty”. In: *Clinical Orthopaedics and Related Research* (299), pp. 81–85.

ISO 14243-1 (2009). *Implants for surgery - Wear of total knee-joint prostheses - Part 1: Loading and displacement parameters for wear-testing machines with load control and corresponding environmental conditions for test*. Tech. rep. International Organization for Standardization (ISO).

Iwaki, H., V. Pinskerova, and M. A. R. Freeman (2002). “Tibiofemoral movement 1: the shapes and the unloaded cadaver knee”. In: *The Journal of Bone and Joint Surgery* 82-B(8), pp. 1189–1195.

Jasty, M., C. Bragdon, D. Burke, et al. (1997). “In vivo skeletal responses to porous-surfaced implants subjected to small induced motions.” In: *The Journal of Bone and Joint Surgery* 79-A(5), pp. 707–714.

Johal, P., a. Williams, P. Wragg, et al. (2005). “Tibio-femoral movement in the living knee. A study of weight bearing and non-weight bearing knee kinematics using ’interventional’ MRI.” In: *Journal of biomechanics* 38(2), pp. 269–76.

Jolliffe, I. T. (2002). *Principal Component Analysis*. 2nd. New York: Springer-Verlag.

Kadaba, M. P., H. K. Ramakrishnan, and M. E. Wootten (1990). “Measurement of lower extremity kinematics during level walking”. In: *Journal of Orthopaedic Research* 8(3), pp. 383–392.

Kahnt, M., F. Galloway, H. Seim, et al. (2011). “Robust and Intuitive Meshing of Bone-Implant Compounds”. In: *Jahrestagung der Deutschen Gesellschaft für Computer- und Roboterassistierte Chirurgie e. V.(CURAC)*, pp. 71–74.

Kass, M., A. Witkin, and D. Terzopoulos (1988). “Snakes: Active Contour Models”. In: *International Journal of Computer Vision* 1(4), pp. 321–331.

Kaus, M. R., V. Pekar, C. Lorenz, et al. (2003). “Automated 3-D PDM Construction From Segmented Images Using Deformable Models”. In: *IEEE Transactions on Medical Imaging* 22(8), pp. 1005–1013.

Keaveny, T. M., E. F. Morgan, G. L. Niebur, et al. (2001). “Biomechanics of Trabecular Bone”. In: *Annual Review of Biomedical Engineering* 3, pp. 307–333.

Keaveny, T. M., E. F. Wachtel, C. M. Ford, et al. (1994). “Differences between the tensile and compressive strengths of bovine tibial trabecular bone depend on modulus”. In: *Journal of Biomechanics* 27(9), pp. 1137–1146.

Keja, M., H. W. Wevers, D. Siu, et al. (1994). “Relative motion at the bone-prosthesis interface”. In: *Clinical Biomechanics* 9(5), pp. 275–283.

Khaw, F. M., L. M. G. Kirk, R. W. Morris, et al. (2002). “A randomised, controlled trial of cemented versus cementless press-fit condylar total knee replacement: Ten-year survival analysis”. In: *Journal of Bone and Joint Surgery* 84B(5), pp. 658–666.

Klein, S., M. Staring, and J. P. W. Pluim (2007). “Evaluation of Optimization Methods for Nonrigid Medical Image Registration Using Mutual Information and B-Splines”. In: *IEEE Transactions on Image Processing* 16(12), pp. 2879–2890.

Knight, L. A., S. Pal, J. C. Coleman, et al. (2007). “Comparison of long-term numerical and experimental total knee replacement wear during simulated gait loading.” In: *Journal of Biomechanics* 40(7), pp. 1550–1558.

Kopperdahl, D. L. and T. M. Keaveny (1998). “Yield strain behavior of trabecular bone”. In: *Journal of Biomechanics* 31(7), pp. 601–608.

Kutzner, I., B. Heinlein, F. Graichen, et al. (2010). “Loading of the knee joint during activities of daily living measured in vivo in five subjects”. In: *Journal of Biomechanics* 43(11), pp. 2164–2173.

Lafortune, M., P. Cavanagh, H. Sommer, et al. (1992). “Three-dimensional kinematics of the human knee during walking”. In: *Journal of Biomechanics* 25(4), pp. 347–357.

Laz, P. J., S. Pal, J. P. Halloran, et al. (2006). “Probabilistic finite element prediction of knee wear simulator mechanics”. In: *Journal of Biomechanics* 39(12), pp. 2303–2310.

Leardini, A., L. Chiari, U. Della Croce, et al. (2005). “Human movement analysis using stereophotogrammetry: Part 3. Soft tissue artifact assessment and compensation”. In: *Gait & Posture* 21(2), pp. 212–225.

Lee, R. W., R. G. Volz, and D. C. Sheridan (1991). “The role of fixation and bone quality on the mechanical stability of tibial knee components”. In: *Clinical Orthopaedics and Related Research* (273), pp. 177–183.

Lemaire, P., D. P. Pioletti, F. M. Meyer, et al. (1997). “Tibial component positioning in total knee arthroplasty: bone coverage and extensor apparatus alignment”. In: *Knee Surgery, Sports Traumatology, Arthroscopy* 5(4), pp. 251–7.

Levitz, C. L., P. A. Lotke, and J. S. Karp (1995). “Long-Term Changes in Bone Mineral Density Following Total Knee Replacement”. In: *Clinical Orthopaedics and Related Research* 321, pp. 68–72.

Li, M. G. and K. G. Nilsson (2000). “The effect of the preoperative bone quality on the fixation of the tibial component in total knee arthroplasty”. In: *The Journal of Arthroplasty* 15(6), pp. 744–53.

Lindahl, O. (1976). “Mechanical properties of dried defatted spongy bone”. In: *Acta Orthopaedica Scandinavica* 47(1), pp. 11–19.

Linde, F., I. Hvid, and F. Madsen (1992). “The effect of specimen geometry on the mechanical behaviour of trabecular bone specimens”. In: *Journal of Biomechanics* 25(4), pp. 359–68.

Lombardi, A. V., C. C. Berasi, and K. R. Berend (2007). “Evolution of Tibial Fixation in Total Knee Arthroplasty”. In: *The Journal of Arthroplasty* 22(4, Supplement 1), pp. 25–29.

Maintz, J. B. A. and M. A. Viergever (1998). “A survey of medical image registration”. In: *Medical Image Analysis* 2(1), pp. 1–36.

Mann, K. A., D. C. Ayers, F. W. Werner, et al. (1997). “Tensile strength of the cement-bone interface depends on the amount of bone interdigitated with PMMA cement”. In: *Journal of Biomechanics* 30(4), pp. 339–346.

Mann, K. A., M. A. Miller, R. J. Cleary, et al. (2008). “Experimental micromechanics of the cement-bone interface.” In: *Journal of Orthopaedic Research* 26(6), pp. 872–9.

Martin, S. D., J. L. McManus, R. D. Scott, et al. (1997). “Press-Fit Condylar total knee arthroplasty: 5- to 9-year follow-up evaluation”. In: *Journal of Arthroplasty* 12(6), pp. 603–614.

Maurer, C. R., R. J. Maciunas, and J. M. Fitzpatrick (1998). “Registration of head CT images to physical space using a weighted compination of points and surfaces”. In: *IEEE Transactions on Medical Imaging* 17(5), pp. 753–761.

McInerney, T. and D. Terzopoulos (1996). “Deformable models in medical image analysis: a survey”. In: *Medical Image Analysis* 1(2), pp. 91–108.

Miller, C. W. and R. Pettygrow (2001). “Long-Term Clinical and Radiographic Results of a Pegged Tibial Baseplate in Primary Total Knee Arthroplasty”. In: *The Journal of Arthroplasty* 16(1), pp. 70–75.

Miyoshi, S., T. Takahashi, M. Ohtani, et al. (2002). “Analysis of the shape of the tibial tray in total knee arthroplasty using a three dimension finite element model”. In: *Clinical Biomechanics* 17(7), pp. 521–525.

Morgan, E. F., H. H. Bayraktar, and T. M. Keaveny (2003). “Trabecular bone modulus-density relationships depend on anatomic site”. In: *Journal of Biomechanics* 36(7), pp. 897–904.

Morgan, E. F. and T. M. Keaveny (2001). “Dependence of yield strain of human trabecular bone on anatomic site”. In: *Journal of Biomechanics* 34(5), pp. 569–577.

Morlock, M., E. Schneider, A. Bluhm, et al. (2001). “Duration and frequency of every day activities in total hip patients”. In: *Journal of biomechanics* 34(7), pp. 873–81.

Morrison, J. B. (1970). “The mechanics of the knee joint in relation to normal walking”. In: *Journal of Biomechanics* 3(1), pp. 51–61.

Moshfeghi, M., S. Ranganath, and K. Nawyn (1994). “Three-Dimensional Elastic Matching of Volumes”. In: *IEEE Transactions on Image Processing* 3(2), pp. 128–138.

Murphy, K., B. Ginneken, J. P. W. Pluim, et al. (2008). “Semi-automatic Reference Standard Construction for Quantitative Evaluation of Lung CT Registration”. In: *Medical Image Computing and Computer-Assisted Intervention – MICCAI 2008*. Vol. 5242. Lecture Notes in Computer Science. Berlin: Springer Berlin Heidelberg. Chap. 121, pp. 1006–1013.

Nagura, T., C. O. Dyrby, E. J. Alexander, et al. (2002). “Mechanical loads at the knee joint during deep flexion”. In: *Journal of Orthopaedic Research* 20(4), pp. 881–886.

Nakagawa, S., Y. Kadoya, S. Todo, et al. (2000). “Tibiofemoral movement 3: full flexion in the living knee studied by MRI”. In: *The Journal of Bone and Joint Surgery* 82-B(8), pp. 1199–1200.

National Joint Registry for England and Wales (2010). *National Joint Registry for England and Wales 7th Annual Report*. Tech. rep. National Joint Registry, pp. 1–128.

National Joint Registry for England and Wales (2011). *National Joint Registry for England and Wales 8th Annual Report*. Tech. rep. Hemel Hempstead, UK: National Joint Registry, pp. 1–170.

New Zealand Orthopaedic Association (2010). *The New Zealand Joint Registry: Eleven Year Report*. Tech. rep. January 1999. Christchurch, NZ: New Zealand Orthopaedic Association.

NHANES (1999). *National Health and Nutrition Examination Survey Data*. Tech. rep. Hyattsville, MD: Centers for Disease Control and Prevention (CDC).

Nilsson, K. G., J. Kärrholm, L. Carlsson, et al. (1999). "Hydroxyapatite coating versus cemented fixation of the tibial component in total knee arthroplasty: prospective randomized comparison of hydroxyapatite-coated and cemented tibial components with 5-year follow-up using radiostereometry". In: *The Journal of Arthroplasty* 14(1), pp. 9–20.

Palastanga, N., D. Field, and R. Soames (2002). *Anatomy and Human Movement*. 4th. Edinburgh: Butterworth-Heinemann.

Perillo-Marcone, A., L. Ryd, K. Johnsson, et al. (2004). "A combined RSA and FE study of the implanted proximal tibia: correlation of the post-operative mechanical environment with implant migration". In: *Journal of Biomechanics* 37(8), pp. 1205–1213.

Perillo-Marcone, A. and M. Taylor (2007). "Effect of Varus/Valgus Malalignment on Bone Strains in the Proximal Tibia after TKR: An Explicit Finite Element Study". In: *Journal of Biomechanical Engineering* 129(1), pp. 1–11.

Petersen, M. M., P. T. Nielsen, A. Lebech, et al. (1999). "Preoperative bone mineral density of the proximal tibia and migration of the tibial component after uncemented total knee arthroplasty". In: *The Journal of Arthroplasty* 14(1), pp. 77–81.

Pilliar, R. M., J. M. Lee, and C. Maniatopoulos (1986). "Observations on the Effect of Movement on Bone Ingrowth into Porous-Surfaced Implants". In: *Clinical Orthopaedics and Related Research* (208), pp. 108–113.

Prendergast, P. J. (1997). "Finite element models in tissue mechanics and orthopaedic implant design". In: *Clinical Biomechanics* 12(6), pp. 343–366.

Primal Pictures Ltd (2009). *Functional Anatomy*. London.

Primal Pictures Ltd (2010). *Interactive Knee*. London.

Querol, L. B., P. Büchler, D. Rueckert, et al. (2006). "Statistical Finite Element Model for Bone Shape and Biomechanical Properties". In: *Medical Image Computing and Computer-Assisted Intervention – MICCAI 2006*. Vol. 4190. Lecture Notes in Computer Science. Springer Berlin Heidelberg. Chap. 50, pp. 405–411.

Radcliffe, I. A. J. and M. Taylor (2007a). "Investigation into the affect of cementing techniques on load transfer in the resurfaced femoral head: a multi-femur finite element analysis". In: *Clinical Biomechanics* 22(4), pp. 422–30.

Radcliffe, I. A. J. and M. Taylor (2007b). "Investigation into the effect of varus-valgus orientation on load transfer in the resurfaced femoral head: A multi-femur finite element analysis". In: *Clinical Biomechanics* 22(7), pp. 780–786.

Rakotomanana, R. L., P. F. Leyvraz, A. Curnier, et al. (1992). “A finite element model for evaluation of tibial prosthesis-bone interface in total knee replacement”. In: *Journal of Biomechanics* 25(12), pp. 1413–1424.

Rasmussen, J., M. Damsgaard, and M. Voigt (2001). “Muscle recruitment by the min/max criterion — a comparative numerical study”. In: *Journal of Biomechanics* 34(3), pp. 409–415.

Rawlinson, J. J., L. E. Peters, D. A. Campbell, et al. (2005). “Cancellous Bone Strains Indicate Efficacy of Stem Augmentation in Constrained Condylar Knees”. In: *Clinical Orthopaedics and Related Research* 440, pp. 107–116.

Reid, S. M., R. B. Graham, and P. A. Costigan (2010). “Differentiation of young and older adult stair climbing gait using principal component analysis”. In: *Gait & Posture* 31(2), pp. 197–203.

Riemer, R., E. T. Hsiao-Wecksler, and X. Zhang (2008). “Uncertainties in inverse dynamics solutions: A comprehensive analysis and an application to gait”. In: *Gait & Posture* 27(4), pp. 578–588.

Ritter, M. A. (1997). “Postoperative pain after total knee arthroplasty”. In: *The Journal of Arthroplasty* 12(3), pp. 337–339.

Robinson, R. P. (2005). “The early innovators of today’s resurfacing condylar knees”. In: *The Journal of Arthroplasty* 20(1 (S1)), pp. 2–26.

Røhl, L., E. Larsen, F. Linde, et al. (1991). “Tensile and compressive properties of cancellous bone”. In: *Journal of Biomechanics* 24(12), pp. 1143–1149.

Rueckert, D., L. I. Sonoda, C. Hayes, et al. (1999). “Nonrigid Registration Using Free-Form Deformations: Application to Breast MR Images”. In: *IEEE Transactions on Medical Imaging* 18(8), pp. 712–721.

Rueckert, D., A. F. Frangi, and J. A. Schnabel (2003). “Automatic Construction of 3-D Statistical Deformation Models of the Brain Using Nonrigid Registration”. In: *IEEE Transactions on Medical Imaging* 22(8), pp. 1014–1025.

Ryd, L., B. E. Albrektsson, L. Carlsson, et al. (1995). “Roentgen stereophotogrammetric analysis as a predictor of mechanical loosening of knee prostheses”. In: *Surgery* 77(3), pp. 377–383.

Ryd, L., A. Lindstrand, A. Stenström, et al. (1990). “Porous coated anatomic tricompartmental tibial components. The relationship between prosthetic position and micromotion”. In: *Clinical Orthopaedics and Related Research* 251, pp. 189–197.

Schnabel, J. A., D. Rueckert, M. Quist, et al. (2001). “A Generic Framework for Non-rigid Registration Based on Non-uniform Multi-level Free-Form Deformations”. In: *Lecture Notes in Computer Science*. Vol. 22. 8. Berlin / Heidelberg: Springer-Verlag. Chap. Medical Im, pp. 573–581.

Sharkey, P. F., W. J. Hozack, R. H. Rothman, et al. (2002). “Why are total knee arthroplasties failing today?” In: *Clinical Orthopaedics and Related Research* 404, pp. 7–13.

Shelburne, K. B., M. R. Torry, and M. G. Pandy (2006). “Contributions of Muscles, Ligaments, and the Ground-Reaction Force to Tibiofemoral Joint Loading During Normal Gait”. In: *Journal of Orthopaedic Research* 24(10), pp. 1983–90.

Stammberger, T., J. Hohe, K.-H. Englmeier, et al. (2000). “Elastic Registration of 3D Cartilage Surfaces From MR Image Data for Detecting Local Changes in Cartilage Thickness”. In: *Magnetic Resonance in Medicine* 44, pp. 592–601.

Staring, M., S. Klein, and J. P. W. Pluim (2007). “Nonrigid registration with tissue-dependent filtering of the deformation field”. In: *Physics in Medicine and Biology* 52(23), pp. 6879–92.

Stern, S. H., R. D. Wills, and J. L. Gilbert (1997). “The effect of tibial stem design on component micromotion in knee arthroplasty”. In: *Clinical Orthopaedics and Related Research* (345), pp. 44–52.

Strickland, M. A. and M. Taylor (2009). “In-silico wear prediction for knee replacements—methodology and corroboration”. In: *Journal of Biomechanics* 42(10), pp. 1469–1474.

Subsol, G., J.-P. Thirion, and N. Ayache (1998). “A scheme for automatically building three-dimensional morphometric anatomical atlases: application to a skull atlas”. In: *Medical Image Analysis* 2(1), pp. 37–60.

Swedish Knee Arthroplasty Register (2008). *The Swedish Knee Arthroplasty Register Annual Report 2008*. Tech. rep. Lund, Sweden: Department of Orthopedics, Lund University Hospital.

Swedish Knee Arthroplasty Register (2010). *The Swedish Knee Arthroplasty Register Annual Report 2010*. Tech. rep. Lund, Sweden: Department of Orthopedics, Lund University Hospital.

Taddei, F., A. Pancanti, and M. Viceconti (2004). “An improved method for the automatic mapping of computed tomography numbers onto finite element models”. In: *Medical Engineering & Physics* 26(1), pp. 61–69.

Taylor, M. and K. E. Tanner (1997). “Fatigue failure of cancellous bone: a possible cause of implant migration and loosening”. In: *The Journal of Bone and Joint Surgery* 79-B(2), pp. 181–182.

Taylor, M., K. E. Tanner, and M. A. Freeman (1998). “Finite element analysis of the implanted proximal tibia: a relationship between the initial cancellous bone stresses and implant migration”. In: *Journal of Biomechanics* 31(4), pp. 303–310.

Taylor, M., D. S. Barrett, and D. Deffenbaugh (2012). “Influence of loading and activity on the primary stability of cementless tibial trays”. In: *Journal of Orthopaedic Research*.

Taylor, S. J. and P. S. Walker (2001). “Forces and moments telemetered from two distal femoral replacements during various activities”. In: *Journal of Biomechanics* 34(7), pp. 839–848.

Taylor, W. R., M. O. Heller, G. Bergmann, et al. (2004). “Tibio-femoral loading during human gait and stair climbing”. In: *Journal of Orthopaedic Research* 22(3), pp. 625–632.

Tissakht, M., H. Eskandari, and A. M. Ahmed (1995). “Micromotion analysis of the fixation of total knee tibial component”. In: *Computers and Structures* 56(2/3), pp. 365–375.

Trew, M. and T. Everett (2001). *Human Movement: An Introductory Text*. 4th. Churchill Livingstone.

Vince, K. G. (2003). “Why knees fail”. In: *The Journal of Arthroplasty* 18(3 (S1)), pp. 39–44.

Vollmer, J., R. Mencl, and H. Muller (1999). “Improved Laplacian Smoothing of Noisy Surface Meshes”. In: *Computer Graphics Forum* 18(3), pp. 131–138.

Vos, F. M., P. W. de Bruin, J. G. M. Aubel, et al. (2004). “A statistical shape model without using landmarks”. In: *Pattern Recognition, 2004. ICPR 2004. Proceedings of the 17th International Conference on*. IEEE, pp. 714–717.

Waanders, D., D. Janssen, K. A. Mann, et al. (2010). “The mechanical effects of different levels of cement penetration at the cement-bone interface.” In: *Journal of biomechanics* 43(6), pp. 1167–1175.

Walker, P. S., D. Greene, D. Reilly, et al. (1981). “Fixation of Tibial Components of Knee Prostheses”. In: *The Journal of Bone and Joint Surgery* 63(2), pp. 258–267.

Walker, P. S. and S. Sathasivam (2000). “Design forms of total knee replacement”. In: *Proceedings of the Institution of Mechanical Engineers, Part H: Journal of Engineering in Medicine* 214(3), pp. 101–119.

Walker, P. S. (2005). “Biomechanics of Total Knee Replacement Designs”. In: *Basic Orthopaedic Biomechanics and Mechano-Biology*. Ed. by V. C. Mow and R. Huiskes. 3rd. Philadelphia, PA, USA: Lippincott Williams & Wilkins. Chap. 15, pp. 657–702.

Walker, P. S., G. W. Blunn, D. R. Broome, et al. (1997). “A knee simulating machine for performance evaluation of total knee replacements”. In: *Journal of Biomechanics* 30(1), pp. 83–89.

Westrich, G., M. A. Agulnick, R. S. Laskin, et al. (1997). “Current analysis of tibial coverage in total knee arthroplasty”. In: *The Knee* 4(2), pp. 87–91.

Winter, D. A. (1990). *Biomechanics and Motor Control of Human Movement*. 2nd. New York: John Wiley & Sons, Inc., pp. 51–52.

Wong, J., N. Steklov, S. Patil, et al. (2010). “Predicting the effect of tray malalignment on risk for bone damage and implant subsidence after total knee arthroplasty”. In: *Journal of Orthopaedic Research* 29(3), pp. 347–353.

Worsley, P. (2011). “Assessment of Short-term Knee Arthroplasty Function using Clinical Measures, Motion Analysis, and Musculoskeletal Modelling”. PhD thesis. University of Southampton, pp. 1–243.

Worsley, P., M. Stokes, and M. Taylor (2011). “Predicted knee kinematics and kinetics during functional activities using motion capture and musculoskeletal modelling in healthy older people.” In: *Gait & Posture* 33(2), pp. 268–273.

Yang, Y., A. Bull, D. Rueckert, et al. (2006). “3D Statistical Shape Modeling of Long Bones”. In: *Biomedical Image Registration*. Vol. 11. 1. Berlin / Heidelberg: Springer-Verlag, pp. 306–314.

Yang, Y., D. Rueckert, and A. Bull (2008). “Predicting the shapes of bones at a joint: application to the shoulder”. In: *Computer Methods in Biomechanics and Biomedical Engineering* 11(1), pp. 19–30.

Yoshii, I., L. A. Whiteside, M. T. Milliano, et al. (1992). “The effect of central stem and stem length on micromovement of the tibial tray”. In: *The Journal of Arthroplasty* 7(S1), pp. 433–438.

Young, P. G., T. B. H. Beresford-West, S. R. L. Coward, et al. (2008). “An efficient approach to converting three-dimensional image data into highly accurate computational models”. In:

Philosophical Transactions of the Royal Society A: Mathematical, Physical and Engineering Sciences 366(1878), pp. 3155–3173.

Zilske, M., H. Lamecker, and S. Zachow (2008). "Adaptive Remeshing of Non-Manifold Surfaces". In: *Eurographics 2008 Annex to the Conference Proceedings*, pp. 211–214.

Appendix A

Publications

The work described in this thesis has led to the following conference publications:

- F. Galloway, R. Bryan, et al. (2010). "An improved registration scheme with application to statistical shape modelling of the human femur". In: *Computer Methods in Biomechanics and Biomedical Engineering*. Valencia
- F. Galloway, M. Kahnt, H. Seim, et al. (2010). "A large scale finite element study of an osseointegrated cementless tibial tray". In: *Proceedings of the International Society for Technology in Arthroplasty*. Dubai
- M. Kahnt et al. (2011). "Robust and Intuitive Meshing of Bone-Implant Compounds". In: *Jahrestagung der Deutschen Gesellschaft für Computer- und Roboterassistierte Chirurgie e. V.(CURAC)*, pp. 71–74
- F. Galloway, P. B. Nair, et al. (2012). "Population based finite element study of the effect of under sizing a cementless tibial tray on primary stability". In: *Transactions of Orthopaedic Research Society*. San Francisco, CA

The following Journal papers have been accepted or submitted for peer review:

- F. Galloway, P. Worsley, et al. (2012). "Development of a statistical model of knee kinetics for applications in pre-clinical testing". In: *Journal of Biomechanics* 45(1), pp. 191–195
- F. Galloway, M. Kahnt, H. Ramm, et al. (2012). "A large scale finite element study of a cementless osseointegrated tibial tray". In: *Journal of Biomechanics* Submitted